



HAL
open science

Investigation of PV soiling and condensation in desert environments via outdoor microscopy

Benjamin Figgis

► **To cite this version:**

Benjamin Figgis. Investigation of PV soiling and condensation in desert environments via outdoor microscopy. Mechanics of materials [physics.class-ph]. Université de Strasbourg, 2018. English. NNT : 2018STRAD006 . tel-01827881

HAL Id: tel-01827881

<https://theses.hal.science/tel-01827881>

Submitted on 2 Jul 2018

HAL is a multi-disciplinary open access archive for the deposit and dissemination of scientific research documents, whether they are published or not. The documents may come from teaching and research institutions in France or abroad, or from public or private research centers.

L'archive ouverte pluridisciplinaire **HAL**, est destinée au dépôt et à la diffusion de documents scientifiques de niveau recherche, publiés ou non, émanant des établissements d'enseignement et de recherche français ou étrangers, des laboratoires publics ou privés.

**ÉCOLE DOCTORALE MATHÉMATIQUES, SCIENCES DE L'INFORMATION ET DE
L'INGÉNIEUR - ED 269**

**ICube : UMR 7357 CNRS-Université de Strasbourg
Laboratoire des sciences de l'ingénieur, de l'informatique et de l'imagerie**

THÈSE présentée par :

Benjamin W. FIGGIS

soutenue le: 6 Avril 2018

pour obtenir le grade de: Docteur de l'université de Strasbourg

Discipline/ Spécialité: Mécanique des Matériaux

**Investigation of PV Soiling and
Condensation in Desert Environments
via Outdoor Microscopy**

THÈSE dirigée par :

Mr Said AHZI

Professor, Hamad bin Khalifa University, QEERI, QF, Qatar &
Professeur, Université de Strasbourg, France

Mr Yves RÉMOND

Professeur, Université de Strasbourg, France

RAPPORTEURS :

Mr Jörg BAGDAHN

President, Anhalt University of Applied Sciences, Germany

Mr Alain DOLLET

Directeur de Recherche, Directeur du Laboratoire PROMES — CNRS, France

AUTRES MEMBRES DU JURY :

Examineurs:

Mr Abdullah OUGAZZADEN

(President du jury) Professeur & Directeur, Geogise Tech Lorraine, France

Mr Ahmed ENNAOUI

President of Scientific Council, IRESEN, Morocco

Investigation of PV Soiling and Condensation in Desert Environments via Outdoor Microscopy

Résumé

La salissure des modules photovoltaïques (PV) dégrade grandement leurs performances dans les environnements désertiques. Les études précédentes en extérieur ont tendance à trouver de faibles corrélations entre les taux de salissure et les paramètres météorologiques. On pensait que l'une des raisons était le long intervalle de mesure - jours ou semaines - des techniques traditionnelles de mesure des salissures sur le terrain. Dans la présente étude, un «microscope de souillure extérieur» (OSM) a été développé pour mesurer le dépôt et le détachement de particules de poussière individuelles, toutes les 10 minutes, dans des conditions extérieures, de jour comme de nuit. En utilisant une paire d'OSM graissés et non graissés, il était en outre possible de séparer les salissures en trois vitesses de flux de poussière de composants - dépôt, rebondissement immédiat et remise en suspension retardée. Les OSM ont été utilisés pour mesurer les taux de flux dans des expériences sur le terrain à Doha, au Qatar. La nouvelle méthode a révélé des effets explicatifs de paramètres environnementaux qui avaient auparavant été obscurcis par de longs intervalles de mesure des salissures et des taux de flux de poussière confondus. L'OSM pouvait également mesurer l'apparition et la croissance de gouttelettes de condensation microscopiques dans des conditions de terrain et de laboratoire. De telles expériences, ainsi que des mesures isothermes et des analyses de composition, ont démontré que la condensation sur les surfaces sales au terrain d'études était fortement influencée par la présence de matière hygroscopique dans la poussière autre que NaCl. En raison de cette matière, la condensation microscopique peut persister à la surface même si elle est bien supérieure à la température du point de rosée. Les résultats de l'étude suggèrent que la souillure des modules photovoltaïques pourrait être atténuée en tirant parti des variations naturelles des conditions météorologiques au cours de la journée.

Mots-clés: Photovoltaïque, salissure, dépôt, condensation, microscopie, hygroscopique

Abstract

Soiling of photovoltaic (PV) modules greatly degrades their performance in desert environments. Previous field studies have tended to find weak correlations between the soiling rate and weather parameters. It was thought that one reason was the long measurement interval — days or weeks — of conventional field soiling measurement techniques. In the present study, an “outdoor soiling microscope” (OSM) was developed able to measure deposition and detachment of individual dust particles, every 10 minutes, in outdoor conditions, day and night. By using a greased and ungreased pair of OSMs, it was further possible to separate soiling into three component dust flux rates — deposition, immediate rebound, and delayed resuspension. OSMs were used to measure flux rates in field experiments in Doha, Qatar. The novel method revealed explanatory effects of environmental parameters that had previously been obscured by limits of conventional long soiling measurement intervals and confounded dust flux rates. The OSM could also measure the onset and growth of microscopic condensation droplets in field and laboratory settings. Such experiments, along with isotherm measurements and composition analysis, demonstrated that condensation on soiled surfaces at the test site was strongly influenced by the presence of hygroscopic matter in the dust other than NaCl. Because of such matter, microscopic condensation could persist on both hydrophilic and hydrophobic surfaces well above the dew-point temperature. Results of the study suggest that soiling of PV modules might be mitigated by taking advantage of natural time-of-day variations in weather conditions.

Keywords: Photovoltaic, soiling, deposition, condensation, microscopy, hygroscopic

Contents

Résumé de Thèse	6
Acknowledgements	17
Abbreviations.....	18
1. Introduction	20
1.1. Motivation	20
1.2. Background and Objectives	22
1.3. Research Program	24
2. Review of PV Soiling Measurement and Modeling.....	26
2.1. PV Soiling Problem	26
2.2. Soiling Modeling	28
2.3. Soiling Measurement	35
3. Review of Dust Particle Mechanics.....	40
3.1. Deposition.....	41
3.2. Rebound.....	55
3.3. Resuspension	59
3.4. Overview of Adhesion Mechanisms.....	67
4. Review of Moisture in Soiling	71
4.1. Relative Humidity.....	71
4.2. Surface–Dew Point Temperature Difference	73
4.3. Hygroscopic Material	75
4.4. Surface Wettability	77
5. Part I – Development of Outdoor Soiling Microscope.....	80
5.1. Design	80
5.2. Image Evaluation.....	82
5.3. Relation to Soil Mass and Light Transmission	85
5.4. Dust Flux Rate Calculation	87
5.5. Comparison and Future Development.....	91
6. Part II – Explanation of Soiling Variation	93
6.1. Experiment Set-Up.....	93

6.2.	Dust Flux Distribution Analysis.....	95
6.3.	Correlations between Environmental Parameters	99
6.4.	Dust Flux Relations to Environmental Parameters	101
6.5.	Dust Flux Models.....	117
7.	Part III – Condensation Causes and Effects.....	129
7.1.	Experiments	130
7.2.	Results and Discussion	138
8.	Summary and Conclusions.....	154
9.	References	161

Résumé de Thèse

Étude des Salissures et de la Condensation PV dans des Environnements Désertiques par Microscopie Extérieure

Introduction

Le but de cette étude est d'améliorer la compréhension des mécanismes d'accumulation de poussière sur les modules photovoltaïques (PV) dans les environnements désertiques. Des systèmes PV à grande échelle sont déployés dans les régions arides, où l'accumulation de salissures peut réduire considérablement leur production d'énergie [1]. Le taux de salissure est régi par des paramètres environnementaux, mais les recherches antérieures n'ont pas clairement déterminé leurs effets [2][3]. En outre, il est connu que l'humidité joue un rôle important dans l'adhérence de la poussière aux surfaces [4], et peut conduire à la cimentation [5], cependant la condensation sur les surfaces souillées dans les conditions ambiantes n'a pas été complètement étudiée.

On pensait que l'une des principales raisons expliquant les faibles corrélations entre le taux de salissure et les paramètres environnementaux trouvés dans des travaux de recherches antérieures était la période de mesure relativement longue de l'accumulation de poussière [3]. Les techniques conventionnelles exposent les surfaces de jours [2] à des mois [6] pour recueillir une quantité mesurable de poussière, alors que les conditions météorologiques changent bien sûr de façon continue. Pour surmonter cette contrainte, un nouveau microscope pour l'analyse du cumul de salissures à l'extérieur, ou «*outdoor soiling microscope*» (OSM), a été développé dans la présente étude. L'OSM est capable de mesurer le dépôt de particules de poussière individuelles toutes les quelques minutes dans des conditions ambiantes (Figure 1). Les OSMs ont ensuite servi à étudier les effets des paramètres météorologiques sur le taux de salissure, la formation de condensation et ses effets sur les surfaces souillées.

Partie I - Développement du microscope à salissure extérieur (OSM)

La conception de base de l'OSM consiste en un microscope portatif de faible puissance, avec un coupon en verre borosilicaté de 5×5 cm fixé à l'avant, et un rétro-éclairage à LED placé derrière le collecteur (voir Figure 1). L'OSM a été connecté par un câble USB à un ordinateur, ce qui permet le déclenchement de la prise des images ainsi que le stockage de celles-ci. Dans cette étude, l'intervalle de prise d'images était généralement fixé à 10 minutes, mais en principe il pouvait être aussi court que quelques secondes.



Figure 1. Un microscope d'analyse de salissures pour l'extérieur (OSM) a été développé pour (i) mesurer le dépôt et le détachement des poussières dans de courts intervalles de temps, et (ii) étudier la formation et la croissance de la condensation dans les conditions ambiantes.

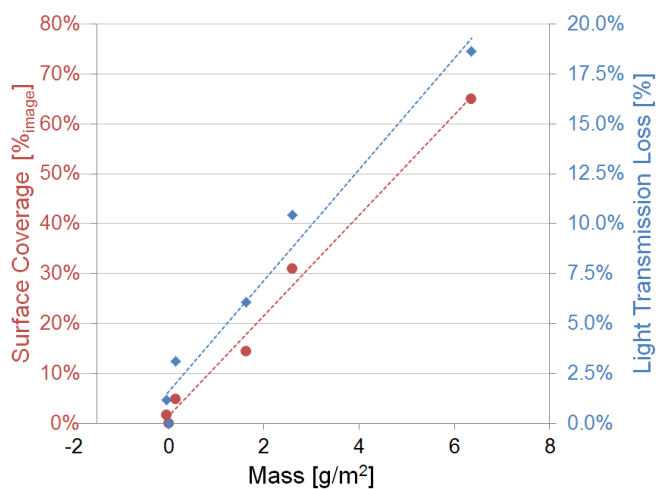


Figure 2. Les mesures de couverture de surface de l'OSM (marqueurs ronds rouges, axe de gauche) et les mesures de perte de transmission de lumière (marqueurs losanges bleus, axe de droite) ont toutes deux répondu approximativement linéairement à la masse de poussière.

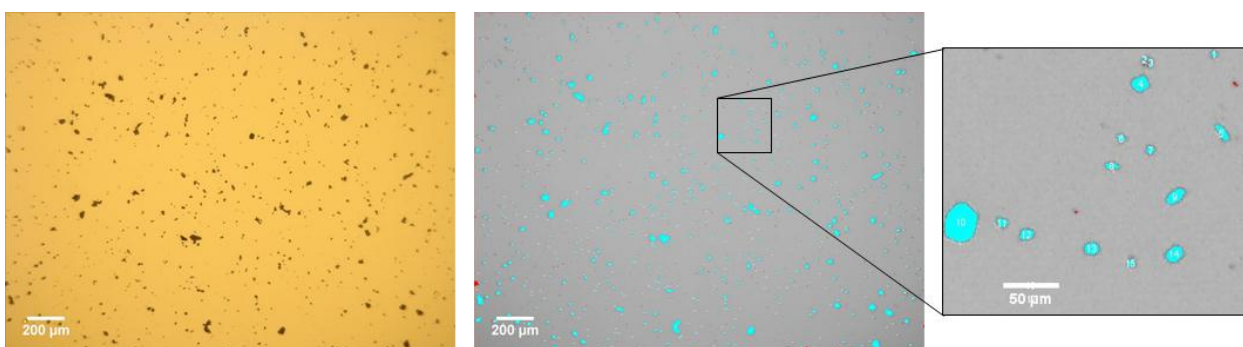


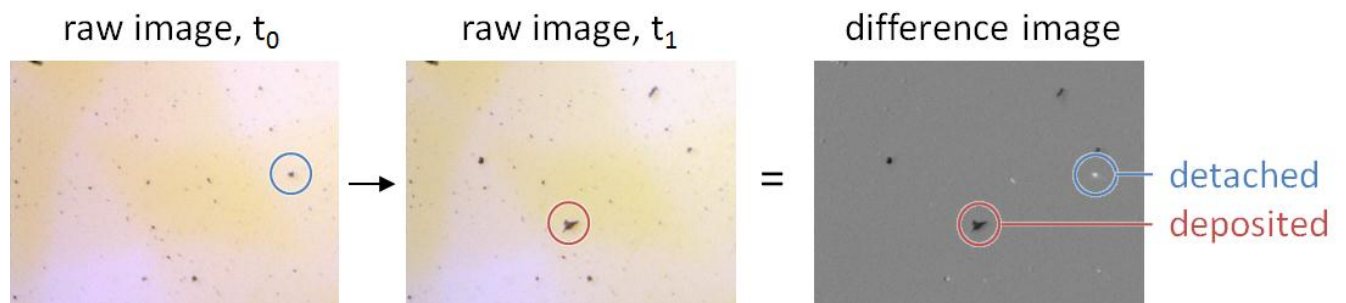
Figure 3. Image OSM brute d'un coupon sale (à gauche), image analysée (au centre) et détail (à droite). Les particules de plus de 4 µm de diamètre équivalent sont masquées en bleu, alors que les plus petites (et celles sur la limite de l'image) sont masquées en rouge.

En comparant des images du même coupon souillé pris avec l'OSM et avec un microscope de laboratoire, on a déterminé que l'OSM pouvait dimensionner de manière fiable des particules d'un diamètre supérieur à environ 4 µm (Figure 3). Les particules plus petites que cette limite ont été rejetées dans les mesures OSM, une simplification acceptable car le pic (en masse) des particules déposées dans l'air ambiant est compris entre 10 et 30 µm [7].

Pour évaluer la validité de la technique OSM, des coupons ont été exposés sur le terrain pendant diverses périodes et la quantité de salissures caractérisée par des techniques traditionnelles (masse, perte de transmission lumineuse) a été comparée à celle de l'OSM (couverture de surface projetée). La couverture de surface de l'OSM et la perte de

transmission de la lumière étaient toutes deux essentiellement proportionnelles à la masse de poussière (voir Figure 2), indiquant que l'analyse par l'OSM est valide pour caractériser les salissures malgré l'exclusion des particules inférieures à 4 μm . En outre, le flux de poussière quotidien le plus faible mesurable par l'OSM était effectivement de $0.044 \text{ mg}\cdot\text{m}^{-2}\cdot\text{jour}^{-1}$, tandis que la limite inférieure des mesures de terrain traditionnelles est de l'ordre de $10 \text{ mg}\cdot\text{m}^{-2}\cdot\text{jour}^{-1}$ [3]. C'est-à-dire que l'OSM permettait des mesures des salissures de deux à trois ordres de grandeur plus fines que les méthodes de terrain existantes et habituelles.

Une autre caractéristique importante de l'OSM est qu'il peut mesurer le dépôt et le détachement de la poussière individuellement (on peut voir des particules arriver et sortir du collecteur), alors que les techniques traditionnelles ne mesurent que l'accumulation nette de poussière (voir Figure 4). En outre, lorsqu'une paire d'OSM à surface de dépôt graissée / non graissée est utilisée, trois mécanismes distincts peuvent être quantifiés : dépôt de particules, rebond (décollement immédiat) et remise en suspension (décollement retardé). Pour ce faire, une technique d'analyse d'image a été développée dans laquelle des images d'OSM successives ont été comparées pour générer une « image différentielle », à partir de laquelle les flux individuels peuvent être directement mesurés ou déduits de simples hypothèses (telles qu'un même flux de poussière supposé incident sur les coupons graissés et non graissés, cf. Figure 4). La dissociation des débits calculés en flux élémentaires a fourni une compréhension physique plus détaillée du processus de dépôt de poussière que les expériences de terrain classiques, qui ne mesurent que l'accumulation nette de poussière.



Dépôt = poussière ajoutée au collecteur graissé (« *deposited* »)

Re-suspension = poussière retirée du collecteur non graissé (« *detached* »)

Rebond = poussière ajoutée au collecteur graissé – poussière ajoutée au collecteur non graissé

Accumulation = Dépôt – Rebond – Re-suspension

Figure 4. Les images successives ont été comparées pour calculer les dépôts de poussière et les taux de détachement. En comparant les résultats des coupons graissés et non graissés, l'accumulation de poussière pourrait être séparée en taux de dépôt, de rebond et de remise en suspension.

Les forces et les faiblesses de l'OSM en tant qu'outil expérimental ainsi que la comparaison avec les techniques conventionnelles de laboratoire et de terrain sont résumées dans le Tableau 1. L'OSM est particulièrement adapté pour étudier le dépôt et le détachement de particules de poussière grossière en extérieur. En outre, il était facile d'exploiter

deux OSM côte à côte, ce qui est bien adapté pour étudier l'effet relatif des traitements de surface dans des conditions ambiantes – par exemple les flux de poussière et les gouttelettes de condensation sur un revêtement hydrophobe contre hydrophile. Les souffleries de laboratoire sont plus appropriées lorsque les conditions d'essai doivent être contrôlées et que les petites particules (<4 µm) sont d'un intérêt primordial. Des essais sur le terrain à long terme avec des modules PV fonctionnant à grande échelle sont essentiels pour vérifier les taux de salissure et les pertes d'énergie qui en résultent sur les systèmes PV en conditions réelles. En résumé, si l'on considère les objectifs expérimentaux du « réalisme » et de « l'information » (sur les mécanismes physiques sous-jacents), l'OSM se situe entre les expériences en soufflerie en laboratoire et les essais sur le terrain.

Approche expérimentale	Révèle la mécanique des particules	Contrôle des paramètres	Conditions naturelles	Géométrie PV réaliste	Durée de l'expérience courte	Plus grande convenance
Soufflerie de laboratoire	••	••			••	Expériences de salissures paramétriques précises, par ex. traitement de surface, vitesse du vent, angle d'inclinaison, taille / composition de la poussière.
Outdoor soiling microscope (OSM)	•		••	• ⁽¹⁾	•	Observation des flux de poussières grossières dans des conditions naturelles. Essais de traitement de surface détaillés dans des conditions naturelles.
Modules PV extérieurs			••	••		Vérification de l'encrassement et de la perte d'énergie des modules PV actuels.

Table 1. Points forts et points faibles des approches expérimentales de l'étude des salissures PV. •• = grande force, • = force modérée. (1) En principe, l'OSM pourrait être installé dans la géométrie d'un système PV, bien que cela n'ait pas été fait dans la présente étude

Partie II - Effets des paramètres environnementaux sur les taux de flux de poussière

L'une des principales motivations de l'étude était d'améliorer la compréhension de la façon dont les paramètres environnementaux influencent les souillures ambiantes. Un essai de 51 jours a été réalisé au site de tests solaires de Doha au Qatar, où des mesures OSM (paire graissée / non graissée) et des conditions environnementales ont été enregistrées : vitesse du vent (WS ou *wind speed*), humidité relative (RH) et concentration de particules (PM). En raison du court intervalle de mesure autorisé par l'OSM, l'expérience a donné 6186 « observations » (périodes de 10 minutes de flux de poussière et paramètres environnementaux correspondants). Les principales conclusions sont les suivantes :

— Le dépôt de poussière a été fortement contrôlé par WS, et a montré une «réponse seuil» distincte qui était indépendante de PM (voir Figure 5). C'est-à-dire que le dépôt est resté constant jusqu'à ce que WS dépasse $\approx 3 \text{ ms}^{-1}$, puis augmente approximativement linéairement avec WS. Le dépôt de particules minérales de $\approx 1\text{--}100 \mu\text{m}$ est influencé à la fois par la gravité et l'inertie ; il est proposé que le flux d'air sur le site devienne significativement plus turbulent lorsque $\text{WS} \gg 3 \text{ ms}^{-1}$ ce qui augmente le degré de dépôt inertiel.

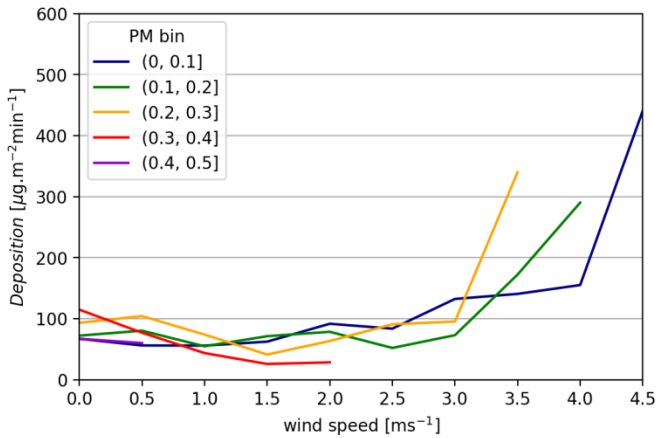


Figure 5. Dépôt vs. WS, maintien de PM constant.

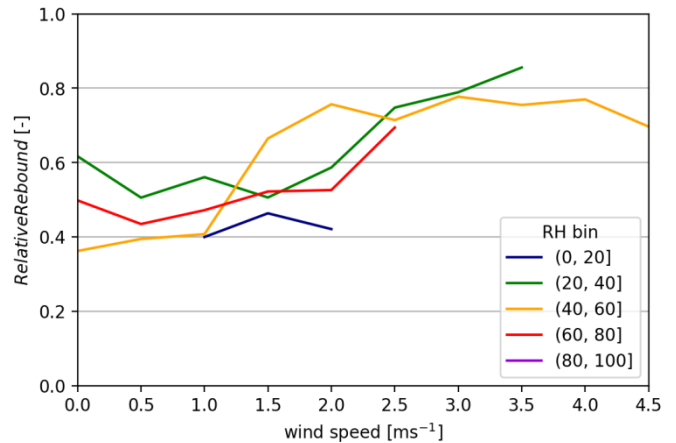


Figure 6. Rebond vs. WS, maintien de RH constant.

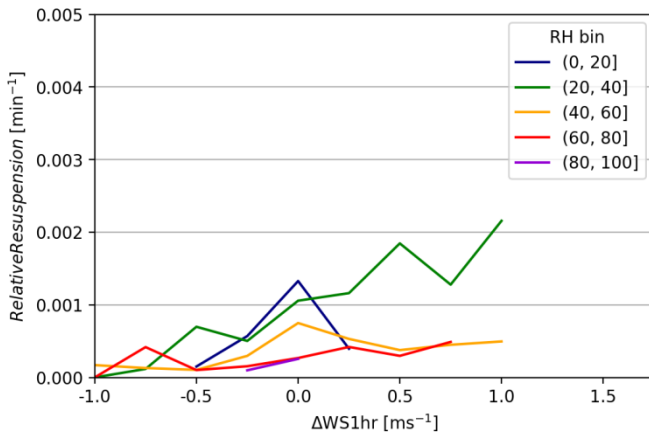


Figure 7. Resuspension vs $\Delta\text{WS}_{1\text{hr}}$, maintien de RH constant.

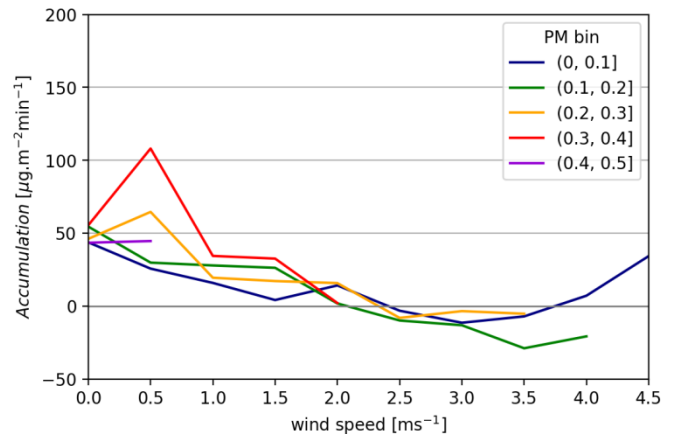


Figure 8. Accumulation vs. WS, maintien de PM constant.

— La réponse au seuil de dépôt était cohérente avec un modèle particulier de dépôt inertiel (contrôlé par le vent) dans la littérature, par Kim et al. [8]. Ce modèle avait (comme la présente étude) été dérivé des mesures d'encrassement extérieur, alors que les modèles dérivés des expériences en soufflerie ne correspondaient pas aux résultats actuels. Cela suggère qu'il est difficile de prédire les taux de salissures en plein air à partir des études en soufflerie. Lorsqu'il est

combiné avec une équation standard pour le taux de dépôt par sédimentation (gravité contrôlée), le modèle de Kim et al. prédit de près les résultats actuels (cf. Figure 9).

— La réponse seuil de dépôt en fonction de WS s'explique en partie par l'augmentation de la taille de l'aérosol avec WS. Lorsque WS dépassait $\approx 3,5 \text{ ms}^{-1}$, la taille des particules piégées par le coupon graissé augmentait (voir Figure 10). Les plus grosses particules ont une plus grande vitesse de dépôt, donc le taux de dépôt augmentera pour la même concentration de particules.

— Le rebond était également contrôlé par WS (voir Figure 6), ce qui découle du fait que le rebond se produit lorsque l'énergie cinétique d'une particule au moment de l'impact dépasse l'énergie d'adhérence à la surface.

— La remise en suspension a également été influencée par la vitesse du vent par rapport à l'heure précédente (ΔWS_{1hr}) et RH (voir Figure 7). Ceci s'explique en considérant que l'augmentation ou la diminution de la vitesse du vent a un effet plus important sur la remise en suspension de la poussière que sa valeur absolue. Dans une humidité relative modérée à élevée, la condensation capillaire colle fortement les particules de poussière à la surface du verre, ce qui inhibe leur remise en suspension. De plus, les deux paramètres interagissent, de sorte que l'effet d'adhésion capillaire n'est observé que dans des conditions venteuses.

— L'accumulation globale a été principalement expliquée par WS (voir Figure 8). Pour $WS \leq 2 \text{ ms}^{-1}$, le coupon devenait généralement plus sale, et pour $WS > 3 \text{ ms}^{-1}$, il perdait généralement de la poussière, quelle que soit la concentration en particules. Ceci est un résultat important, car il y a des résultats conflictuels dans la littérature à savoir si la vitesse du vent élevée aggrave [6][8][9] ou améliore [10][11] les salissures PV. L'ensemble complet des résultats de flux de poussière dans la présente étude montre que la vitesse du vent augmente à la fois le dépôt et le rebond / la remise en suspension, mais en plus petite proportion pour le premier (dépôt).

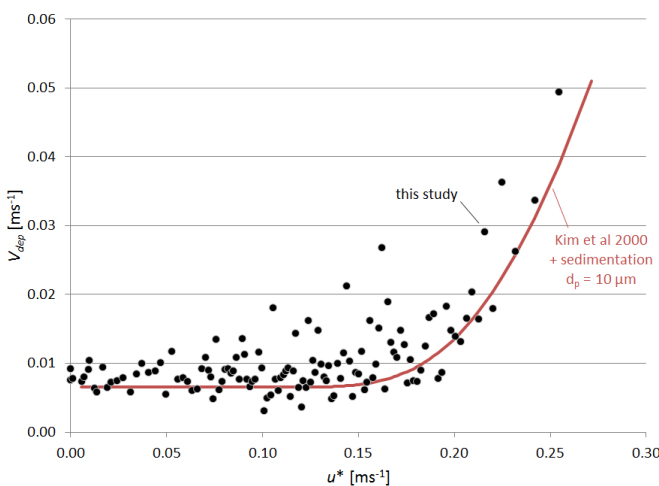


Figure 9. Vitesse de dépôt de particules vs. WS. Marqueurs noirs: Résultats expérimentaux de la présente étude. Ligne rouge : Modèle combiné de sédimentation et de dépôt inertiel (de Kim et al. [8]).

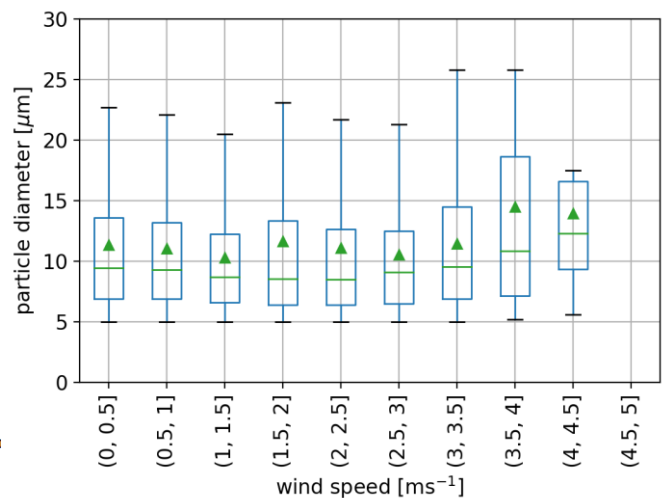


Figure 10. Taille des particules déposées en fonction de WS (taille minimale des particules à $5 \mu\text{m}$). Bords de boîte et intervalles = quartiles, marqueurs verts = moyennes.

Partie III - Étude de la condensation sur les surfaces souillées

La condensation contribue à la salissure ambiante en adhérant des particules à la surface et, dans certains cas, en dissolvant les poussières hygroscopiques qui recristallisent ensuite et « cimentent » la particule en place [5]. La condensation sur des surfaces propres en équilibre thermodynamique avec leur environnement a été étudiée en détail, mais pas la condensation sur des surfaces sales dans des conditions ambiantes. Une série d'expériences en laboratoire et sur le terrain a été menée pour étudier les facteurs affectant la condensation de la surface souillée, et résumée dans le Tableau 1.

Paramètre	Expériences	Équipement
Humidité relative (RH)	Isothermes d'adsorption d'eau ⁽¹⁾ de poussières naturelles	Machine d'adsorption de vapeur
	Croissance des gouttelettes de surface de la poussière naturelle (laboratoire et extérieur)	OSM extérieur Chambre d'humidité avec microscopes
Différence de température du point de rosée de surface (T_{S-DP})	Croissance des gouttelettes de surface de la poussière naturelle	OSM
	Accumulation de poussière sur des surfaces chauffées ou non chauffées	Paire d'OSMs
Matériau hygroscopique	Analyse de la composition de la poussière ⁽²⁾	XRD, chromatographie ionique
	Isothermes d'adsorption d'eau de poussières naturelles vs. poussières traitées	Machine d'adsorption de vapeur
	Croissance des gouttelettes de surface de la poussière naturelle par rapport à la poussière traitée	Chambre d'humidité avec microscopes
Mouillabilité de la surface	Croissance des gouttelettes de surface sur le verre par rapport aux surfaces en PTFE (terrain)	Paire d'OSMs

Table 2. Essais effectués pour étudier la condensation des surfaces souillées. ⁽¹⁾ Réalisés par LaSIE, Université de la Rochelle–CNRS. ⁽²⁾ Réalisée par Central Materials Facility, Texas A&M University at Qatar.

La poussière recueillie des modules PV au Qatar a été séparée en une partie soluble et une partie insoluble. Un échantillon synthétique a été préparé dont le seul composant hygroscopique était NaCl. Les principaux résultats sont :

— La poussière naturelle au Qatar contient un matériau hygroscopique qui absorbe modérément l'humidité lorsque le RH dépasse ≈60%, et beaucoup quand il dépasse ≈80% (Figure 8). Les composants hygroscopiques les plus puissants ont été réduits en nitrate et sulfate — le NaCl seul n'a pas entraîné de déliquescence (Figure 11, Figure 12).

— Sur le terrain, des gouttelettes de condensation microscopiques ont été observées sur des surfaces hydrophobes (PTFE) et hydrophiles (verre borosilicaté) même lorsque les températures de surface étaient supérieures de plusieurs degrés au point de rosée (voir Figure 13 et Figure 14). Ceci a été attribué à la matière hygroscopique sur les surfaces ou aux gouttelettes aéroportées.

— Comparé à la surface du verre, le matériau hydrophobe inhibait grandement la croissance de la condensation et empêchait l'inondation de la surface lorsque le point de rosée était atteint (voir Figure 13 et Figure 14).

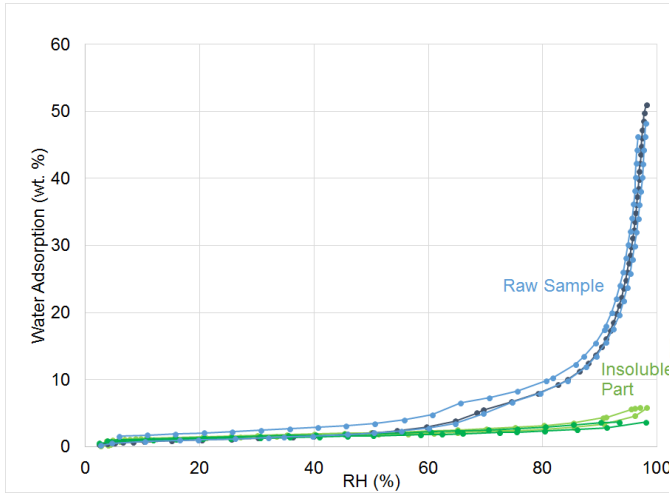


Figure 11. Courbes isothermes d'adsorption de vapeur de l'échantillon brut (lignes bleu clair et bleu foncé) et de la partie insoluble (lignes vert clair et vert foncé).

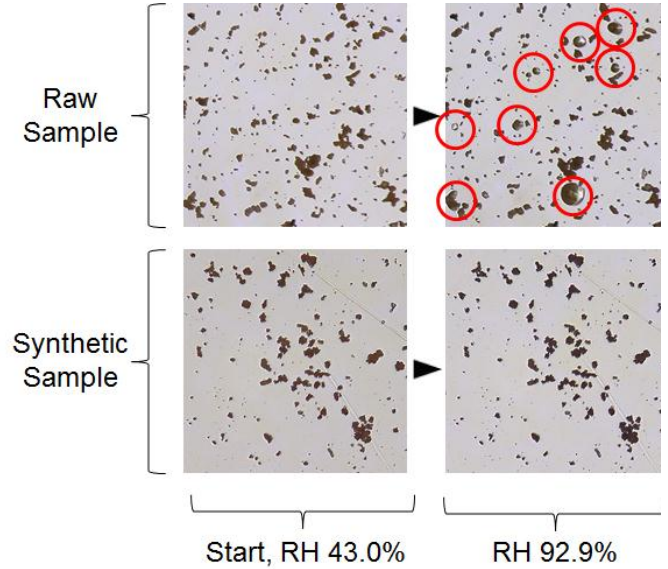


Figure 12. Comportement d'adsorption d'eau d'échantillons exposés dans une chambre d'humidité de laboratoire à différentes RH.

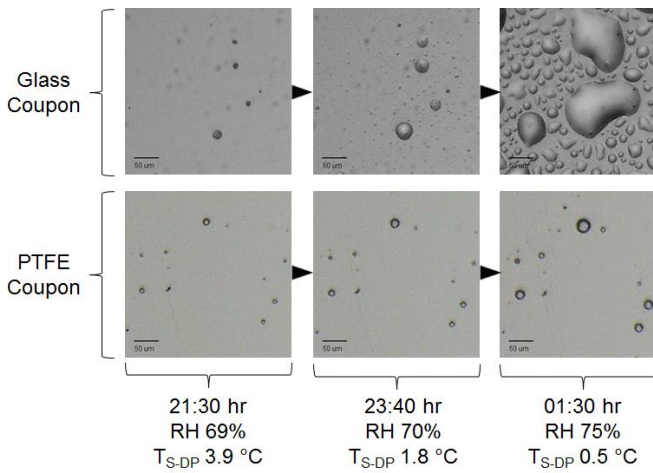


Figure 13. Images OSM de gouttelettes de surface sur des surfaces de verre et de PTFE dans des conditions ambiantes sur une période nocturne de 4 heures.

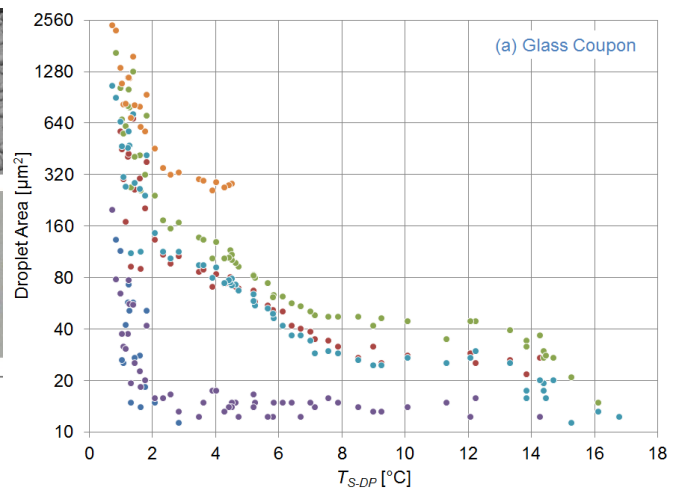


Figure 14. Zones de gouttelettes par rapport au T_{S-DP} (différence de température de surface / point de rosée) sur le coupon en verre.

Le rôle important de l'humidité de surface dans l'adhérence de la poussière a provoqué des tendances de salissures remarquables selon l'heure de la journée. En raison de la capacité de l'OSM à mesurer les flux de poussière sur de courtes périodes, on a pu observer pour la première fois ces tendances dans des conditions désertiques naturelles. Un

coupon OSM chauffé a été fabriqué en attachant un fil de nichrome résistif à une source d'alimentation (voir Figure 15), ce qui a éliminé la condensation. En comparant les taux de flux sur les coupons chauffés et non chauffés, on a constaté que l'humidité de surface provoquait l'accumulation de poussière sur le coupon non chauffé la nuit (mais pas sur le coupon chauffé). Cependant, au cours de la journée suivante, lorsque la surface s'est asséchée et que la vitesse du vent a augmenté, une grande partie de cette poussière accumulée a été dispersée. Ceci est démontré par les taux de flux de remise en suspension relatifs des coupons (voir Figure 16). Le résultat suggère que l'encrassement PV pourrait être atténué en agissant sur la salissure et la condensation nocturnes, par ex. en programmant un *tracker* solaire pour incliner les modules en position verticale la nuit, ou en utilisant des revêtements ou des technologies de chauffage passifs qui inhibent la condensation.



Figure 15. Un coupon OSM chauffé a été fabriqué pour isoler l'effet de l'humidité de surface sur les taux de flux de poussière, sur le terrain.

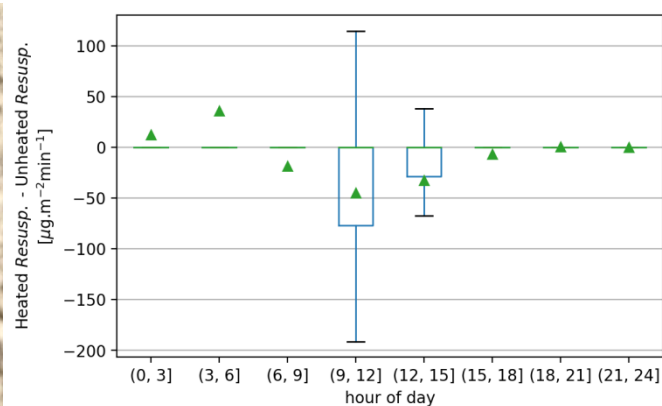


Figure 16. Taux de remise en suspension relatifs des coupons chauffés et non chauffés, montrant que certaines poussières accumulées durant la nuit (sur le coupon non chauffé) étaient naturellement dispersées le jour suivant.

Conclusions

Un microscope de souillure extérieur (OSM) a été développé, qui s'est avéré être un outil pratique et utile pour étudier les mécanismes de salissure dans les conditions de terrain. Ses principales caractéristiques sont : le fonctionnement dans des conditions ambiantes ; l'opérabilité jour et nuit ; l'intervalle de mesure en minutes ou même en secondes ; les quantités mesurées appropriées pour des particules de poussière individuelles $> 4 \mu\text{m}$; la mesure des mécanismes d'encrassement sous-jacents – dépôt, rebond et remise en suspension ; l'observation de la formation de la condensation, sa croissance et sa coalescence ; des composants peu coûteux et facilement disponibles. De ces caractéristiques, en particulier, l'intervalle temporel court et la détection individuelle des particules permettent à l'OSM de mesurer efficacement les taux de flux de poussière de deux à trois ordres de grandeur plus petits que les techniques habituelles. Les limites et les inconvénients de l'OSM sont qu'il ne peut pas évaluer de manière fiable des particules plus

petites que $\approx 4 \mu\text{m}$; il ne peut mesurer qu'une petite surface de la surface totale du collecteur ($\approx 4 \text{ mm}^2$) ; et il doit être connecté à un ordinateur.

Lors d'un essai sur le terrain au Qatar, l'OSM a révélé des effets de paramètres environnementaux sur le taux de salissure qui avaient été auparavant masqués par de longues périodes de mesure au travers des techniques habituelles. Il a été constaté que : (i) il y a une réponse seuil de dépôt de poussière à la vitesse du vent WS de $\approx 3.2 \text{ ms}^{-1}$, qui peut être dû à l'air devenant turbulent et causant ainsi plus de dépôt inertiel ; (ii) les particules de poussière ont une grande tendance à rebondir sur la surface, en fait la fraction de rebond atteignait même $\approx 80\%$ à vitesse élevée ; (iii) la remise en suspension était corrélée avec le changement de la vitesse du vent par rapport à l'heure précédente, et inhibée par l'humidité relative $\text{RH} > 40\%$; (iv) l'accumulation globale de poussière a été fortement contrôlée par la vitesse du vent, et la surface est devenue plus propre avec $\text{WS} \gg 3 \text{ ms}^{-1}$.

Les facteurs affectant la condensation sur les surfaces sales ont été étudiés par une série d'expériences sur le terrain et en laboratoire. Il a été constaté que la poussière du Qatar contenait des espèces hygroscopiques autres que NaCl – par ex. nitrate, sulfate, ou d'autres sels – qui contrôlent l'absorption de l'humidité par la couche de salissure. Une telle matière a également permis à des gouttelettes de condensation microscopiques d'exister sur des surfaces ambiantes bien au-dessus de la température du point de rosée. Comparé à une surface de verre (hydrophile), un polymère hydrophobe a inhibé la croissance de la condensation et l'a empêché « d'inonder » la surface lorsque le point de rosée a été approché. Les résultats suggèrent que dans les environnements avec des particules hygroscopiques et une humidité élevée, la présence d'humidité sur les surfaces ambiantes est omniprésente.

Le rôle important de l'humidité de surface dans la salissure a été démontré en comparant les taux de flux de poussière sur les coupons chauffés et non chauffés. Ces expériences (et la courte période de mesure de l'OSM) ont également révélé des tendances prononcées de salissures : la poussière avait tendance à s'accumuler principalement de nuit et une partie de cette accumulation avait été dispersée le jour suivant. La découverte que la poussière s'accumule principalement du jour au lendemain suggère des stratégies pratiques pour atténuer les salissures PV, par ex. inclinaison des modules la nuit ou lutte contre la condensation.

Bibliographie

1. Costa, S.C.S., Sonia, A., Diniz, A.C., and Kazmerski, L.L. (2016) Dust and soiling issues and impacts relating to solar energy systems: Literature review update for 2012 – 2015. *Renew. Sustain. Energy Rev.*, **63**, 33–61.
2. Guo, B., Javed, W., Figgis, B.W., and Mirza, T. (2015) Effect of dust and weather conditions on photovoltaic performance in Doha, Qatar. *2015 1st Work. Smart Grid Renew. Energy, SGRE 2015*.
3. Boyle, L., Flinchpugh, H., and Hannigan, M. (2016) Assessment of PM Dry Deposition on Solar Energy Harvesting Systems: Measurement - Model Comparison. *Aerosol Sci. Technol.*, **6826** (February 2016).

4. Fujii, M., Machida, K., Takei, T., and Watanabe, T. (1999) Effect of Wettability on Adhesion Force between Silica Particles Evaluated by Atomic Force Microscopy Measurement as a Function of Relative Humidity. *Langmuir*, **15** (13), 4584–4589.
5. Cuddihy, E.F. (1980) Theoretical considerations of soil retention. *Sol. Energy Mater.*, **3** (1–2), 21–33.
6. Qiang, M., Chen, F., Zhou, A., et al. (2007) Impacts of wind velocity on sand and dust deposition during dust storm as inferred from a series of observations in the northeastern Qinghai – Tibetan Plateau , China. *Powder Technol.*, **175**, 82–89.
7. Noll, K.E., and Fang, K.Y.P. (1989) Development of a dry deposition model for atmospheric coarse particles. *Atmos. Environ.*, **23** (3), 585–594.
8. Kim, E., Kalman, D., and Larson, T. (2000) Dry deposition of large, airborne particles onto a surrogate surface. *Atmos. Environ.*, **34** (15), 2387–2397.
9. Goossens, D., Offer, Z.Y., and Zangvil, A. (1993) Wind tunnel experiments and field investigations of eolian dust deposition on photovoltaic solar collectors. *Sol. Energy*, **50** (1), 75–84.
10. Goossens, D., and Kerschaeffer, E.V.A.N. (1999) Aeolian Dust Deposition on Photovoltaic Solar Cells: the Effects of Wind Velocity and Airborne Dust Concentration on Cell Performance. *Sol. Energy*, **66** (4), 277–289.
11. Qasem, H., Mnatsakanyan, A., and Banda, P. (2016) Assessing Dust on PV Modules Using Image Processing Techniques. *2016 IEEE 43rd Photovolt. Spec. Conf.*, 2066–2070.
12. Assi, A., and Chaar, L. El (2008) Effect of wind blown sand and dust on photovoltaic arrays. *23rd Eur. Photovolt. Sol. Energy Conf. Exhib. (EU PVSEC 2008)*.

Acknowledgements

For their valuable guidance and assistance I sincerely thank Said Ahzi, Abdelkarim Ait-Mokhtar, Nicolas Barth, Rafik Belarbi, Ahmed Ennaoui, Bing Guo, Wasim Javed, Klemens Ilse, Armelle Nouviaire, Yves Rémond, and Yiming Wubulikasimu.

For their encouragement and support I thank my wife Carly-Jane Figgis, son Adam Arfal, and parents Jane and Brian Figgis.

I thank the invited member of the soutenance jury M. Abdelilah SLAOUI and M. Nicolas BARTH

Abbreviations

$\%_{\text{image}}$	percentage of imaged surface area
α	level of significance (5% unless stated otherwise)
ε	eddy diffusion coefficient [$\text{m}^3 \text{g}^{-1} \text{s}^{-1}$]
γ	surface tension [Nm^{-1}]
θ, θ_x	contact angle [°]
θ_f	filling angle [°]
μ	dynamic viscosity (of air unless stated otherwise) [N.s.m^{-2}]
ν	kinematic viscosity (of air unless stated otherwise) [$\text{m}^2 \text{s}^{-1}$]
ρ	density (of air unless stated otherwise) [kg.m^{-3}]
ρ_p	particle density [kg.m^{-3}]
σ	Stefan–Boltzmann constant; population standard deviation
τ	particle stop distance [m]
τ^+	dimensionless particle stop distance [-]
C	atmospheric particulate concentration [mg.m^{-3}]
C_D	particle drag coefficient [-]
CI, CI_{90}	confidence interval (90%)
D_a	particle diameter – equivalent aerodynamic mechanics [μm]
D_e	particle diameter – equivalent volume [μm]
D_p, d_p	particle diameter [μm]
D_{pa}	particle diameter – equivalent projected area [μm]
F	dust flux rate [$\text{mg.m}^{-2} \text{s}^{-1}$]
F_{adh}	particle adhesion force [N]
F_{cap}	particle capillary adhesion force [N]
F_{drag}	particle drag force [N]
g	gravitational acceleration [ms^{-2}]
I_{SC}	short circuit current [A]
l	characteristic length [m]
n	sample size
OSM	outdoor soiling microscope
p	vapor pressure [Pa]
p_0	saturation vapor pressure [Pa]
p_L	Laplace pressure [Pa]
PM, PM_{total}	particulate matter (total) concentration [mg.m^{-3}]
PM_x	particulate matter (diameter smaller than $x \mu\text{m}$) concentration [mg.m^{-3}]
PTFE	polytetrafluoroethylene (Teflon)
PV	photovoltaic
r_p	particle radius [m]
r_x	radius of curvature [m]
R_x	particle deposition impedance [s.m^{-1}]
Re	Reynolds number [-]
Re_p	particle Reynolds number [-]
RH	relative humidity [%]
s	sample standard deviation
St	Stokes number [-]
St_{eddy}	eddy Stokes number [-]
STF	Solar Test Facility in Doha, Qatar
T_{amb}	ambient temperature [°C]
T_{DP}	dew-point temperature [°C]
T_s	surface temperature [°C]
T_{S-DP}	difference between surface and dew-point temperatures [°C]

T_{sky}	sky temperature [°C]
TL	transmission loss [%]
U	free-stream wind speed [ms^{-1}]
U_x	wind speed at height x above ground [ms^{-1}]
u	flow velocity [ms^{-1}]
u^+	dimensionless flow velocity [-]
u^*	friction velocity [ms^{-1}]
u_p	flow velocity at particle mid-point [ms^{-1}]
v_{dep}	particle deposition velocity [ms^{-1}]
v_{inertial}	particle deposition velocity from inertial (turbulence) mechanism [ms^{-1}]
v_{sed}	particle deposition velocity from sedimentation mechanism [ms^{-1}]
v_{Stokes}	Stokes velocity [ms^{-1}]
vdW	van der Waals adhesion
WS	wind speed [ms^{-1}]
$WS_{\text{threshold}}$	threshold wind speed [ms^{-1}]
$WS_{\text{supercritical}}$	wind speed excess to $WS_{\text{threshold}}$ [ms^{-1}]
$\Delta WS_{1\text{hr}}$	difference between current WS and average WS of preceding hour [ms^{-1}]
\bar{x}, \bar{X}	sample mean
y	distance from wall [m]
y^+	dimensionless distance from wall [-]

1. Introduction

This study investigated the physical mechanisms of dust accumulation on glass surfaces in a desert environment, by developing and using a novel instrument for field measurement of dust deposition and condensation. This chapter describes the motivation for the study, background of PV soiling, and objectives and scope of the research program.

1.1. Motivation

Soiling of PV modules by dust is a severe problem in desert environments (Figure 1). Variation in the PV soiling rate over time should, in principle, be explainable by changes in environmental conditions. Yet previous research has not revealed clear and consistent links between weather and the soiling rate. It was thought that reasons for this include:

- (i) Soiling is usually measured by exposing collectors for days, whereas the weather changes constantly
- (ii) Soiling is the net result of competing processes — dust deposition and detachment — which are difficult to distinguish in field studies
- (iii) Moisture contributes greatly to soiling by trapping and binding dust particles, however condensation on collectors is rarely taken into account.



Figure 1. Cleaned and un-cleaned PV modules at the Solar Test Facility in Doha, Qatar. The study aimed to improve understanding of how soiling and condensation form on ambient surfaces in desert environments, via a novel outdoor microscopy

The challenge of field-study of soiling was highlighted by Aluko and Noll [1], from a recognized aerosol research group at the Illinois Institute of Technology in Chicago:

“Experimental results [of dust deposition] produced highly variable results. Much of this variation can be attributed to experimental errors associated with the nature of the atmospheric experiments.”

To improve field measurement of dust accumulation and condensation, a novel “outdoor soiling microscope” (OSM) was developed (Figure 2). The OSM allowed dust deposition, detachment and condensation to be measured in microscopic quantities, in ambient conditions, in 10-minute intervals. This fine-time and fine-quantity data was then used to quantify relations between dust particle mechanics and environmental parameters that had previously been obscured by traditional soiling measurement methods. Finally, the OSM was combined with laboratory experiments to investigate the effect on soiled-surface condensation of hygroscopic dust content, surface wettability, and surface/dew point temperature difference. The resulting insights on how dust and moisture accumulate on ambient surfaces suggest strategies for mitigating PV soiling in desert environments.



Figure 2. A pair of “outdoor soiling microscopes” (OSMs). Dust particles settle on glass coupons attached to the microscopes, and LED back-lights enable consistent images to be taken day and night

1.2. Background and Objectives

Soiling of photovoltaic (PV) modules is a major problem in desert environments, where there is much dust and little rain. At the Solar Test Facility (STF) in Qatar (Figure 3) — where the present study was conducted and whose details have been previously reported [2] — soiling causes PV specific yield (kWh/kW_p) to decrease by roughly 12 %/month. More than 200 days can pass without rain at the site, hence soiling losses can become large and have even exceeded 70% (Figure 4). Further, there are currently no simple and effective technologies to combat PV soiling, and the largest PV plants in the region are still cleaned manually (at the time of writing, 2018). Efforts have been made to develop “anti-soiling coatings” but they have not shown consistent and significant effectiveness against PV soiling, and they are not yet used commercially. Cleaning machines and robots have been introduced to the market but are not yet widely adopted. The issue is especially pressing because the largest deployment of PV is planned in dry and dusty locations such as the Middle East, China and India.



Figure 3. Solar Test Facility in Doha, Qatar

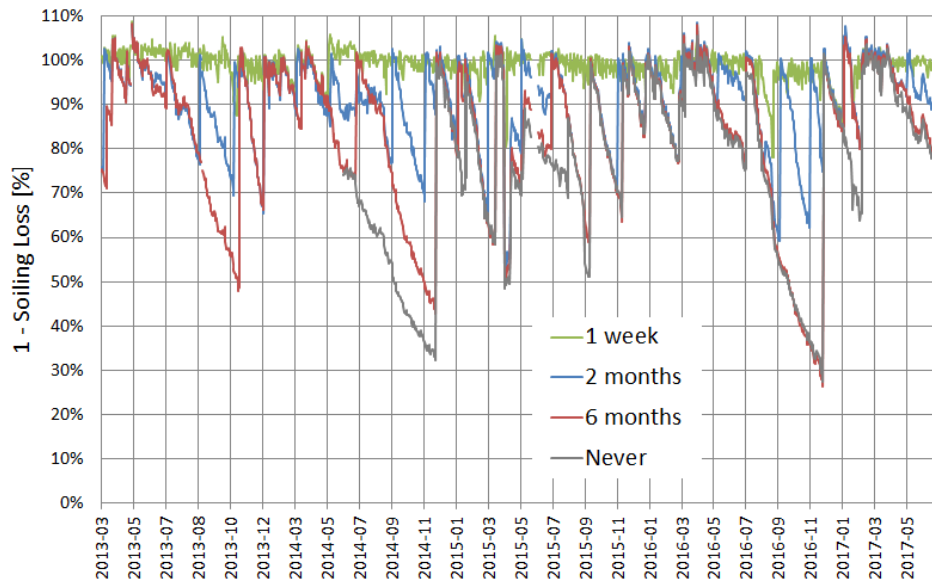


Figure 4. Soiling Loss of PV modules at the STF with different cleaning schedules over ~4 years. Soiling Loss = energy yield of soiled module/avg. energy yield of clean module. Key: cleaning interval

What causes PV soiling? Unfortunately there is no simple answer, because soiling is a complicated process comprising multiple underlying processes (e.g. particle deposition, adhesion, cementation, detachment), each subject to multiple forces (e.g. inertial, aerodynamic, mechanical, van der Waals, capillary, electrostatic) and controlled by multiple parameters (e.g. environmental conditions, dust characteristics, surface characteristics). This study focuses on two aspects of PV soiling, below. They were chosen because they are necessary for a fundamental understanding of how soiling accumulates, and they have not been fully investigated.

- Relations between environmental parameters and dust flux rates

Intuitively, the amount of dust deposit and detachment on outdoor surfaces (the flux rate) should be largely controlled by principle environmental variables such as wind speed (WS), particulate matter concentration (PM) and relative humidity (RH). The effect of such variables on flux rate in controlled laboratory experiments is well established, however outdoor tests tend to produce imprecise and inconsistent correlations between soiling and meteorological conditions (examples in section 2.2.1). This study aimed to improve understanding of how dust flux rates are controlled by environmental parameters in field conditions, by developing the OSM to measure ambient deposition and detachment of individual dust particles in fine time increments.

- Factors affecting surface moisture in PV soiling

Moisture has a powerful role in dust adhesion: when condensation is present capillary forces dominate all other particle adhesion forces, and it can lead to “cementation” in which soluble matter dissolves and re-crystallizes upon

drying, leaving a strong material bridge between dust particles and the surface. Even in deserts, humidity can be very high [3]. Condensation studies typically deal with clean surfaces and constant-temperature systems, whereas condensation of soiled surfaces in outdoor conditions has not been extensively investigated. In this study the effects of (i) RH, (ii) hygroscopic dust content, (iii) surface/dew point temperature difference, and (iv) surface wettability on condensation on soiled surfaces was explored by a variety of experimental methods.

Accordingly, the objectives of the study are stated as follows:

- Objective 1 — Improve understanding of relations between dust flux rates (deposition and detachment) and environmental parameters (WS, PM, and RH) in desert field conditions
- Objective 2 — Determine how condensation on soiled substrates in ambient conditions is affected by key parameters (RH, dust composition, surface temperature, and surface wettability).

1.3. Research Program

The study is organized in three parts:

- Part I – Development of outdoor soiling microscope (Chapter 5)

The initial part of the study was development of the OSM apparatus. Traditionally, soiling in the field has been measured by exposing PV modules or collector plates for timescales in the order of days. This long timescale obscures relations between the soiling rate and environmental parameters (also termed “meteo parameters”), which change constantly. It also obscures understanding of how dust actually accumulates — for example, is a certain quantity of soiling the result of few impacting particles that stick well, or many impacting particles that stick poorly? In this study an inexpensive, low-power microscope (OSM) was adapted to capture images of dust particles and microscopic condensation droplets that collect on a transparent coupon, in timescales of minutes, day and night, in the field. The first phase of the study was dedicated to developing the OSM: testing and optimizing hardware components; programming the computerized control system; developing image-analysis techniques and scripts; evaluating OSM measurement quality and limits through comparison with a laboratory-grade microscope; and experimentally calibrating the measurements to soil mass and light transmission loss. A technique was developed using a pair of OSM coupons — one greased and the other not — to separate dust accumulation into three components: particle deposition, rebound (immediate detachment), and resuspension (delayed detachment). These components were quantified as dust flux rates, with units of $\mu\text{g}\cdot\text{m}^{-2}\cdot\text{min}^{-1}$.

— Part II – Explanation of soiling variation (Chapter 6)

Having developed the OSM, it was next used for observational study of soiling in the field at the STF in Doha, Qatar. The aim was to improve physical understanding of how PV soiling occurs by quantifying relations between meteo parameters and dust flux rates. Measurements were made of dust fluxes on a greased/ungreased pair of OSMs on 51 days in July-November 2016, resulting in 6186 complete “observations” (10-minute sets of an OSM image and accompanying weather data). This data-set — extremely large in comparison with traditional soiling field studies — allowed the response of flux rates to individual meteo parameters to be determined while holding others constant, thus eliminating correlation between the parameters as a potential explanation. Further, effects of the meteo parameters were assessed quantitatively by constructing multiple linear regression models of the dust flux rates using a stepwise technique. The explanatory contribution of each meteo parameter was statistically evaluated, so that parameters that most powerfully controlled each flux component (deposition, rebound, resuspension) could be identified. Although the models were mainly constructed for inferential purposes, their predictive performance was assessed by comparing their daily predictions of dust accumulation against actual amounts in a subsequent 24-day field trial.

— Part III – Condensation causes and effects (Chapter 7)

The third major part of the study investigated factors affecting the onset and growth of condensation on soiled surfaces, and effects of the condensation on dust flux rates. A series of experiments was performed:

1. Paired OSM field observations of condensation on glass vs. PTFE coupons
2. Paired OSM field observations of dust accumulation on heated vs. unheated coupons
3. Microscope observations in a specially-built humidity chamber of condensation with different dust mixtures
4. Water-vapor adsorption isotherms of dust mixtures via an instrument at l’Université de la Rochelle, France
5. X-ray diffraction (XRD) and ion chromatography of natural Qatar dust at Texas A&M University at Qatar.

Combinations of these experiments and analyses were used to determine the effects of (i) RH, (ii) hygroscopic material, (iii) surface/dew-point temperature difference, and (v) surface wettability on soiled-surface condensation in desert environments. Of particular interest was the existence of moisture on ambient surfaces above the dew point, due to hygroscopic material, and identification of the exact hygroscopic species involved. A novel aspect of this study was use of paired heated/unheated OSMs to directly measure the influence of condensation on dust flux rates, and how those flux rates varied with daily weather patterns.

2. Review of PV Soiling Measurement and Modeling

In this section the subject of PV soiling is introduced and the literature review. Emphasis is placed on the physical processes underlying soiling, especially particle mechanics and capillary adhesion, and measurement techniques that have traditionally been used for studying particle deposition and detachment.

2.1. PV Soiling Problem

Soiling of PV modules by dust can severely reduce their power output, especially in desert environments where there is much dust but little rain. Summaries of PV soiling research have been presented [4][5][6][7][8] which show that the problem is severe, widespread, and the subject of increasing attention as PV use expands. That literature shows that soiling rates vary widely among arid regions, but typical values are in the order of tenths of a percent per day (~0.1-1 %/day) [8], (Figure 5). That is, the amount of energy produced by PV relative to the amount of insolation received decreases in the order of ~10 %/month in deserts.

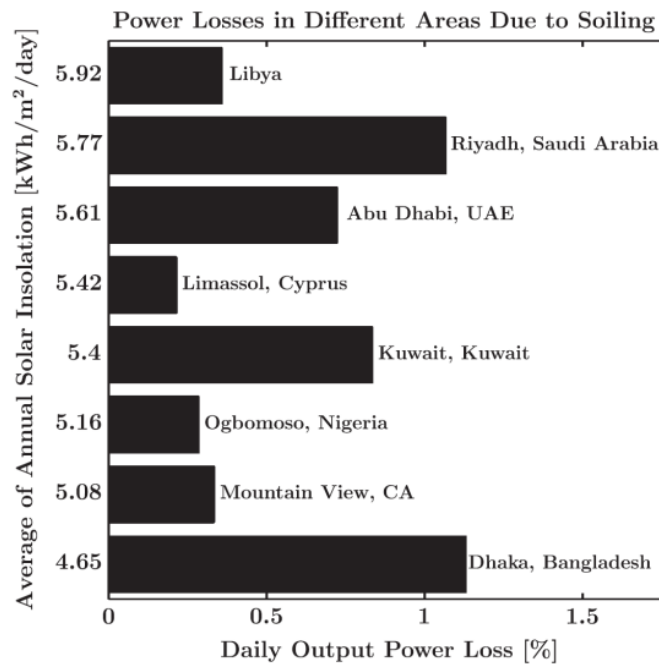


Figure 5. Soiling rate in dry climates is typically in the order of ~0.1-1 %/day. (Reprinted from Solar Energy, vol 107 (2014), Arash Sayyah, Mark N. Horenstein, Malay K. Mazumder, Energy yield loss caused by dust deposition on photovoltaic panels, pp 576-604, copyright 2014, with permission from Elsevier)

To convey the significance of this problem, consider that the record efficiency of polycrystalline PV cell (the most widely used PV technology) has increased by approximately 5% over the past 25 years (Figure 6). This improvement is

annulled in just half a month without cleaning in typical desert environments! Thus, when considering pathways to lower the levelized cost of electricity from PV, reducing the soiling rate offers large potential gain.

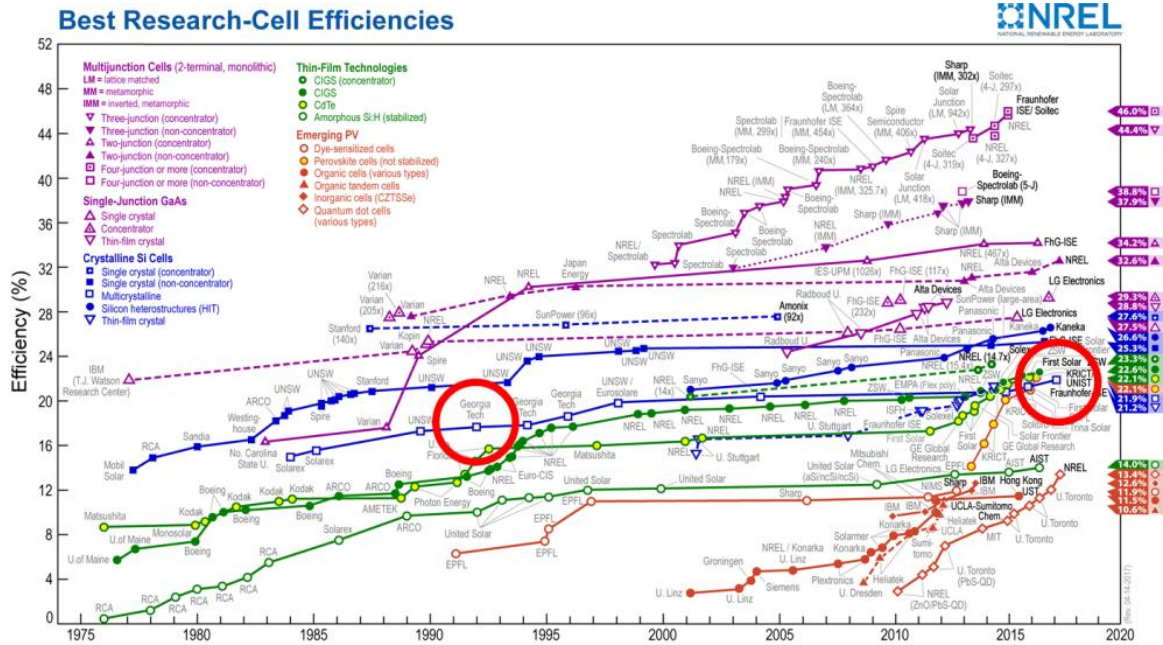


Figure 6. The record efficiency of polycrystalline PV cells has increased by ~5 percentage points since the early 1990s, indicated by red-circled points (National Renewable Energy Lab, www.nrel.gov/pv)

Soiling conditions at the present study site are in the mid-range of those presented in Figure 5. The Solar Test Facility (STF) in Doha, Qatar, is a 35,000 m² outdoor test site for solar-related research, operated by Qatar Environment & Energy Research Institute, part of Hamad Bin Khalifa University. The daily soiling rate of PV arrays (8 X polysilicon modules at 22° tilt south) has been measured continuously since March 2013, yielding more than 4 years of data at the time of writing. Using procedures described previously [9] the long-term average soiling rate at the STF has been found to be 0.41 %/day, with greater quantity and variation of soiling in winter than summer (Figure 7). Noted from Figure 4, PV modules that were never cleaned suffered soiling losses up to ~70%, and even those cleaned every two months reached soiling losses up to ~40% after dust storms. The results of a particularly severe dust storm are shown in Figure 8, which caused an immediate drop in PV performance of around 50%.

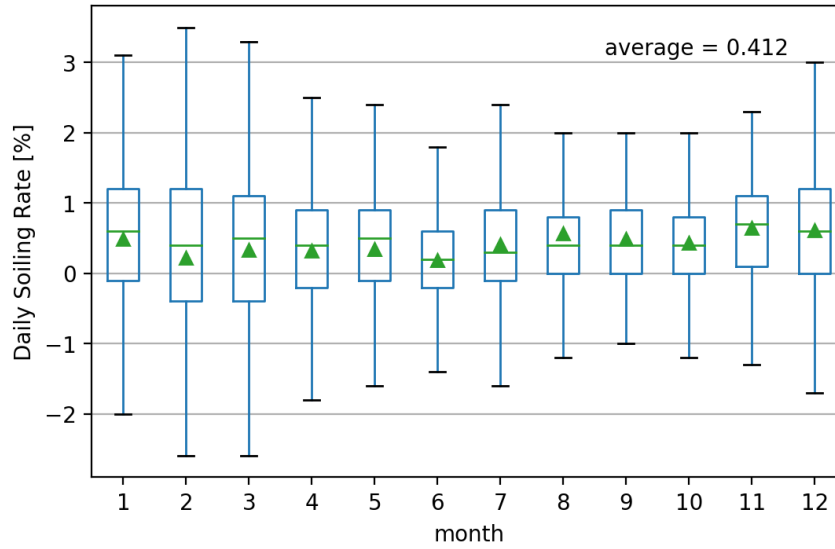
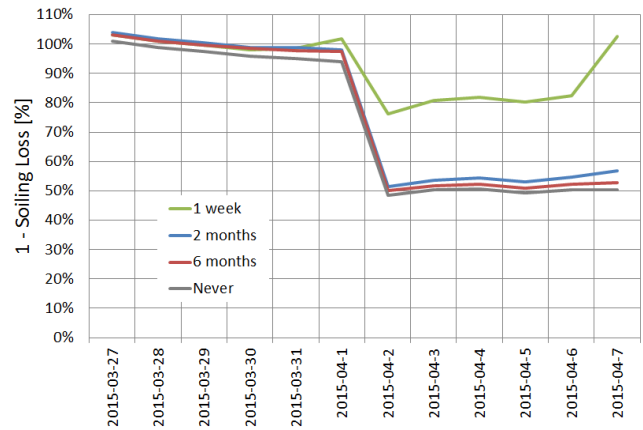


Figure 7. Variation of daily soiling rate by month at the STF, from Mar. 2013 to Jun. 2017. Positive values indicate soiling increase. (Month 1 = Jan. In this report boxplots are constructed as follows: Box top, mid-line and bottom indicate quartiles; whiskers indicate furthest data point within 1.5 X interquartile range of nearest quartile; triangle markers indicated means.)



(a)



(b)

Figure 8. (a) Soiled PV modules at STF following a severe dust storm in April 2015. (b) The dust storm caused an instant soiling loss of approximately 50% on most PV arrays

2.2. Soiling Modeling

Soiling can be considered the net result of three processes: particle deposition, rebound (immediate detachment), and resuspension (delayed detachment). Research and theoretical models of these individual processes are presented in detail in chapter 3. Modeling of PV soiling in field conditions has met with limited success due to inherent complexity and experimental difficulties, which are discussed in this section.

2.2.1. Relation to Environmental Parameters

Which environmental parameters have the greatest impact on PV dust accumulation? This fundamental question has not been comprehensively answered, and was a main motivation for this study. The rate of dust accumulation on surfaces is influenced by many factors, including characteristics of the surface (roughness, surface energy, conductivity, temperature), characteristics of the dust particles (composition, size, shape, electrical charge), geometry of the surface (tilt, size, orientation to wind) and environmental parameters (rain, wind speed, turbulence, RH, PM) [10]. For a PV module held in a fixed position at a certain location (i.e. so that dust composition and surface properties are fairly constant), variation in soiling rate “should” be fully explained by changes in environmental parameters. Yet field studies have tended to find weak or even contradictory effects of environmental parameters on PV soiling. Examples from the literature are provided:

In an analysis of soiling rates at the STF, it was previously reported [9] that daily averages of wind speed, RH and PM_{10} (concentration of airborne dust particles up to 10 μm diameter) had low correlations with the daily soiling rate (Figure 9). In Stellenbosch, South Africa, Musango [11] measured soiling in terms of optical reflection degradation on a building roof and found that its coefficient of determination (R^2) with wind speed was only 0.126, and with RH was only 0.105 (PM was not measured). Boyle et al. [10] measured soiling mass on ungreased collector plates over 1-5 week periods along with prevailing weather conditions at two Colorado locations, and by linear regression found that wind speed, PM_{10} , and air temperature together accounted for only 26% of variation in soiling, nor was RH a significant predictor of the amount of soiling. Micheli et al. [12] measured daily soiling loss on PV cells tilted at 20° at six sites across the US; wind speed and RH were measured concurrently at the sites, while PM_{10} and PM_{100} (particulate matter up to 100 μm) were 10-year averages from measurement stations within 10 km of the experiment sites obtained from a government database. Soiling correlation was moderate with wind speed and RH (R^2 of 0.42 and 0.44 respectively), and was mixed with PM (0.95 for PM_{10} and 0.34 for PM_{100}). As the authors noted, it is counter-intuitive that correlation would be lower for PM_{100} , which encompasses a greater proportion of the aerosol population than PM_{10} , and suggested that this may be partly explained by the small sample size of six. A reason for low correlations between dust accumulation and environmental parameters is that particles both deposit and detach from the surface, and these competing effects complicate the soiling response to meteo conditions. Using greased collector plates that eliminated particle detachment, on a building roof in Chicago, Noll et al. [13] reported relatively high correlation coefficients for deposition velocity with PM (0.82) and WS (0.66).

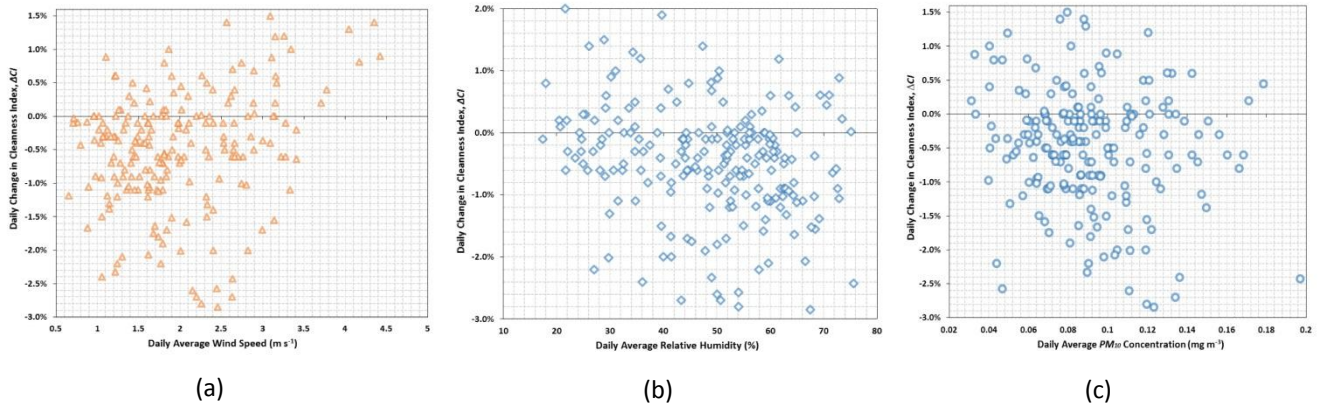


Figure 9. Daily soiling rate at the STF showed low correlation with daily averages of (a) WS, (b) RH, and (c) PM_{10} . “Daily Change in Cleanness Index” is equivalent to daily soiling rate, of opposite sign [9]. Copyright 2015 IEEE

2.2.2. Complexity

Researchers have occasionally remarked on the inherent complexity and unpredictability of dust mechanics. Emphasis is gained from the authors’ own words:

The mechanisms of transport, deposition and suspension are complex and thus the processes are not able to be modeled at the most fundamental level. — Aluko & Noll, 2006 [1]

There are, to date, practically no physical models of [particle] adhesion which relate adhesive strength to established fields of physics. — Bowling, 1985 [14]

In general, presently available experimental data do not support the existing theoretical models [of particle detachment.] — Ziskind, 1995 [15]

The dust fluxes from direct wind resuspension will depend on the time of exposure and potentially on the exposure history. These issues have not been addressed by the models. — Loosmore & Hunt, 2000 [16]

In studies of dust fluxes it is common to encounter orders-of-magnitude differences between modeled and experimental results [17], between experimental results of different studies [18], and among the data collected within a given experiment [10][19][20]. Difference between deposition model prediction and experimental observation of 3-10 times is considered “slight” [21]. Even in laboratory experiments — where surfaces, particles, geometry and airflow conditions can be controlled — widely ranging dust fluxes are encountered. In outdoor settings of course there are many uncontrolled influences and soiling behavior is even more complex. Nicholson [22] noted that field reports of dust resuspension rates varied by six orders of magnitude.

Reasons for this complexity and disparity of results include:

- Models of particle mechanics derived from physical principles usually rely on simplifying assumptions, such as perfectly spherical particles and flat, clean surfaces. Such as assumptions can be unrealistic, as seen by comparing an “ideal” adhered particle (Figure 19, page 60) and an actual example (Figure 24, page 68)
- Many variables affect particle motions and adhesion forces. In order to distil fundamental physical relationships, particle-mechanics models usually omit influential parameters such as RH [23] or surface roughness [24][25]
- There is interaction between parts of the soiling “system”, for example the effect of wind speed might be modulated by the level of humidity, and a greater amount of deposition leads later to a greater amount of detachment

This complexity, interaction and competition mean that the soiling rate is highly sensitive to experimental conditions, and effects of meteo parameters on the soiling rate are found to be weak or inconsistent.

2.2.3. Experimental Errors and Constraints

Another factor which has impeded field study of soiling is constraints and errors of measurement techniques. As noted in the introduction, Aluko & Noll [1] remarked that

Experimental results [of dust deposition] produced highly variable results. Much of this variation can be attributed to experimental errors associated with the nature of the atmospheric experiments.

Sources of experimental error are discussed in this section.

— Measurement interval

Meteo parameters vary minute-to-minute. In the case of wind speed, strong gusts might last only a few seconds. Weather stations readily record measurements every minute, yet in outdoor studies dust accumulation is usually measured in timescales of days [9], weeks [10], months [26] or even years [27]. (Soiling measurement methods are discussed further in section 2.3). Meteo measurements are averaged over the same (long) period as the soiling measurement interval for analysis purposes. This averaging obscures the relations of interest [10]. To illustrate: RH might vary between 20% and 80% over a day but to compare it against daily soiling value it is treated as having constantly been 50%. Also, such averaging eliminates extreme values of meteo parameters that might reveal interesting insights about the soiling mechanism. Continuing the same example: the soiling rate during the short-lived peak of 80% RH would never be known. A case from the literature is the study of dust deposition in a China desert [26], in which monthly averages of deposition and wind speed were found to have low correlation ($R^2 = 0.05$), despite wind

speed being known to powerfully influence dust deposition (section 3.1). Thus, shortening the time interval of soiling measurements might better reveal its physical connection with meteo parameters.

— Competing processes

Dust accumulation is the net outcome of competing processes: deposition and detachment. Knowledge only of the net accumulation rate results in two severe limitations:

- (i) The physical mechanics of dust accumulation are hidden. For example, if a coupon attains a steady-state quantity of dust over time, it is not known whether “turn over” of particles is occurring (new particles continually deposit and old ones detach) or the situation is “static” (no new particles deposit or detach)
- (ii) Effects of meteo parameters on soiling are obscured. For example, higher wind speed causes greater dust deposition and also greater detachment, so if only net accumulation is measured then wind speed might be (incorrectly) interpreted as having no influence on dust flux rates.

Customarily, separating dust accumulation into its component flux rates has required laboratory wind-tunnels and instruments. Goossens [28] remarked as recently as 2018, in a study of anti-soiling coatings, that:

it is necessary to know the effect of the coating on dust sedimentation and dust removal separately. This is difficult to assess in field measurements because there, dust patterns are always the result of accumulation.

— Sample size

A corollary of long period between measurements is small sample size. This makes it more difficult to detect relations between meteo parameters and soiling rate, and reduces the statistical confidence of those relations. Soiling field studies typically have sample sizes (exposure periods over which dust accumulation is measured) of tens or hundreds. The mentioned study by Boyle et al. [10], in which coupons were exposed at two field sites in rounds of 1-5 weeks for more than a year, was designed to “collect a large data set” for modeling dry deposition from PM and other parameters. “Large” in this case meant 174 samples from one site and 40 from the other. The previous section noted that particle mechanics are complex and dust flux rates exhibit much scatter, hence in soiling studies large sample sizes are especially advantageous when inferring the influences of meteo parameters.

— PM size distribution

Airborne dust concentration is often characterized by PM₁₀. This measure by definition excludes particles larger than 10 µm diameter, and does not reveal the size distribution of particles that are included. However in outdoor settings large particles tend to dominate soiling mass [13], partly because they have a greater tendency to deposit from the

atmosphere than small particles (see section 3.1.1). In a field study in Chicago, Lin et al. [29] found that remarkably, more than 99% of soil mass collected on greased plates comprised particles larger than 10 μm . At the STF in Qatar, the median particle size of dust collecting on PV modules for one month was found to be 14 μm [30]. This prevalence of particles larger than 10 μm suggests that PM_{10} is an imperfect measure of aerosol concentration for the purposes of studying ambient soiling, and may partly explain low correlations observed between aerosol concentration and dust accumulation [10]. However, it is inherently difficult to measure airborne particles larger than 10 μm using traditional particulate monitors because large particles tend to deposit in the instrument before being drawn through the sensor. For this, specialized instruments are required such as a rotary impactor [13] which are not commonly available and require expertise to use.

— Measurement limit

Methods of measuring ambient soiling are reviewed principally in section 2.3; here their uncertainties are discussed. An inherent challenge to soiling measurements is the small quantity of dust that naturally accumulates on surfaces in the field, which makes it difficult to measure accurately. Boyle et al [10] noted that uncertainty of gravimetric surface soiling measurement is typically in the order of $10 \text{ mg}\cdot\text{m}^{-2}\cdot\text{day}^{-1}$, and identified this uncertainty as one of the main sources of error in their ambient soiling model. In some investigations [10][13] experimental results were discarded, or rounded off to zero, because the amount of accumulated dust on coupons was below detection or measurement limits (in the case of Noll et al. [13], 15 of 24 samples were discarded because deposition mass was below the minimum weighable). In some [13][31][32], the duration of the experiment was dictated by the need to wait for a weighable amount of dust to accumulate.

In studies of soiling on PV modules, it is typical to quantify soiling by changes in the modules' electrical performance (e.g. short circuit current, power, or energy yield). Such parameters change little with the amount of soiling that accumulates over the course of a day, and suffer interference from other factors such as module temperature, irradiation intensity, spectrum, and angle of incidence [33]. Also, light attenuation by the soiling layer does not vary linearly with the mass of that layer (Figure 10), hence the electrical response of a PV module does not directly convey the physical quantity of dust on its surface.

— Rain and condensation

Measurements of dust accumulation on outdoor surfaces are interrupted by rain and heavy condensation (sufficient to run off and remove dust). Such events interfere when interpreting the effects of meteorological parameters on dust flux rates. It is common for soiling field studies to therefore be carried out only during dry periods [34]. While not an experimental error as such, this approach may give a biased view of the dust accumulation process, for example by excluding observation of cementation which is caused by dew.

2.2.4. Constraints Addressed by OSM

A main motivation of this study was to address the above constraints of field measurement of soiling, and thereby gain a better understanding its mechanisms. This led to development of the OSM, whose design and operation are described in chapter 5. Below, the OSM's ability to overcome some of those constraints is briefly discussed:

- Complexity

Traditional soiling field studies measure dust accumulation only (i.e. the net amount of deposition minus detachment). Nicholson noted in 1988 [22] that particle resuspension “cannot be directly measured in field experiments and can only be deduced by fitting the results to a numerical model”. The OSM enabled such direct measurements, by being able to detect dust particles both added to and removed from the collector over time. By “disentangling” the competing processes of deposition and detachment, the underlying physics of dust accumulation could be described more completely.

- Measurement period and sample size

In principle the OSM could capture images of the collector surface every few seconds, although in practice they were taken every 10 minutes. As noted, field studies usually allow dust to accumulate for days or weeks between measurements. As a result of the 10-minute interval, thousands of soiling measurements could be obtained within a few weeks with the OSM instead of tens or hundreds. The main advantages of the short measurement period were (i) dust fluxes were measured at the same timescale as changes in weather conditions, and (ii) large sample sizes were obtained which benefited statistical analysis and confidence of results.

- Measurement limit

The OSM could detect individual dust particles depositing on the collector, and reliably measure their size when greater than $\sim 4 \mu\text{m}$. Its lower measurement limit could therefore be estimated by a single $4 \mu\text{m}$ particle of silica depositing within the 4 mm^2 imaged area over the course of a day, resulting in a measurement of $0.044 \text{ mg}\cdot\text{m}^{-2}\cdot\text{day}^{-1}$. The gravimetric measurement limit of soiling collector plates is in the order of $10 \text{ mg}\cdot\text{m}^{-2}\cdot\text{day}^{-1}$ [10]. That is, the OSM enabled field soiling measurements orders of magnitude finer than common existing methods.

- Rain and condensation

When rain or heavy condensation occurred, only the affected OSM images could be discarded. E.g. if it rained for a few minutes on a day, then OSM observations for that period would be discarded but those for the rest of the day could still

be used. In contrast, to avoid disruption of dust collection by rain, other field studies have been limited to dry seasons [34] or employed a “roof” over the collector plate [10]. An advantage of the OSM was it could be used in all seasons and weather conditions.

In summary, the main advances of this study were the OSM’s abilities to (i) measure soiling rate at the same timescale as the weather, (ii) separate soiling into its underlying components of deposition and detachment, and (iii) obtain very large sample sizes for robust statistical inference, and using those features to more clearly understand how soiling is governed by environmental parameters.

2.3. Soiling Measurement

In this section traditional methods for measuring soiling rate in the field are reviewed. Techniques for quantifying the amount of soiling on PV modules and surrogate coupons can be broadly categorized as gravimetric (soil mass), light transmission loss, response of a photoelectric device, and imaging (photography and microscopy).

2.3.1. Soil Mass

Mass provides the most direct characterization of soiling extent [35][36][37]. The collector surface can either be full-size PV modules and arrays [38] or surrogate coupons [35][39][40][41]. The advantage of collecting dust from PV arrays is that it is a direct — rather than proxy — measurement of PV soiling. However it is labor intensive, difficult to completely collect all dust, and ends the test period. Small coupons, on the other hand, can be easily and accurately weighed before and after soiling [35][39][40], and then returned to the field if desired. Removing soil from the surface allows further properties to be analyzed such as its chemical composition and particle size distribution [8][37][42][43][44][45].

What is the relation between soil mass and PV performance? In some cases mass was found to be proportional to PV power output loss [8] and transmission loss [46][47]. Yet two phenomena can disrupt this linear relation [35][48][49], (Figure 10): First, for the same mass of soil, smaller particles have a larger total cross-sectional area and hence occult more light [36]. Second, for surfaces that are already soiled, newly-depositing particles may settle on existing particles and so may increase soil mass but not transmission loss [35][50]. Therefore: Characterizing soiling by its mass directly portrays the quantity of soil accumulated, which is useful for studying physical soiling processes; but to characterize soiling in the context of PV performance, methods based on light transmission are more useful.

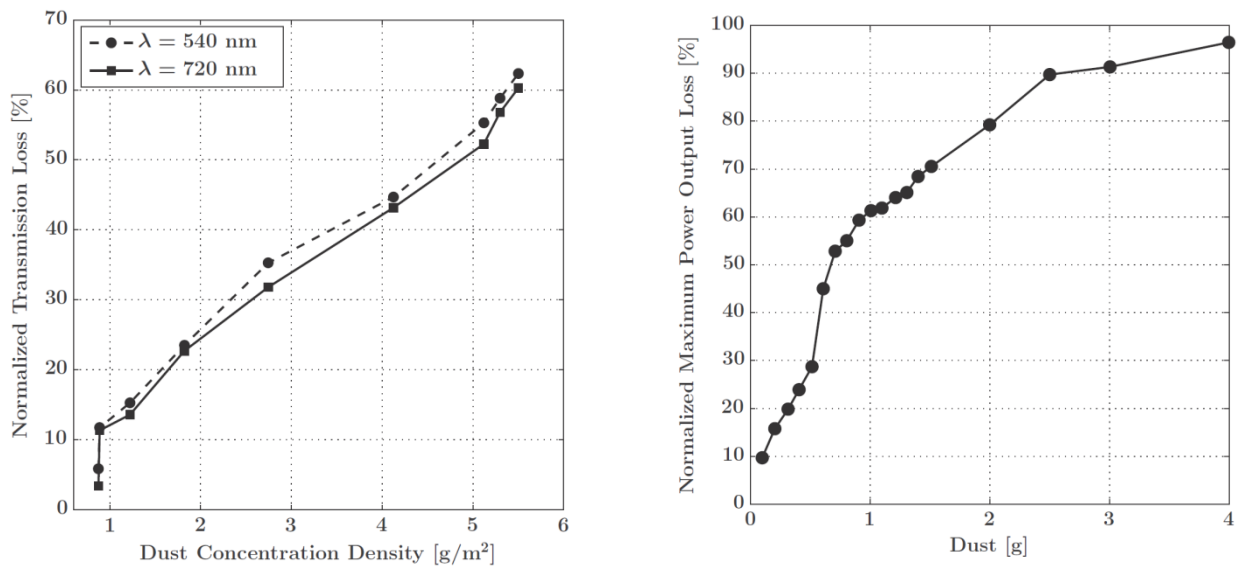


Figure 10. Examples from the literature of linear (left) and non-linear (right) effects of soil mass on light transmission/PV power loss. In right figure, surface area was 12x8 cm. (Reprinted from Solar Energy, vol 107 (2014), Arash Sayyah, Mark N. Horenstein, Malay K. Mazumder, Energy yield loss caused by dust deposition on photovoltaic panels, pp 576-604, Copyright 2014, with permission from Elsevier)

2.3.2. Light Transmission

Soiling can be characterized by attenuation of light passing through a transparent substrate, which can be easily measured with a pyranometer or spectrometer [43][45][50][51][52]. Although those are the most common instruments, others have also been used: Bahattab [51] measured light scattering of soiled samples with an integrating sphere, haze meter and angular detector. Burton [52] also measured specular reflectance with an integrating sphere. Brown [53] reported that gloss was the most sensitive and repeatable of measurement techniques tried. John [45] used a quantum efficiency meter to measure transmission of light of different wavelengths.

Pyranometers tend to either be based on a silicon PV cell [54] or else measure total (global) irradiation. Dust tends to preferentially attenuate short light wavelengths, causing a slight red-shift in the transmitted light [39][45][55]. An advantage of PV-based pyranometers is that their spectrum response matches that of widely-used silicon PV modules, so the measured soiling value mirrors the effect on actual PV performance. In contrast, global pyranometers have a “flat” spectral response and hence provide a more universal measure of accumulated soiling (not biased by the type of PV cell). Gostein [56] developed a compact CdTe-based pyranometer to achieve both spectral response match with the particular PV technology of interest, and small device size for ease of operation. If the main intent is to measure soil accumulation (rather than predict power loss of an actual PV system), it is advantageous to measure light transmission of samples using an indoor test stand with repeatable, artificial lighting, which eliminates variation in intensity, spectrum and diffusivity of natural sunlight [37][43][45].

Typically, soiling loss is portrayed as the change in transmission loss (TL) of a sample when it is clean versus soiled [51]. This approach is adequate if different samples have similar clean TLs, and the degree of soiling is moderate; otherwise soiling loss calculations may be distorted. For example: Substrates A and B have 5% and 20% TL respectively when clean. Both are then covered with identical thick layers of dust that block all light. The apparent soiling loss of Substrate A will be 95%, while that of Substrate B will be 80%, despite bearing the same dust load.

Different soiling loss readings for the same dust load can occur between outdoor and indoor test conditions, e.g. due to light spectrum and intensity, beam pathways, pyranometer positioning, and pyranometer temperature. It is recommended that these effects be studied further to better understand the comparability of lab and field results.

2.3.3. PV Device Output

For solar-energy practitioners, the ultimate interest in soiling is its effect on the energy generated by a PV system. This encourages use of soiling measurements based on characteristics of a photoelectric device, such as a PV cell, module or array. Using PV modules allows the effect of soiling on real-world, commercial PV products to be measured. PV modules can experience uneven soiling over their surface [8][57], so another advantage of using full-size modules is that they capture soiling patterns that may not be replicated by smaller work-pieces such as PV cells or glass coupons.

These attractions of using PV modules for soiling measurement are reflected in a summary of soiling studies presented by Sarver [46]. Of the 73 studies mentioned, 35 used PV modules or arrays, 6 used PV cells, 8 used transparent plates (glass or plastic), 2 used pyranometers, and the others technologies not related to PV, e.g. mirrors, heliostats, and solar thermal collectors. Reviews by Costa et al. [5] and Sayyah et al. [8] also showed dominant use of PV modules for soiling studies.

Soiling can be characterized by its effect on PV short-circuit current (I_{sc}) [45][48][52][57][58][59][60][61], I-V curve [35][36][45][62][63][64], power (P_{max}) [37][43][56][57][62][63][65][66] or the associated performance ratio [67], or energy yield (e.g. kWh/day) [9][68]. By installing a reference PV module and a “treatment” test module, it is possible to measure soiling rate over time, or the effect on soiling of coatings and tilt angles [8][64][65][68]. Module I_{sc} is often used as a proxy for module performance in soiling measurements because PV voltage remains fairly constant for moderate changes in irradiance [35], and I_{sc} is easier to measure than power (which requires maximum power point operation) (e.g. Abdulameer [69] used an ordinary multimeter to measure I_{sc} manually). However as shown in a series of papers by Gostein and associates on soiling measurement of utility-scale PV plants [57][64][70], non-uniform soil coverage may disrupt the correlation between I_{sc} and module power, especially for crystalline silicon modules where shading of some cells can affect the electrical operation other cells. Further, I_{sc} is less sensitive to temperature than is module power, so the two methods will indicate different soiling losses if the module temperature changes between measurements [60], unless corrected for using module’s power temperature coefficient [57][64]. For these reasons, I_{sc} of a PV device is a simple and effective method for characterizing degree of soiling, however it may not precisely reflect the soiling power loss of an actual PV system.

2.3.4. Imaging Techniques

In laboratory studies of particle mechanics, micro-photography and micro-videography have been used for decades to count and size particles, and observe their trajectories. In 1975 Dahneke [71] measured particle rebound from a surface by recording laser beams scattered by particles with an oscilloscope. Wu et al. [72] measured particle resuspension in a wind tunnel with a stereo-microscope coupled to a videotape recorder. Kassab et al. [73] and Farzi et al. [74] traced paths of particles detaching from a surface via a microscope equipped with high-speed camera. Biryukov [75] used a 42X lens attached to a digital microscope in the lab to observe particle deposition on a horizontal PV module. A microscope/camera combination was used by Barth et al. [76] to study effects of airflow turbulence and velocity on particle resuspension. Kim et al. [77] noted that a larger imaged area provides more data points of particle detachment, which is useful because such motions are stochastic in nature.

In recent years, as cameras and computers have become cheaper and more powerful, photography has been adopted for soiling studies in the field as well. Yap et al. [78] evaluated five algorithms for analyzing photographs of soiled PV modules, and found the most accurate was that which matched them to a database of photographs of known PV soiling. It was proposed that such a tool could be deployed by a drone aircraft. Microscope images of soiled coupons provide data on surface coverage (projected area of dust particles as a proportion of the surface area) and particle sizes [47][51][52][79]. Traditionally microscopes have been used in laboratories, however inexpensive, low-power portable microscopes are now available as mass-market consumer electronics. They are so inexpensive as to be virtually disposable, which lead to the idea of using them in outdoor settings in the present study.

2.3.5. Measurement of Individual Dust Fluxes

A challenge to experimental study of soiling is that it is the net result of simultaneous and competing processes: (i) dust deposition, (ii) rebound (immediate detachment) and (iii) resuspension (delayed detachment). To understand the overall soiling process, it is necessary to study these three mechanisms *individually* and *simultaneously*. In both laboratory and field experiments, it is straightforward to achieve either of these goals but not both (see chapter 3). For example, deposition can be measured by exposing a greased collector to dust-laden airflow, and resuspension can be measured by exposing a soiled collector to clean airflow. However it is difficult to separately measure deposition and resuspension when a soiled collector is exposed to dust-laden airflow, especially in field conditions.

First, consider separating dust accumulation into only two processes: deposition and “detachment” (which includes both immediate rebound and delayed resuspension). They can be measured individually and simultaneously using a pair of collectors, one greased and the other not. Dust accumulation on the greased collector represents deposition, and the difference in accumulation between the collectors represents detachment. Biryukov [34] used this technique in an Israel desert to quantify particle “attachment coefficient” (the complement of rebound fraction). Wu et al. [72] exposed greased and ungreased Teflon surfaces to uranine particles in a wind tunnel, and measured the mass of

particles adhering to each to quantify rebound fraction. Yet in both these studies, rebound and resuspension were confounded.

Now, consider separating dust detachment into rebound and resuspension. This is more difficult to measure experimentally. The only known study in which this was attempted in an outdoor setting was also by Wu et al. [41]. The researchers measured dust accumulation at different heights in a forest in Tennessee using “Frisbee” shaped collector discs. One greased (A) and two ungreased collectors (B, C) were used. One of the ungreased collectors (B) was replaced with a clean one half-way through the test, while the other (C) was left in place undisturbed. Each half of the test was approximately one day. The difference in dust accumulation on B vs. C during the second half of the test was used to estimate resuspension, and (like the aforementioned studies) the difference in accumulation on A vs. C indicated combined rebound and resuspension. While this method allowed all three fluxes to be quantified with simple apparatus in the field, it relied on the approximation that there was no resuspension from B in the second half of the test, and indeed the authors refer to the resuspension measure as being an estimate.

To summarize: It is desirable to individually and simultaneously measure dust deposition, rebound and resuspension in ambient conditions. Only one known study attempted this, which relied on gravimetric soiling measurement and long measurement period, both of which lead to experimental error (section 2.2.3). The main goal of the present study was to obtain these measurements with greater accuracy and ease, via optical microscope imaging in the field with 10-minute measurement interval.

3. Review of Dust Particle Mechanics

Soiling of PV modules occurs through accumulation of dust particles from the atmosphere. This accumulation can be separated into three processes: particle deposition, rebound, and resuspension (Figure 11). (This study deals only with “dry” deposition, not removal of dust from the atmosphere by rain). Terminology in this report is as follows:

- “deposition” — all dust particles that impact the surface
- “rebound” — those particles which immediately detach again
- “resuspension” — those particles which detach at a later time
- “accumulation” — the remaining deposited particles, i.e. which collect on the surface.

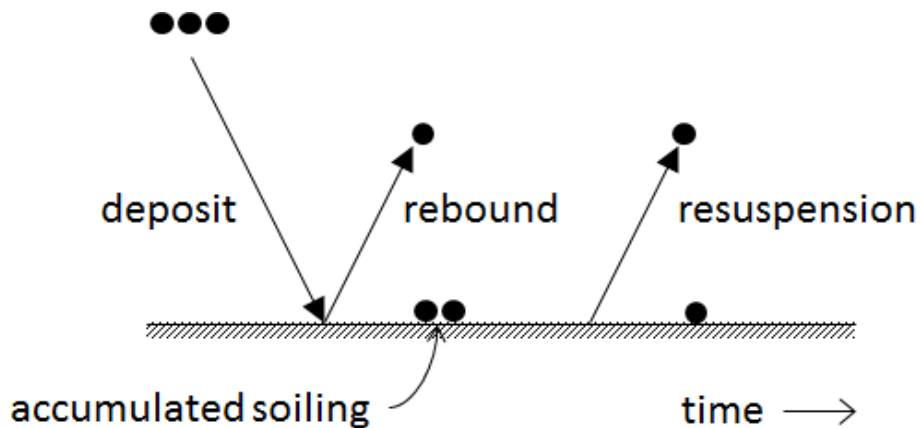


Figure 11. Soiling is the net result of particle deposition, immediate rebound, and delayed resuspension. The mechanisms can be modeled and summed to describe dust accumulation over time.

The processes are quantified as dust flux rates — mass of dust transported to or from a unit area of the collector surface per unit time. For dust flux rates typical of ambient desert conditions, it is convenient to work in units of $\mu\text{g}\cdot\text{m}^{-2}\cdot\text{min}^{-1}$. To provide a sense of scale, the average deposition flux rate on a horizontal coupon at the Solar Test Facility in Qatar was $86 \mu\text{g}\cdot\text{m}^{-2}\cdot\text{min}^{-1}$. Hereafter, italics are used to denote the above quantitative dust flux rates. E.g. “*Deposition*” denotes the quantitative flux rate (having dimension $\mu\text{g}\cdot\text{m}^{-2}\cdot\text{min}^{-1}$), whereas “deposition” is used when discussing the general principle.

The flux rates balance arithmetically:

$$\textit{Accumulation} = \textit{Deposition} - \textit{Rebound} - \textit{Resuspension} \quad (1)$$

Deposition, rebound and resuspension are largely controlled by airflow characteristics, and have been studied for decades via controlled wind-tunnel experiments and observational outdoor studies. With the rapid expansion of PV plants in desert regions, there is also a growing body of research on PV soiling. This chapter reviews literature at the intersection of these topics — particle mechanics relevant to desert conditions — to explain PV soiling behaviors.

3.1. Deposition

A survey of relations between deposition and airflow relevant to PV systems in desert environments is presented in this section. Broader reviews of dry deposition literature have been provided by Ruijgrok et al. [20] and Habchi et al. [24].

3.1.1. Dominant Deposition Conditions and Mechanisms

The three main mechanisms of particle deposition in natural environments are gravity settling (sedimentation), inertial or turbulent deposition, and Brownian motion [80]. Their relative importance depends on the ratio of inertial to viscous forces, i.e. particle size and air-stream acceleration. Large and dense particles have more inertia and fast, turbulent airflow has greater acceleration. Different deposition mechanisms dominate under different particle size/flow velocity combinations, see for example Figure 12 [81]. Small particles (diameter in the order of $\sim 1 \mu\text{m}$ and smaller) are controlled by Brownian motion [82][83][84]: they diffuse randomly in space and tend to remain entrained in flow streams. Very large particles (order of $\sim 100 \mu\text{m}$ and larger) exhibit sedimentation only: they are governed solely by gravity and rapidly deposit from the air regardless of flow conditions [1]. Mid-sized particles (order of $\sim 10 \mu\text{m}$, i.e. several microns to tens-of-microns in diameter) experience viscous forces comparable to their inertia, and exhibit inertial deposition [1][84][85] which increases with flow velocity. Particles of this size are entrained by air flow (they remain aloft for long periods) but if that flow accelerates sharply, due to obstruction by an object for example, the particles may deviate from the stream and impact the object. Thus, in calm conditions (low flow velocity) mid-sized particles deposit by sedimentation alone, and in windy conditions their deposition rate is enhanced by the inertial mechanism.

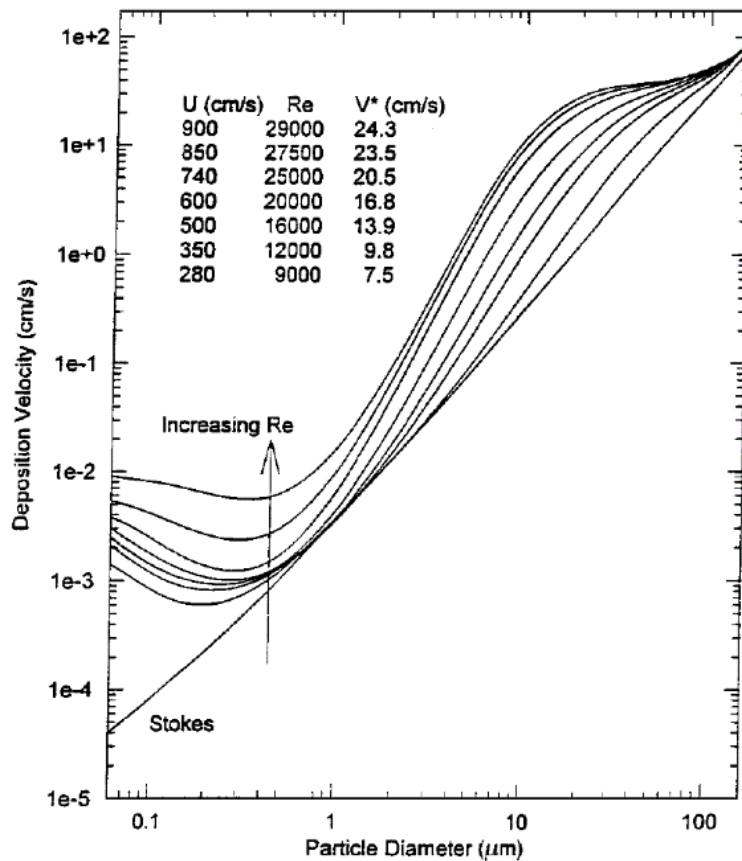


Figure 12. Deposition of particles in the order of $\sim 10 \mu\text{m}$ is governed by both gravity (shown by Stokes line) and air flow (inertial deposition). U is mean flow velocity, V* is friction velocity. [81]. (Aerosol Science & Technology: Development of an Atmospheric Dry Deposition Model, 35:2, 627-636. 2001. Reston, VA. Reprinted with permission)

Which deposition mechanism(s) are relevant to PV soiling in desert environments? To answer this, consider particle sizes and wind speeds typical of deserts. Data from previous studies are reviewed:

- Typical particle size

Sizes of particles accumulating on outdoor surfaces have been reported in many studies (Table 1). It is seen that the dominant size is generally reported as between 10 and $30 \mu\text{m}$. This was corroborated in the present study, for the Solar Test Facility in Doha, Qatar: A horizontal glass coupon was exposed to ambient soiling for 24 hours at the STF; a micrograph of the surface is shown in Figure 33 (p84). The accumulated dust particles were sized by converting their projected areas to diameters using circles of equivalent area, and those smaller than $3.6 \mu\text{m}$ were excluded (the cut-off is explained in section 5.2). Particle-size distributions by frequency, surface coverage (projected area), and volume are shown in Figure 13. The quantity most relevant to PV soiling is surface coverage, as this correlates with the fraction of light blocked from reaching the solar cell. It is seen in Figure 13.b that surface coverage was dominated by particles in

the 10-40 μm size range. That is, the size distribution of dust accumulating in the present study was consistent with other examples reported in the literature.

Particle size [μm]	Diameter definition*	Parameter description	Collector surface	Location	Ref.
10-30	$D_{a,r}$ converted from D_{pa}	Coarse particle mass peak	Horizontal greased Mylar film	USA (Chicago)	[31]
>10	$D_{a,r}$ converted from D_{pa}	Dominant size by mass	Horizontal greased Mylar film	USA (Chicago)	[29]
>2	D_a	99% of deposited mass	Horizontal greased Mylar film	USA (Chicago)	[1]
~32	D_{pa}	Transmission loss peak	Solar collector	Israel	[79]
17	Not stated (presumed D_e)	Mean diameter peak	Tubular dust collector	Mexico (Mexico City)	[86]
30	Not stated (presumed D_e)	Median diameter	Dust sample prepared from aeolian loess	Belgium	[61]
8-16	Not stated (presumed D_{pa})	Dominant size by count	Tilted plate	Kuwait	[55]
18	D_e	Mean diameter by volume	PV modules at 22° tilt	Qatar (Doha)	[38]

* D_a = aerodynamic equivalent diameter, D_{pa} = projected area equivalent diameter, D_e = equivalent mass diameter

Table 1. Examples of dominant size range of particles accumulating on outdoor surfaces

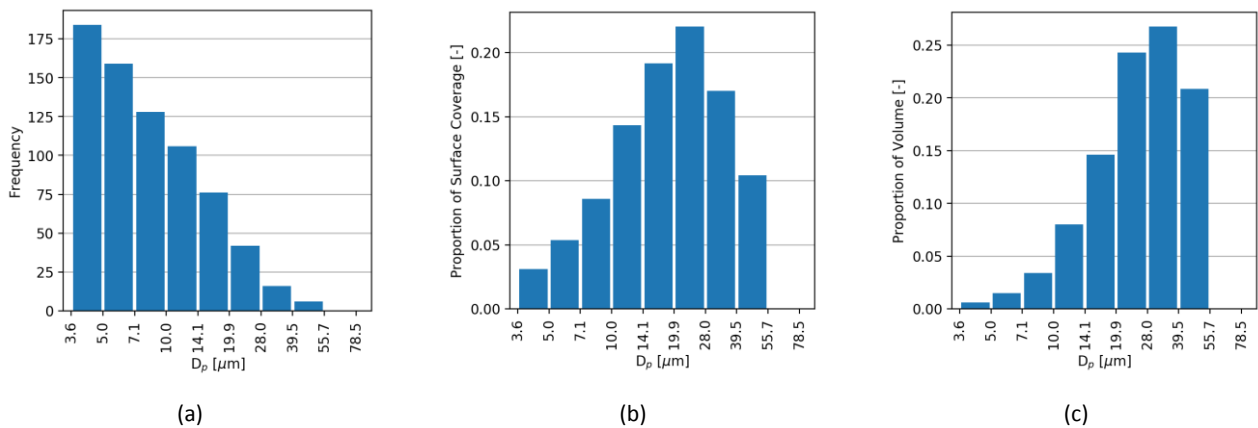


Figure 13. Distribution of particles sizes accumulating in 24 hours on a horizontal collector at the Solar Test Facility, presented as (a) frequency (number), (b) proportion of surface coverage, (c) proportion of dust volume. Excludes particles smaller than 3.6 μm . D_p bins are logarithmic

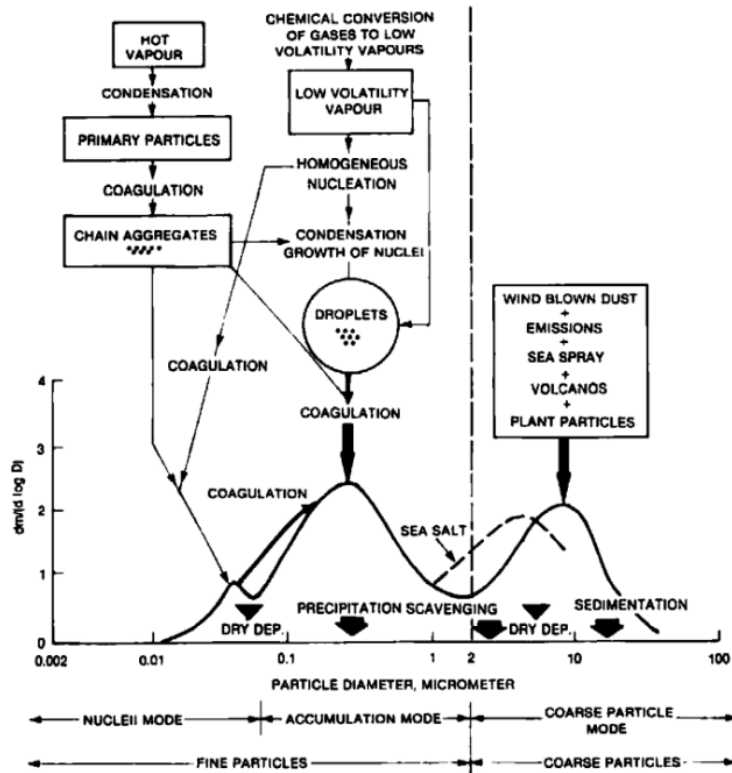


Figure 14. Worldwide there is a population of airborne mineral dust in the order of 10 μm [87]. (Reprinted from the Annals of Glaciology with permission of the International Glaciological Society)

Regarding airborne (as opposed to deposited) particulate matter, the world’s atmosphere at large exhibits a coarse mode of mineral particles (Figure 14). Its dominant size range has been variously reported as microns to tens of microns [32], 5-10 μm [80], $\sim 10 \mu\text{m}$ [87], 15 μm [31], 10-20 μm [14] and 10-50 μm [1]. Thus, the dominant particle size range observed at the Solar Test Facility of 10-40 μm is broadly consistent with global norms of aerosol size. From the literature and local observations, it is concluded that the size range of dust particles most relevant to PV soiling is tens of microns.

Finally, it is noted that previous studies highlight the importance of coarse particles to soiling in outdoor settings. Lin et al. [29] reported that deposition from the atmosphere near Chicago was dominated by particles larger than 10 μm , and their colleagues Holsen & Noll [21] noted that “large particles control dry deposition flux” in ambient conditions because of their great deposition velocities.

— Typical wind speed

Wind speeds encountered in deserts are harder to generalize than particle size. An atlas of wind speed 10 m above ground in the Middle East showed that it averages less than 4.43 ms^{-1} in all but a few locations [88]. At the STF in Doha, wind speed was measured at 2 m above ground every minute during 2015 (anemometer: Thies Clima Wind Speed Transmitter), it was found that median speed was 1.70 ms^{-1} and the 90th percentile was 4.1 ms^{-1} . Further, the

projected area of dust particles depositing onto a horizontal glass collector 1.2 m above ground was measured with an OSM every 10 minutes during August 2016, along with wind speed at the same height, and showed that 96% of deposition occurred when wind speed was less than 3 ms^{-1} . Overall it appears that most dust accumulation on PV modules in deserts (in the Middle East at least) occurs in low wind speeds, simply because that is the dominant weather condition.

In summary, dust surface coverage on PV modules in desert environments is largely accounted for by particles tens of microns in diameter, depositing in low wind-speed conditions. Therefore it is expected that sedimentation is the major deposition mechanism, while inertial deposition may also contribute during windy periods [34][89]. Brownian motion is negligible because small particles contribute little surface coverage and their deposition rates are relatively slow; it is not further considered. Literature on sedimentation and inertial deposition is next reviewed in more detail.

3.1.2. Sedimentation

Particle descent under the action of gravity is referred to as sedimentation. Large particles descend faster than small ones because their weight is proportionally greater than their aerodynamic drag force. All particles exhibit some degree of sedimentation, but it dominates deposition when particles are larger than $\sim 1 \text{ }\mu\text{m}$ and inertial forces are absent (i.e. wind speed is low). It solely governs the behavior of particles larger than $\sim 100 \text{ }\mu\text{m}$, regardless of airflow conditions (see again Figure 12).

The rate at which particles deposit from the atmosphere is characterized by their deposition velocity, v_{dep} [ms^{-1}]:

$$v_{dep} = F/C \quad (2)$$

where F is the mass flux rate of particles impacting the collector [$\text{g}\cdot\text{m}^{-2}\cdot\text{s}^{-1}$] and C is the atmospheric particle concentration [$\text{g}\cdot\text{m}^{-3}$]. Higher v_{dep} value indicates greater rate of deposition.

As illustrated by Figure 12 a particle's deposition velocity has sedimentation (v_{sed}) and inertial ($v_{inertial}$) components, i.e.:

$$v_{dep} = v_{sed} + v_{inertial} \quad (3)$$

A particle's v_{sed} is its terminal velocity reached due to gravity. One of three equations is used to calculate v_{sed} depending on the flow regime surrounding the falling particle. The flow regime is governed by the ratio of viscous to inertial forces experienced by the particle, which is characterized by dimensionless particle Reynolds number, Re_p :

$$\text{Re}_p = U D_p / \nu \quad (4)$$

where U is the particle's velocity through the air [$\text{m}\cdot\text{s}^{-1}$], D_p is its diameter [m], and ν is the kinematic viscosity of air [$\text{m}^2\cdot\text{s}^{-1}$]. The flow regimes and corresponding sedimentation velocities are determined as follows:

- 1) $\text{Re}_p < 1$ — The particle falls sufficiently slowly that Stokes (creeping) flow is exhibited, and v_{sed} is given by:

$$v_{sed} = \rho_p D_p^2 g / 18\mu \quad (5)$$

where ρ_p is the particle's density [$\text{kg}\cdot\text{m}^{-3}$], g is gravitational acceleration [$9.81 \text{ m}\cdot\text{s}^{-2}$], and μ is the dynamic viscosity of air [$\text{N}\cdot\text{s}\cdot\text{m}^{-2}$]. Buoyancy of atmospheric dust particles is small and can be ignored [80]. For particles smaller than $1 \mu\text{m}$ a Cunningham slip correction factor would need to be applied because of non-zero fluid velocity at the particle's surface, however such small particles are not relevant to the present study.

- 2) $1 < \text{Re}_p < 600$ — The particle falls at sufficient velocity that transition flow is exhibited, and v_{sed} can be estimated from the following empirical equations [80]:

$$v_{sed} = \frac{\mu}{\rho_{air} D_p} e^{(-3.070 + 0.9935J - 0.0178J^2)} \quad (6)$$

$$J = \ln\left(\frac{4\rho_{air}\rho_p D_p^3 g}{3\mu^2}\right) \quad (7)$$

where ρ_{air} is the density of air [$\text{kg}\cdot\text{m}^{-3}$].

- 3) $\text{Re}_p > 600$ — Newtonian flow is encountered and another equation for v_{sed} would be used. This situation is not encountered for natural dust particles.

To determine whether Stokes or transition flow (i.e. case 1 or 2) is relevant for the present study, consider characteristics of typical dust depositing in deserts. As discussed in the previous section, the dominant particle size is $10\text{-}30 \mu\text{m}$. Dust composition in Qatar and surrounding carbonate-rich regions is predominantly calcite (density $2710 \text{ kg}\cdot\text{m}^{-3}$) and quartz ($2650 \text{ kg}\cdot\text{m}^{-3}$) [30]; their average density can be approximated as $2700 \text{ kg}\cdot\text{m}^{-3}$. At $25 \text{ }^\circ\text{C}$ the kinematic viscosity of air ν is $1.57 \times 10^{-5} \text{ m}^2\cdot\text{s}^{-1}$ and its density is $1.18 \text{ kg}\cdot\text{m}^{-3}$. Since eq. (4) requires knowledge of v_{sed} (as U), which one is trying to determine, it must be solved iteratively with eqs. (5) and (6). Doing so reveals that mineral particles up to roughly $60 \mu\text{m}$ (which easily encompasses the dominant size range) experience Stokes flow, hence eq. (5) adequately estimates sedimentation velocity for the purposes of this study.

Substituting the particle density of 2700 kg.m^{-3} and air dynamic viscosity of $1.983 \times 10^{-5} \text{ N.s.m}^{-2}$ into eq. (5) simplifies v_{sed} [ms^{-1}] to a function only of D_p [m]:

$$v_{sed} = \frac{23700 \times D_p^2 \times 9.81}{18 \times 1.983 \times 10^{-5}} = 6.51 \times 10^7 D_p^2 \quad (8)$$

Irregular (non-spherical) particle shape slows particle settling, hence in natural conditions v_{sed} will be lower than that predicted by eqs. (5) and (8) [17]. Empirical adjustments to v_{sed} to account for particle shape have been reported in previous studies[42][90][91].

To verify the broad validity of eq. (8) for the present study, the aerosol population at the Solar Test Facility can be treated as having a dominant (by surface coverage) particle size of $20 \mu\text{m}$ (see Figure 13.b). Then from eq. (8) $v_{sed} \approx 0.026 \text{ ms}^{-1}$. The estimate is roughly consistent (within a factor of two) with the experimental data presented by Noll et al. [81] in Figure 12 for the same particle size, providing confidence for the validity of eq. (8).

The expected sedimentation flux rate at the STF can also be estimated, using the long-term average aerosol concentration (PM) at the site of $C = 0.144 \text{ mg.m}^{-3}$. Using the dominant particle size of $20 \mu\text{m}$ and its commensurate v_{sed} of 0.026 ms^{-1} , the estimated flux rate is $F = C v_{sed} = 225 \mu\text{g.m}^{-2}.\text{min}^{-1}$. Due to irregular shapes of real particles (and hence lower terminal velocities), the expected sedimentation flux rate will be somewhat lower than this. As will be shown later (e.g. Figure 42 on page 102) this rough estimate of deposition flux rate agrees well with observed rates measured by the outdoor soiling microscope in this study. Again, this brief analysis validates eqs. (5) and (8) for broadly predicting the dust sedimentation rate in deserts.

Inertial deposition is reviewed in the next section. However here it is briefly noted that some outdoor studies found that turbulence contributed significantly to the deposition rate (i.e. $v_{inertial}$ is of similar scale to v_{sed}), while others found it did not. Prominent reports in the latter category include: (i) Biryukov [34] studied soiling of solar-energy collectors in an Israel desert and concluded that particles larger than $4 \mu\text{m}$ deposited via sedimentation alone (however the experiments were conducted in wind speed less than 4 ms^{-1}). (ii) Boyle et al. [10] measured particle deposition on collectors at two Colorado sites and determined that the flux rate could be explained solely by Stokes-regime sedimentation. On the other hand, evidence for significant inertial deposition came from a series of studies conducted on the roof of a 4-story building in Chicago by Noll et al. [13], who found that the underside of a greased horizontal collector received approximately one third as much soiling as its upper face — which could only have been produced by the inertial mechanism. Overall, the expectation for the present desert study site is that sedimentation will dominate dust deposition, but in windy conditions inertial deposition may also be significant.

3.1.3. Inertial Deposition

Except at very low wind speed, the atmosphere tends to be turbulent [32]. Its turbulence is further increased by the presence of large-scale roughness in the flow field such as PV arrays. If a turbulence eddy causes a volume of air to be directed toward a surface, particles larger than $\sim 1 \mu\text{m}$ [84][92] to $5 \mu\text{m}$ [31] have sufficient inertia to deviate from the air volume, potentially traverse the viscous (i.e. laminar) sublayer that exists immediately adjacent to the surface, and impact the surface [20][25][31][29][83][85]. This mechanism is referred to as turbulent or inertial deposition. Particles smaller than $\sim 1\text{-}5 \mu\text{m}$ tend to remain entrained in the air flow even as it accelerates sharply, and hence not do exhibit turbulent deposition. Particles larger than $\sim 100 \mu\text{m}$ are controlled almost exclusively by gravity, and their deposition rate is likewise independent of turbulence intensity [25][31][43]. That is, inertial deposition is relevant for particles several to tens of μm in diameter.

The tendency for particles to penetrate the viscous sublayer depends on their inertia relative to the fluid viscosity. This quality is characterized by the dimensionless Stokes number, St , defined as the ratio of a particle's stop distance to a characteristic length, l [m], such as the sublayer thickness [84]. The stop distance is the product of the particle's relaxation time, τ [s], and the free-stream flow velocity, U [ms^{-1}] [84]:

$$St = \tau U / l \quad (9)$$

$$\tau = \rho_p D_p^2 / 18\mu \quad (10)$$

Deposition via this impact mechanism is characterized by inertial deposition velocity, $v_{inertial}$. It is additive to the deposition velocity due to gravity, v_{sed} , per eq. (3). The significance of inertial deposition is indicated in Figure 12, where it manifests as a "bulge" additional to the Stokes settling velocity (v_{sed}) for $1\text{-}100 \mu\text{m}$ particles. The bulge widens (i.e. $v_{inertial}$ increases) as flow velocity increases, because flow velocity in turn causes turbulence to increase. The degree of turbulence can be characterized by flow Reynolds number [25][81], turbulence intensity [82], or most commonly friction velocity, u^* [1][89]. Friction velocity is roughly proportional to free-stream velocity and for simplicity can usually be approximated as a certain percentage of wind speed [1][16][93].

The inertial deposition mechanism was first described in 1957 [25] and subsequently became widely adopted for particle deposition theory. In 1973 Sehmel [94], in wind-tunnel experiments with uranine particles, demonstrated that turbulence caused significantly more deposition than could be explained by gravity and other mechanisms. He introduced the concept of an effective eddy diffusion coefficient, ε , which characterized particle transport from the bulk flow to the surface due to diffusion by turbulence eddies and particle inertia:

$$v_{inertial} = \varepsilon \frac{dC}{dy} \quad (11)$$

where y is distance from the surface. That transport can be considered to comprise two mechanisms: eddy diffusion of particles to the top of the viscous sublayer, and then their (possible) penetration of the sublayer resulting in impact with the surface [89]. Slinn & Slinn [95], addressing deposit of pollutants onto lakes and oceans, developed a resistance model in which the driving potential was particulate concentration and those two mechanisms were represented by resistance terms:

$$v_{inertial} = \frac{1}{R_a + R_b} \quad (12)$$

R_a quantified impedance to particle transport by atmospheric turbulence to the top of the sublayer, and R_b impedance to transport through the sublayer [96]. R_b also had terms related to Brownian diffusion, dust interception by protruding structures (e.g. foliage), and surface roughness. In the case of PV soiling, where Brownian motion is not important and surfaces are relatively smooth, impaction dominates [85] and the resistance terms can be approximated by:

$$R_a = \frac{1}{C_D U} \quad (13)$$

$$R_b = \frac{1}{u^* \left(\frac{St}{St + \alpha} \right)^\beta} \quad (14)$$

where C_D is the particle drag coefficient (approximately 0.01 on land), $\alpha = 0.8$, and $\beta = 2$ [96].

Resistance deposition models have been widely used, and a general review of them was provided by Barrie [87]. Zhao & Wu [97] developed a model for deposition from turbulent flow based on an eddy diffusion parameter, in which v_{dep} was proportional to u^* and inversely proportional to resistance terms derived from particle properties. Their model accounted for all deposition mechanisms and surface directions (floor, ceiling and wall).

An important body of research on ambient deposition emanated from the Illinois Institute of Technology from the 1980s, e.g. [21][31][29][81][85]. Much of this work employed greased collection plates. Inertial deposition was assumed equal in all directions, therefore soiling on a plate's upper surface was interpreted as inertial plus gravity deposition ($v_{inertial} + v_{sed}$), while that on the lower surface was the difference ($v_{inertial} - v_{sed}$). In a 1989 study [31] Noll and Fang deduced that $v_{inertial}$ could be empirically modeled as a function only of friction velocity and particle size:

$$v_{inertial} = 1.12 u^* e^{(-30.36/D_p)} \quad (15)$$

where D_p is expressed in [μm] and the velocities in [ms^{-1}]. In this model, inertial deposition is effectively linearly proportional to wind speed. A more complex influence of wind speed was allowed by a model of Kim et al. [85], who

obtained experimental data by injecting glass spheres and other particles of 10-100 μm into the air and measuring their deposition onto nearby coupons. Their model for inertial deposition was similar in form to that of Noll & Fang [31] above, but with the exponent based on flow eddy Stokes number, St_{eddy} :

$$v_{inertial} = u^* 10^{(-2.8/St_{eddy})} \quad (16)$$

$$St_{eddy} = v_{Stokes} u^{*2} / g\nu \quad (17)$$

The significance of this modification to the model was that wind speed had a more powerful effect on inertial deposition, i.e. $v_{inertial}$ increased more rapidly as wind speed increased. Using a model of the same form, Slinn and Slinn [95] experimentally derived the constant in eq. (16) to be -3 rather than -2.8.

Later, in 2001, Noll et al. [81] developed an alternative deposition model which used an expression for inertial deposition based on flow Reynolds number and dimensionless particle relaxation time, τ^+ (mathematically identical to St_{eddy}). Its origin lay in a model for turbulent deposition in pipes [98] which used Re as the flow characteristic (as opposed to the more customary u^*). Again, the authors used a greased collector plate outdoors in Chicago to calibrate the model. It was found that deposition of 1-8 μm particles was sensitive to both Re and τ^+ , while for particles $>8 \mu\text{m}$ deposition was governed by τ^+ alone. For the latter size range, which dominates PV soiling, $v_{inertial}$ could be modeled by:

$$v_{inertial} = b_1 u^* e^{-0.5 \left[(\ln \tau^+ - \ln b_2) / b_3 \right]^2} \quad (18)$$

$$\tau^+ = \tau u^{*2} / \nu = St_{eddy} \quad (19)$$

where b_{1-3} are dimensionless constants. In this model u^* appears in both the exponent and as a scalar, allowing more complex (non-linear) relation between wind speed and inertial deposition.

Which of the models presented best describes PV soiling? First, differences between analytical and empirical models are considered. Analytical models tend to be based on several, fundamental attributes such as drag coefficient and characteristic lengths of the boundary layer and surface. In contrast empirical models tend to be based on fewer, empirical parameters such as particle size and free-stream flow velocity. Analytical models derived from laboratory experiments usually deal with micron/sub-micron size particles in ducts and pipes, whereas empirical models derived from ambient experiments involve particles in the tens of microns and natural winds [23]. Consequences of laboratory simulations of soiling include:

- Wind-tunnel ducts and pipes — employed to study particle mechanics by many researchers [25][94][99][100] — tend to imperfectly recreate ambient flow characteristics, particularly atmospheric turbulence [20]. Noll & Fang [31] wrote that their study “overcomes the major disadvantage of wind tunnel studies, i.e. the need to extrapolate to atmospheric conditions. This is important because the atmospheric turbulent regime is difficult to simulate in the laboratory.” Ruijgrok [20] commented that a shortcoming of models derived from wind-tunnel experiments is that they necessarily assume stable or neutral atmospheric conditions (i.e. little motion of air parcels due to atmospheric dynamics). This is not always valid and can cause deposition to be under-estimated by 2-3 times if atmospheric transport of aerosols is significant.
- Wind-tunnel studies tend to use particles smaller than those present in natural conditions, whereas large particles in fact dominate deposition flux in natural settings. This is illustrated by a comparison of model predictions presented by Kim et al. [85], Figure 15. A reason for wind tunnels’ reliance on small particles is that large particles “are difficult to generate and stabilize in wind tunnel studies” [31]. Kim et al. alluded to unspecified “sampling problems” in duct experiments and noted that, as a result, less deposition research had been conducted for 10-100 μm particles than for smaller ones, despite the dominance of the larger size in ambient soiling. Holsen & Noll [21] compared wind-tunnel and outdoor deposition studies and found that the latter show greater influence of coarse particles (1-100 μm) on deposition. One reason, they said, is that wind-tunnel derived models greatly underestimate inertial deposition of large particles. They reported that the eddy-diffusivity model of Sehmel (eq. (11)) predicts that turbulence does not affect deposition of particles larger than $\sim 10 \mu\text{m}$, and the model of Slinn & Slinn arrives at the same prediction for particles $> 3 \mu\text{m}$, whereas ambient experiments by Noll & Fang [31] found that inertia contributed to deposition of particles even up to 100 μm . Lin [29] noted that because of its lack of consideration of large particles, the eddy-diffusion model of Sehmel underestimated deposition of 5-80 μm particles in outdoor conditions. This was a significant drawback because — as Lin further reported — particles larger than 10 μm accounted for more than 90% of dust mass deposited from the atmosphere.

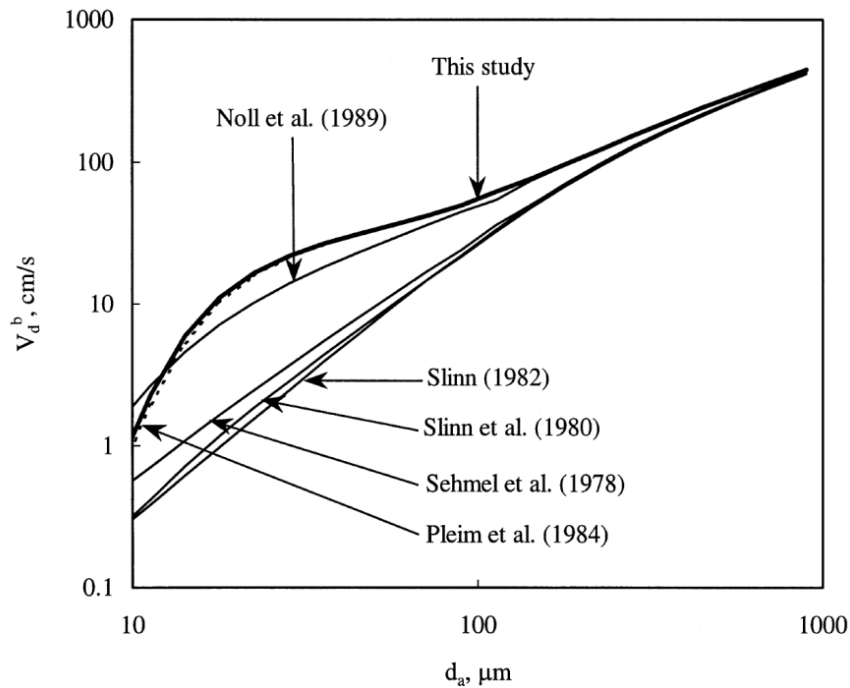


Figure 15. Deposition rate of large particles, which dominate desert soiling, tends to be more accurately predicted by empirical models derived from studies in ambient conditions than lab-derived analytical models. “This study” in the figure refers to the model of Kim et al. [85], i.e. eq. (16). V_d^b = dry deposition velocity, d_a = particle aerodynamic diameter, $U = 2 \text{ ms}^{-1}$. [85]. (Reprinted from Atmospheric Environment, vol 34, Eugene Kim, David Kalman, and Timothy Larson, Dry deposition of large, airborne particles onto a surrogate surface, pp 2387-2397, 2000, with permission from Elsevier)

In Figure 15, inertial deposition predicted by certain models was plotted against particle size. The present study focuses on effects of meteo parameters on soiling rate, so it is of interest to also compare models’ predictions as a function of wind speed. To simplify this comparison, a single particle size of $20 \mu\text{m}$ was chosen (being the dominant size at the present study site, Figure 13.b). Using assumptions shown in Table 2, the predicted $v_{inertial}$ values and corresponding dust flux rates were calculated, Figure 16. Notable results are that the model of Noll et al. [81] predicted significantly higher deposition rates than the others, while the model of Kim et al. [85] predicted the existence of a threshold wind speed below which $v_{inertial}$ was negligible. As will be shown (section 6.4.1), the present study also encountered a threshold relationship between deposition and wind speed, and inertial deposition flux even greater than that of Noll et al.

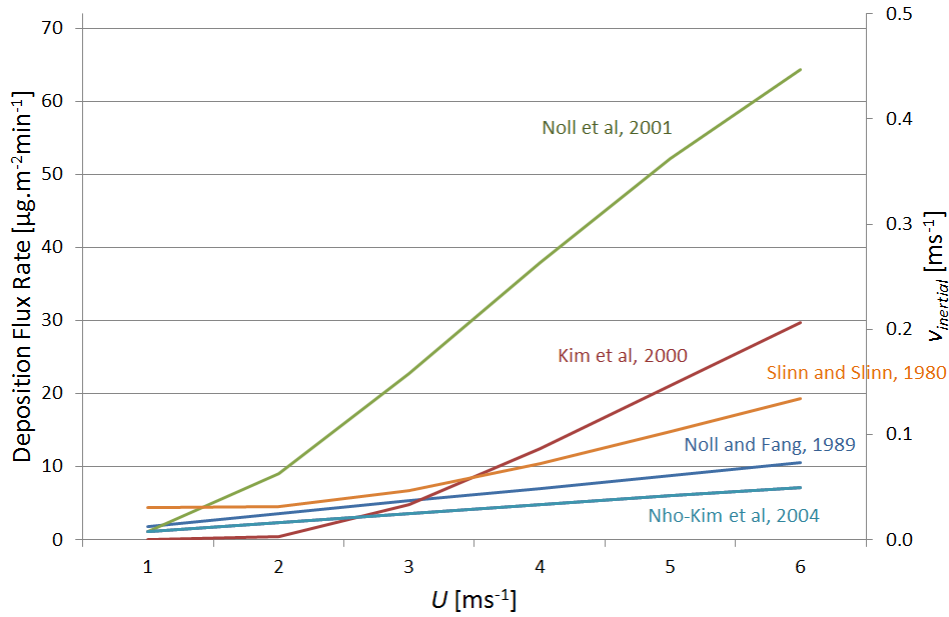


Figure 16. Predicted inertial deposition velocity for 20 μm particle as a function of wind speed (U) (right axis), and corresponding inertial deposition flux rate for a 0.144 mg.m^{-3} airborne concentration of 20 μm particles (left axis), from certain previous models

Parameter	Value	Units
D_p	20	μm
ρ_p	2700	kg.m^{-3}
u^*	5% of $U^{(1)}$	ms^{-1}
ν	1.57E-05	$\text{m}^2 \text{s}^{-1}$
μ	1.98E-05	$\text{kg.m}^{-1} \text{s}^{-1}$
ρ_{air}	1.18	kg.m^{-3}
v_{Stokes}	2.97E-02	ms^{-1}
τ	3.03E-03	s
C	0.144 ⁽²⁾	mg.m^{-3}
C_D	0.01	-
l	100	μm

(1) 5% was chosen after [16][73][101]

(2) Average PM concentration at the Solar Test Facility

Table 2. Parameter values used to generate Figure 16

In summary, coarse dust particles (predominantly 10-30 μm) and low wind speeds encountered in Qatar and similar desert environments mean that sedimentation is the dominant deposition mechanism, while inertial deposition may also be significant in windy conditions. Inertial deposition velocity in natural environments has been modeled more successfully with empirical equations (derived from atmospheric studies) than analytical ones (derived from ducts and pipes), because of the importance of large particles in deposition in natural conditions. Models in the literature vary greatly in their prediction of deposition rates, especially of large particles which dominate PV soiling.

3.1.4. Airborne Particle Size Distribution

As mentioned, a particle's deposition velocity is strongly dependent on its size. Therefore to estimate deposition flux rate, F , from airborne dust concentration, C , two approaches are possible:

- 1) Use a single effective deposition velocity for the entire aerosol population ($v_{dep_effective}$) and a single parameter for the aerosol concentration ($C_{effective}$) [19]. A common proxy for $C_{effective}$ is PM_{10} . Then eq. (2) is applied as:

$$F = v_{dep_effective} C_{effective} \quad (20)$$

- 2) Segment the aerosol population into particle-size bins (of number i), each with its own concentration (C_i) and deposition velocity ($v_{dep,i}$). I.e.:

$$F = \sum v_{dep,i} C_i \quad (21)$$

The second approach results in more accurate flux prediction because the ambient particulate size distribution varies over time [17][21]. However measuring that distribution (i.e. measuring C_i values over time) requires specialized instruments such as a rotary impactor [32][102].

Ruijgrok [20] examined the use of mass median diameter (MMD, the diameter which divides the particle population into halves when sorted by their mass) as the single descriptor of the aerosol size, and found that for fine particles (MMD of 0.5 μm) it under-predicted deposition velocity by a factor of 3-6. Boyle et al. [10] found that a soiling model segmenting aerosol into 52 sizes was as accurate as an equivalent one with only two sizes ($PM_{2.5}$ and PM_{10}). Yet neither approach found a strong correlation between aerosol concentration and soiling — it explained only 9% of soiling mass variation — which the authors proposed was because the largest particle size measurable in either approach was only 10 μm (PM_{10}). Holsen & Noll [21] also concluded that knowledge of concentration of large particles is essential because they dominate accumulated soiling mass, yet noted that in practice it is difficult to capture and measure particles larger than 10 μm . Further, Holsen & Noll compared predictions of three deposition models from the literature and found that using nine particle-size segments was more accurate than using a single effective concentration, in particular because the latter failed to account for variation in abundance of large particles (which dominated soiling mass). In observational studies, use of many segments decreases the number of data points in each segment, which reduces statistical confidence. For this reason Barth et al. [76] actually did the opposite and merged data bins when interpreting wind-tunnel resuspension results. Even when complete information on particle size distribution is available, orders of magnitude difference in deposition velocities are often observed between theoretical and field measurements, and even between results of different experiments run under the same conditions [20].

In summary, it is sometimes found that accounting for changing particle-size distribution improves accuracy of deposition models, and it is especially important to know concentration of large particles (as they dominate outdoor

soiling). However measurement of aerosol size distribution requires specialized equipment, and even then it is difficult to measure particles larger than 10 μm . Hence, use of a single concentration metric (e.g. PM_{10}) and effective deposition velocity are common simplifications. In this study, airborne particle-size distribution could not be measured directly, however a particulate monitor with total (“TSP”) PM inlet — as opposed to PM_{10} — was used in attempt to account for large particles. It is noted that particulate monitors even with TSP inlets do not capture all large particles, as they are prone to settling out of the induced airflow before the detector.

3.2. Rebound

“Rebound” refers to particles immediately bouncing off a surface upon deposition, and being re-entrained in the air flow. In contrast, particles that adhere for some time before being re-entrained are said to “resuspend”, which is covered in section 3.3. This section reviews research methods and findings on particle rebound.

3.2.1. Rebound Theory

In principle rebound occurs when a particle’s kinetic energy with which it impacts the surface is greater than its work of adhesion to that surface (i.e. the energy required to overcome the adhesion forces) [72][80][82][103][104]. Bateman et al. [105] developed a quantitative model which calculated a particle’s “residual kinetic energy” as the difference between its pre-impact kinetic energy and energy dissipated by inelastic collision and overcoming van der Waals and capillary adhesion; rebound was predicted to occur if the residual energy was positive. The model was reported to describe rebound observations well. Paw U and Braaten [104] reported that rebound was enhanced when flow is parallel to the surface. Together these results indicate that rebound is dependent on particle size, flow velocity and surface orientation, in addition to adhesion factors such as surface energy, humidity and roughness.

Rebound can help explain size distribution of accumulated soiling particles, in a conceptual model advanced by Bateman et al. [105] (Figure 17). Small particles have low deposition velocities, as they tend to remain entrained in air streams and not collide with surfaces in their path. At the other extreme, large particles are susceptible to rebound from the surface in rapid flow because of their great kinetic energy. Therefore maximum net deposition (deposition minus rebound) may be expected for mid-sized particles, having sufficient inertia to separate from eddies but insufficient energy to overcome adhesion.

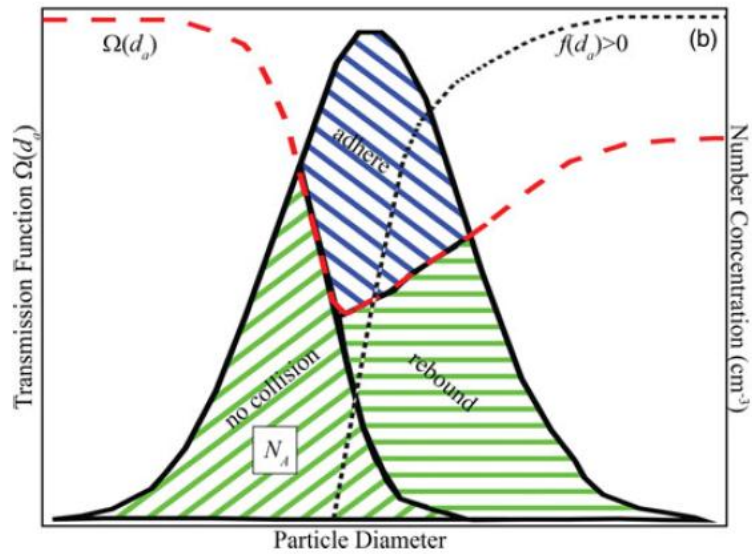


Figure 17. Low deposition of small particles and increasing rebound of larger particles result in dominant net deposition of mid-sized particles [4]. (Aerosol Science and Technology: Impactor Apparatus for the Study of Particle Rebound: Relative Humidity and Capillary Forces, vol. 6826, pages 42-52. 2014. Reston, VA. Reprinted with permission)

Consider the pattern of particle deposition velocities portrayed in Figure 12 (p42). This figure represents (total) deposition, i.e. without particle rebound, because greased collectors were used. If rebound were allowed and followed Bateman's description, one would expect to see a reduction in *net* deposition for mid-sized particles. This is indeed observed in the results of Ruijgrok et al. [20] (Figure 18), who compared four models' predictions of net deposition velocity in a forest canopy. A red line has been added to their figure in the present report to show a typical (total) deposition velocity profile (i.e. akin to Figure 12). Figure 18 also illustrates that although very large particles have the greatest tendency to rebound, they also have a strong tendency to settle again on a horizontal surface due to gravity, therefore the red line and settling velocity converge for very large particles.

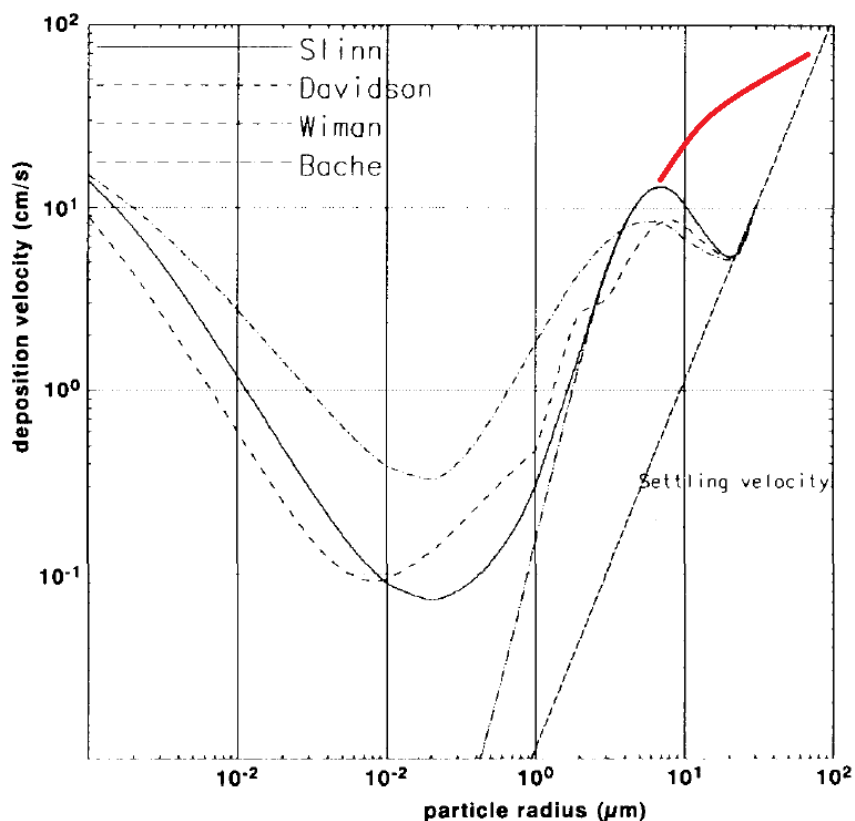


Figure 18. Effect of rebound on net deposition velocity on a horizontal surface [9]. Red line added in present report to schematically indicate gross deposition. (Reprinted from *Tellus B*, an Open Access journal)

Further, the work of Ruijgrok et al. provides quantitative information on the particle size range most susceptible to rebound. By regarding the difference between the red line (deposition) and predictions of net deposition, Figure 18 suggests that rebound affects 5-100 μm particles, and is especially relevant for 20-50 μm particles. Since the dominant particle size range for PV soiling in Qatar is 10-30 μm (section 3.1.1), it is expected that rebound is an important mechanism in the present study.

3.2.2. Experimental Results

Particle rebound is characterized by the fraction of particles impacting a surface that rebound again. In experimental work, fractions of particle numbers or fractions of masses are used.

Dahneke [106] showed that 1.27 μm latex spheres in vacuum tended to rebound completely (i.e. their rebound velocity approached their impact velocity) when their impact velocity exceeded $\sim 5 \text{ ms}^{-1}$. Nho-Kim et al. [96] stated that only particles larger than 5 μm are susceptible to rebound, although an explanation was not provided. Wu et al. [72] studied rebound of uranine particles in a wind tunnel using greased and ungreased surfaces. As expected, rebound fraction (by mass) increased with flow speed and the largest particles (10 μm) had the highest rebound fraction. Unexpectedly, 8.6 μm particles rebounded less than 5.4 μm ones, which was attributed to higher relative humidity during experiments

with the 8.6 μm particles. It was also found that humidity had a greater effect on rebound at low flow speeds. The researchers proposed that rebound fraction followed a power law with flow velocity, i.e.:

$$\text{rebound fraction} = U^b \quad (22)$$

where the parameter b varies with particle size and flow turbulence.

An alternative relation between rebound and characteristic velocity was used to model saltating particles, which is a different physical process than dust deposition from the atmosphere but nevertheless involves particle rebound. Kok [107] described the probability that a saltating particle will rebound upon impacting the sand bed again — a similar concept to rebound fraction — by:

$$\text{rebound probability} = b_1(1 - e^{-b_2 u_{\text{impact}}}) \quad (23)$$

where b_1 and b_2 are constants and u_{impact} is the velocity with which the particle impacts the bed.

Biryukov [108], in desert experiments mentioned previously, found that the fraction (by number) of rebounding particles was consistently around 0.14, regardless of particle size. This result contrasts with the expectation that rebound fraction increases with particle size (although for the largest particle size, 64 μm , increased rebound was indeed observed). The unexpected result was attributed to low wind speed during the study, i.e. particles impacted with little kinetic energy and adhered to both greased and ungreased surfaces. Paw U [104] performed computer simulations of particle rebound and resuspension, incorporating particles' coefficient of restitution. The simulations predicted that rebound and resuspension were relevant only for particles larger than 10 μm . For particles that are relatively inelastic (i.e. with coefficient of restitution less than that of the surface) they would need to be even larger to rebound.

Humidity decreases particle rebound because it promotes capillary adhesion between particle and surface. In a study of impact-based aerosol samplers, Winkler [109] reported that above 75% RH particles were captured “efficiently” by the collector plate. Bateman et al. [105] also found that higher RH decreased particle rebound, and that as RH increased the minimum particle size observed to rebound also increased. Further, particle hygroscopicity was shown to be important to rebound behavior: Hygroscopic ammonia sulfate particles exhibited suppressed rebound above 20% RH, and reached a minimum at 70% RH. In contrast, hydrophobic polystyrene particles showed rebound decrease only above 50% RH, and reached a minimum at 95% RH. These results are relevant to the present study, as RH frequently exceeds 70% at the Solar Test Facility and the dust contains hygroscopic material (see section 7.2.1).

In summary, the common model of rebound is that it occurs when a particle's kinetic energy exceeds its work of adhesion to a surface, and hence increases with particle size and flow velocity. This has been generally, but not universally, supported by experiments. Rebound can contribute to a decrease in net deposition velocity (deposition minus rebound) of particles of 20-50 μm . Unlike deposition and resuspension, there are no widely-adopted models

that quantitatively describe rebound in arbitrary conditions. However the mechanism is important — in their review Ruijgrok et al. [20] concluded “particle bounce-off and resuspension are major factors influencing deposition from ambient surfaces”. Presence of moisture, due either to high humidity or hygroscopic matter, can greatly inhibit rebound.

3.3. Resuspension

Resuspension is the process by which particles detach from a surface to which they have adhered for a period of time, and re-entrain into the air flow. In this section literature on particle resuspension relevant to desert PV soiling is reviewed. Resuspension theory has been reviewed in further detail by others [15][22][76][82][92][110].

3.3.1. Detachment Mechanics

Particles can detach initially from a surface by sliding, rolling, or lift-off (perpendicular to the surface) [18][111]. In principle the observed motion is that which occurs at the lowest flow friction velocity. In practice this is generally found to be rolling. Ahmadi et al. [112] calculated that rolling occurs at a much lower flow speed than does sliding, and lift-off force is negligible. Ibrahim [113] studied detachment of various types of particles (10-65 μm) from glass with a video camera and deduced that in all cases the initial particle motion was primarily rolling. Wu [72] observed that particles move along the surface before being resuspended. Likewise Kassab [73], using a high-speed camera to photograph trajectories of detaching particles, found the most common removal trajectory was “complex liftoff” (particles rolled and bounced for some time before being resuspended), followed roughly equally by “immediate liftoff” and “pure rolling/bouncing”. In a review of resuspension studies Ziskind [15] concluded that rolling was the most probable motion for initial particle detachment, and would certainly occur before sliding. Cleaver [114] studied turbulent bursts causing particle detachment by the generation of lift forces, however noted findings by other researchers that in creeping flow lift forces are negligible. Henry & Minier [82] wrote that the presence of the surface itself dampens flow velocity fluctuations normal to it, which suggested that longitudinal (i.e. drag) detachment was more likely than lift-off. He also noted much experimental evidence in the literature indicating rolling detachment of smaller particles, whereas larger particles were more susceptible to lift-off by turbulent bursts. Benito [115] performed Monte Carlo simulations of particle detachment and found that modeling it as a rolling process yielded better fit to experimental data than lift-off or sliding processes.

Assuming that rolling is the dominant detachment motion, the aerodynamic force necessary to initiate rolling (and thus resuspension) is considered. A perfect sphere on a perfectly flat surface experiences no moment to oppose rolling. In reality, there will exist some deformation in the contact area or roughness of the particle and surface that creates a pivot point and a moment that opposes rolling (Figure 19). Flowing air creates a drag force, F_{drag} , which acts at a vertical distance from the pivot approximately equal to the particle radius. This establishes a moment about the pivot point that is counteracted by the adhesion force, F_{adh} , acting in the area of particle-surface contact (similar principles

have been reported previously [82][116]). Rolling occurs when the drag moment exceeds the adhesion moment. Particle weight and lift force are ignored in this balance because they are negligible compared to the drag force [16][18][23][24][112][113].

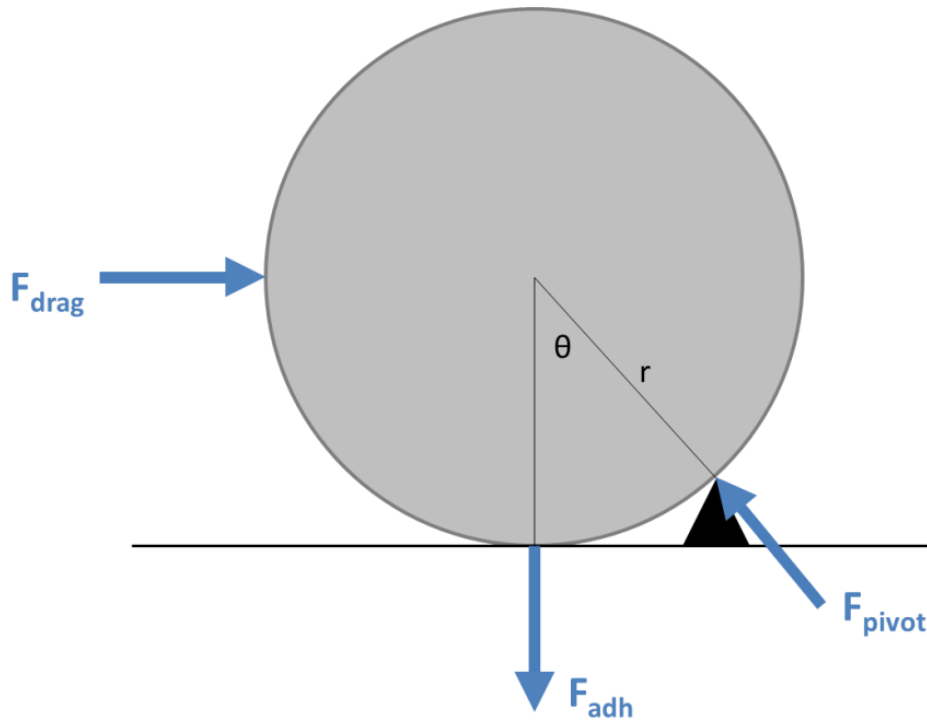


Figure 19. Schematic diagram of forces acting on an adhered particle, in which an irregular feature (e.g. an asperity on the surface) creates a pivot point. Rolling can be modeled as occurring when the drag moment about the pivot exceeds the adhesion moment

Resuspension models can be divided into force and energy approaches [15][24][82]. In force approaches, like that described above, resuspension occurs when the instantaneous drag moment overcomes the particle-surface adhesion moment. In energy approaches, it occurs when a particle accumulates sufficient vibrational energy to overcome the work of adhesion [20][24]. Vibrational energy is acquired as the particle is excited by fluctuating (i.e. turbulent) air motions that cause it to vibrate or “rock” about a pivot point on the surface. The energy-based theory was developed by Reeks et al. [117] to help explain observed resuspension of particles at flow velocities below those predicted by the force-balance approach [15]. Vibrational energy is gained by adhered particles most efficiently when the frequency of turbulence fluctuations matches the resonant frequency of the particle’s elastic motion [118]. The mechanism can only happen if the particle damping or relaxation time is longer than the period between turbulence events, otherwise the particle’s energy dissipates before the next impulse occurs. Therefore energy-balance models are more relevant for large particles and high-Reynolds number flow [104]. Paw U & Braaten [104] stated that Reeks’ model implies that particles need to be around 100 μm to experience this mechanism, but that it could also apply to smaller ones depending on particle and surface characteristics.

In this study the relation between wind speed and particle detachment in the force-balance approach is considered. The energy-balance approach requires information on particle and surface properties and near-surface flow characteristics that is not readily available, and as mentioned is most applicable for larger particles and faster airflow than are experienced in desert PV soiling.

3.3.2. Resuspension – Wind Speed Relation

What is the expected relation between wind speed and particle resuspension rate? The goal here is not to quantitatively predict the detachment wind speed — which is impossible to achieve with any accuracy due to the many factors affecting particle adhesion force (section 3.4) — rather to understand the qualitative form of the relationship.

In order to choose the appropriate equation for aerodynamic drag force (F_{drag}) the Reynolds number of flow experienced by the particle (Re_p) needs to be known. This in turn requires an estimate of the maximum flow velocity in the boundary layer at a height equivalent to the particle's center. As will be shown in detail in the following section, the particle can be assumed to reside within the viscous sublayer immediately adjacent to the surface. If the physical height above the surface is denoted y [m], then position in the sublayer can be described in by the dimensionless distance y^+ and flow velocity can be described by dimensionless u^+ , defined:

$$y^+ = yu^*/\nu \quad (24)$$

$$u^+ = u/u^* \quad (25)$$

Within the viscous sublayer, the following relation holds [15]:

$$u^+ = y^+ \quad (26)$$

How thick is the viscous sublayer for PV modules in deserts? To estimate this, the following values are assumed: $D_p = 20 \mu\text{m}$ particle (dominant size found at the STF), $U = 7 \text{ ms}^{-1}$ (98th percentile of wind speed at the STF), $u^*/U = 0.1$ (higher end of the range found in the literature), and $\nu = 1.57 \times 10^{-5} \text{ m}^2\text{s}^{-1}$. Then from eq. (24) $y^+ = 0.45$, from eq. (25) $u^+ = 0.32$, and from eq. (4) $Re_p \approx 0.4$. Since $Re_p < 1$ it appears that adhered particles experience Stokes (creeping) flow regime, even in the windiest conditions encountered at the study site. This conclusion is supported by (i) Habchi et al. [24] who noted that particles completely within the viscous sublayer have a “relatively small” Reynolds number and hence the Stokes flow regime applies, and (ii) Benito et al. [115] reported that it is common practice to assume that particles on a surface are within the viscous sublayer and experience Stokes drag.

In the Stokes regime drag force experienced by a particle on a surface is given by [24]:

$$F_{drag} = \frac{3\pi}{C} f \mu D_p u_p \quad (27)$$

where f is a correction factor due to account for presence of the wall whose value is 1.7009 [119], u_p is the flow velocity at the height of the particle's center, and C is the Cunningham slip correction factor which in this case is unity. Similar formulae have been used in resuspension studies by other researchers [15][113][120].

Eq. (27) indicates that the particle drag force is proportional to the flow velocity at its mid-point, u_p . What is the relation between u_p and the free-stream wind speed? Eqs. (24)-(26) can be rearranged to give the flow velocity at any height inside the viscous sublayer:

$$u = u^+ u^* = y^+ u^* = y u^{*2} / \nu \quad (28)$$

Since u^* is approximately proportional to U [31][85], the flow velocity inside the sublayer is proportional to U^2 and from eq. (27) so is the drag force. That is, $F_{drag} \propto U^2$, a relation consistent with much literature on particle resuspension [72][82][112][114][115][116][120][121].

For completeness it is noted that other relations have also been reported: Wu et al. [72] cited observations that resuspension of 7 μm particles was proportional to $U^{1.3}$, and resuspension rate of sub-micron particles from a sand bed was proportional to a third-order of polynomial of u^* . Using a smoothed bed of Arizona Test Dust, Loosmore & Hunt [16] also found that resuspension flux was best modeled as a cube of u^* , and cited the same finding in other research. A survey of resuspension literature by Sehmel [92] showed that concentration of resuspending particles, C_R , had been described as an exponent of wind speed ranging from 1.0 to 6.4, i.e. $C_R \propto U^a$ where $1.0 \leq a \leq 6.4$. Nicolson [22] wrote that this wide range of a , and its instability over time, indicate that resuspension is a complex phenomenon and dependent on environmental factors beyond wind speed alone. Less specifically, Kim et al. [23] reported that drag force on an adhered particle is proportional to some positive power of flow Reynolds number (and therefore U).

As an alternative to relating resuspension rate to U^2 , it can be described in terms of a critical flow velocity, u_{crit} . In this approach negligible resuspension occurs when flow velocity $< u_{crit}$, and resuspension advances rapidly once u_{crit} is exceeded. Fromentin [101] studied resuspension of different kinds of 2-4.3 μm aerosols in a wind tunnel and found that resuspension flux was proportional to the quantity $(u^* - u_{crit})^3$. He stated that the model was only valid for the particular experimental set-up and its uncertainty was an order of magnitude. (Sehmel [92] also reported that resuspension factors within an experiment can vary by several orders of magnitude, showing high sensitivity of detachment to experimental conditions). Ibrahim [113] presented data on detachment of glass microspheres of two sizes in a wind tunnel, which revealed existence of a u_{crit} that was larger for smaller particles. In the case of erosion, Loosmore & Hunt [16] wrote that a commonly-used model for saltation flux (detachment and transport of sand-sized particles) sets the flux proportional to $u^{*2}(u^* - u_{crit})$. Sehmel [92] and Qiang et al. [26] also found that soil erosion commenced when wind speed exceeded some threshold.

Eq. (27) predicts that the resuspension force on an adhered particle is $\propto D_p^2$, whereas adhesion forces are generally $\propto D_p$ [80][122]. Therefore large particles tend to resuspend from a surface at lower wind speeds than do small particles [80][76]. This results in experimental observations that dust accumulating on PV modules is generally finer than the ambient particulate matter [46][86].

3.3.3. Turbulence

Degree of turbulence of the airflow — in addition to its free-stream velocity — is important in both force and energy models of particle resuspension [18][72][82][113][121]. In the force approach, turbulence causes flow velocity at every point to fluctuate, and it is the peak instantaneous velocity that determines resuspension rate [112]. In the energy approach, as mentioned, if the period between exciting turbulent motions is greater than the time for the particle's vibration to dissipate then the particle will not accumulate energy and detach [104].

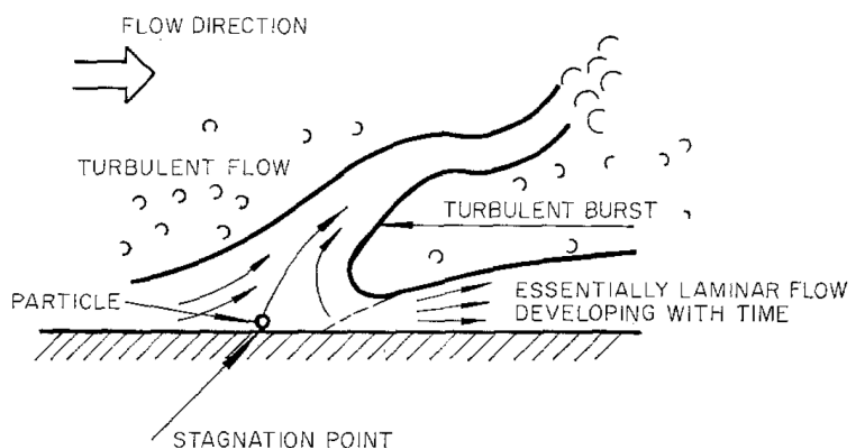


Figure 20. Schematic diagram of turbulent burst at the surface, causing particle resuspension [114]. (Reprinted from Journal of Colloid and Interface Science, Vol 44, Issue 3, J.W Cleaver, B Yates, Mechanism of detachment of colloidal particles from a flat substrate in a turbulent flow, 464-474, Copyright 1973, with permission from Elsevier)

Turbulence acts on particles by creating “ejections and sweeps of fluid from the wall” [15] which are largely responsible for detaching them [24]. Such fluid motions are also described as “turbulent bursts”, and were helpfully illustrated by Cleaver [114] (Figure 20). Ibrahim et al. [18] measured the removal rate of 70 μm stainless-steel spheres from a glass surface, and powerfully demonstrated that turbulence enhances detachment (Figure 21): changing the flow condition from laminar ($\text{Re} = 1.05 \times 10^5$) to turbulent ($\text{Re} = 1.05 \times 10^6$) decreased the mean wind speed necessary to detach 50% of the spheres from 17.7 ms^{-1} to 8.2 ms^{-1} . In a related paper [113] the same researchers calculated the critical mean flow velocity required for particle detachment under different roughness and turbulence scenarios, and estimated that turbulent bursts reduce the critical mean velocity by roughly a third. In wind-tunnel experiments Wu et al. [72] found that the upper 20% of flow velocity fluctuations (i.e. the moments with the highest instantaneous airflow velocity)

accounted for 65% of particle resuspension, when the mean velocity was 6 ms^{-1} . The researchers placed a thin metal strip 2 cm above and parallel to a particle-laden surface, which served to reduce turbulence below the strip. The strip was found to reduce stream-wise velocity variation, confirming that turbulence was indeed inhibited, which in turn reduced dust resuspension by a factor of around three.

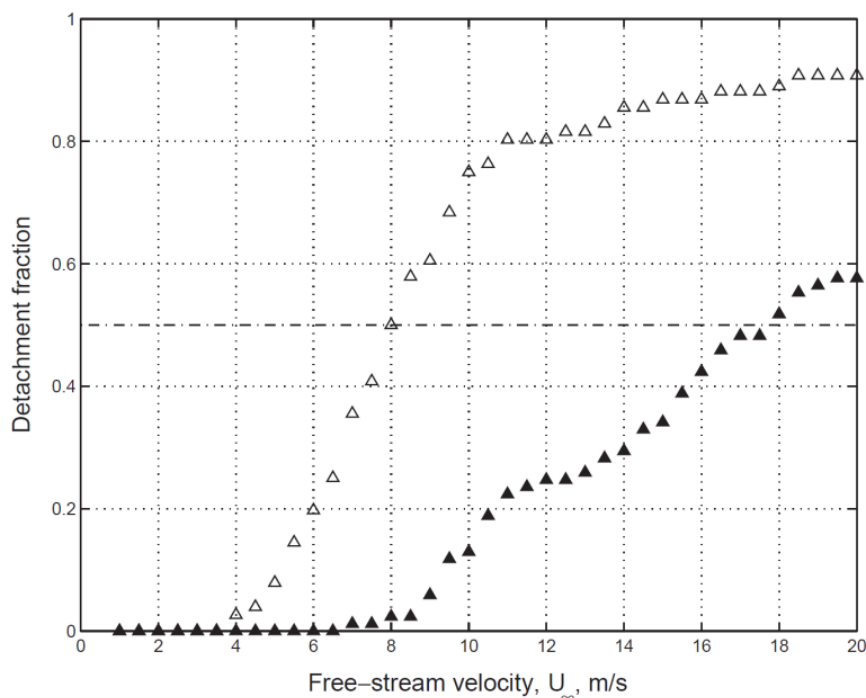


Figure 21. Turbulent flow causes greater resuspension of particles than laminar flow of the same free-stream velocity. Detachment fraction of $70 \mu\text{m}$ stainless steel spheres from a glass surface, black markers – $\text{Re} = 1.05 \times 10^5$, white markers – $\text{Re} = 1.05 \times 10^6$. [18]. (Reprinted from Journal of Aerosol Science, Vol 35, Issue 7, A.H. Ibrahim, P.F. Dunn, R.M. Brach, Microparticle detachment from surfaces exposed to turbulent air flow: Effects of flow and particle deposition characteristics, 805-821., Copyright 2004, with permission from Elsevier)

A study [104] described by Ziskind et al. [15] investigated resuspension of different types of particles in a wind tunnel and demonstrated that detachment occurred during turbulence bursts, and in a quantity related to the intensity of the burst. For rectangular ducts it was reported [123] that volume airflow rate, Q , had a linear effect on wall shear stress, τ , when flow was laminar ($\tau \propto Q$) but had a more powerful influence when flow was turbulent ($\tau \propto Q^{1.75}$), indicating that turbulence brings faster-moving air closer to the surface. Paw U and Braaten [104] cited their own work and that of others showing that particles resuspended mainly during turbulent bursts, so much so that “average fluid motion is not considered important”. For $10\text{-}50 \mu\text{m}$ particles (i.e. of a size range comparable to that important for PV soiling), they cited results that those particles were predominantly resuspended by large-scale turbulence events. Further studies showing that turbulence increases resuspension were cited by Cleaver and Yates [114]. Qualitatively, Barth et al. [124] observed that resuspension of graphite particles was enhanced behind steps protruding from a wind-tunnel floor, whose effect was to induce turbulent vortices. This phenomenon may also explain the tendency for the windward edges of PV modules at the present study site tended to remain cleaner than other parts of the module (Figure 8a).

While the above-mentioned research demonstrates that flow turbulence affects particle resuspension, its influence is moderated by the existence of the thin, viscous sublayer immediately adjacent to the surface described in section 3.1.3. In this sublayer air flow is essentially laminar [15] and turbulent motions are suppressed [15][72][82][113][114]. Particles small enough to reside fully inside the viscous sublayer are therefore “protected” [80] from resuspension, whereas particles that extend beyond it are more susceptible to removal [15][16][18][22][23][72][80][82][112]. Quantitatively, Ahmadi et al. [112] reported that maximum flow velocity in the viscous sublayer is $1.1365y^+$ (y^+ being the dimensionless distance from the surface defined in eq. (24)), while absent the sublayer particles are subject to flow velocity up to $1.72y^+$. That is, the viscous sublayer subdued the maximum flow velocity experienced at the surface by 34% for the same free-stream flow velocity.

The viscous sublayer thickness is usually assumed to extend to where $y^+ \approx 5$ [15][73][76][82]. Knowledge of the viscous sublayer thickness would appear to be important to resuspension modeling [15], because if adhered particles are much smaller than the sublayer thickness then turbulence intensity will have relatively little effect on the resuspension rate, and vice versa. However according to Kim et al. [23] such knowledge is not essential: They noted that direct measurement of turbulence intensity (e.g. turbulence kinetic energy or turbulence shear stress) is not generally made, and that turbulence intensity is anyway captured by the magnitude of friction velocity. They therefore opted not to include an explicit turbulence intensity parameter in their resuspension modeling work.

To estimate whether dust particles on surfaces at the present Doha study site are typically within the viscous sublayer, consider the thinnest sublayer practically encountered. This will be at the highest wind speed (again 7 ms^{-1} is chosen, being the 98th percentile of wind speed at the site) and friction velocity u^* at the upper range of typical values ($u^*/U = 0.1$). Then from eq. (24), with $y^+ = 5$ and $\nu = 1.57 \times 10^{-5} \text{ m}^2 \text{ s}^{-1}$, the viscous sublayer thickness is approximately $110 \mu\text{m}$. This is consistent with Cleaver & Yates [114] who reported that the thickness is generally in the order of $100 \mu\text{m}$. These estimates are much larger than dust particles typically encountered at the site of $10\text{-}40 \mu\text{m}$ (Figure 13b). That is, for locations with wind speeds and particle sizes no greater than Qatar’s, almost all surface particles are completely within the viscous sublayer and the influence of turbulence is subdued.

A caveat to this analysis is noted: for the geometry of the OSM apparatus used in this study, the collector surface is small and hence the boundary layer above it is unlikely to be fully developed (Barth et al. [76] noted that an incomplete or disturbed boundary layer would affect resuspension measurements), also the free-stream atmospheric airflow may not have been perfectly parallel to the surface. Therefore the viscous sublayer may have a thickness quite different from that estimated above. However the difference between the thinnest estimated sublayer ($\sim 110 \mu\text{m}$) and largest particle of interest ($\sim 40 \mu\text{m}$) is great enough that it still appears reasonable to assume that adhered particles experience subdued turbulence. Also, natural particles are not spherical and tend to settle “flat” on a surface (i.e. a particle whose projected area is equivalent to a sphere of diameter $40 \mu\text{m}$ may have a height much less than $40 \mu\text{m}$) which would further support the working assumption.

3.3.4. Resuspension distribution

Particles on a surface experience a diversity of adhesion forces because of their differing size, shape, composition, contact area, and other factors. Hence resuspension will be observed over a range of flow velocities [113][125]. Adhesion forces can be assumed to be log-normally distributed [20][126], and it follows that the fraction of resuspending particles as a function of flow velocity can be described by a sigmoid shape (Figure 22), or the similar “error expression” or Hill equation [127]. For example, Barth et al. [76] studied resuspension of 3-45 μm glass and polypropylene beads in a wind tunnel and described resuspension fraction by an error function of u^* . They found that resuspension occurred suddenly, i.e. the fraction of particles resuspended went from 0 to 1 within a narrow range of flow velocity. They also cited findings that 0.4 μm particles of SnO_2 similarly exhibited sudden resuspension at a certain friction velocity (3 ms^{-1}). Reeks and Hall [125] measured resuspension of alumina and graphite particles from a steel plate and showed that resuspension fraction traced a sigmoid shape when plotted against $\log(u^*)$.

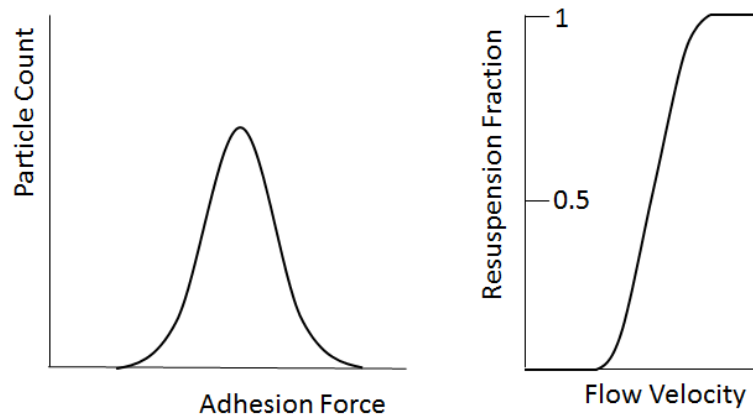


Figure 22. Normal distribution of particle adhesion forces (left) allows resuspension fraction to be described by a sigmoid function of flow velocity (right)

To summarize the established understanding of particle resuspension: Air flow causes particles to usually detach in a rolling motion, which is theoretically governed by drag force and thus the square of flow velocity. Experimental research has shown that the relation between resuspension and flow velocity can be even more powerful than this, and it is common to incorporate a critical flow velocity below which no resuspension occurs. Much modeling of resuspension was derived from dry wind-tunnels experiments with homogenous particles where resuspension, once initiated, progresses quickly to almost complete removal. In contrast, in outdoor conditions there is a wide diversity of particles and adhesion forces, which causes resuspension to escalate gradually over a spread of flow velocities, and never to completion (even in the strongest wind. Because the ratio of adhesion to detachment forces is greater for small particles, dust accumulating on PV modules tends to be finer than airborne particulate matter.). One may expect dust removal from PV modules to be strongly linked to wind speed, but not necessarily proceed as suddenly and completely as models derived from wind tunnels predict.

3.4. Overview of Adhesion Mechanisms

So far this chapter has reviewed wind-related dust mechanics. In this section mechanisms that adhere particles to a surface are reviewed, with a focus on moisture-related mechanisms— capillary condensation (Figure 23) and “cementation” (Figure 24). This is because, as will be shown, moisture (when present) dominates dust adhesion on PV modules. Surface properties such as roughness and hardness also affect particle adhesion but are beyond the scope of this report.

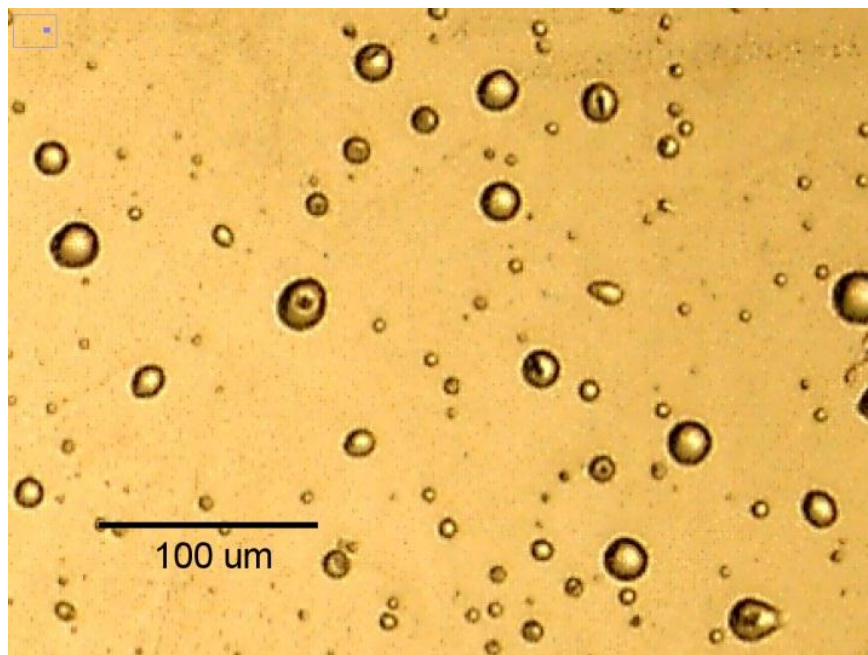


Figure 23. Sample image of microscopic condensation droplets on a soiled glass coupon at the Solar Test Facility, imaged with an outdoor soiling microscope.

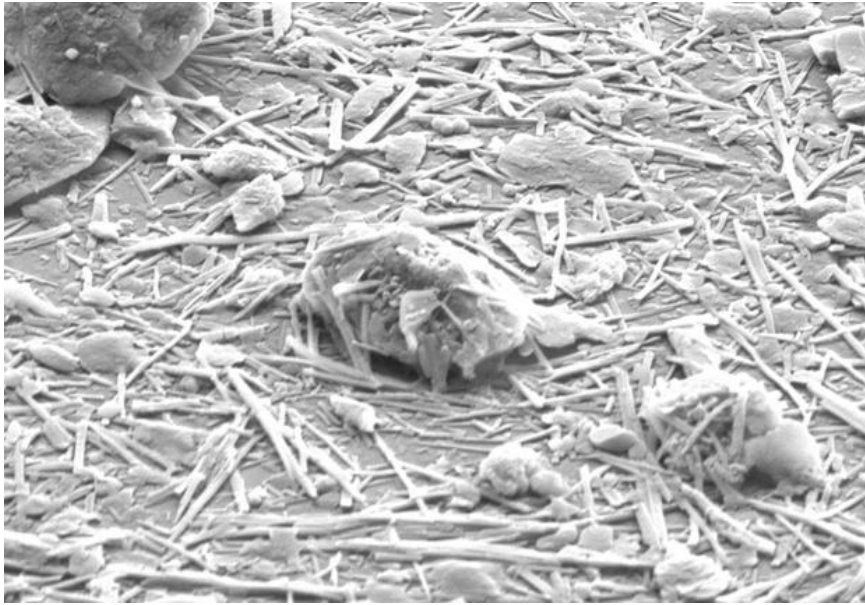


Figure 24. Needles of palygorskite following condensation on a soiled glass coupon at the STF, which visibly “cement” dust particles to the surface. The dust grain at the center of the image is $\sim 1.5 \mu\text{m}$ long. Photo courtesy of Klemens Ilse, Fraunhofer CSP, Germany.

The adhesion of particles to surfaces and each other is important in many applications (e.g. electronics manufacturing, environmental health, processing of powders) and has been comprehensively researched and reviewed [14][23][122][128][129][130]. The main particle-adhesion forces generally considered are van der Waals force, capillary adhesion (liquid bridge), coulomb (electrostatic) attraction, and contact electrification [131]. In the case of PV soiling “cementation” is also highly relevant (as illustrated above), wherein soluble material in the dust dissolves in condensation and re-solidifies upon drying, forming a solid bridge between the particle and surface.

A summary of these primary adhesion forces, and conditions in which they are most applicable, is provided in Table 3. The relative magnitude of some of the forces, based on theoretical models, was conveniently illustrated by Tomas [132], Figure 25. It is seen that for mid-sized particles the strongest forces, in order, are capillary (when moisture is present), van der Waals (when it is not), and electrostatic interactions. The dominance of capillary adhesion was even more pronounced when the surface and/or particles exhibited some roughness. This ranking of forces was essentially corroborated by Berbner & Loeffler [133] — who added solid bridges (such as are formed through cementation) as the strongest mechanism — as well as other reports [14][120].

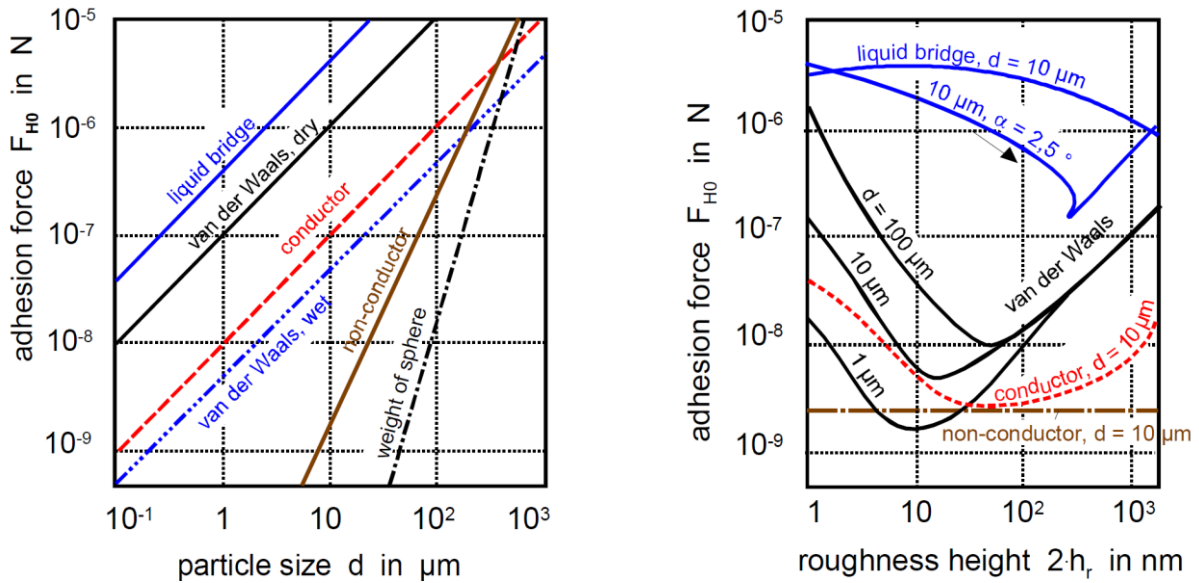


Figure 25. Relative strength of various adhesion forces vs. particle size (left) and surface roughness (right) [132]. (Copyright Prof. Dr. J. Tomas 09.01.2006)

Adhesion mechanism	Description	Relevant conditions	References
van der Waals (vdW) force	Momentary fluctuations in electron distribution (polarization) in molecules of one body induces an opposite and attractive dipole in the other body. Acts over short distances and is greatly reduced by surface roughness. Water between particle and surface greatly reduces its strength	Dry environment Very smooth surfaces	[14][120][130][134][135]
Capillary adhesion	Bridge/meniscus of liquid water forms between particle and surface, whose surface tension reduces its internal pressure below that of the air, and exerts an attractive force along the meniscus edges. Capillary force exhibited even in moderate humidity (<50% RH). Less sensitive than vdW to separation of the bodies (surface roughness). Greater on hydrophilic surfaces	Humid environment Hygroscopic dust Rough surfaces & particles	[14][120][130][135][136][137]
Coulomb force	Airborne dust particles acquire electrical charge by collisions and irradiation. On the other surface, an opposing and attracting "mirror" charge is induced. Presence of conducting medium (e.g. water) dissipates the electrical charges. Acts over a greater distance than vdW hence is less sensitive to roughness. Relative to other forces, strength increases more rapidly with particle size so more relevant for larger particles. When particles are highly charged, coulomb force can dominate dry adhesion	Charged particles Dry environment Large particles (>~50 μm) Rough surfaces & particles	[14][120][136][138][139]

Contact electrification	When materials having different electron energy states come into contact, electrons can transfer from one body to the other, establishing an attractive electrostatic force. Diminished by surface contamination and water layer. Relevant only for very small particles.	Dry environment, Charge-exchanging materials, Clean surfaces, Very small particles	[14][140][141]
Cementation	Soluble material on the surface dissolves in condensation and recrystallizes upon drying, leaving a solid bridge of material between the particle and surface	Dew conditions, Soluble dust content	[14][40][138][142][143]

Table 3. Principle particle adhesion forces and conditions in which they are most relevant

The relation between ambient humidity and capillary adhesion is addressed fully in chapter 4; here it is briefly noted that RH has been comprehensively shown to strongly increase particle adhesion [18][77][82][109][122][135][144][145]. Because capillary adhesion is observed even at moderate RH, and is more powerful than van der Waals forces, it appears to be of greater importance to PV soiling. Yet the strongest mechanism that binds particles to the surface is cementation, which in turn is driven by dew formation.

Given the importance of moisture to PV soiling, it was decided to investigate parameters affecting condensation (in addition to parameters affecting dust flux rates) in this study. Because PV modules always carry some amount of dust or contamination, and condensation is usually studied on clean surfaces, a novel avenue for research in this study was condensation on soiled surfaces. Previous research on capillary condensation and particle cementation is presented in the following chapter.

4. Review of Moisture in Soiling

In the previous chapter it was seen that moisture plays a very important role in PV soiling, due to the strong particle-adhesion forces of capillary condensation and cementation. In this chapter, a review of condensation and cementation processes is provided, with a focus on the environmental factors that influence them. This review guided the experimental part of the project on condensation and PV soiling, which is reported in chapter 7.

4.1. Relative Humidity

Relative humidity (RH) is defined as the ratio of prevailing water vapor pressure to the saturation vapor pressure at that temperature, hence water nominally condenses at 100% RH. However a nano- or micro-scale meniscus of liquid water can condense in surface scratches or crevices between a particle and surface in RH less than 100% [136][137][146][147], and then persist as RH decreases even further [137]. The meniscus is stable at RH below saturation because water molecules at the liquid's (concave) surface experience attraction to more neighboring molecules than do molecules on a flat liquid surface, which inhibits evaporation. This effect is described by the Kelvin equation:

$$\ln \frac{p}{p_0} = \frac{2\gamma V}{r_k RT} \quad (29)$$

where p is vapor pressure near the liquid's surface, p_0 is saturation vapor pressure, γ is the liquid's surface tension, V its molar volume, r_k its radius of curvature, R is the gas constant, and T is temperature of the system. The radius r_k is related to the radii of curvature of the meniscus as illustrated in Figure 26:

$$\frac{1}{r_k} = \frac{1}{r_1} + \frac{1}{r_2} \quad (30)$$

The difference between the atmospheric pressure (p) and pressure inside meniscus (p_0) presses the particle to the surface; this is the Laplace or capillary pressure p_L given by:

$$p_L = \gamma / r_k \quad (31)$$

Surface tension at the liquid-solid edge also contributes to the capillary force, however it is negligible compared to the Laplace pressure (unless the meniscus volume is very small or the contact geometry sharp) [77][144][136][148].

In principle the capillary adhesion force is independent of RH when r_2 is small, but in experiments with natural particles and surfaces it usually observed to increase with RH [144][136][146]. This has been explained by (i) gaps progressively “flooding” with condensation as RH rises, so that the water layer covers surface asperities [77][149], (ii) condensed water collecting into patches on the surface rather than forming a continuous film [130], or (iii) r_2 being large enough to be comparable to r_1 , which may be the case when the water layer is thick or the contact point sharp [136][146].

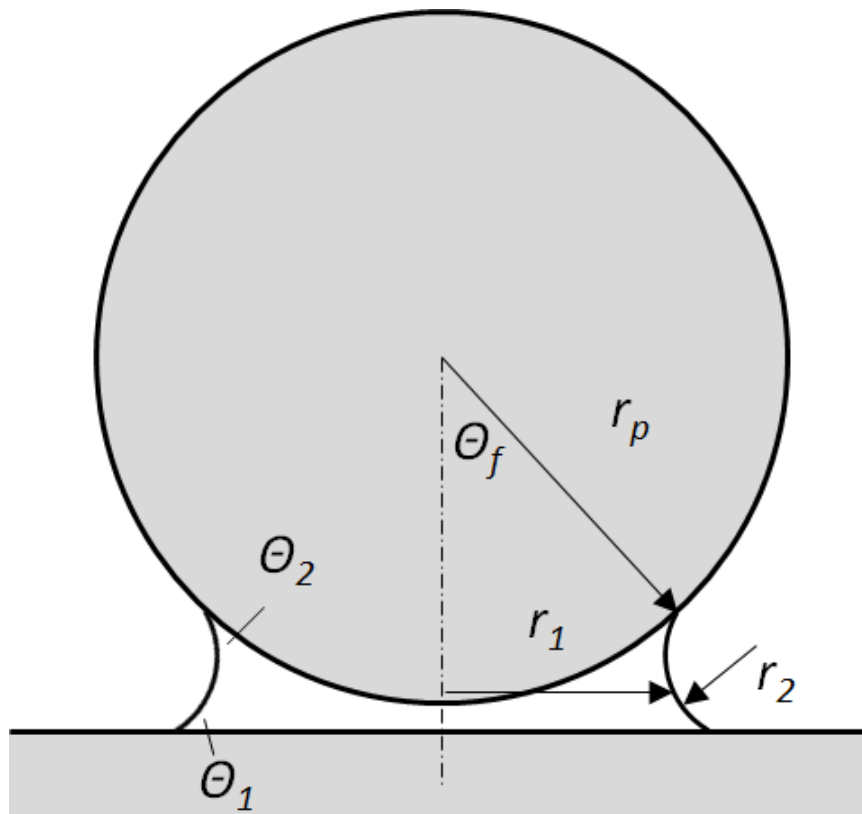


Figure 26. Capillary adhesion force of a particle to a flat surface is dependent on the dimensions and curvature of the meniscus. r_p – particle radius, r_1 and r_2 – meniscus radii of curvature, θ_f – filling angle, θ_1 and θ_2 – contact angles.

How prevalent is moisture on outdoor surfaces? It is reported that in ambient conditions, most surfaces possess a thin layer of adsorbed water vapor [130][146]. On glass, water adsorption has been found to commence at less than 25% RH [147] and near saturation it reaches several [135][150] to tens [147] of molecular layers. Leite et al. [130] measured water-film thickness on quartz at ~70% RH to be 0.4-0.8 nm, and cited that the film thickness is less than 10 nm up to 90% RH. These values indicate the scale of the film thickness but cannot be reliably extended to other situations because the thickness varies greatly with surface conditions [136]. The thickness of the adsorbed water film is said to control capillary adhesion [130][136][150][151], although some researchers hold that a continuous film so thin is not sufficiently mobile to form a liquid bridge and instead capillary adhesion is caused by droplets nucleating at discrete locations (crevices) [135][147][152]. This highlights a terminology distinction: “Adsorbed water” generally describes a continuous film molecular-layers thick across a surface, whereas “capillary condensation” indicates a volume of free

liquid whose shape governs its behavior (by the Kelvin equation) and often exhibits a hysteresis between rising and falling humidity [147].

Regardless of the depth and mobility of surface moisture, it is the effect of RH on capillary adhesion force that is of interest in this study. Atomic force microscopy has been useful for studying this relation [144][136][151][153]. Overall the adhesion force of particles to surfaces has been found to commence when RH exceeds 30-50%, and strengthens greatly when RH reaches 60-70% [120][122][136][148]. Some specific measurements from the literature are mentioned: Fuji et al. [145] found that capillary adhesion of silica particles increased to “remarkable” strength when RH reached 60-80%; Grant [147] found a rapid increase of water adsorption onto soda-lime glass at 70% RH; Kim et al. [77] reported that on glass capillary adhesion becomes significant at 50-60% RH; Ranade [137] reported that in decreasing RH, liquid water may persist in the particle-surface contact area down to 50% RH; Jones et al. [136] determined that capillary condensation dominates particle adhesion on glass when RH exceeds ~40%; and studies cited by Kim et al. [77] and Brambilla et al. [148] showed that adhesion forces increased with RH above just 30% RH.

Roughness of the surface or particle tends to retard and weaken capillary adhesion forces [136][146]. Rabinovich et al. [149] reported that capillary adhesion commenced at 25% RH on a smooth surface (0.2 nm roughness) yet at 70% RH on a rougher one (0.7 nm roughness). Brambilla et al. [148] estimated that capillary force would strongly diminish when surface roughness reached a few nanometers, i.e. of similar scale as the meniscus height. Jones et al. [136] found that surface roughness decreased the measured adhesion force by a factor of ~300 compared to the theoretical force between smooth bodies in dry conditions, but only by 3-20 times in humid conditions, possibly due to presence of a water film thick enough to cover the asperities. This suggests that anti-soiling coatings that target roughness to reduce particle-substrate contact area might be more effective in dry environments than humid ones.

In summary, capillary adhesion of dust on surfaces is essentially ubiquitous in natural environments [151], partly because a concave water meniscus is stable even at moderate RH. The literature indicates that capillary adhesion on glass can be significant in the range 40-70% RH, and strengthen further at higher RH. Yet condensation and capillary forces are sensitive to surface and ambient conditions, hence it is not possible to accurately predict the RH at which condensation will form or the strength of capillary bonds [136].

4.2. Surface–Dew Point Temperature Difference

In the preceding section, the dependence of condensation on RH was reviewed in the specific case that the surface and surrounding air are at the same temperature. In real-world situations — especially outdoors — the surface temperature of objects can of course differ from the ambient air temperature, which will also affect condensation.

Dew point (T_{DP}) is defined as the air temperature at which water vapor begins to condense and form droplets of dew. If the surface temperature (T_S) is less than T_{DP} then condensation will commence in $RH < 100\%$. Similarly, if $T_S > T_{DP}$ then condensation is prevented (in principle) even when $RH = 100\%$.

It is usual for outdoor objects to cool below the air temperature (T_{amb}) at night due because they radiate heat to the sky, at temperature T_{sky} , which at night tends to be colder than ground-level ambient air [154][155]. Radiative heat transfer R is given by the Stefan-Boltzmann law:

$$R = \varepsilon_S \sigma (T_S^4 - \varepsilon_{sky} T_{sky}^4) \quad (32)$$

where ε_S is the emissivity of the object's surface, ε_{sky} is the emissivity of the sky, σ is the Stefan–Boltzmann constant, and temperatures are expressed in K. A simple model cited by Tang et al. [155] estimates the night sky temperature as $0.0552T_{amb}^{1.5}$. In the Qatar example above where $T_{amb} \approx 30$ °C, this rule gives $T_{sky} \approx 18$ °C. Hence the PV modules is radiating heat to the sky at ~ 18 °C while absorbing heat by convection from the ambient air at ~ 30 °C, resulting in its observed 5.1 °C temperature suppression. It is difficult to predict the equilibrium temperature that a given object will attain on a night of a given T_{amb} because this depends also on sky conditions (cloud coverage and emissivity) and local wind speed [155]. Temperature suppressions in the vicinity of 6-8 °C have been reported for different materials, and when the object is shielded from convective heat transfer temperature suppressions of 11-21 °C can be observed [154].

It was possible to directly demonstrate the night-time radiative cooling of PV modules at the present study site, the Solar Test Facility in Doha. The back-surface temperature of a PV module (glass-backsheet construction, 22° tilt) and ambient air temperature were recorded over a 24-hour period of the 2016 autumnal equinox (Figure 27). It is seen that the PV module was cooler than the ambient air for roughly 13 hours over the night, and the relative cooling reached a maximum of 5.1 °C just before dawn. Clearly, radiative cooling as great as this will significantly influence condensation on PV modules.

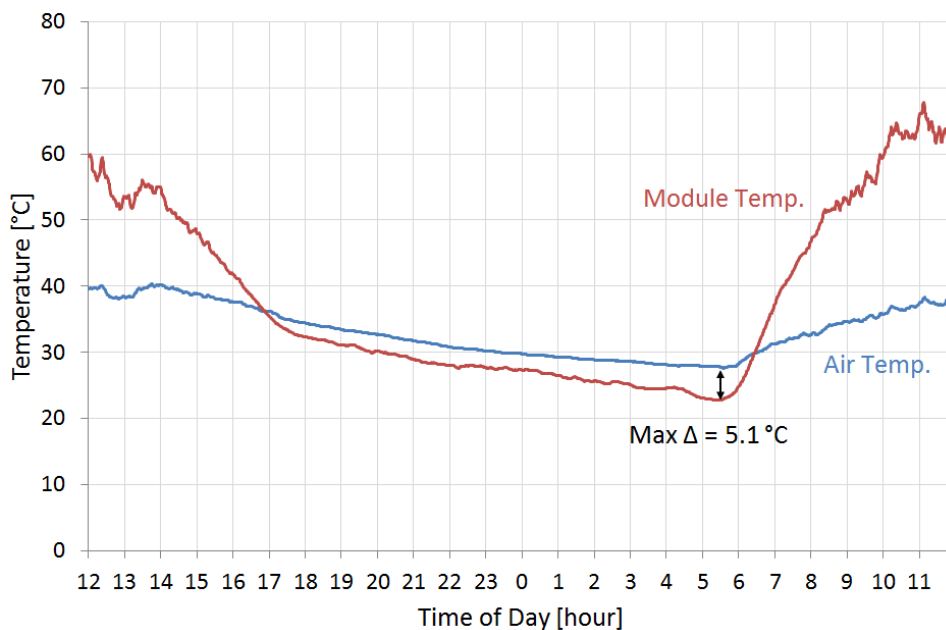


Figure 27. Example of a PV module cooling to well below the air temperature during the night, at the STF. Blue line = air temperature, red line = module back-surface temperature, module at 22° tilt.

While surface/dew point temperature difference is an important factor for condensation in outdoor settings, it is not expected to completely govern condensation. That is, condensation will not necessarily commence the instant that T_{s-dp} falls below zero. For example, in a study of radiative cooling panels [156] no condensation was observed until chilled water pumped through them was more than 2.4 °C cooler than the ambient dew point. Further, once condensation has initiated, the droplet growth rate is affected by many factors such as ambient air conditions (RH and wind speed), solute concentration in the droplet, droplet shape, and the rate at which the latent heat of condensation is dispersed [80]. Characteristics of the surface and the dust upon it can also affect condensation, as discussed in the following sections.

4.3. Hygroscopic Material

Studies of capillary condensation reviewed in section 4.1 were performed in laboratory settings with clean surfaces. In the case of real-world PV modules, the dust layer itself may influence condensation. Although pure mineral dusts tend to be hydrophobic [90][157][158][159][160], in natural conditions they can contain hygroscopic species that promote condensation [135][142][147][161][162][163]. For example, Herich et al. [164] determined that Arizona Test Dust was not hygroscopic and Saharan dust only moderately hygroscopic, but when the dust's soluble content exceeded ~3% by mass its water uptake increased significantly. Important environmental hygroscopic species include:

- Salts

The atmosphere everywhere contains NaCl originating from oceans [80][87], which deliquesces at 76% RH [142]. McCormick & Westwater [152] measured condensation on particles of 24 different substances and found the most hydrophilic substances were most effective at nucleating condensation. Further, NaCl particles were so hygroscopic that, when present, droplets formed only on those particles and not on any others nor at surface crevices. Upon evaporating seawater yields NaCl and also magnesium salts (hydrated forms of $MgSO_4$ and $MgCl_2$) which are even more soluble than NaCl [165]. Lombardo et al. [27] noted the tendency for salts (including sulfates and nitrates) to nucleate condensation and deliquesce which in turn enhances surface soiling. (They further noted that, upon drying, the salts can “neocrystallize” and cause cementation.)

- Nitrate and sulfate ions

NO_3^- and SO_4^{2-} ions are widely present in the atmosphere from industrial and natural processes (especially ocean spray [166]). Various accounts of their hygroscopicity are given: Zelenyuk et al. [162] wrote that both species are hygroscopic. Ma et al. [163] reported that sulfate ions are usually present on the surface of natural mineral-dust

particles and significantly enhance their hygroscopicity. Shi et al. [159] found that nitrate-containing dust was extremely hygroscopic (it deliquesced at just 15% RH) but sulfate-containing dust was not hygroscopic (possibly because in their sample, the detected sulfate was bound up as non-hygroscopic gypsum). Vlasenko et al. [160] found that the soluble part of Arizona Test Dust was almost entirely sulfate, with little nitrate or chloride, yet the dust was essentially hydrophobic, indicating that even soluble sulfate in dust did not render it hygroscopic. Interestingly, through studying soiling of glass coupons at thirty European sites, Lomardo et al. [27] found that atmospheric NO₂ levels had similar correlation to soiling as did PM₁₀, while SO₂ had roughly half as much influence, because these pollutants dissolved and reacted in surface moisture to form nitrate and sulfate ions in-situ. (This mechanism might partly explain relatively low correlations between soiling and PM₁₀ alone reported in previous studies [9][10][47].)

Yet dust has been shown to sometimes adsorb water even when it contains no hygroscopic species [142]. Arsalan [157] found that silica and calcite — major components of dusts in deserts [30][42][46][167] — are nominally hydrophobic but showed hygroscopic action due to water layers or patches on their surfaces. Some surface water was present at all RH, and above 70% RH the particles' water adsorption was pronounced. Extensive water layers on mineral dust at 70% RH were also reported by Gustafsson et al. [167]. Yet Grant [147] noted debate in the literature as to whether surface layers of water on mineral particles contribute to condensation. Size and structure of the dust appears to have an influence: McCormick & Westwater [152] found that insoluble particles 2-30 μm in diameter could nucleate condensation but other sizes did not (soluble particles of all sizes nucleated condensation). Vlasenko et al. [160] determined that aggregated dust particles contain cavities which induced capillary condensation, and thus condensation was more prevalent on larger (agglomerated) particles. Finally, presence of electrical charges on dust particles can also promote droplet nucleation.

The many and varied factors affecting condensation on dust [80][161], especially the presence of hygroscopic species, make it difficult to predict *a priori* when condensation will form on a soiled PV module. This variability was demonstrated in a simple experiment at the Doha test site in which part of a PV module was wiped daily with a dry cloth for one month, while the rest of the module remained soiled. When condensation occurred, it was usually on the (relatively) clean part of the module but sometimes instead occurred on the soiled part (Figure 28). Likely this variation was linked to the amount of hygroscopic species in the soiling layer, which was shown to vary considerably month-by-month at this location [30].

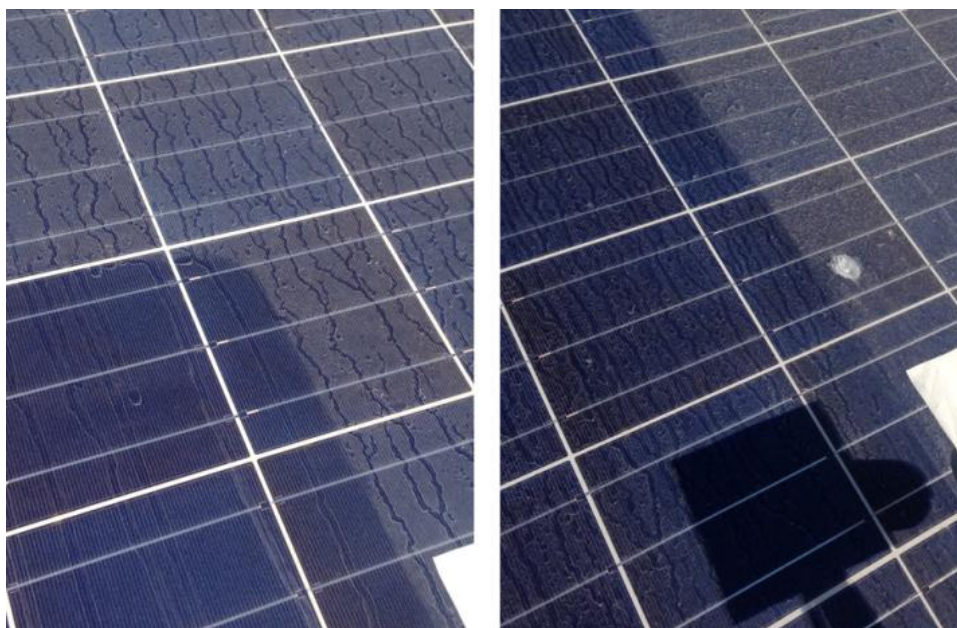


Figure 28. One section of a PV module in Doha was regularly cleaned, and the remainder was left soiled. On different days condensation occurred on the different sections, indicating the influence and variability of dust composition.

If the soiling layer contains soluble material, condensation droplets will consist of a brine solution. Higher concentration of solutes in a liquid lowers its vapor pressure, and hence lowers the RH at which droplets of the liquid are stable [47][147][161][168]. This mechanism (sometimes referred to as Raoult's Law [147]) will promote the growth and persistence of condensation droplets on a surface bearing soluble matter. Further, upon drying such brine droplets can leave a solid bridge of material (cementation) that strongly binds particles to the surface.

Overall, the presence of hygroscopic species in the soiling layer is expected to have a significant effect on condensation on PV modules — especially in coastal locations as sea-spray contains highly-hygroscopic salts. In this study the water-uptake behaviors of natural and synthetic dust mixtures, with and without hygroscopic material, were compared (experiments are reported in chapter 7).

4.4. Surface Wettability

A surface's wettability (i.e. the degree to which it is hydrophilic or hydrophobic) has an important but complicated role in soiling. The surface of clean glass tends to bear hydroxyl ($-OH$) groups which are polar and form hydrogen bonds with water molecules, rendering glass nominally hydrophilic [147][150][167][169][170]. Hydrophobic coatings commonly function by capping these hydroxyls with non-polar molecules, e.g. methyl or fluorine groups. In a comprehensive review Grant [147] concluded that on both hydrophilic and hydrophobic surfaces, condensation commences at cracks and crevices; where they differ is that on hydrophilic surfaces the remaining surface (between the crevices) gradually accumulates a water film as RH increases whereas on hydrophobic surfaces it does not. A material's

hydrophilicity is usually characterized by its water contact angle, however McCormick & Westwater [152] found that heat of adsorption better predicted a particle's tendency to nucleate condensation.

Consider the case of a particle on a flat hydrophilic surface, forming a small concave meniscus as illustrated in Figure 26 (page 72). The adhesive capillary force F_{cap} is given [144] by:

$$F_{cap} = 2\pi\gamma \frac{r_p^2}{r_k} \sin^2 \theta_f \quad (33)$$

If the filling angle θ_f is sufficiently small (which has been reported to “usually” be the case [137]) the equation simplifies and the capillary force is clearly related to the wettability of the surface and particle (θ_1 and θ_2 respectively):

$$F_{cap} = 2\pi r_p \gamma (\cos \theta_1 + \cos \theta_2) \quad (34)$$

Equation (34) predicts that capillary adhesion is maximized between hydrophilic bodies — i.e. when θ_1 and θ_2 are small — and minimized between hydrophobic ones. Indeed it is reported that, in theory, if one surface has a contact angle of more than 90° [148] or the sum of the two surfaces' contact angles is greater than 180° [144] then a liquid bridge cannot form. In practice droplets do form even on hydrophobic surfaces and coalesce around particles, as this study will demonstrate. Nevertheless it has been widely shown that in general, particles tend to experience lower adhesion forces on hydrophobic surfaces: Quon et al. [151], using coated mica and gold films, showed that adhesion force increased with RH on the hydrophobic surface, but was always lower than the adhesion force on the hydrophilic surface at the same RH. Jones et al. [136] measured adhesion of 20 μm glass spheres to various surfaces and showed that adhesion on hydrophobic glass was less than on hydrophilic glass in both dry (10% RH) and humid (90% RH) conditions. Further, capillary force increased with RH on hydrophilic glass but was essentially independent of RH on hydrophobic glass. They also noted that natural surfaces tend to bear contaminants which reduce their wettability and “can have a dramatic effect on the RH behavior” of capillary adhesion. Curry & Kim [144] studied capillary adhesion on various self-assembled monolayer (SAM) coatings and likewise found that capillary adhesion increased with RH on hydrophilic surfaces due to condensation, but was independent of RH on a hydrophobic (methyl-capped) surface up to 60% RH. However in reviewing other studies of SAMs they noted there was “substantial variability” in the degree to which hydrophobic coatings inhibited adhesion in humid conditions. Kim et al. [77] experimented with particles and surfaces of various wettability in a wind tunnel and found that RH had “remarkably little” influence on adhesion of hydrophobic particles, particularly when the surface was also hydrophobic.

Hydrophobic surfaces have usually been reported to increase the RH needed for condensation to commence. In the tests of Kim et al. [77] capillary adhesion was observed at 50-60% RH on glass but only above 80% on a hydrophobic substrate. Grant [147] cited results showing that much higher water vapor pressure was required to initiate condensation on a surface whose contact angle was 80° than on one of contact angle 10°. Fuji et al. [145] determined that this behavior was caused by hydrophobic surfaces preventing a continuous, multilayer water film from forming.

On the other hand, Simpson et al. [171] (who recently developed coatings that are super-hydrophobic throughout their volume) stated that hydrophobic coatings repel liquid water but not vapor.

The laboratory experiments cited above consistently found that particles experience less adhesion on hydrophobic surfaces than on hydrophilic ones, in both humid and dry conditions. Yet soiling in real-world settings is complicated by surface contamination and variable weather conditions, and field results on the relative performance of hydrophilic and hydrophobic anti-soiling coatings are inconsistent [10][46][53][54][172][173][174][175][176][177]. Both types of coating aim to promote run-off of rain from the surface, hydrophilic ones by promoting water sheeting and hydrophobic ones by promoting water beading [175][176]. Of course a coating's performance depends not just on its behavior in rain; PV coatings have actually been shown to be more beneficial in low-rainfall environments [54][142] because rain tends to clean both coated and uncoated PV modules. Aside from water shedding, droplet beading on hydrophobic surfaces may have other benefits: (i) A droplet in a bead shape will have a smaller radius of curvature than one of the same volume in a flattened shape, and thus should evaporate more readily as discussed in section 4.1, and (ii) a bead-shaped droplet concentrates its entrained dust into a small clump upon drying which — compared to uniformly-distributed dust — occults less light and is more easily blown away by wind [143][172][174].

In summary, in lab experiments hydrophobic coatings have consistently been reported to reduce particle adhesion regardless of RH, although this has not consistently translated to less soiling in the field. Hydrophobic coatings are also reported to inhibit condensation, however the existing body of research on this was performed on clean surfaces in laboratory conditions. To better understand soiling mechanisms in real-world conditions (i.e. soiled surfaces), in this study we carried out field observations and laboratory experiments of condensation on dust-laden surfaces.

5. Part I – Development of Outdoor Soiling Microscope

The initial part of this study involved developing a novel outdoor soiling microscope (OSM) and using it to study dust accumulation and condensation mechanisms in the field. The motivation for developing the OSM was described in section 1.2, and a brief comparison of the OSM's features to traditional soiling-measurement techniques was presented in section 2.2.4 **Error! Reference source not found.**. In this chapter the detailed design, capabilities and operating limits of the OSM are described, and suggestions made for future improvements.

5.1. Design

The OSM comprised a small portable microscope with a glass coupon glued immediately to its front (Figure 29). The microscope was mounted "looking" up, so that dust particles and condensation droplets accumulated on the coupon and were imaged from below. An LED lamp was mounted behind the coupon to create a consistent illuminated background, enabling the OSM to be used day and night. (However the image contrast between particles and the illuminated background did vary slightly between day and night, which affected image analysis as discussed in section 5.4). The distance between the lamp and microscope was maximized to avoid interference with dust deposition, while still providing sufficiently intense and constant background illumination. A distance of approximately 10 cm, depending on the size of the lamp, was found to be suitable.

In many experiments it was useful to compare a "treatment" and "reference" coupon, for which a pair of OSMs was used side-by-side (Figure 30). The apparatus was mounted on a tripod so that the coupon was approximately 1.2 m above ground. A 3-cup anemometer was also mounted on the tripod. The OSM was located in the shade of a small building at the STF, as it was found that direct sunlight on the coupon sometimes caused "flares" in the images. The microscope was connected by a 10 m boosted USB cable to a computer in the adjacent building which controlled the microscope and saved its images. Details of the components and apparatus dimensions are provided in Table 4.



Figure 29. The outdoor soiling microscope (OSM) comprised a portable low-power microscope with a glass coupon glued to its front



Figure 30. In many experiments a pair of OSMs was used to compare soiling on “treatment” and “reference” coupons in identical environmental conditions

Component	Product and Specifications	Notes
Microscope	<p data-bbox="304 1279 552 1406">Celestron® Handheld Digital Microscope Pro Maozua® 5MP USB Microscope</p> <p data-bbox="304 1442 576 1536">5 MP camera sensor, 20-300X magnification, USB computer connection</p>	<p data-bbox="930 1279 1430 1373">The Celestron and Maozua microscopes were found to be technically identical despite bearing different brand names</p>
Coupon	<p data-bbox="304 1709 568 1832">Borosilicate glass, 2” square, 1/16” thick, Chemglass Life Sciences (CG-1904-36)</p>	

Back-lights	COB LED lights 3W and 10W, 12 Vdc, mounted on heat-sink		COB LED lights (pictured) of various sizes and power were used in different experiments. Eventually it was found that a 10W LED with reflective housing and covered with a translucent material produced the best images
-------------	---	---	--

Table 4. Details of OSM components

Image analysis was performed with imageJ, an open-source software coordinated by the US National Institutes of Health. Details of the image analysis procedures are presented in section 5.4.

5.2. Image Evaluation

The microscope was operated at its greatest magnification, which captured a coupon surface area of 2.42 X 1.82 mm in an image of 2592 X 1944 pixels, yielding a resolution of 0.935 $\mu\text{m}/\text{pixel}$. In the images, particles as small as 2-3 pixels across (i.e. \sim 2-3 μm diameter) could be clearly seen against the bright background. However when analyzing images digitally, the precise detected position of particle edges was sensitive to the threshold setting, which introduced variability to the measured particle area. This variability was more important the smaller the particle, because a given difference in edge location caused a proportionally greater change to measured particle area. Also, in outdoor conditions the surface coverage of a soiled coupon is overwhelmingly governed by large particles — recall the peak size range (by projected area) of particles at the STF was 10-40 μm (Figure 13b). For these reasons (inconsistent area measurement and low coverage contribution of small particles) it was decided to exclude particles smaller than a certain size in image analyses.

To determine this size limit, images of a soiled coupon were obtained from the OSM and a laboratory-grade optical microscope (Leica DM2700M RL/TL, 5X objective lens). The resolution of the lab microscope image was 0.332 $\mu\text{m}/\text{pixel}$, and as mentioned the outdoor images were 0.935 $\mu\text{m}/\text{pixel}$. The two microscopes were used to photograph the same part of the coupon (Figure 31).

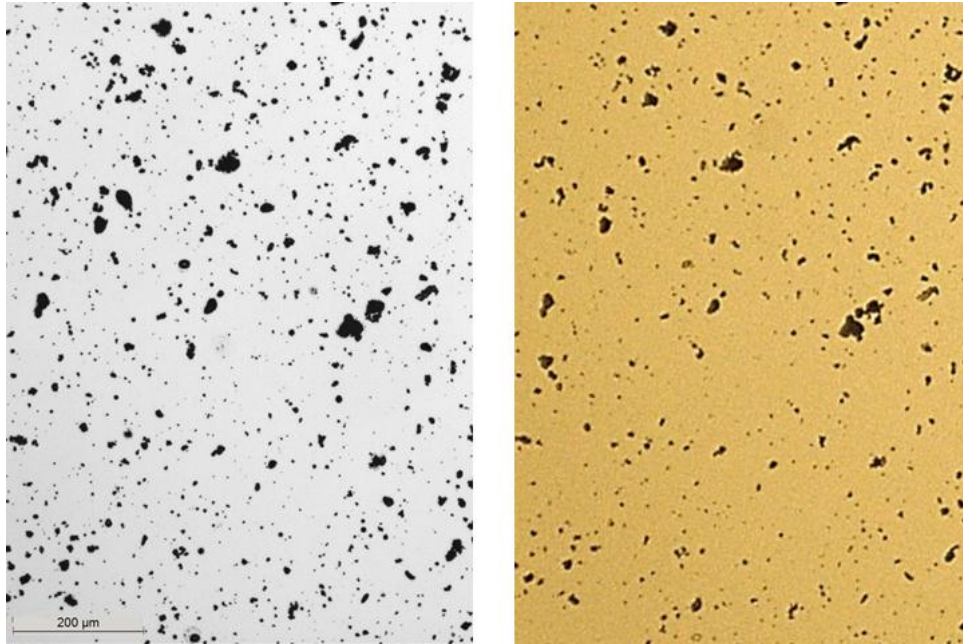


Figure 31. Images of the same soiled surface taken by a laboratory microscope (left) and the OSM (right), to evaluate the particle-area measurement accuracy of the OSM. The OSM image was cropped to coincide with the lab microscope image

Because of its greater resolution (image pixels per surface area), the lab microscope revealed smaller particles than did the OSM. (Note that the “cost” of high resolution is surface area surveyed — the OSM captured 4.39 mm² of the surface while the lab microscope captured 1.30 mm². For soiling rate measurement, it is desirable to image a large surface area to minimize stochastic variability.) The projected areas of particles in each image were measured, and the areas sorted large to small and summed (Figure 32).

Compared to the lab microscope, the OSM slightly under-estimated the areas of large particles. I.e. At the left of the chart, the sum of areas measured by the OSM (red markers) was less than from the lab microscope (blue markers). Conversely, the OSM significantly over-estimated the size of small particles (the sums cross and then diverge going right). The point at which the under- and over-measurement errors cancel out (the sums coincide) is approximately 10 μm². That is, if particles smaller than 10 μm² are excluded from measurements by the OSM, its total surface coverage measurement roughly matches that of the lab microscope. This filtering method was applied to all image analysis conducted in this study.

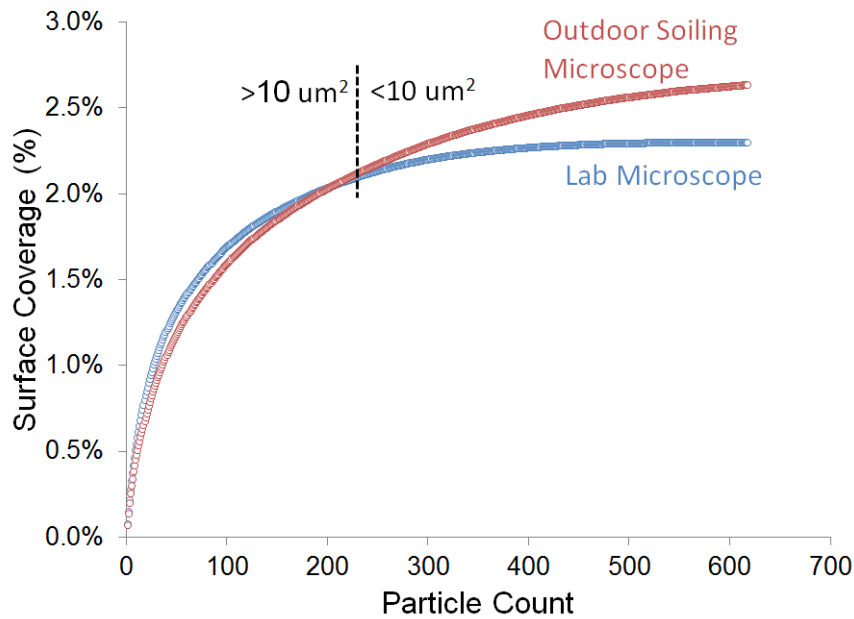


Figure 32. Cumulative surface coverage of particles from laboratory microscope (red line) and OSM (blue line) images of the same soiled coupon. Particles sorted large to small, left to right. This study adopted the practice of discarding particles $< 10 \mu\text{m}^2$ from particle-area measurements by the OSM.

To gain a visual sense of the effect of discarding particles smaller than $10 \mu\text{m}^2$, an example is provided (Figure 33). At left is the raw OSM image of the coupon in the field, which had 24 hours of outdoor soiling. The center image shows the digitally-analyzed image, with particles $> 10 \mu\text{m}^2$ masked blue and those $< 10 \mu\text{m}^2$ masked red. At right is a zoomed-in detail of the analyzed image. It is visibly clear that particles smaller than $10 \mu\text{m}^2$ are insignificant to surface coverage of soiled coupons at the Solar Test Facility, confirming the quantitative particle-area information presented in Figure 13b. (In that Figure, note that the cut-off at the left edge of the distributions — $3.6 \mu\text{m}$ diameter — matches the image-analysis cut-off of $10 \mu\text{m}^2$ area). This gives confidence that excluding particles $< 10 \mu\text{m}^2$ has little effect on coupon surface-coverage measurements.

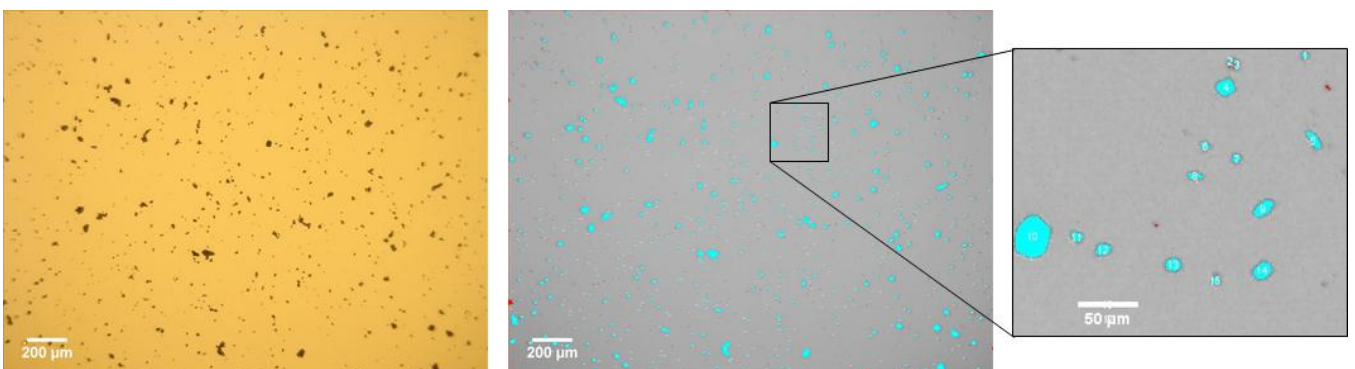


Figure 33. Raw OSM image of a soiled coupon (left), analyzed image (center), and detail (right). Particles larger than $10 \mu\text{m}^2$ projected area are masked in blue, while smaller ones (and those on image boundary) are masked in red

In summary, the OSM is not a precise tool for measuring the sizes of individual dust particles, especially those smaller than $10\ \mu\text{m}^2$. However it does appear useful for quantifying the approximate surface coverage of dust on the coupon. Next, its usefulness is evaluated for characterizing the rate of change of that surface coverage, i.e. the soiling rate

5.3. Relation to Soil Mass and Light Transmission

The OSM used the novel approach of quantifying ambient soiling by the projected area of dust particles on the coupon surface, whereas conventional techniques measure dust mass or light transmission loss of the coupon (as discussed in section 2.3). Therefore it was interest to compare the three measurements (surface coverage, mass, and light transmission) for the same amount of surface dust, to determine whether they “agreed”. Possible reasons that surface coverage measurements might deviate from mass or light-transmission were proposed to be: (i) particles smaller than $10\ \mu\text{m}^2$ were excluded from image analysis (although the preceding section indicated this was insignificant), (ii) natural dust particles are irregular in shape and tend to settle flat on the surface, so their projected are might not accurately reflect their mass/volume, and (iii) dust particles can forward-scatter photons, so their projected area might not highly correlate with light transmission loss.

Five glass coupons, each 5x5 cm, were exposed outdoors at the STF for periods ranging from one day to four weeks. Dust mass was on each coupon was measured by comparing the coupon’s start and end weights with a laboratory microbalance. Light transmission loss was measured by illuminating the coupon with a halogen lamp at a distance of 20 cm perpendicular to the coupon, and measuring the proportion of incident irradiation that was transmitted through the coupon (“transmission ratio”) with a pyranometer (mono-silicon PV cell) placed directly behind it. “Light transmission loss” was calculated as the arithmetic difference between transmission ratios of the coupon when clean and soiled. Surface coverage was determined from OSM images of the soiled coupon, as the total projected area of all dust particles divided by the total image area (while discarding particles smaller than $10\ \mu\text{m}^2$ as mentioned).

As shown in Figure 34, it was found that the responses of surface coverage and light transmission loss were very similar, and both correlated linearly with dust mass. Thus, soiling variation measured by the OSM correlated closely with conventional techniques, and the three “flaws” proposed in the preceding paragraph were not significant (or at least they were consistent, so that twice the dust quantity produced twice the measurement response for all techniques). This provided confidence that the OSM was a useful tool for measuring soiling rate, and its particle-area measurements captured the physical mass of dust on the surface and light transmitted through it.

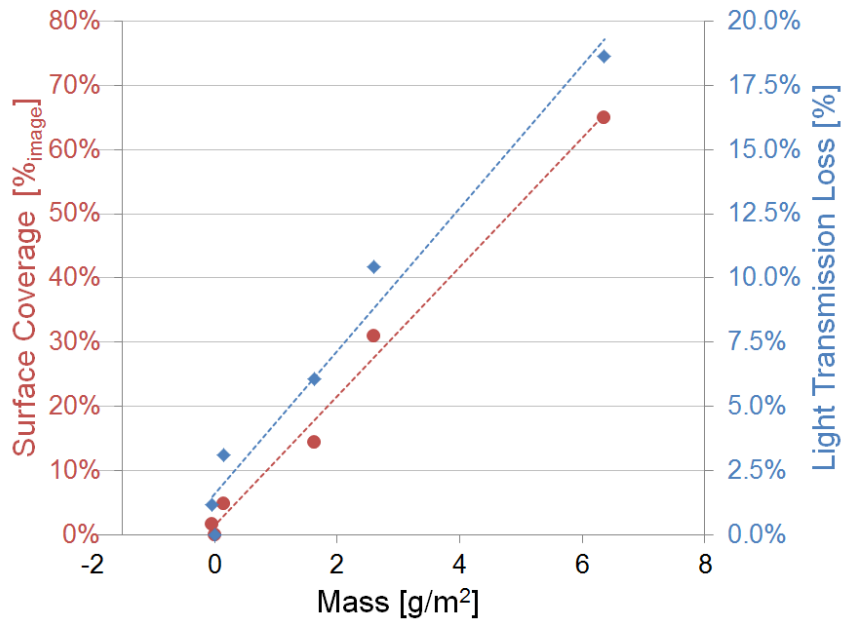


Figure 34. Surface Coverage of dust particles measured by outdoor soiling microscope (red points and line) and light transmission loss (blue points and line) as a function of dust mass.

The above experiment also allowed OSM surface coverage to be converted to soil mass via the gradient of the red line in Figure 34, i.e.

$$dust\ mass = 95,700 \times surface\ coverage \quad (35)$$

where dust mass is expressed in [$\mu\text{g}\cdot\text{m}^{-2}$] and surface coverage in [%_{image}]. This empirical relation is useful for estimating the total dust load on the surface from OSM images, and it aids interpretation of results (it is easier to think in terms of dust mass than surface coverage). However equation (35) is not useful for determining the mass of an individual dust particle, because in nature different particles have different shapes and densities.

In section 2.3.1 it was noted that a dust layer's mass and light transmission loss may cease being linearly proportional at high dust loads, because particles will start to settle on top of each other. This phenomenon will presumably also affect the OSM, because it cannot “see” stacked particles. That is, for heavily-soiled coupons it is likely that the OSM would underestimate the mass of soiling (but still correctly portray the change in light transmission). Because this study mainly works with dust flux rates (which are based on mass), in experiments OSM coupons were maintained in a lightly-soiled condition by cleaning them every 3-4 days.

To provide a sense of scale of the dust quantities reported in this study, the OSM image at the left of Figure 33 (which had 24 hours of outdoor exposure) has a surface coverage of 2.04 %_{image}. From Figure 34 it is seen that this amount of dust is very small compared to that “needed” to produce a significant response in light transmission loss or mass. This illustrates a key point made in section 2.2.3, that the OSM is able to measure much finer differences in soiling than are

possible with other methods. That is, 24 hours of soiling produced a barely-measurable change in light transmission and dust mass, but an easily-measurable (optically) change in surface coverage.

5.4. Dust Flux Rate Calculation

The OSM images could be used to quantify soiling in two ways:

- (i) *Total surface coverage* could be measured in each image, and the difference (between successive images) used as a measure of the soiling rate
- (ii) *Appearance/disappearance of individual particles* could be tracked in successive images, and summed to quantify dust fluxes.

The second method was used in this study because it revealed information about dust deposition and detachment fluxes individually, rather than only their net amount. Also it was found that despite using background lights in the OSM set-up, the image contrast between particles and background changed slightly between day and night, which affected the total surface coverage measurement. This effect was naturally eliminated in the second approach because successive images were “subtracted” from each other, as described below. This subtraction inherently produced more consistent particle/background contrast in images.

For each “raw” image captured by the OSM, the previous raw image (taken 10 minutes earlier) was digitally subtracted from it using imageJ software. This produced a “difference image”, in which particles that deposited during the 10 minutes appeared dark and particles that detached appeared white (Figure 35). Particles’ projected areas were measured and summed, providing quantitative measures of deposition and detachment dust fluxes. Sometimes the coupon moved slightly (a few microns) with respect to microscope between raw images, resulting in a multitude of light and dark patches in the difference image — such images were either analyzed manually or discarded.

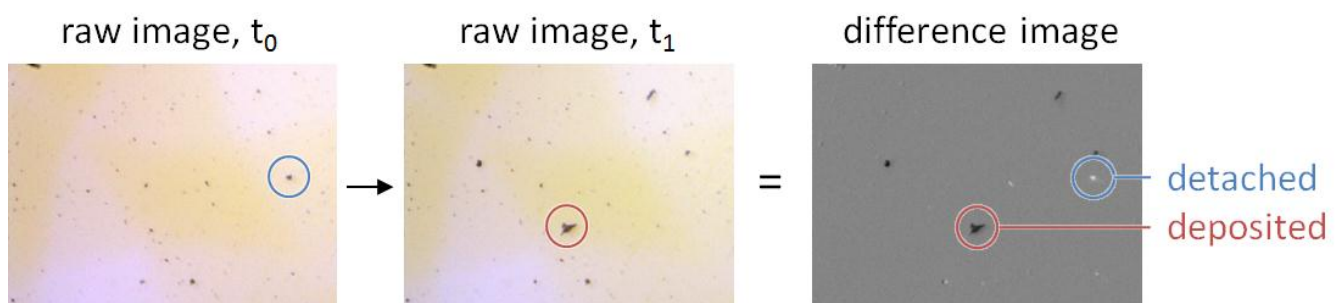


Figure 35. Pairs of successive “raw” OSM images were digitally subtracted to create a “difference image”, which revealed dust particles deposited (dark spots) and detached (white spots) during the intervening 10 minutes. Shown images are cropped from originals and portray surface areas 1.88 mm wide X 1.3 mm high

As illustrated in Figure 11 (page 40) dust accumulation is the net result of particle deposition, rebound (immediate detachment) and resuspension (delayed detachment). By operating two OSMs simultaneously, one with a greased coupon and one with a reference (ungreased) coupon, it was possible to quantify these three processes individually. The function of the greased coupon was to eliminate particle rebound and resuspension, and thus correctly measure deposition (i.e. all particles impacting the surface). The calculation technique, performed for every 10 minute interval, was as follows. (First all raw OSM images were manually reviewed and irregular ones discarded, e.g. due to cleaning, condensation, or image aberrations).

- 1) Subtract the preceding “raw ungreased” image from the current “raw ungreased” image, producing an “ungreased difference” image (showing added particles and detached particles)
- 2) Size and sum particle projected areas in the “ungreased difference” image, yielding two area sums: *ungreased added area* and *ungreased detached area*
- 3) Repeat steps 2-3 for the greased coupon. Because no particles detach from it, a single area sum is generated: *greased added area*
- 4) Dust fluxes in units of [%_{image}] were calculated as follows:

$$Deposition = greased\ added\ area \quad (36)$$

$$Rebound = greased\ added\ area - ungreased\ added\ area \quad (37)$$

$$Resuspension = ungreased\ detached\ area \quad (38)$$

$$Accumulation = Deposition - Rebound - Resuspension \quad (39)$$

- 5) The above dust fluxes are converted from surface coverage to mass via eq. (35), and then divided by the measurement interval of 10 minutes to yield final flux rate units of [$\mu\text{g} \cdot \text{m}^{-2} \text{min}^{-1}$], i.e. dust mass deposited/detached per square meter of coupon surface per minute

- 6) Other quantities are calculated from the dust flux rates:

$$Net\ Deposition = Deposition - Rebound \quad [\mu\text{g} \cdot \text{m}^{-2} \text{min}^{-1}] \quad (40)$$

$$Detachment = Resuspension + Rebound \quad [\mu\text{g} \cdot \text{m}^{-2} \cdot \text{min}^{-1}] \quad (41)$$

$$Relative \ Rebound = \frac{Rebound}{Deposition} \quad [-] \quad (42)$$

$$Surface \ Coverage = \sum_{\text{time last cleaned}}^{\text{present time}} Accumulation \quad [\mu\text{g} \cdot \text{m}^{-2}] \quad (43)$$

$$Relative \ Resuspension = \frac{Resuspension}{Surface \ Coverage} \quad [\text{min}^{-1}] \quad (44)$$

This measurement and analysis technique is discussed:

— Terminology and sign convention

In this report, names of dust fluxes are capitalized and italicized as above to distinguish these quantitative parameters from their lay meanings. For example, in common usage (and some soiling reports) “deposition” can refer to net soiling resulting from particles settling and detaching from a surface. In this study, *Deposition* refers to the gross quantity of impacting particles as collected by the greased coupon.

From the definition of *Accumulation*, a positive value indicates the coupon became more soiled and a negative value indicates it became cleaner.

— *Rebound* and *Resuspension* definitions

Rebound and *Resuspension* carry particular definitions in this report that differ slightly from their common usage. Because of the finite time interval (10 minutes) between images and the calculation method, *Rebound* encompasses particles that immediately bounced from the surface *and also* those that detached in less than the 10 minutes between images. As illustrated in Figure 36, such events were “misclassified” as *Rebound* instead of *Resuspension*. Similarly, *Resuspension* encompassed particles that may have only spent a moment on the surface, but happened to be photographed at that moment (“misclassified” as *Resuspension* instead of *Rebound*). The two “misclassifications” offset each other to some degree although, as will be shown, rebound events were much more common than resuspension events. Further, as the quotation marks around “misclassified” indicate, there is no established definition of particle residence time on a surface that delineates resuspension from rebound. Nevertheless, in this report *Rebound* and *Resuspension* should be considered proximate rather than exact measures of those processes.

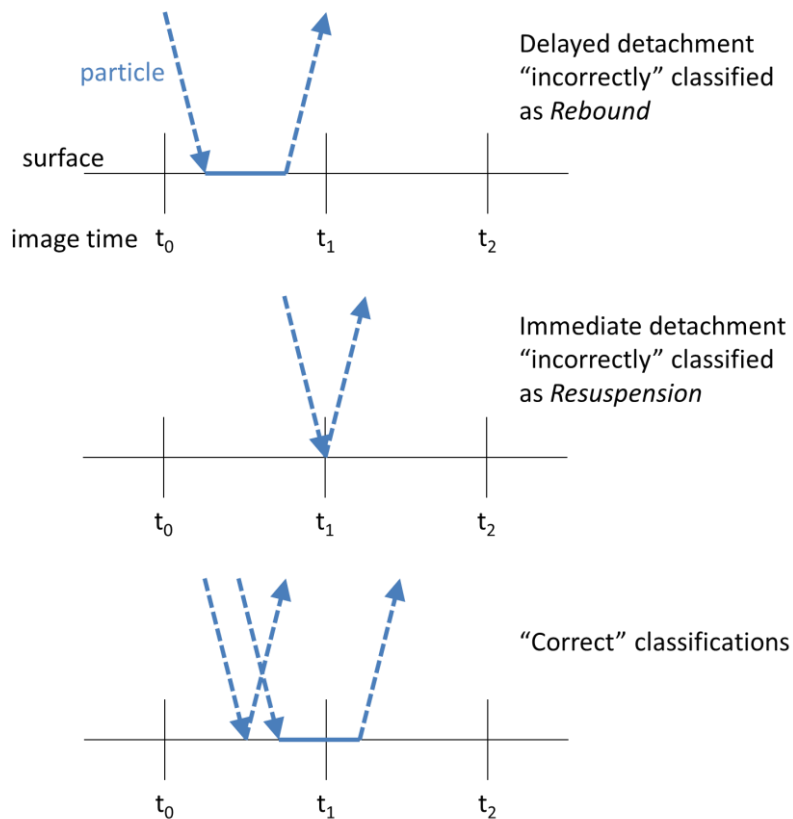


Figure 36. Due to the 10-minute interval between OSM images, some particle motions were “incorrectly” classified as *Rebound* or *Resuspension*

— Unphysical *Rebound* values

A corollary of the dust flux calculation method is that that unphysical *Rebound* values could occur. For example, if the projected area of particles falling on the ungreased coupon during an interval exceeded that on the greased coupon (which has a 50% probability of occurring), and wind speed was so low during the interval that all those particles remained on their respective coupons, then the calculated *Rebound* would be negative. Because thousands of observations were typically made in each experiment, and some rebound usually did occur from the ungreased coupon even in light wind, such negative values usually disappeared upon averaging. Nevertheless in data bins with few observations (i.e. rare combinations of environmental parameters), negative average *Rebound* values were sometimes obtained. In such cases, the *Rebound* average of those bins was set to zero.

— Grease efficiency

Dust flux calculations relied on the assumption that the greased coupon trapped all dust particles that impacted it, and permanently prevented trapped particles from detaching. Through simple inspection of “greased difference” images in

strong wind conditions it confirmed that indeed, almost no detachment from the greased coupon occurred. However it is not straightforward to determine the efficiency of the grease at trapping impacting particles. The grease used was undiluted petroleum jelly, which was refreshed every 3-4 days. Other researchers have used diluted petroleum jelly in toluene [94] or xylol [34], or the hydrocarbon-based laboratory grease Apiezon® L Grease [13][72]. A comparison of different greases in the literature was not found, so it is not possible to comment on their relative performance. To the extent that the greased coupon in this study failed to trap impacting particles, *Rebound* would have been underestimated. This may partly explain an unexpected decrease in *Rebound* observed at high wind speed, reported in section 6.4.2.

5.5. Comparison and Future Development

The OSM is a novel approach to study of soiling in the field that introduces new measurement capabilities. In particular, it allows the ability to measure:

- 1) all component dust flux rates (deposition, rebound and resuspension) individually and simultaneously
- 2) in time intervals of minutes
- 3) in natural field settings.

Previous techniques have possessed pairs of these capabilities but not all three. The review of soiling-measurement techniques (chapter 2) showed the following for each “capability pair”:

- Measuring component flux rates in short intervals (1 & 2)—In laboratory settings, wind-tunnels equipped with high-speed cameras have allowed the three flux processes to be carefully investigated in millisecond time-spans [178]. However soiling in natural environments is influenced by factors difficult to reproduce in wind tunnels (weather conditions, airflow behavior, dust composition) and tends to differ greatly from theoretical models, hence it is useful to complement laboratory experiments with field studies
- Measuring component flux rates in the field (1 & 3) — Only one study was found [41] (discussed in section 2.3.5) which attempted to quantify the three fluxes individually in the field, by exposing greased/ungreased discs in a forest canopy. However the procedure resulted in a single “observation” spanning two days of exposure, and relied on the gross approximation that no dust detached from an ungreased disc during its first 24 hours of exposure
- Measuring field soiling in short time intervals (2 & 3) — Measurement of dust accumulation in short time intervals in the field has not been performed previously, mainly due to the measurement limits of conventional techniques discussed in section 2.2.3. Indeed accomplishing just these two goals was the original motivation for developing the OSM.

The main limitations and possible future development of the OSM are discussed:

- Unable to reliably size particles smaller than $10\ \mu\text{m}^2$. This limit was insignificant when quantifying the amount of dust on the surface and its rate of accumulation, however for other research purposes it would be useful to measure flux rates of smaller particles. For example, $\text{PM}_{2.5}$ (particulate smaller than $2.5\ \mu\text{m}$) is frequently investigated because of its impact on human health. This could conceivably be achieved by using a higher-resolution microscope, although a protective enclosure for the microscope and improved background lighting would likely be required
- Inexact quantification of *Rebound* and *Resuspension*. Because of the finite time interval at which OSM images were taken, there was inherently some misclassification of particle rebound and resuspension events. With the current image-analysis approach, shortening the imaging interval from 10 minutes would reduce such misclassification, at the expense of greater image analysis and stochastic randomness (see below). To directly observe particle rebound would require a high-speed camera and a completely different approach to image analysis
- Stochastic measurements. The OSM captures a surface area of only $\sim 4\ \text{mm}^2$, as a result by far the most common outcome each 10 minutes is that nothing happens — no particles deposit and none detach. This resulted in highly stochastic and non-Gaussian dust flux observations (discussed further in section 6.2), which complicated modeling efforts. The degree of randomness in OSM observations could be achieved by increasing the imaged area, for example by using a microscope with wider field of view or multiple microscopes. (It could also be reduced by lengthening the time interval, however this would defeat the goal of using timescales similar to the weather)
- Manual image analysis. Although scripts were written to automate the measurement of particle areas in images, it was still necessary to manually check each image to ensure they were free of aberrations that would corrupt the measurements, and where possible correct the measurements manually. Because thousands of images were acquired for each study, this resulted in much tedious work. In future it is desirable to improve the image-analysis scripts to automatically identify and handle aberrant images, perhaps via artificial intelligence or machine-learning methods
- Fixed, tripod mounting. So far the OSM has only been used with $5\times 5\ \text{cm}$ coupons in horizontal orientation on a fixed tripod. In order to more accurately measure soiling rates on PV modules, it would be useful to mount the OSM on a module-size glass sheet placed within an actual PV system. Mounting the microscope on such a sheet would be straightforward, although distance-to-computer and background lighting technicalities would be need to be solved. It appears to be feasible and is recommended as a future application of the OSM.

6. Part II – Explanation of Soiling Variation

The main purpose for developing the OSM was to attempt to explain soiling-rate variation by environmental parameters, in desert field conditions. In this chapter, observational field studies at the Solar Test Facility in Doha were carried out using a greased/ungreased pairs of OSMs while measuring airborne particulate concentration, wind speed, and relative humidity. Relations between the parameters were explored qualitatively via binned data plots, and quantitatively via statistical methods. The goal of the work was to reveal effects of environmental parameters that had previously been obscured by existing soiling-measurement techniques, i.e. by using short measurement intervals and separating dust accumulation into its component flux rates. The dust-flux and weather data were used to construct a regression model of soiling in desert conditions, which was compared to models from the literature.

6.1. Experiment Set-Up

In order to quantify the component dust flux rates (deposition, rebound and resuspension) using the technique described in section 5.4, it was necessary to operate a greased/ungreased pair of OSMs simultaneously. This part of the study was conducted at the Solar Test Facility in Doha, Qatar. The OSMs were located approximately 50 m from the site's weather station (Figure 37), which recorded the following parameters: Wind speed (WS) was measured using a Thies Clima Wind Speed Transmitter 4.3303.22. Relative humidity (RH) was measured using a Thies Clima Hygro-Thermo Transmitter-compact 1.1005. Dust concentration (PM) was measured using a TSI DustTrak® DRX dust monitor configured with a total suspended particles (TSP) intake. Wind speed and humidity measurements readings were taken every minute, and PM every 2 minutes. The meteo parameter readings were averaged over 10-minute periods matching the image intervals of the OSM.



Figure 37. Weather station at the STF test site used to record wind speed and relative humidity. A separate, nearby particulate monitor was used for dust concentration measurements

In this experiment, one “observation” refers to a complete set of measurements for the 10-minute interval, including environmental parameters and OSM images. An observation was discarded if it was incomplete in any way, i.e. one or more environmental readings was missing, image quality was inadequate (e.g. out of focus), or irregular events occurred (e.g. the coupon was cleaned or it rained).

Field measurements were recorded over 51 days between July and November, 2016. The number of complete observations obtained was 6186. Weather conditions during the test period are shown in Figure 38. There were large daily cycles in RH, being low during the day and high at night. Average daily WS was predominantly in the range 1-2 ms^{-1} , while peak gusts (not represented in the chart) reached maxima around 6-7 ms^{-1} . PM was usually less than 0.15 $\text{mg}\cdot\text{m}^{-3}$ but on very dusty days reached 0.3-0.5 $\text{mg}\cdot\text{m}^{-3}$. Air temperatures were high in July-August (reaching over 40°C most days) and milder by November (reaching 20-30°C).

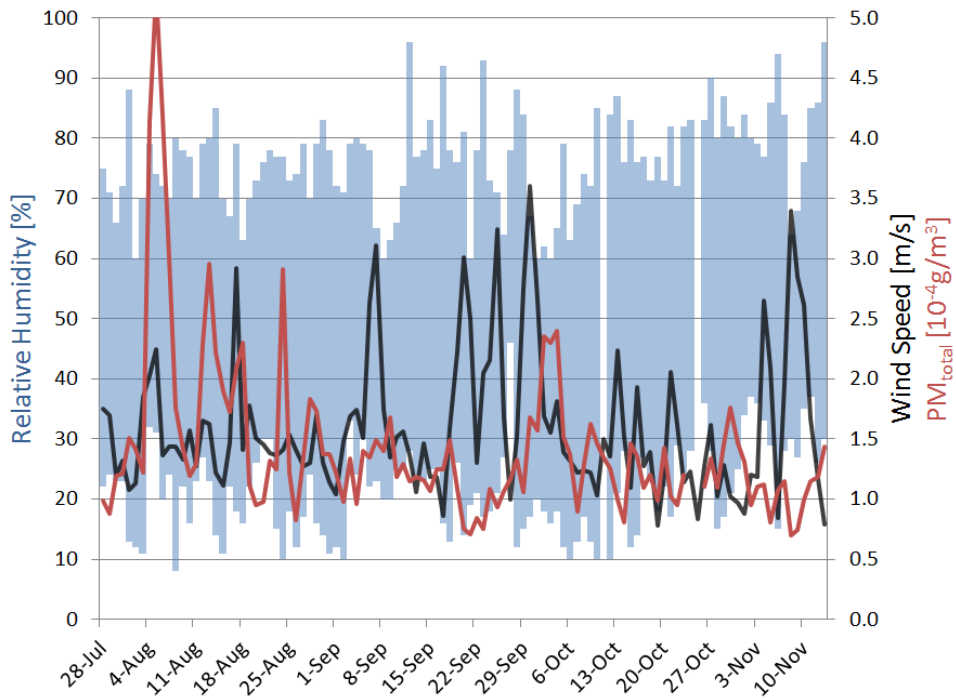


Figure 38. Weather conditions during the test period. Blue bars: Daily RH range [%], left axis. Black line: Average daily wind speed [ms^{-1}], right axis. Red line: Average daily PM [$10^{-4}\text{g}\cdot\text{m}^{-3}$], right axis.

6.2. Dust Flux Distribution Analysis

Dust flux rates measured by the OSM were stochastic. This is because, as mentioned, the imaged surface area was only $\sim 4\text{ mm}^2$ and therefore the most common observation for each 10 minutes was that no new particles appeared or disappeared in the images. When particles did deposit or detach, the measured values spanned several orders of magnitude, from $10\ \mu\text{m}^2$ (i.e. a single particle at the cut-off limit used in the image analysis) to $\sim 15,000\ \mu\text{m}^2$ (the greatest single deposition recording, in which several very large particles deposited at the same time). A typical 3-hour (18-observation) sequence of flux rate measurements is shown in Figure 39, demonstrating the stochastic nature of OSM flux-rate measurements.

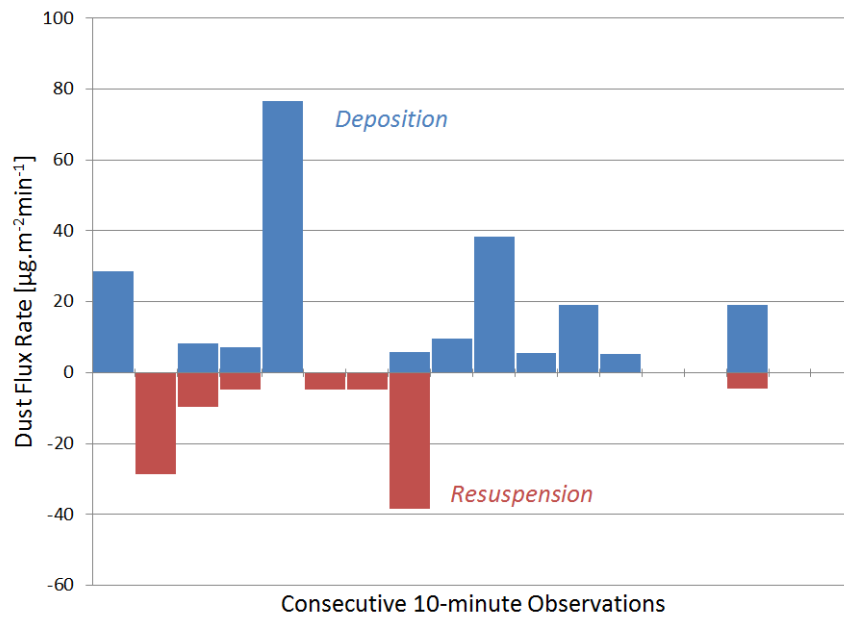


Figure 39. Sample 3-hour sequence of dust flux measurements, illustrating their stochastic nature. *Resuspension* plotted as negative values for clarity

It is important to consider the distribution of flux-rate observations in order to make statistical inferences about their means and the effects of environmental variables on those means. To commence, the distribution *Accumulation* is considered. A histogram of its values is plotted in Figure 40. It is seen that the values are not normally distributed. There is a large peak at zero (the bin $0\text{--}20 \mu\text{g}\cdot\text{m}^{-2}\cdot\text{min}^{-1}$) which accounts for roughly two-thirds of the 6186 observations, and positive values are more frequent than negative ones. (The proportion of observations with precisely zero measured *Accumulation* was 53%). This distribution is expected because, as mentioned, in most 10-minute intervals “nothing happens”, while soiling events (positive *Accumulation*) are more common than cleaning events by wind (negative *Accumulation*).

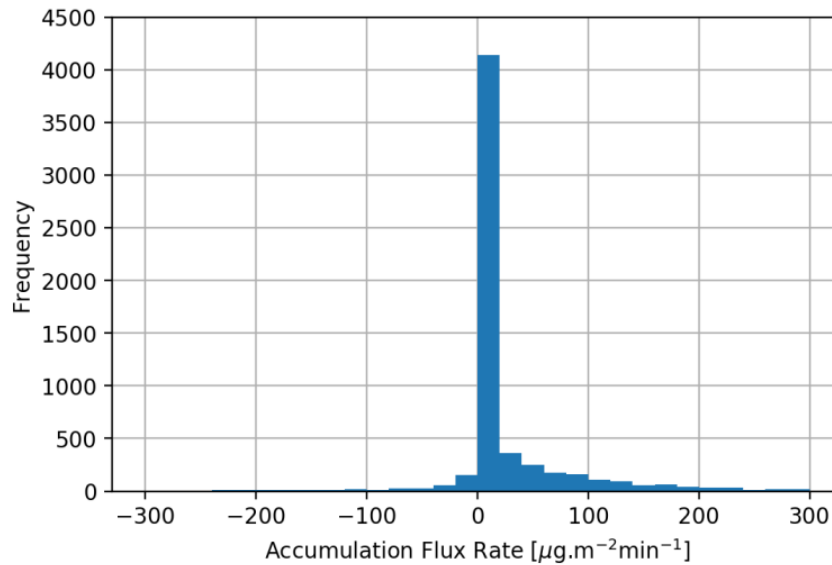


Figure 40. Histogram of the 6186 *Accumulation* measurements from this experiment. The distribution is not normal, with predominantly zero-value measurements and greater occurrence of positive values than negative ones. The frequency of precisely zero *Accumulation* measurements was 3309, i.e. 53% of observations

To analyze relations between environmental parameters and dust flux rates, it is useful to “bin” the environmental parameters and calculate the average flux rate in each bin. (Such plots are presented in the following section). In order to determine the confidence interval of the flux rate in each bin, it is necessary to know the number of observations in each bin and the distribution of flux-rate values.

The Central Limit Theorem holds that means of samples (\bar{X}) drawn from a population are normally distributed about the population’s average (μ) if either (i) the population is normally distributed, or (ii) the sample size (n) is $\geq \sim 30$ and the population is “not too terribly skewed” [179]. In the case of *Accumulation* measurements, it is not immediately obvious whether their distribution (Figure 40) is “too skewed” to invalidate this rule.

To investigate this, a simulation was performed using Python (a programming language for data analysis). First, the average of all 6186 *Accumulation* observations, \overline{Accum} , was calculated (in this experiment \overline{Accum} was $25.2 \mu\text{g.m}^{-2}.\text{min}^{-1}$, and the standard deviation s was $136.1 \mu\text{g.m}^{-2}.\text{min}^{-1}$). An initial estimated of the 90% confidence interval half-width, Cl_{90} , was made. From the full set of *Accumulation* observations, a sample of size n was then randomly drawn. The mean of this sample \bar{X} was calculated, and it was recorded whether or not \bar{X} was within the range $\overline{Accum} \pm Cl_{90}$. This sample-drawing was repeated 10,000 times, and the proportion of times that \bar{X} lay within the confidence interval was calculated. Cl_{90} was then adjusted until that proportion was 90%. The entire process was repeated with $n = 5, 10, 25, 50$ and 100 .

The results are shown in Table 5. Also shown are 90% confidence intervals for an ideal normally-distribution population having the same standard deviation ($\sigma = 136.1$), for the same values of n . When intervals derived from the experimental data and normal distributions differed by more than 10% they are highlighted in red. It is seen that for n

≥ 10 , *Accumulation* observations could be treated as if they were normally distributed (for the purposes of computing confidence intervals). Note that for $n = 5$ the confidence interval of the experimental data was *narrower* than that of a normal population, due to the great frequency of *Accumulation* measurements near zero. The key point from this analysis is that when a bin contained 10 or more *Accumulation* observations, the confidence interval of the *Accumulation* average in that bin could be calculated using standard equations for normally-distributed data.

sample size n	CI_{90} [$\mu\text{g}\cdot\text{m}^{-2}\cdot\text{min}^{-1}$]	90% confidence interval for normal population, $\sigma = 136.1$
5	90.9	100.1
10	71.8	70.8
25	44.0	44.8
50	30.6	31.7
100	22.0	22.4

Table 5. 90% confidence intervals of *Accumulation* sample means for different sample sizes, based on simulations using experimental data (CI_{90}) and an ideal normal population. Values differing by more than 10% are highlighted in red. The confidence intervals are similar when $n \geq \sim 10$

Confidence intervals of *Deposition*, *Rebound* and *Resuspension* were investigated in the same way. Using the same Python simulation procedure described above, CI_{90} values for different dust fluxes and sample sizes were obtained, and compared to confidence intervals of a normal population (Table 6). It is seen that there is much variation between the fluxes in this regard. *Rebound* confidence intervals are similar to those of a normal population for all sample sizes; those of *Resuspension* are only similar only if $> \sim 100$ samples are obtained; and *Deposition* is in between. The reason for these differences is the degree to which the flux-rate distribution differs from a normal distribution, as shown in the histograms at the bottom of the table. *Resuspension* is highly skewed (it is quite rare for particles to resuspend, and values can only be positive), whereas *Rebound* is less skewed (it is common for particles to rebound, and instances can take positive or negative values).

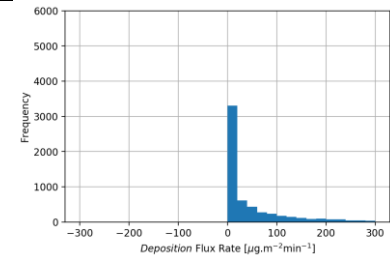
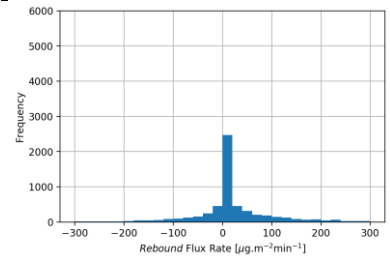
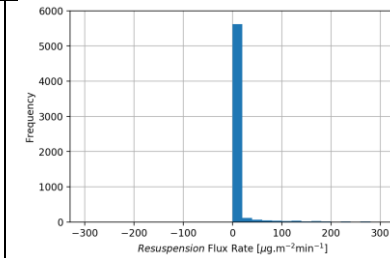
Sample size n	Deposition		Rebound		Resuspension	
	CI_{90} [$\mu\text{g}\cdot\text{m}^{-2}\cdot\text{min}^{-1}$]	90% CI normal $\sigma = 199.9$	CI_{90} [$\mu\text{g}\cdot\text{m}^{-2}\cdot\text{min}^{-1}$]	90% CI normal $\sigma = 223.7$	CI_{90} [$\mu\text{g}\cdot\text{m}^{-2}\cdot\text{min}^{-1}$]	90% CI normal $\sigma = 123.5$
5	105.3	147.1	153.1	164.6	45.9	90.9
10	86.1	104.0	114.8	116.4	45.9	64.2
25	59.3	65.8	72.7	73.6	36.4	40.6
50	44.0	46.5	51.7	52.1	23.9	28.7
100	32.5	32.9	36.4	38.8	19.1	20.3
Histo-gram						

Table 6. 90% confidence intervals from simulations using experimental data (CI_{90}) and the normal distribution, for different dust fluxes. Values differing by more than 10% are highlighted in red.

Based on this analysis, the following approach was taken in this study:

- 1-Parameter Plots

When comparing a dependent variable (e.g. *Accumulation*) against a single independent variable (e.g. WS), the width of each WS bin (the abscissa) was chosen such that it contained exactly 50 observations. 90% confidence intervals were constructed around \overline{Accum} by treating the *Accumulation* measurements as normally distributed.

- 2-Parameter Plots

When comparing a dependent variable (e.g. *Accumulation*) against two independent variables (e.g. WS & RH), it was not possible to achieve a fixed number of observations in every WS/RH bin. In this case, bins containing fewer than 20 observations were discarded on the basis that there was insufficient confidence that their average was close to reality.

6.3. Correlations between Environmental Parameters

In this section relations between environmental parameters and dust fluxes, and correlations between environmental parameters themselves, are first presented. Then, more complex relations between dust fluxes and pairs of environmental parameters are evaluated.

To recap, the environmental variables measured were wind speed (WS), relative humidity (RH), and total particulate concentration (PM). Before interpreting their influence on dust fluxes, it is important to understand any correlations between these parameters. Plots of each pair of environmental parameters for the test period are shown in Figure 41

(as described above, the 6186 observations are grouped into abscissa bins of exactly 50 observations and their average plotted). Correlations coefficients (R) of the parameter-pairs were also calculated and tabulated.

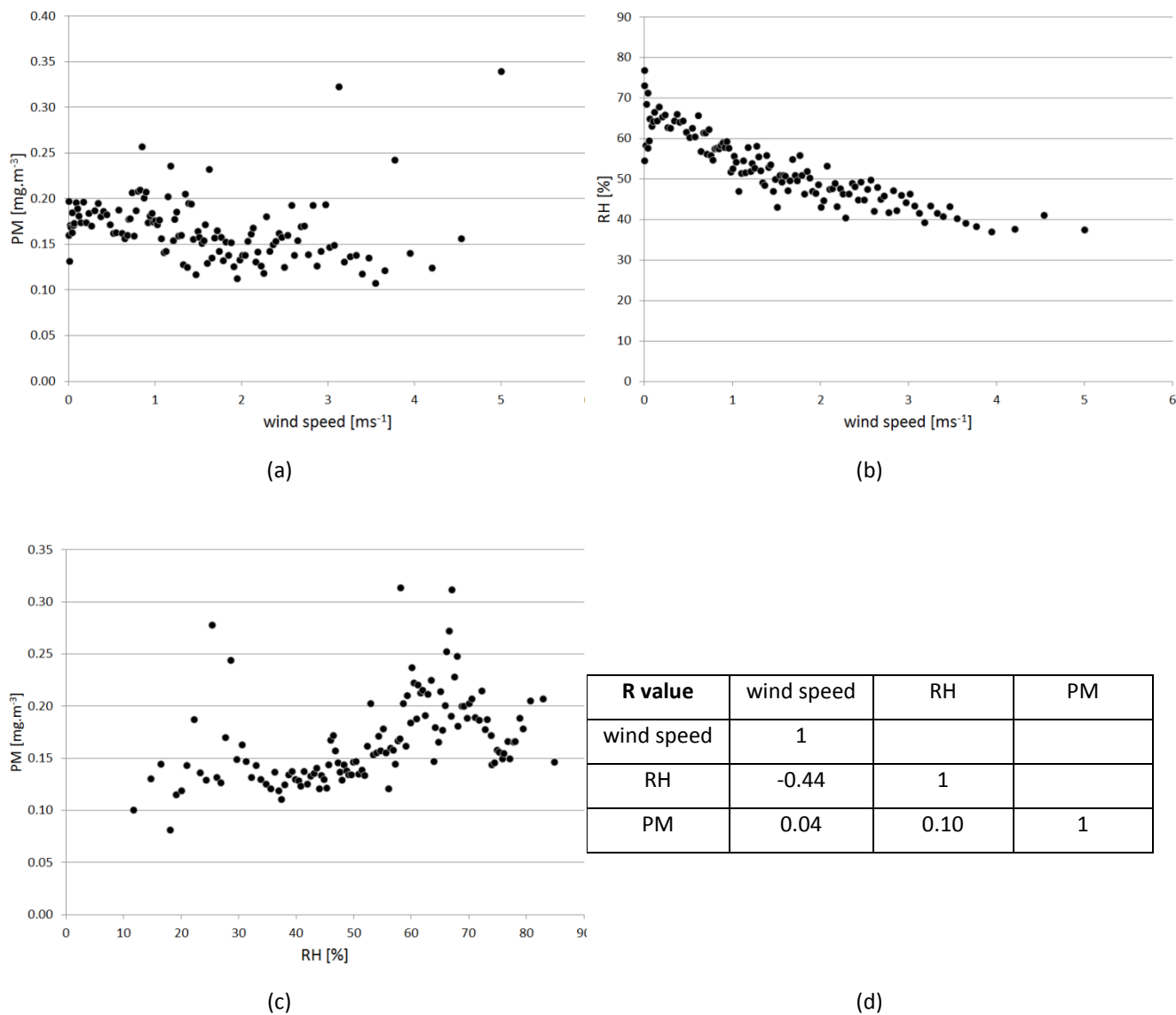


Figure 41. Correlations between environmental parameters. (a) PM vs. wind speed. (b) RH vs. wind speed. (c) PM vs RH. Each data point is an average of 50 observations, binned by the independent variable. (d) Correlation coefficients, R

Some notable correlations are seen:

- There is strong negative correlation between RH and WS, reflecting Doha’s weather pattern of low WS/high RH at night and the opposite during the day. It is anticipated that because the correlation is so strong, models of dust flux rates might employ either WS or RH as predictor variables but not both
- It was expected that higher wind speed would cause a greater amount of dust to be entrained in the air, yet PM in fact decreased slightly with increasing WS. It was proposed by aerosol scientists at Qatar Environment & Energy

Research Institute that this is because the test site is in a semi-urban location, where aerosols are generated by human activity, and a gentle wind dispels those aerosols. The single plotted point for $WS > 5 \text{ ms}^{-1}$ does show elevated PM, suggesting that wind eventually “creates” airborne dust above this velocity, which is consistent with previous reports of saltation in deserts [26][180]

- There is weak positive correlation between PM and RH, possibly due to hygroscopic growth of aerosol particles in high humidity, or detection of airborne water droplets by the particulate monitor.

6.4. Dust Flux Relations to Environmental Parameters

In this section, relations between dust flux rates and environmental parameters are presented and discussed qualitatively. Flux rates are sometimes plotted against individual parameters, sometimes against pairs of parameters, and sometimes both plots are presented. This was because each type of plot has certain advantages: 2-parameter plots allow effects of correlated environmental parameters to be “disentangled” (but their binning method leads to a scarcity of observations at extreme values of the environmental parameters), whereas 1-parameter plots retain information at extreme weather conditions (but their interpretation is confounded by correlated environmental parameters). The plot type was selected with the goal of presenting the most valuable information. Recall that in the 1-parameter plots each data point is an average of 50 observations ($n = 50$), while in the 2-parameter plots each data point is an average of at least 20 observations ($n \geq 20$).

6.4.1. Deposition

Variation of the *Deposition* flux rate with WS is shown in Figure 42.a. It is seen that *Deposition* was essentially independent of WS below $\sim 3 \text{ ms}^{-1}$, and increased approximately linearly with WS above that threshold. Comparing this chart with Figure 9a (page 30) — which plotted similar parameters at the STF but using 24-hour data averages — it is immediately clear that measuring dust flux in 10-minute intervals helps to reveal physical relations between wind speed and soiling.

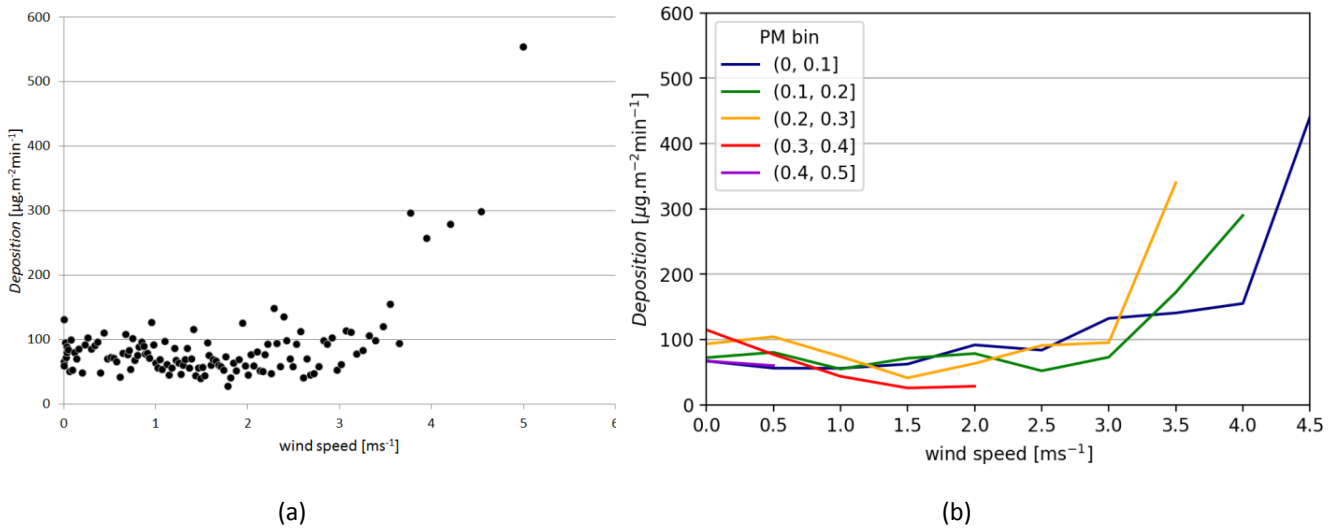


Figure 42. Effect of WS on *Deposition*. (a) Observations binned by WS ($n = 50$). (b) Observations binned by WS and PM ($n \geq 20$)

A key question is whether the threshold response of *Deposition* was consistent with previous dry deposition models from the literature. Recall that predictions of principle models of $v_{inertial}$ for 20 μm mineral particles were calculated and compared Figure 16 (page 53). It was seen that most models did not predict a noticeable threshold response, except for that of Kim et al. [85]. (Nho-Kim et al. [96] also observed a threshold deposition response but for much smaller and lighter particles — 5.6 μm , 1000 $\text{kg}\cdot\text{m}^{-3}$ — as shown in Figure 44).

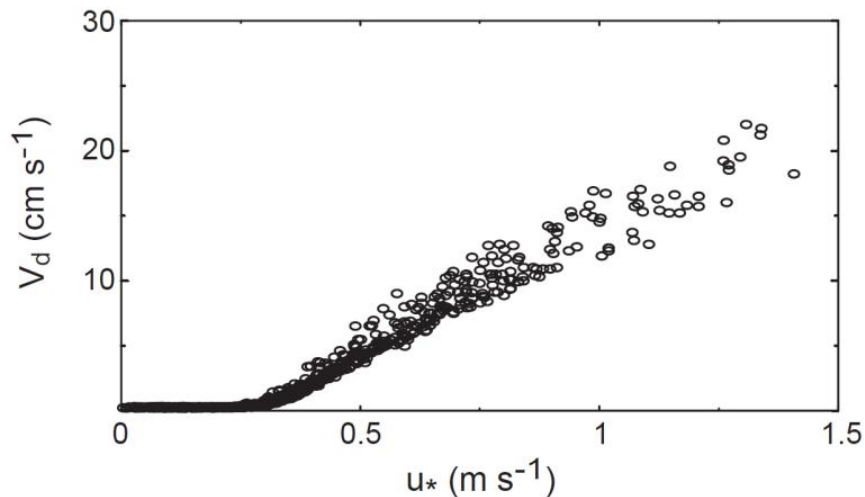


Figure 43. Simulated deposition velocity (v_{dep}) of 5.6 μm , 1000 $\text{kg}\cdot\text{m}^{-3}$ particles showing a predicted threshold wind speed at which the inertial deposition mechanism is significant, and then dominates [96] (Reprinted from Atmospheric Environment, vol 38, E.-Y. Nho-Kim, M. Michou, V.-H. Peuch, Parameterization of size-dependent particle dry deposition velocities for global modeling, pp 1933-1942, copyright 2004, with permission from Elsevier)

In order to plot the results in the same manner as Figure 16, it is necessary to transform WS to friction velocity (u_*) and *Deposition* to deposition velocity (v_{dep}). Friction velocity at the study site was determined empirically following an

approach similar to that of Etyemeziana [181]. Boundary-layer airflow velocity exhibits a logarithmic profile described by:

$$\frac{U(z)}{u^*} = \frac{1}{0.4} \ln\left(\frac{z}{z_0}\right) \quad (45)$$

where z is height above ground and z_0 is a parameter characterizing surface roughness. Wind speeds at heights of 2 m (U_{2m}) and 5 m (U_{5m}) above ground at the test site had been recorded every minute for several years. One year of U_{2m} and U_{5m} data was used to obtain z_0 and u^* from eq. (45). Variations of u^* and the ratio u^*/U_{2m} with U_{2m} are shown in Figure 43. A power function was empirically fitted between u^* and U_{2m} , eq. (46). This was used to transform WS (i.e. U_{2m}) to u^* for the study.

$$u^* = 0.092 U_{2m}^{0.673} \quad (46)$$

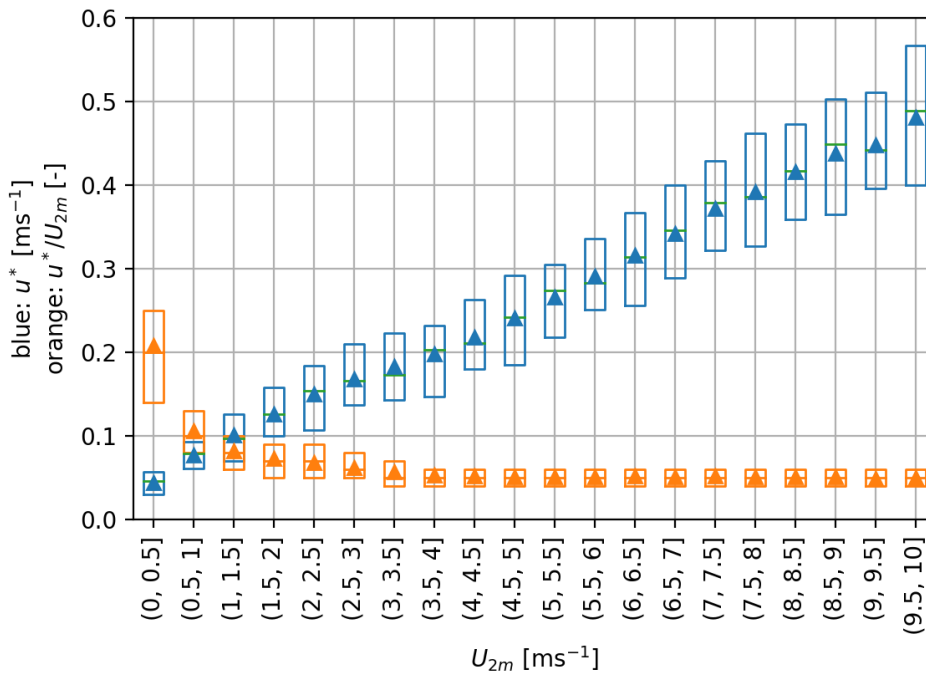


Figure 44. Friction velocity u^* at the site (blue boxplot), also shown as a proportion of U_{2m} (orange boxplot), as a function of U_{2m} .

Aerosol particle size distribution at the site was not directly measured. An effective v_{dep} [ms⁻¹] for the entire aerosol population was approximated by dividing the *Deposition* flux rate [μg.m⁻²s⁻¹] by the PM₁₀ concentration [μg.m⁻³] for each 10-minute observation period. For comparison against the experimental results, v_{dep} for 10 μm 2700 kg.m⁻³

particles was modeled with the inertial component from Kim et al. [85] and the sedimentation component (v_{sed}) from eq. (5). Based on the stated particle characteristics, v_{sed} was $6.51 \times 10^{-3} \text{ ms}^{-1}$.

The experimental results and predicted v_{dep} are plotted against u^* in Figure 45, and show high quantitative and qualitative agreement. The model of Kim et al. was generated from experiments in which 10-100 μm glass spheres (density presumably around 2400 kg.m^{-3}) were injected into ambient air and settled onto nearby coupons. Other models in the literature predict significantly different deposition behaviors (Figure 15, page 52). The results suggest that dry deposition in desert environments can be represented by particles tens of microns in diameter and specific density around 2.4-2.7.

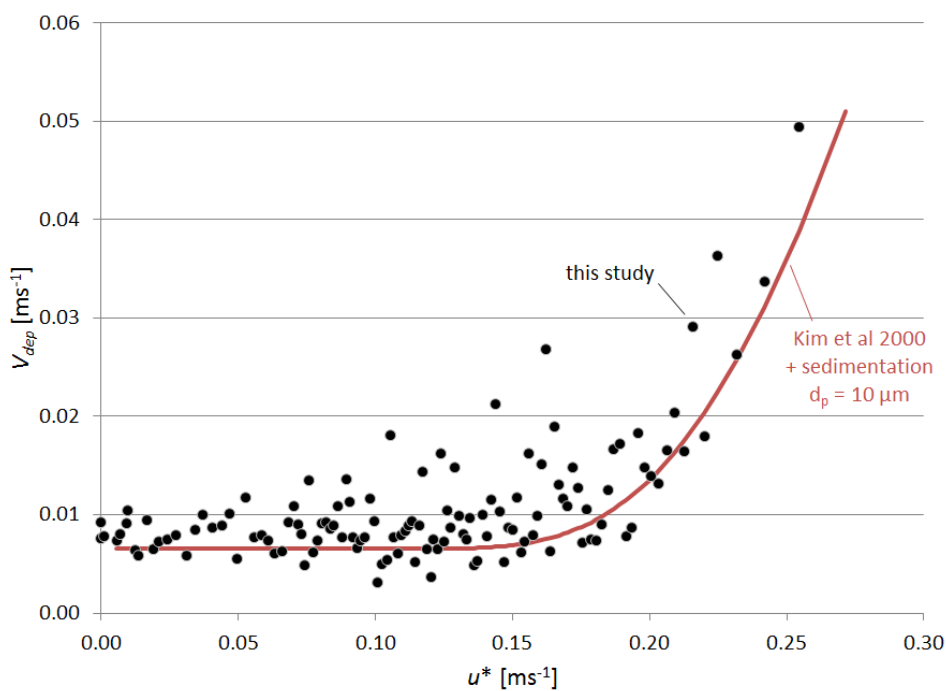


Figure 45. Deposition velocity v_{dep} from this study (black markers), and predicted for 10 μm mineral particles from Kim et al. [85] plus sedimentation (red line), as a function of u^* .

It was noted in the review of previous research (section 3.1.2) that some ambient-soiling studies reported that sedimentation fully accounted for dust deposition, while others found that inertial deposition was also significant. The present results indicate that the distinction might be explained by the existence of threshold wind speed, below which inertial deposition is not significant. I.e. Studies conducted where wind speed was mainly below the threshold (dependent on location and collector geometry) would be expected produce results showing deposition to be fully accounted for by sedimentation. It is not possible to test this hypothesis against the literature as wind speeds in field studies are not usually reported in sufficient detail.

Although the response of *Deposition* to WS was in line with some of the literature, the effect of turbulence at the study site was also considered. Instruments to directly measure air turbulence intensity were not available, as a proxy the ratio U_{2m}/U_{5m} was used. The boundary layer velocity profile of turbulent flow is “steeper” than that of laminar flow for the same free-stream velocity (Figure 46.a), hence an increase in the ratio U_{2m}/U_{5m} was assumed to indicate greater turbulence. In Figure 46.b it is seen that airflow at the site became progressively more turbulent (i.e. U_{2m}/U_{5m} increased) until U_{2m} reached $\sim 2 \text{ ms}^{-1}$, when it appeared the flow had become fully turbulent. This wind speed was significantly lower than that at which *Deposition* dramatically increased ($\sim 3 \text{ ms}^{-1}$), suggesting that transition to turbulent airflow at the site did not by itself cause greater deposition on the coupons.

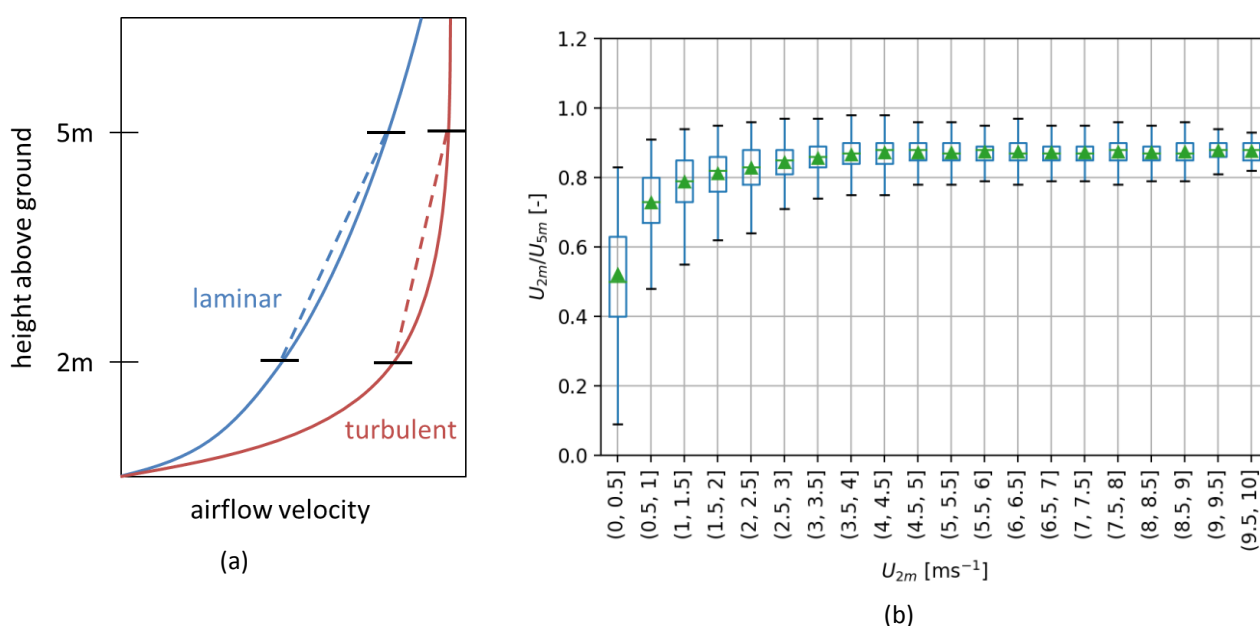


Figure 46. (a) Schematic illustration of airflow velocity profiles in laminar and turbulent flow of same free-stream velocity. The ratio of wind speeds U_{2m}/U_{5m} is expected to increase as the flow transitioned from laminar to turbulent. (b) Degree of turbulence at the test site (characterized by U_{2m}/U_{5m}) as a function of U_{2m}

Finally, aerosol size distribution was considered as a factor in the *Deposition* vs. WS threshold response. Instruments were not available to directly measure the distribution, however sizes of particles depositing on the greased collector during the study could be measured from OSM images. For expediency a subset of 1851 images spanning two weeks of the study period was used for this exercise, and particles smaller than $5 \mu\text{m}$ equivalent diameter were excluded, which yielded a population of 2627 individual particle deposits. The distribution of deposited particle sizes (equivalent diameters) vs. WS is shown in Figure 47. It is seen that the median and mean (by number) particle diameter increased when WS exceeded 3.5 ms^{-1} . Sedimentation and inertial deposition velocities of coarse particles increase with particle size. Therefore this observation simultaneously helps to explain the threshold increase in *Deposition* flux at $WS = 3.2 \text{ ms}^{-1}$ and also its low correlation to PM (see below). I.e. It appears that wind speed above 3.5 ms^{-1} increased the size of airborne dust particles at the study site, but not necessarily their total concentration, and this increase in size partly explains the threshold increase in *Deposition* near that wind speed.

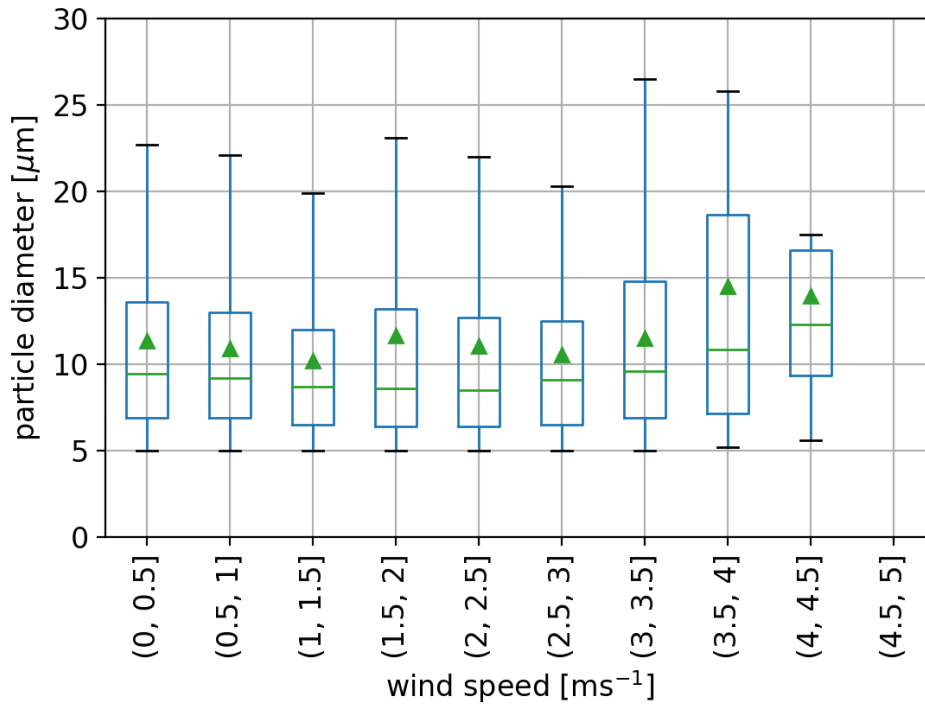


Figure 47. Diameters of 2627 particles (each larger than 5 μm) that deposited onto a horizontal greased coupon at the study site, as function of wind speed.

Deposition decreased slightly with increasing RH (Figure 48.a). A candidate explanation is that this was due to correspondence of low WS (and therefore low *Deposition*) with high RH (Figure 41.b). Yet even holding WS constant, the slight decrease of *Deposition* with RH was generally maintained (Figure 48.b). Another candidate explanation is that higher RH correlated with lower PM, yet the opposite was observed (Figure 41.c). Regarding physical connection between RH and dust deposition, hygroscopic particles enlarge in high humidity and thus would be expected to exhibit increasing deposition with RH [20][96][182], yet the opposite is observed. The observed *Deposition*/RH relation is relatively weak, and may simply be a random event.

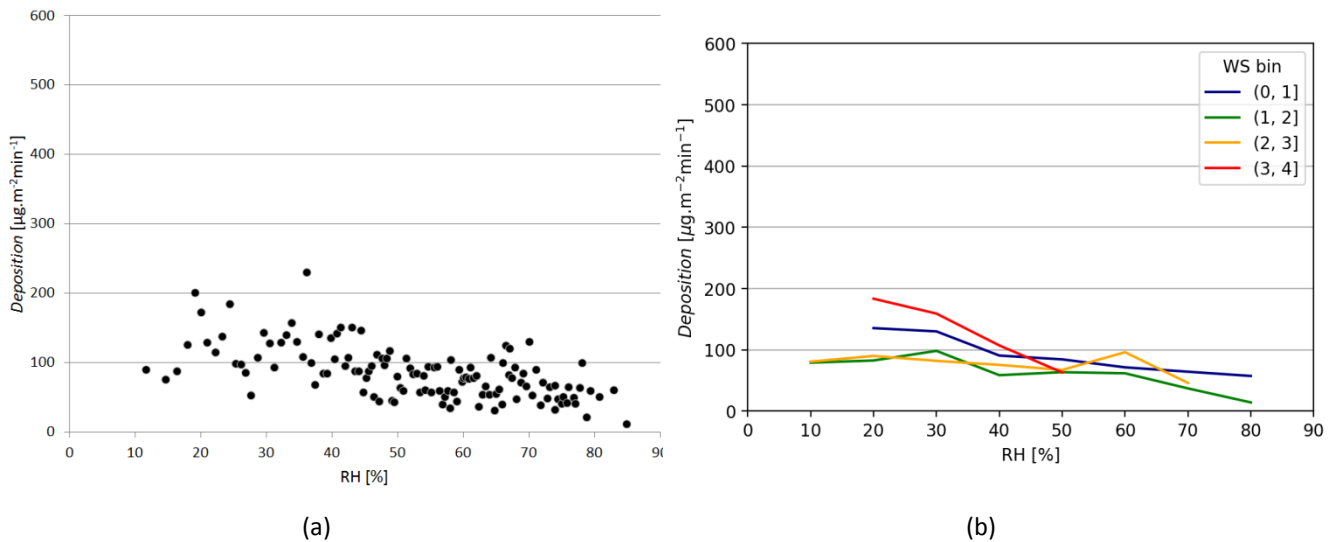
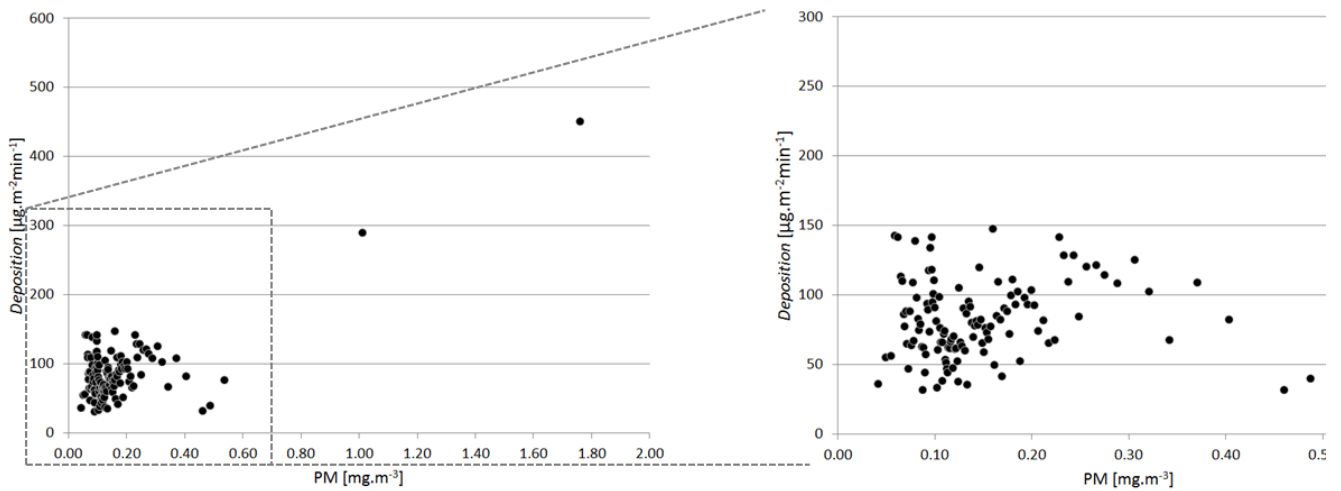


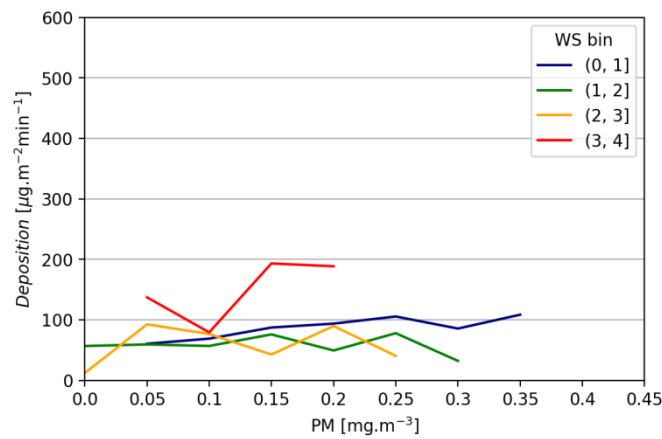
Figure 48. Effect of RH on *Deposition*. (a) Observations binned by RH ($n = 50$) (b) Observations binned by RH and WS ($n \geq 20$)

The relation between PM and *Deposition* is shown in Figure 49.a. There was surprisingly little effect of PM when it was below $\sim 0.6 \text{ mg}\cdot\text{m}^{-3}$, but some dust storms apparently occurred in which PM exceeded $1 \text{ mg}\cdot\text{m}^{-3}$ and in those conditions *Deposition* increased markedly. The independence of *Deposition* from PM at low/moderate levels was unexpected, because the fundamental model of aerosols holds that the quantity of particles impacting a surface is directly proportional to their airborne concentration (i.e. equation (2)).

It is stressed that the PM measure reported herein is total suspended particles, not a subset of PM such as PM_{10} or $\text{PM}_{2.5}$ whose exclusion of larger particles might have helped explain the observed results. The independence of *Deposition* from PM was still observed when WS was held constant (Figure 49.b). At present there is no adequate explanation for the independence of *Deposition* from PM at low/moderate concentrations, and it warrants further investigation.



(a)



(b)

Figure 49. Effect of PM on *Deposition*. (a) Observations binned by PM ($n = 50$) (b) Observations binned by PM and WS ($n \geq 20$)

6.4.2. Rebound

The degree to which particles rebound from the surface is most readily understood via *Relative Rebound*, i.e. the proportion of depositing particles on the OSM coupon which quickly detached again. Previous research of particle mechanics (section 3.2) showed that the rebound fraction is expected to be influenced by WS and RH.

The effect of WS on *Relative Rebound* in this study is shown in Figure 50.a. As expected, a greater fraction of particles rebounded as WS increased, as kinetic energy exceeded adhesion energy for a greater proportion of particles. There was a large spread in *Relative Rebound* for a given WS, indicating that other factors also influenced the degree of particle rebound. When RH held constant, the general trend of greater rebound with increasing wind speed is maintained (Figure 50.b).

As wind speed exceeded $\sim 4 \text{ ms}^{-1}$ *Relative Rebound* decreased again. This was also unexpected from the kinetic-energy model. It is speculated that the undiluted petroleum jelly used to trap particles to the greased coupon was not perfectly effective, and when particles impacted the grease at high velocity some of them did in fact rebound. It was earlier noted (section 5.4) that previous researchers used diluted petroleum jelly or used other greases, and the present results suggest that those may be better techniques.

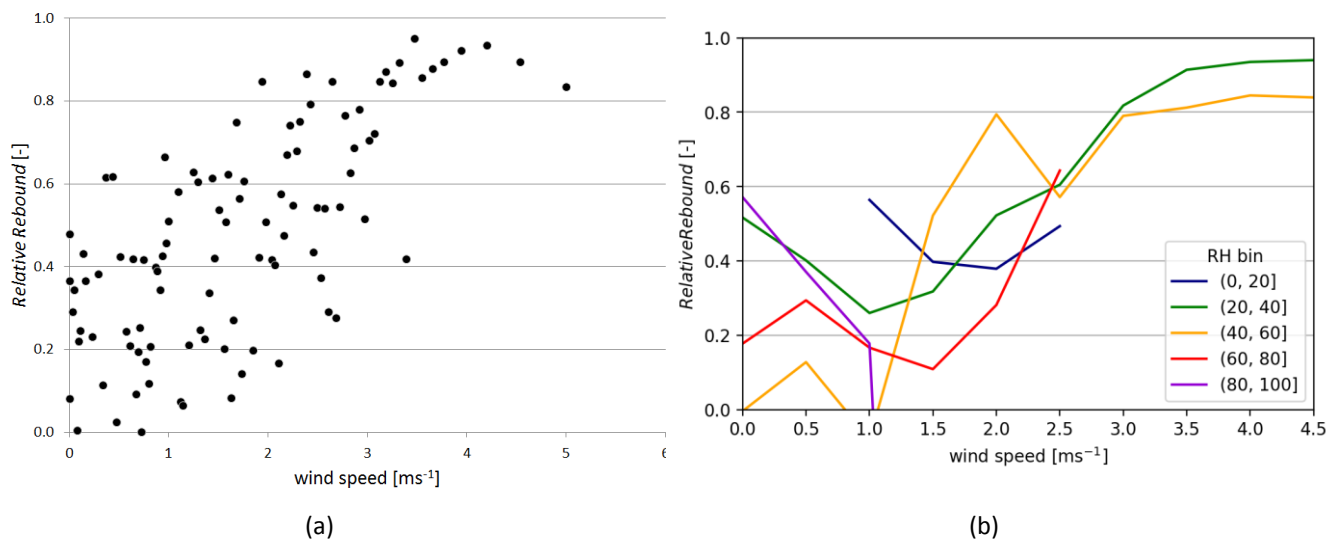


Figure 50. Effect of WS on *Relative Rebound*. (a) Observations binned by WS ($n = 50$) (b) Observations binned by WS and RH ($n \geq 20$)

Previous studies reported that particle rebound was suppressed at high RH due to capillary adhesion (section 3.2). The plot of *Relative Rebound* against RH is highly scattered but a weak negative correlation is discernable (Figure 51.a). Holding WS constant yields an inconsistent plot, providing no insights on the rebound/RH relation (Figure 51.b). The main conclusions from these results are that WS had a significant influence on particle rebound whereas RH did not, and that the present OSM technique for determining rebound (undiluted grease and misclassification of detachment events) introduces errors which should be remedied or quantified in future.

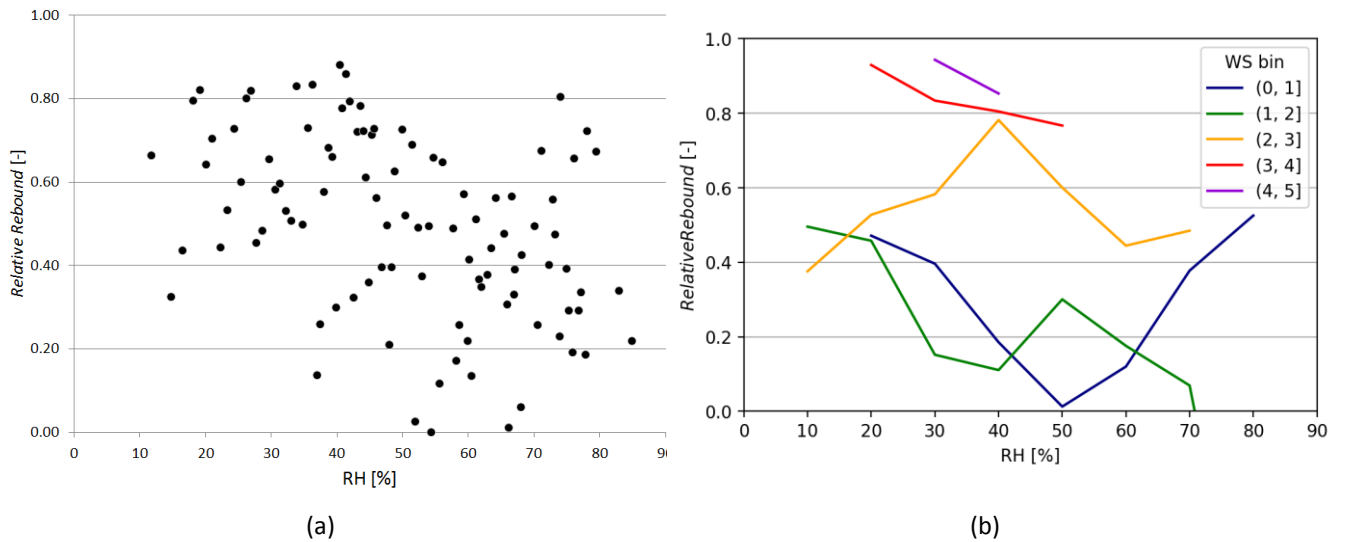


Figure 51. Effect of RH on *Relative Rebound*. (a) Observations binned by RH ($n = 50$) (b) Observations binned by RH and WS ($n \geq 20$)

6.4.3. Resuspension

Response of *Relative Resuspension* to environmental parameters is reported in this section. First it is noted that the range of the vertical axis in these plots is small, extending to just 0.005 min^{-1} (corresponding to 1 in 200 of particles on the coupon resuspending per minute). This highlights that, overall, resuspension plays a relatively minor role in dust accumulation at this site. To briefly illustrate this point further, total *Deposition* flux on the coupon throughout the test period (i.e. summing all 6186 *Deposition* measurements) was 3.20 g.m^{-2} , while total *Resuspension* flux was just 0.87 g.m^{-2} .

A weak positive correlation is observed between *Relative Resuspension* and WS (Figure 52.a). However this appears partly due to the coincidence of high WS with low RH (which results below show did affect resuspension) — when RH is kept constant (Figure 52.b) essentially no influence of WS on resuspension is seen. At face value this seems surprising, because previous studies widely reported (section 3.3) that airflow velocity has a powerful effect on particle detachment, indeed detachment was often described as being proportional to U^2 .

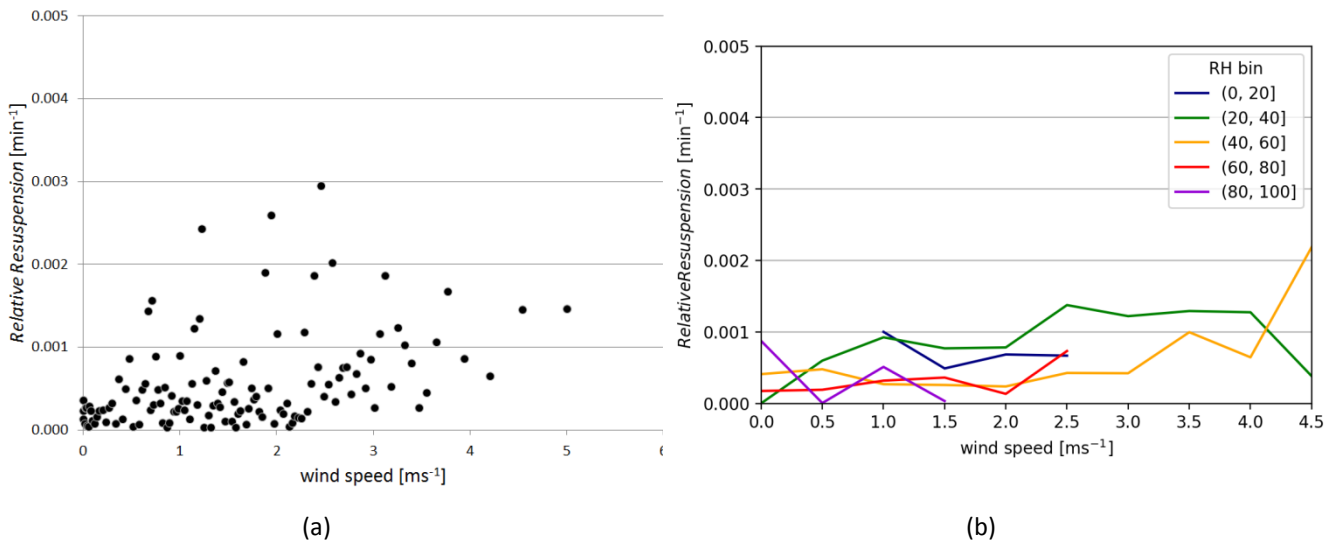


Figure 52. Effect of WS on *Relative Resuspension*. (a) Observations binned by WS ($n = 50$) (b) Binned by WS and RH ($n \geq 20$)

It was thought that the observed independence of *Resuspension* from WS may be because in ambient conditions — where WS continually fluctuates — *change* in WS is more important than its absolute magnitude. This is illustrated schematically in Figure 53. A low-but-rising WS may cause particles to detach from the surface, whereas a high-but-falling WS would not. Such behavior was suggested by Loosmore and Hunt [16], and observed experimentally in a wind tunnel by Ibrahim et al. [113], who showed that steel microspheres did not resuspend from a glass surface when subjected to the same flow velocity evolution as in a previous exposure.

To test this explanation on the present results, for each observation the average WS over the preceding hour was calculated and subtracted from the current WS. This quantity was termed ΔWS_{1hr} [ms^{-1}]. Plots of *Relative Resuspension* against ΔWS_{1hr} (Figure 54) still show much scatter, but do reveal some correlation between particle detachment and positive values of ΔWS_{1hr} (i.e. rising WS).

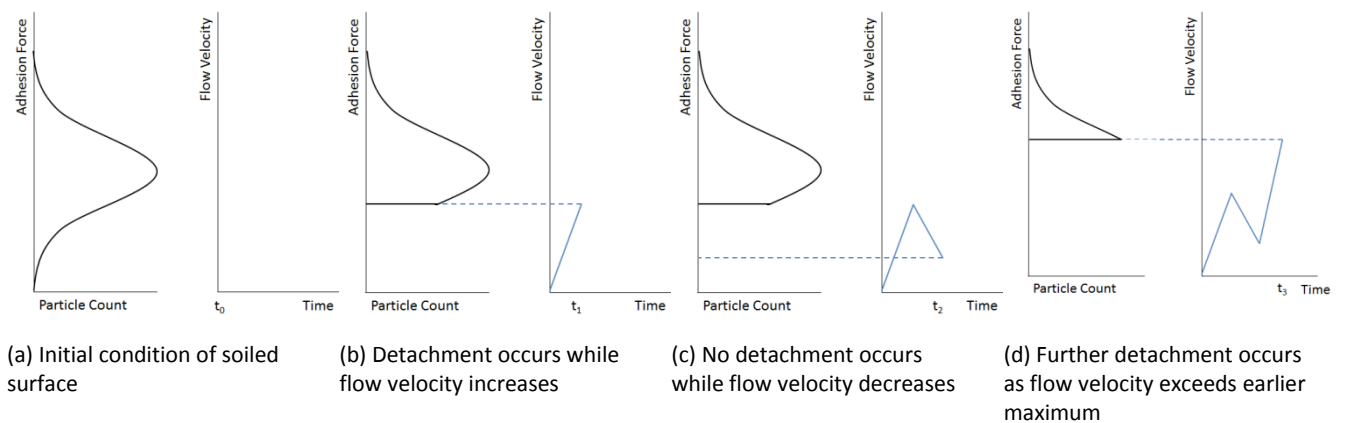


Figure 53. Schematic illustration of wind speed history and amount of particle detachment

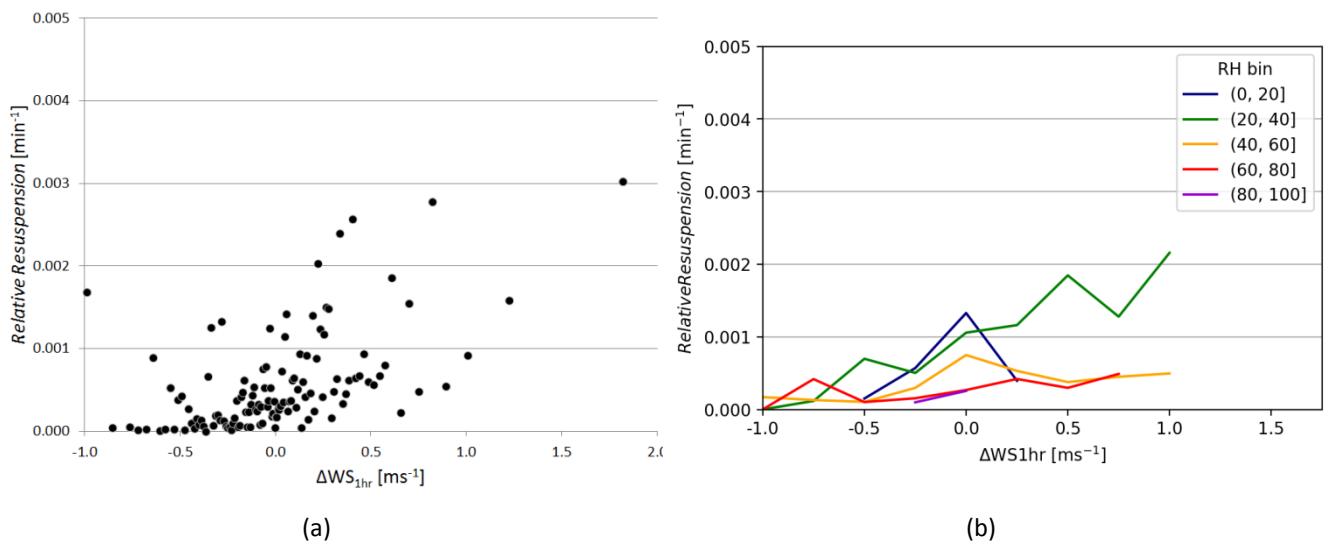


Figure 54. Effect of ΔWS_{1hr} on *Relative Resuspension*. (a) Observations binned by ΔWS_{1hr} ($n = 50$) (b) Observations binned by ΔWS_{1hr} and RH ($n \geq 20$)

Regarding the effect of RH on dust resuspension, Figure 55.a shows that when RH exceeded $\sim 50\%$ only low values of *Relative Resuspension* occurred. Holding WS constant (Figure 55.b) it is seen that, despite some inconsistencies, resuspension is generally suppressed as RH increases and is virtually eliminated above 50% RH. This indicates that presence of capillary adhesion is more important to dust resuspension than is the prevailing WS.

It is interesting to note that *Relative Rebound* (rapid particle detachment) was influenced by prevailing WS but not RH, whereas *Relative Resuspension* (delayed particle detachment) exhibited the opposite influences. The results can be understood by considering that rebound is governed by particles' kinetic energy, while resuspension is mainly governed by the presence of capillary adhesion.

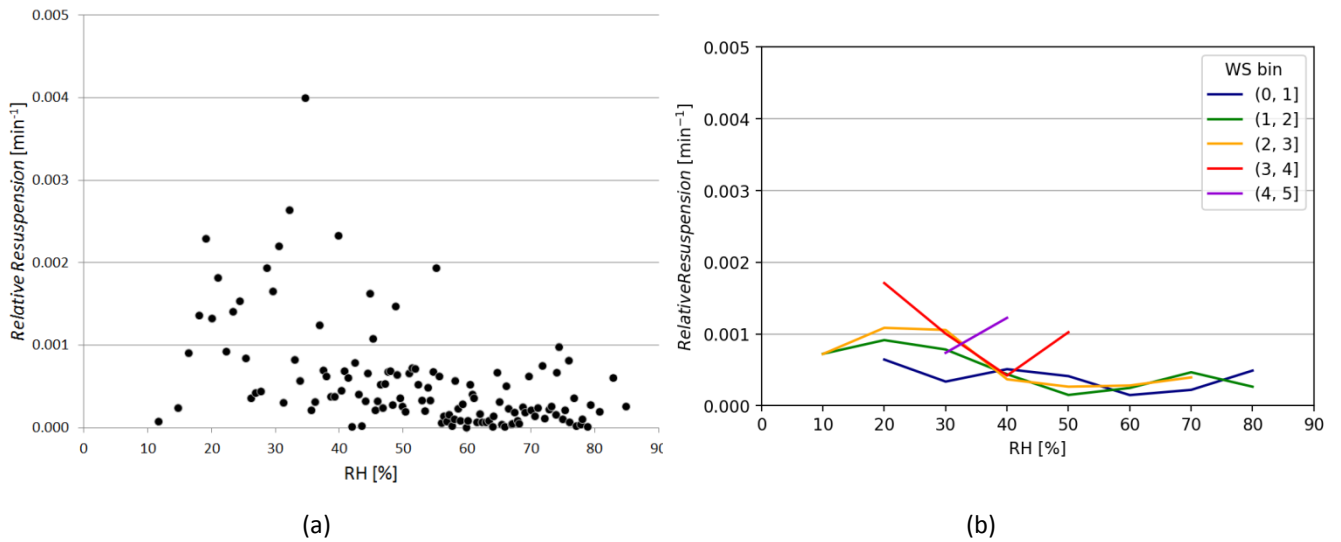


Figure 55. Effect of RH on *Relative Resuspension*. (a) Observations binned by RH ($n = 50$) (b) Binned by RH and WS ($n \geq 20$)

It was noted in section 3.4 that the strongest particle-adhesion mechanism in PV soiling is cementation (dissolution and recrystallization of soluble material in the dust), which can be expected to build up over time. Likewise, Loosmore & Hunt [16] predicted that dust resuspension would be affected by the preceding exposure time and conditions, but noted that these factors had not yet been fully accounted for. Therefore the OSM resuspension measurements were analyzed as a function of Exposure Time, defined as the number of hours since the coupon was last cleaned. In plots of *Relative Resuspension* versus Exposure Time (Figure 56) a weak negative correlation is indeed exhibited. The highest resuspension rates occurred on recently-cleaned coupons (<10 hrs Exposure Time), whereas coupons exposed for roughly four days exhibited very low resuspension rates (fewer than 1 particle in a thousand on the coupon, per minute). This provides evidence that particles became more tightly adhered to the coupon over several days, indicating occurrence of cementation.

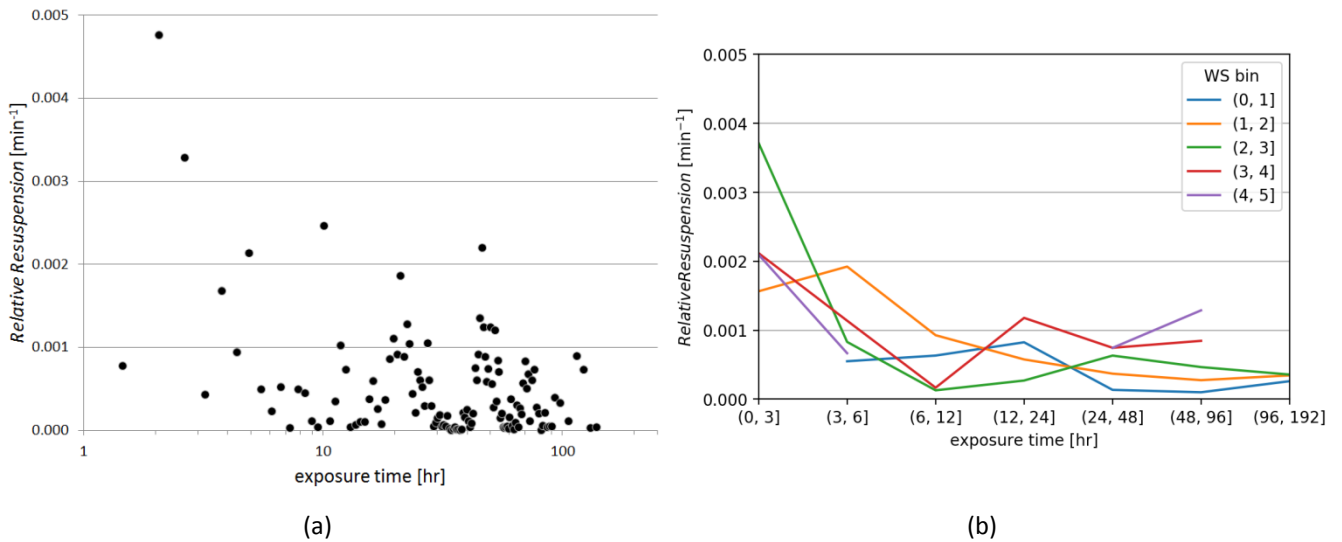


Figure 56. Effect of Exposure Time on *Relative Resuspension*. (a) Observations binned by Exposure Time ($n = 50$) (b) Observations binned by exposure time and WS ($n \geq 20$)

6.4.4. Accumulation

To recap, *Accumulation* represents the net dust flux rate on the coupon (the sum of *Deposition*, *Rebound* and *Resuspension*). Positive values signify the coupon gains dust, negative that it sheds dust.

An important question in PV soiling research is stressed at this point. As noted in chapter 3 higher wind speed increases both dust deposition and detachment, so it is not obvious whether strong wind is “good” or “bad” for PV soiling. Of ambient soiling studies, most stated that greater wind speed increases soiling [3][8][11][26][61], although some the opposite [6].

The results of this study show a strong negative correlation between WS and *Accumulation* (Figure 57.a). In $WS < \sim 1 \text{ ms}^{-1}$ the coupon consistently became more soiled, and in $WS > \sim 3 \text{ ms}^{-1}$ the coupon became cleaner on average. This relation was maintained even when PM was held constant (Figure 57.b) and when RH was held constant (not shown).

Further insight is gained by plotting *Accumulation* against both WS and ΔWS_{1hr} (change in wind speed relative to the preceding hour), Figure 58. The chart can be understood by considering the preceding results for individual dust fluxes. In constant or falling wind speed (the region $\Delta WS_{1hr} \leq \sim 0$): *Accumulation* decreased slightly as WS increased due to greater particle rebound. In rising wind speed (the region $\Delta WS_{1hr} \geq 0$): *Accumulation* decreased even further due to enhanced dust resuspension, in addition to greater rebound. Overall the results provide strong evidence that (for a horizontal surface in desert environments) higher wind speed reduces dust accumulation, due to greater particle rebound and resuspension rates.

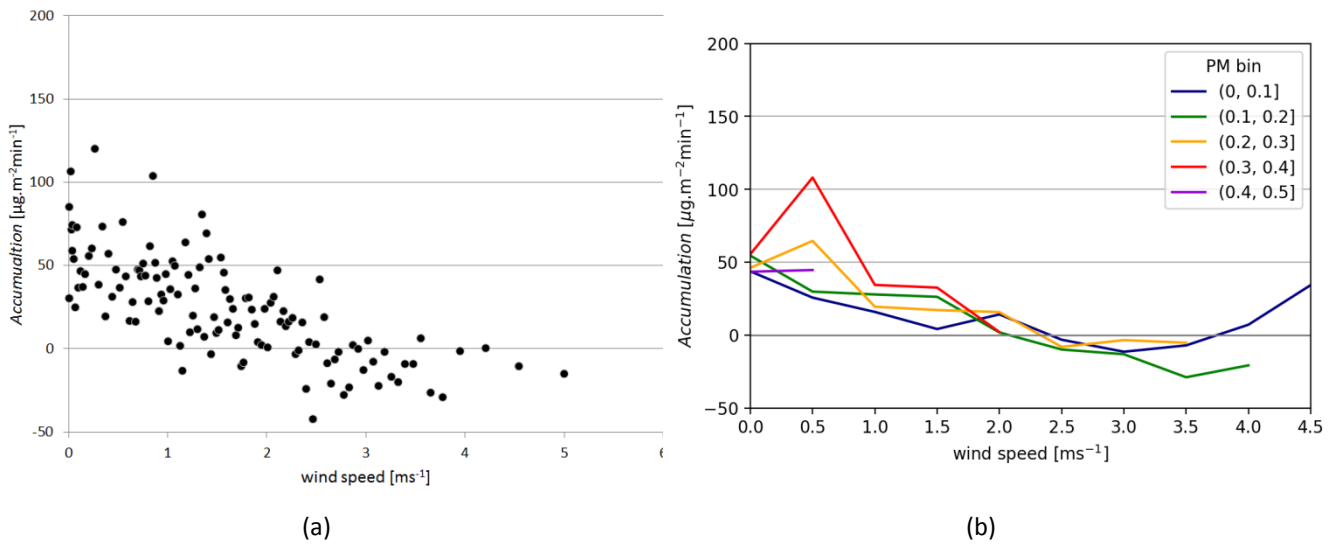


Figure 57. Effect of WS on Accumulation. (a) Observations binned by WS ($n = 50$) (b) Observations binned by WS and PM ($n \geq 20$)

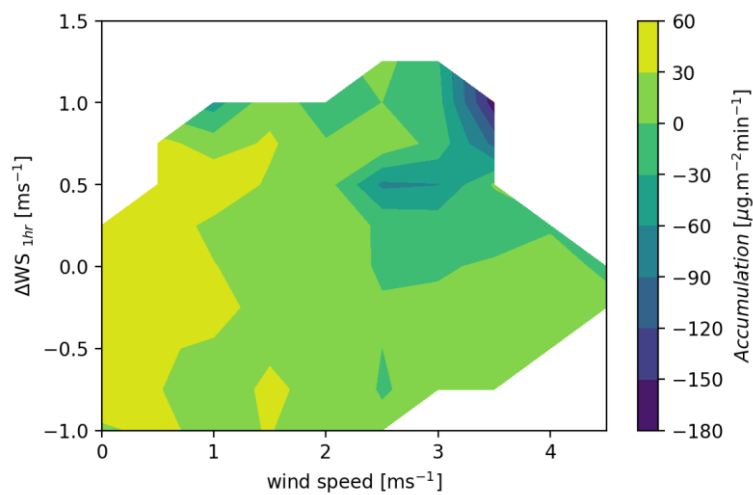


Figure 58. Relation between Accumulation, WS and $\Delta\text{WS}_{1\text{hr}}$. ($n \geq 5$)

The effect of RH on Accumulation is shown in Figure 59.a. A weak positive relation is observed, mainly explained by correspondence of low RH with high WS. When WS is kept constant (Figure 59.b), there is some sign that RH increases Accumulation when in $\text{WS} > \sim 2 \text{ ms}^{-1}$ (yellow and red lines), but not when WS is less than this (blue and green lines). It is speculated that this is because the particle-trapping effect of capillary condensation only becomes apparent when some removal force (i.e. wind) is present, however there is insufficient data to draw a firm conclusion.

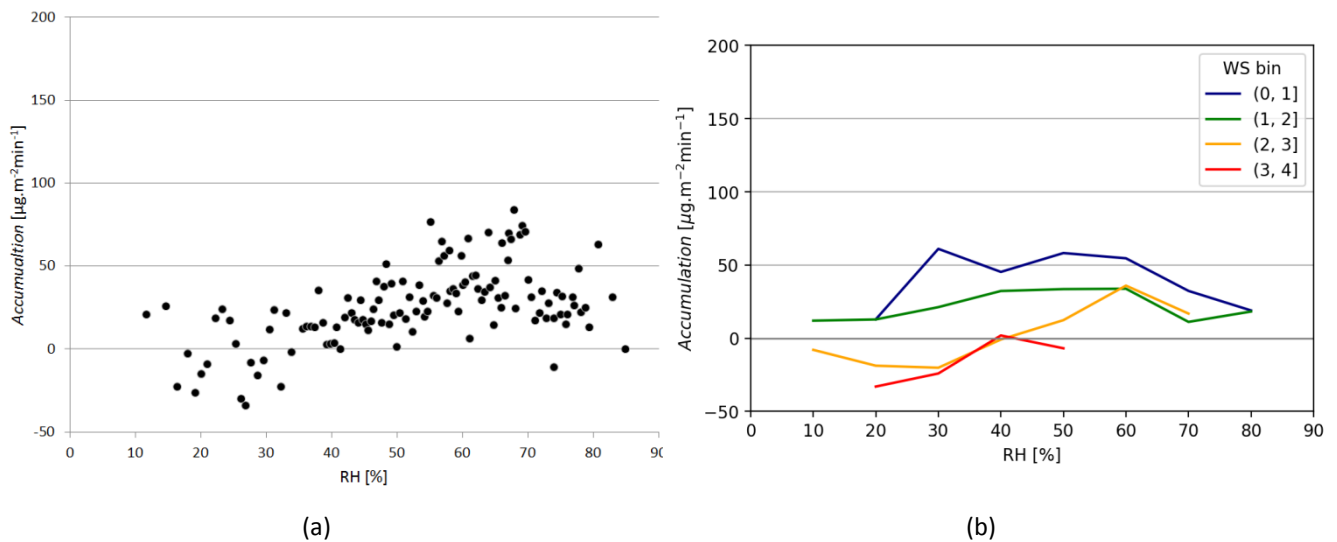


Figure 59. Effect of RH on *Accumulation*. (a) Observations binned by RH ($n = 50$) (b) Observations binned by RH and WS ($n \geq 20$)

Although PM was earlier seen to affect *Deposition* only when it reached extremely high concentrations of $\sim 1 \text{ mg}\cdot\text{m}^{-3}$, its influence on *Accumulation* was visible at lower concentrations. Figure 60.a shows a positive correlation between *Accumulation* and PM at all PM values, although with much scatter indicating influence of other parameters. Holding WS constant (Figure 60.b) reveals a scattered increase in *Accumulation* with PM, but the increase only became consistent when PM exceeded $\sim 0.2 \text{ mg}\cdot\text{m}^{-3}$. It is noted that this is quite a high PM value — for 81% of the experiment's duration PM was less than this. I.e. In usual weather conditions PM had little direct influence on the soiling rate, and it only became important in very dusty conditions ($> \sim 0.2 \text{ mg}\cdot\text{m}^{-3}$).

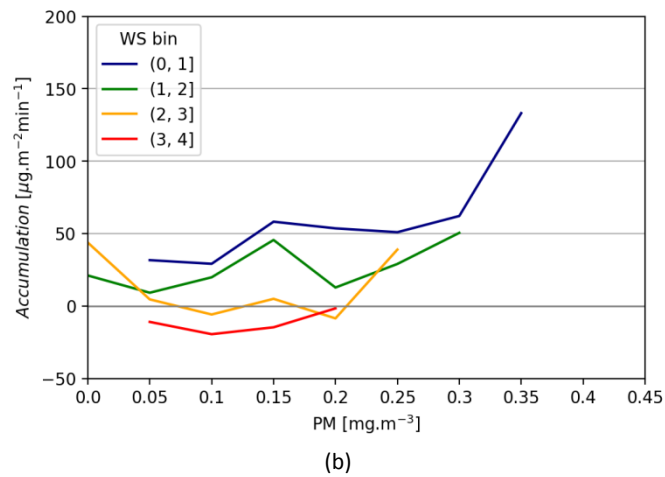
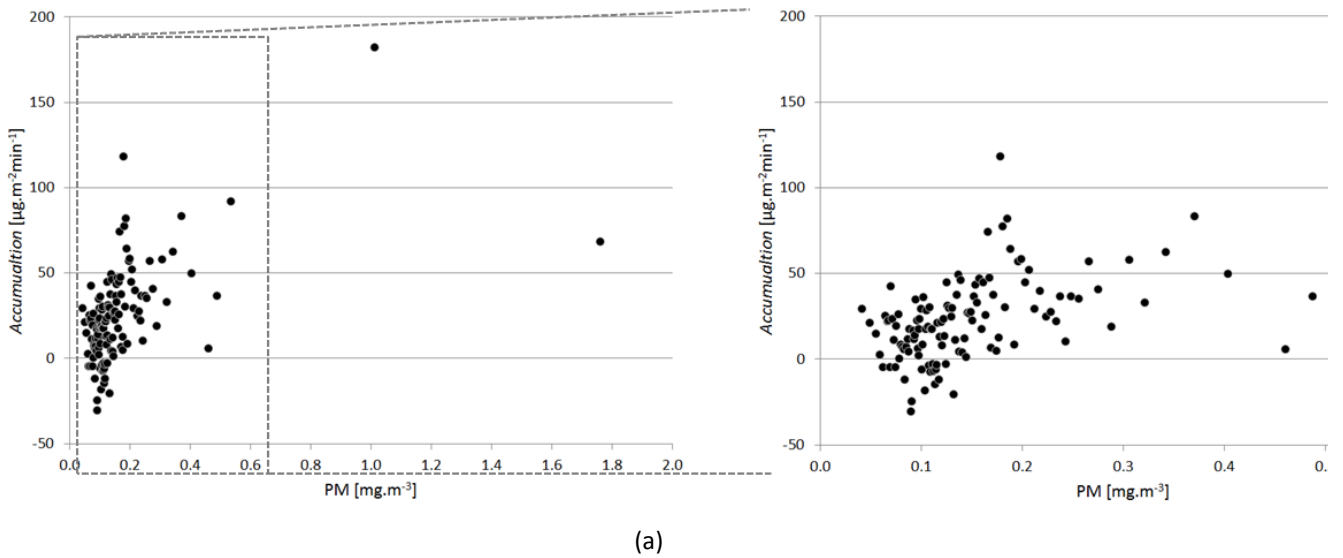


Figure 60. Effect of PM on Accumulation. (a) Observations binned by PM ($n = 50$) (b) Observations binned by PM and WS ($n \geq 20$)

6.5. Dust Flux Models

So far, relations between environmental parameters and dust fluxes have been qualitatively assessed. Next, quantitative models of dust flux rates are constructed using statistical methods. The goal of the models was to infer the nature and strength of relationships between predictor/independent variables (environmental parameters) and response/dependent variables (flux rates) — in other words, to quantify which environmental parameters most controlled the processes of ambient soiling.

6.5.1. Modeling Process

Multiple-variable models of dust flux rates were constructed via stepwise linear regression, following approaches described in Walpole et al. [179] and Tamhane & Dunlop [183]. Models took the form:

$$Y_i = \beta_0 + \beta_1 x_{1i} + \beta_2 x_{2i} + \dots + \beta_k x_{ki} \quad (47)$$

where Y is a dust flux rate (i.e. *Deposition, Relative Rebound, Relative Resuspension* or *Accumulation*); $x_1, x_2 \dots x_k$ are variables based on environmental parameters; and each i represents one observation (10-minute measurement period). The parameters $\beta_0, \beta_1 \dots \beta_k$ are estimated by least-squares fitting. As discussed in the preceding section, in some cases it was found that transforming predictor variables lead to improved correlation with response variables. E.g. Comparing Figure 52.a and Figure 54.a, *Relative Resuspension* appeared qualitatively to be more highly correlated with ΔWS_{1hr} (change in wind speed relative to the preceding hour) than absolute wind speed, hence this “transformed” variable was tested in the models.

Further, the possibility of interaction between environmental parameters was considered. E.g. In Figure 54b it appears that resuspension increases with ΔWS_{1hr} to a high degree when $RH < 40\%$, but to a low degree when $RH > 40\%$. Such interactions are incorporated into the regression model through product terms of the interacting variables:

$$Y = \beta_0 + \beta_1 x_1 + \beta_2 x_2 + \beta_3 x_1 x_2 + \dots \quad (48)$$

The approach used in constructing the model was stepwise regression based on techniques described in the mentioned texts. In essence, predictor variables (including transformations and products of environmental parameters) were successively added to the model until they made no further significant improvement to its predictive performance. Whether a predictor made a “significant improvement” was assessed statistically, using the F test on the quantity {increase in regression sum of squares / model mean square error} at the 5% level of significance. The approach is summarized in Figure 61.

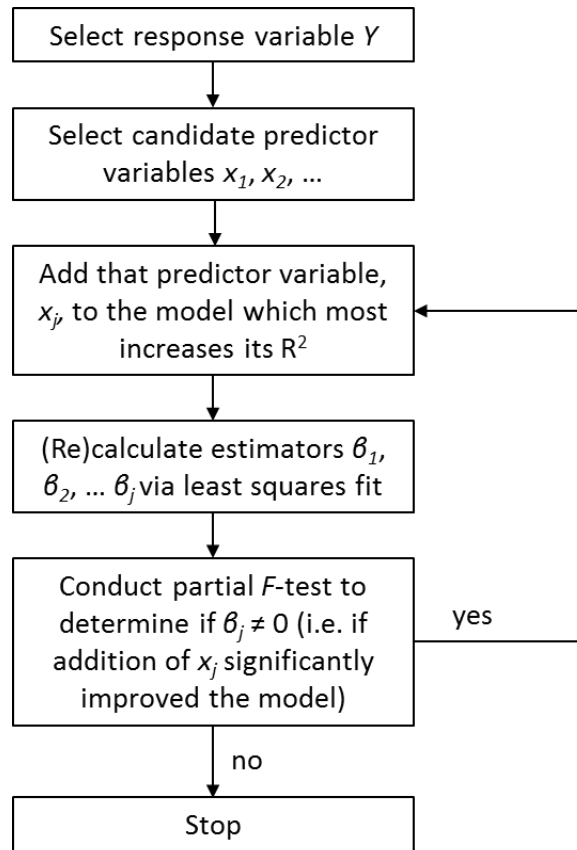


Figure 61. Process of stepwise addition of parameters used to construct dust flux rate models

6.5.2. Dust Flux Regression Models

Construction of the *Deposition* model is first described in detail as an example, with discussion of the methodology. Other flux-rate models were then constructed using the same method. Recall that units of measure of predictor variables in this report are: WS [ms^{-1}], RH [%], PM [$\text{mg}\cdot\text{m}^{-3}$], Exposure Time [hr].

— *Deposition* model

1. Candidate predictors were selected. Recall from section 6.4.1 that *Deposition* remained fairly constant until WS exceeded a certain threshold, and then increased linearly with WS. Therefore a synthetic variable of “supercritical wind speed”, $WS_{\text{supercritical}}$, was defined as follows:

$$WS_{\text{supercritical}} = \begin{cases} 0, & WS < WS_{\text{threshold}} \\ WS - WS_{\text{threshold}}, & WS \geq WS_{\text{threshold}} \end{cases} \quad (49)$$

where WS is the prevailing wind speed and $WS_{\text{threshold}}$ is the threshold wind speed. Linear regression of *Deposition* vs. $WS_{\text{supercritical}}$ showed that $WS_{\text{threshold}}$ was 3.2 ms^{-1} , which can be seen visually in Figure 42. Exploration of interactions indicated that there was significant interaction of RH and $WS_{\text{supercritical}}$ on dust deposition. The final set of predictors tested were WS , $WS_{\text{supercritical}}$, RH, PM, and $RH \cdot WS_{\text{supercritical}}$.

2. Single-variable linear regression models of *Deposition* were constructed, one for each of the candidate predictors. R^2 values of the models were: WS – 1.8%, $WS_{\text{supercritical}}$ – 6.3%, RH – 1.3%, PM – 2.0%, $RH \cdot WS_{\text{supercritical}}$ – 4.4%. Having the largest R^2 value, $WS_{\text{supercritical}}$ was the first variable added to the model
3. Two-variable linear regression models were constructed, comprising $WS_{\text{supercritical}}$ (denoted x_1 below) and one other variable (denoted x_2). The second variable producing the greatest increase in R^2 of the model was $RH \cdot WS_{\text{supercritical}}$. An F -test was performed on the significance of its parameter, β_2 , as follows:

$H_0: \beta_2 = 0$ in presence of x_1

$H_1: \beta_2 \neq 0$ in presence of x_1

$SSR(x_1, x_2) = 2.10 \times 10^7$ – regression sum of squares of model with both x_1 and x_2

$SSR(x_1) = 1.56 \times 10^7$ – regression sum of squares of model with only x_1

$SSR(x_2 | x_1) = 0.54 \times 10^7$ – contribution to SSR of x_2 in presence of x_1

$n = 6186$ – number of observations (sample size)

$k = 2$ – number of predictor variables included in the model

$SSE = 2.26 \times 10^8$ – error sum of squares of model with both x_1 and x_2

$s^2 = 3.66 \times 10^4$ – mean square error = $SSE / (n - k - 1)$

$F = 147$ – F statistic = $SSR(x_2 | x_1) / s^2$

$\alpha = 0.05$ – level of significance

$f_{1, n-k-1, \alpha} = 3.8$ – cumulative f distribution

$F > f_{1, n-k-1, \alpha}$ therefore reject H_0 and accept H_1

That is, β_2 was significantly greater than zero, and the addition of $RH \cdot WS_{\text{supercritical}}$ to the model significantly increased its explanatory power (relative to the loss of one degree of freedom of the model from adding another variable to it)

4. Three-variable regressions and tested in the same way as step 3. The most powerful third predictor variable was PM. The F statistic in this case — based on the SSR contribution of PM in the presence of both $WS_{\text{supercritical}}$ and $RH \cdot WS_{\text{supercritical}}$ — was 80.7. Again, this was much larger than the critical f value of 3.8 and hence its addition to the model was accepted
5. A four-variable regression model with the addition of RH was tested. The F statistic was 30.5, hence RH the addition was accepted

6. No further predictor variables were added because the only remaining candidate was *WS*, and the inclusion of closely-related variables (in this case *WS* and $WS_{\text{supercritical}}$) in a regression model is generally to be avoided
7. The final regression model of *Deposition* [$\mu\text{g}\cdot\text{m}^{-2}\cdot\text{min}^{-1}$] was as follows

$$Deposition = 96.3 + 624 WS_{\text{supercritical}} - 10.9 RH \cdot WS_{\text{supercritical}} + 125 PM - 0.792 RH \quad (50)$$

N.B. In this report, predictors appear in regression models in the sequence that they were added via the above process. I.e. From left to right, the predictors were decreasingly powerful.

The R^2 value of the model was 10.1%.

Compared to models of other dust fluxes, the *Deposition* model accounted for a large amount of observed variation (10.1%). That is, dust deposition rate is more predictable (by environmental parameters) than rebound or resuspension rates. This is expected, because deposition is independent of surface properties (it was measured from the gross number of particles impacting the greased coupon), whereas rebound, resuspension and accumulation rates are all influenced by the degree of particle adhesion to the (ungreased) surface.

The *Deposition* rate was overwhelmingly governed by “supercritical” wind speed, i.e. the amount by which wind speed exceeded the threshold of 3.2 ms^{-1} . There was significant interaction of this parameter with RH on the deposition rate. There were weak but statistically significant correlations of deposition with PM and (negatively) RH. These inferences from the regression models complement the qualitative observations from section 6.4.1.

— *Rebound* model

The candidate predictors chosen for *Relative Rebound* were *WS* and RH. As discussed in section 3.2, particle rebound is generally reported to be governed by airflow velocity, with some tendency for humidity to suppress it. The fraction of particles to rebound should be independent of their abundance in the atmosphere, hence PM is not explored as a candidate variable.

The final regression model for *Relative Rebound* [dimensionless] was:

$$Relative\ Rebound = 0.395 + 0.0998 WS \quad (51)$$

The R^2 value of the model was 7.0%, which is moderate compared with the other flux rate models in this study. Neither RH nor RH.WS, when added to the above model, explained a significant amount of rebound variation. The regression

model confirmed the qualitative observation (section 6.4.2) that dust rebound fraction was essentially governed by wind speed alone.

— *Resuspension model*

Predictor variables considered for *Relative Resuspension* were: WS, ΔWS_{1hr} , RH and Exposure Time. It was found that all these variables explained a statistically-significantly amount of resuspension variation when added sequentially to the model. The final regression model of *Relative Resuspension* [min^{-1}] was:

$$\text{Relative Resuspension} = 1.45 \times 10^{-3} - 1.70 \times 10^{-5} RH + 1.47 \times 10^{-3} \Delta WS_{1hr} - 1.56 \times 10^{-5} RH \cdot \Delta WS_{1hr} \quad (52)$$

The model reinforces the qualitative results reported in section 6.4.3, i.e. dust resuspension from the glass coupon was most strongly governed by RH and change in wind speed. Compared to other flux rate models, the *Relative Resuspension* one accounted for a small amount of observed variation (1.7%), indicating it is a complex phenomenon influenced by many factors. This is not surprising, given the unpredictability and strong influence of adhesion forces on dust resuspension.

Acceptance of Exposure Time in the *Relative Resuspension* model (at the 5% level of significance) is noteworthy in the context of a comment in 2000 by Loosmore & Hunt [16]: “The dust fluxes from direct wind resuspension will depend on the time of exposure and potentially on the exposure history. These issues have not been addressed by the models”. That is, the OSM’s ability to measure soiling in fine time intervals, and separate deposition from detachment, help achieve an earlier-recommended goal to empirically model dust resuspension as a function of Exposure Time in ambient conditions.

— *Accumulation model*

The above regression models of the component dust fluxes showed that *Relative Resuspension* was better explained by ΔWS_{1hr} than absolute WS, because dust particles tend to detach from the surface only when the wind speed increases. On the other hand, particle deposition and rebound in principle have no connection to change in wind speed, only its absolute value. It is of interest — and not obvious — whether the net dust accumulation rate is better explained by WS or ΔWS_{1hr} . Because they are not expected to be strongly codependent (changes in wind speed will be of smaller magnitude when wind speed is low, but otherwise unrelated) both were included as candidate predictors in the *Accumulation* model. Also tested were PM, RH, Exposure Time, $WS_{\text{supercritical}}$ and the interaction parameters WS.PM and WS.RH.

The final regression model for *Accumulation* [$\mu\text{g} \cdot \text{m}^{-2} \cdot \text{min}^{-1}$] was:

$$Accumulation = 10.6 - 4.99 WS + 247 PM - 73.4 WS \cdot PM - 14.9 \Delta WS_{1hr} \quad (53)$$

The R^2 value of the model was 5.2%, which is less than that of the *Deposition* model and greater than that of the *Relative Resuspension* model. *WS* had the greatest influence on *Accumulation*, its individual R^2 value of 2.6% was much larger than that of the other individual predictors. Surprisingly, $WS_{supercritical}$ alone explained little variation of *Accumulation* (0.4%) despite dominating the *Deposition* model. The interaction parameter *WS*·*PM* made a highly statistically-significant improvement to the model's explanatory power, despite the apparent absence of such interaction in Figure 57.b.

6.5.3. Discussion of Modeling Approach

Comments on the modeling process and statistical analysis are as follows.

- Random component

R^2 values of models were small, due to stochastic observations. For example, only 10.1% of the variation of *Deposition* was accounted for by its regression model, and ~90% was due to other factors (principally randomness). However this does not indicate an absence of physical influence of environmental conditions. Rather, it reflects the inherently stochastic distribution of observations when measuring dust particles settling on a surface area of only ~4 mm² in the time-span of minutes. This is evident in the histogram of *Deposition* measurements (Table 6, page 99), which shows that in the great majority of 10-minute observation periods no particles deposited onto the surface. Only occasionally was a non-zero measurement recorded.

Because data was stochastic and responses non-linear, it is essential to consider the qualitative relations between dust fluxes and environmental parameters, in addition to the explained variation of the regression models (their R^2 value). For example, the plot of *Deposition* vs. *WS* in Figure 42.a (page 102) — in which each data point is an average of 50 observations — shows a strong and non-linear relationship between the variables. Yet the R^2 value of the linear estimator between the same variables (using all 6186 individual observations) was just 1.8%. It is to be kept in mind that the main purpose of regression modeling in this study was to statistically quantify which environmental parameters had the *most influence* on dust fluxes (explained the greatest amount of variation), rather than predict the amount of soiling in arbitrary weather conditions.

- Predictor effects were weak but statistically significant

The large sample size (6186 ten-minute periods) means that although the predictive power of the environmental parameters is small, their effects are often statistically significant. For example, in the above exposition of *Deposition*

model construction, the addition of RH to the model in step 5 increased its R^2 value by just 0.4% (from 9.7% to 10.1%). Yet because of the large sample size, this increase was highly statistically significant: the F statistic was 30.5 which corresponds to a p value of just 3.4×10^{-8} . That is, although the OSM technique inherently yielded stochastic measurements and thus low R^2 values, it also yielded large sample sizes which rendered those weak relations statistically significant. It is expected that increasing the magnitude of dust measured — e.g. by increasing the surface area surveyed [77] or time interval between images — would produce more consistent dust flux measurements and thus increase correlation with predictors. (Increasing the time interval, however, would defeat a main purpose of this study which was to measure dust fluxes in the same timescale as changes in weather conditions).

— Judgement was needed to avoid addition of excess predictors

The stepwise model-construction process is designed to prevent over-fitting of predictors to the model, by “punishing” the loss of degrees of freedom of the error residuals ($n - k - 1$) every time a predictor is added (k increases by 1). However when the sample size is very large, as in the present case ($n = 6186$), $k \ll n$ and there is effectively no punishment to adding predictors. This is conceptually correct, because the predictive power of the model is not diminished by the predictor’s addition, as it would be if n and k were of similar magnitude. However, the goal of the present study is determine how dust flux rates are influenced by environmental parameters, and therefore one seeks to identify the *most* influential parameters. Accordingly, judgment was used when adding parameters to the flux rate models, rather continuing until H_0 was accepted (which was rare because of the large n).

As mentioned, judgment was also applied in the selection of the candidate predictor variables, so that those which could not conceivably have a physical effect on the dust flux response were excluded. E.g. the fraction of particles to rebound from a surface should be independent on their airborne concentration, hence PM was not a candidate predictor of *Relative Rebound*.

6.5.4. Prediction Evaluation

The above models of dust flux rates were constructed for inferential purposes — to determine how environmental conditions affect dust accumulation, and the relative strengths of those effects. Having constructed the models, their predictive performance can also be tested.

The predictive performance of the *Accumulation* model, eq. (53), was assessed. This model alone was tested because it represents the overall soiling of the surface, and the data set used to the test the model did not employ a greased coupon and hence could not be used to measure most other flux rates.

As noted the stochastic nature of measurements, inherent in the OSM technique, resulted in low R^2 values of the flux rate models. The random component of the measurements could be reduced (and their predictability increased) if they

are aggregated over an extended time. For the model-prediction analysis, it was decided to aggregate (sum) *Accumulation* measurements over 24-hour periods.

The method used to assess the model was as follows.

- 1) In order to have separate “training” and “testing” data-sets for the model, a separate set of OSM measurements was obtained to test the model. These were the 2550 observations from the glass coupon in Part III of this study (section 7.1.7). I.e. the 6186 observations (51-day test) from Part II were used to train the model, and the 2550 observations (23-day test) from Part III were used to test it. The rest of this section refers to the testing data-set
- 2) For each ten-minute period, the predicted *Accumulation* was calculated from eq. (53) based on the measured environmental parameters. These predictions are referred to as *Model Accumulation*, and the experimentally-measured amounts as *Actual Accumulation*
- 3) *Model Accumulation* and *Actual Accumulation* values were each summed over 1-day periods, of which there were 24 in the data set. The sums are respectively termed *Model Daily Accumulation* and *Actual Daily Accumulation*, and their units are $[\text{mg}\cdot\text{m}^{-2}]$.

The comparison of predicted and actual daily dust accumulation is shown in Figure 62. A weak positive correlation is seen, indicating that at a broad level the model captured the influences of environmental conditions on coupon soiling. However there are notable flaws in the model: (i) It systematically underestimated dust accumulation, by a large degree. (ii) On several days the model predicted negative accumulation, whereas the actual daily accumulation was always positive.

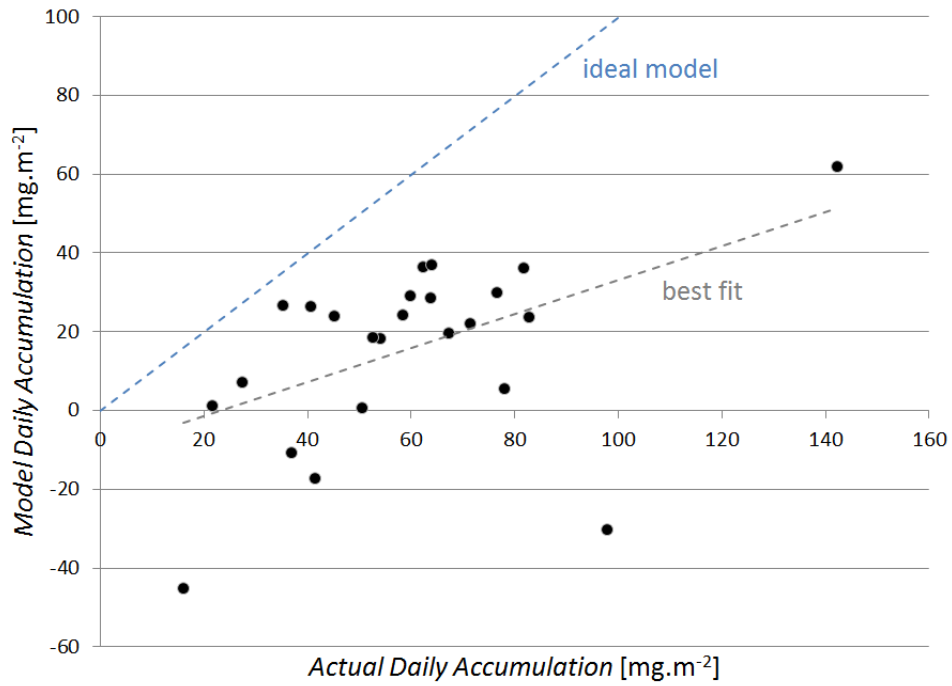


Figure 62. Model Daily Accumulation vs. Actual Daily Accumulation, aggregated into 24-hour periods. The model systematically under-estimated the amount of daily dust accumulation

To further explore the model performance, all 2550 *Model Accumulation* and *Actual Accumulation* data points (as opposed to their 24 daily aggregates) were plotted, Figure 63. It is seen that *Actual Accumulation* periods greater than $\sim 50 \mu\text{m.m}^{-2}.\text{min}^{-1}$ could not be distinguished by the model, i.e. heavier deposition events seemed to be random and not predicted by weather conditions.

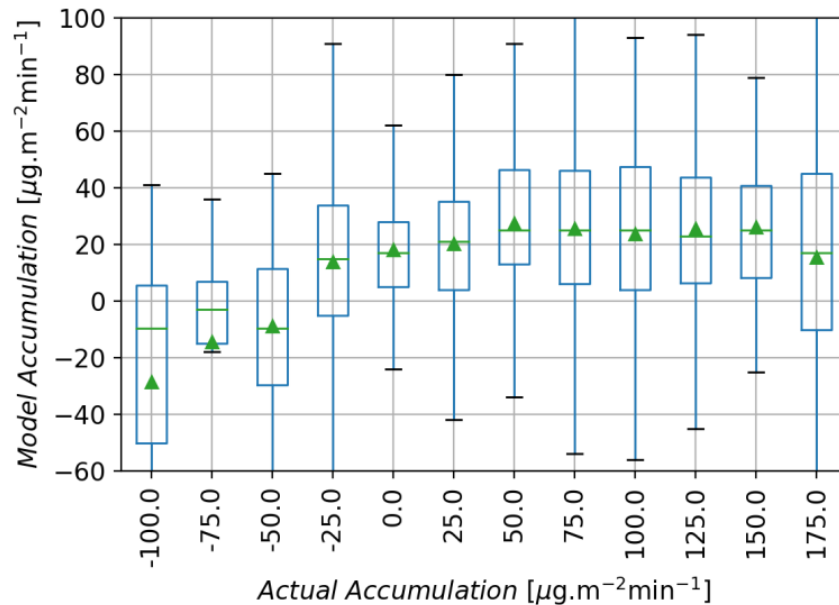


Figure 63. *Model Accumulation vs. Actual Accumulation*, not aggregated (i.e. all 2550 ten-minute periods). The model especially failed to predict moments of heavy soiling

Recall that in the exercise above, the *Accumulation* model was “trained” with data from Part II of the study (conducted in August-November 2016), and “tested” with data from Part III (conducted May-July 2017). It was speculated that part of the reason for the model’s under-estimation of soiling might be due to different atmospheric conditions between these seasons. To investigate this, the model was next “re-trained” with the May-July 2017 data-set, and tested against that data-set (i.e. same training and testing data). Obviously one would expect greater prediction accuracy by doing so, but it is still instructive to observe the effect on the model’s performance. The results are plotted in Figure 64. It is seen that in this case, the model’s predictions much better fit the actual observations (compared to Figure 62), and there was only one severe outlier.

This suggests that outdoor dust deposition was significantly influenced by atmospheric conditions other than WS, RH and PM. It is speculated that wind direction may have been such a factor, because WS was measured at the site’s weather station which was ~50 m from the soiling collector. Although the soiling collector was horizontal, and therefore supposedly independent of wind direction, possibly the wind velocity and turbulence at the collector varied with wind direction (for the same WS) due to disturbance by nearby structures such as cabins and PV rows. This theory is supported by wind-rose plots for the two test periods, which show somewhat different distributions (Figure 65).

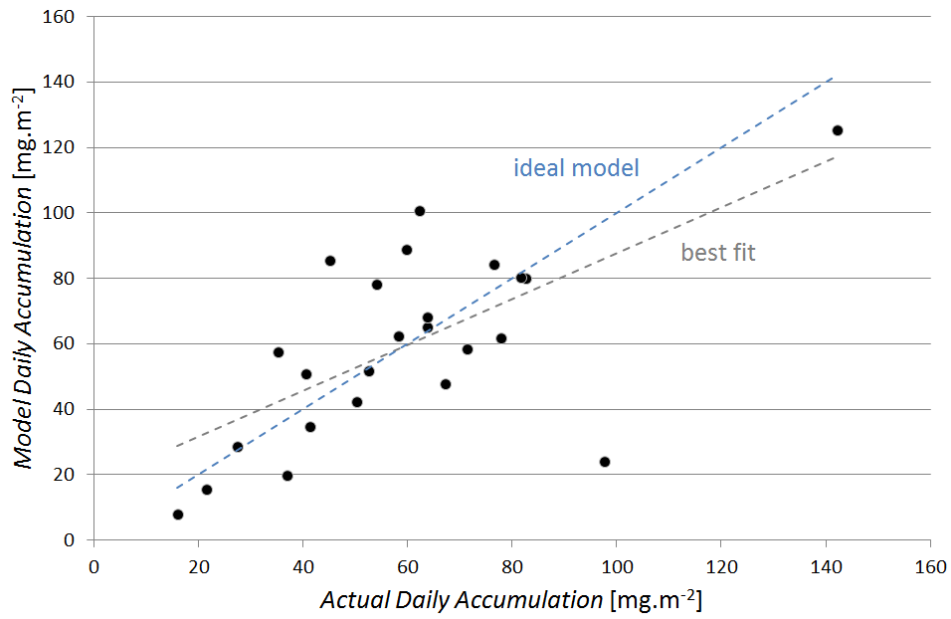


Figure 64. Model Daily Accumulation vs. Actual Daily Accumulation. In this case, the Accumulation model was trained and tested on the same dataset (May-Jul. 2017)

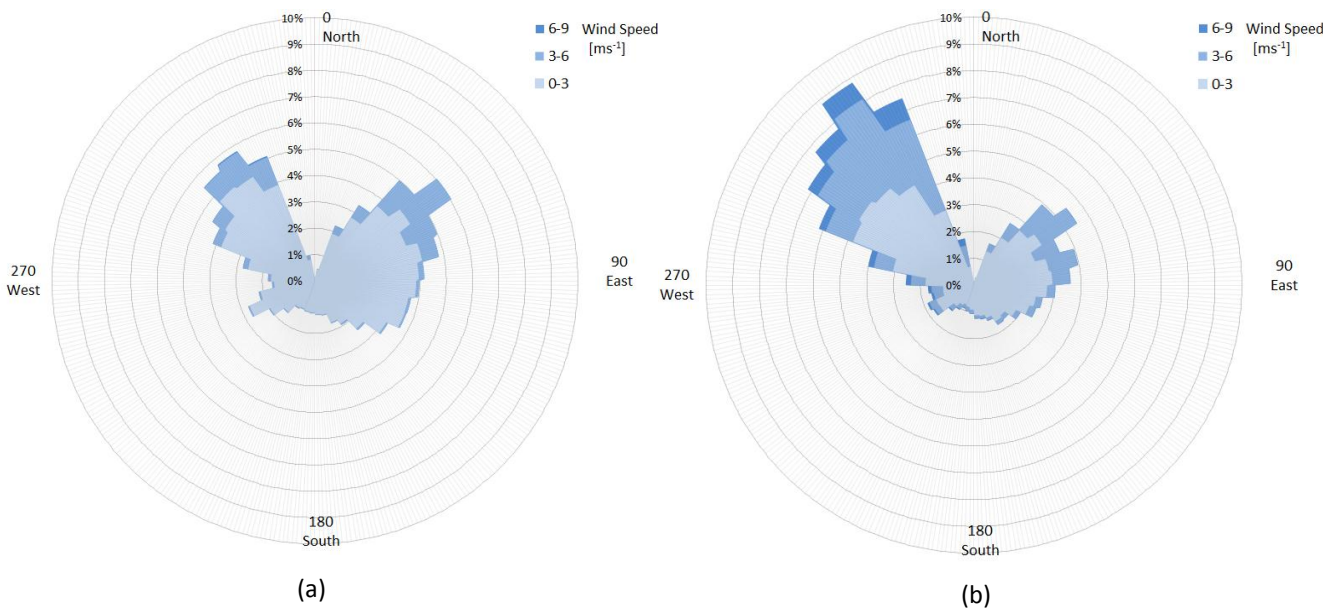


Figure 65. Wind speed and direction at the STF test site for (a) Aug.-Nov. 2016 (used for model training) and (b) May-Jul. 2017 (used for model testing)

7. Part III – Condensation Causes and Effects

The literature review and experimental flux-rate results of the last chapter showed that moisture profoundly affects surface soiling even in desert environments. To recap, previous studies from the laboratory and field showed that:

- Capillary forces dominate particle adhesion when moisture is present
- Rebound and resuspension of dust particles are inhibited by capillary condensation
- PV soiling is more severe in conditions of high humidity

In this study, OSM measurements of component flux rates at the Solar Test Facility in Qatar showed that higher RH inhibited particle *Resuspension* but not *Rebound*, and it influenced the overall *Accumulation* rate only in windy conditions.

The review of factors affecting condensation (chapter 4) showed that few studies have addressed condensation on surfaces which are already soiled, which is obviously the case for PV modules in the field. That is, the exact conditions under which condensation forms on dust-laden surfaces are not fully established.

In this part of the study, experiments are reported which aimed to investigate condensation on soiled surfaces in desert environments. Four parameters were investigated: RH, surface/dew point temperature difference (T_{S-DP}), hygroscopic content of the dust, and surface wettability. Natural and synthetic dust mixtures of various compositions were studied via water adsorption isotherms, XRD, ion chromatography and optical microscopy. Controlled experiments were conducted by varying surface properties (hydrophilic vs. hydrophobic, heated vs. unheated), in the lab and field. Because many experiments were carried out it is helpful to summarize them, see Table 7.

Parameter Investigated	Experiments	Equipment
Relative humidity (RH)	Water adsorption isotherms of natural dust	Vapor adsorption machine
	Surface droplet growth of natural dust (lab and field)	Outdoor soiling microscope Humidity chamber with microscopes
Surface–dew point temperature difference (T_{S-DP})	Surface droplet growth of natural dust (field)	Outdoor soiling microscope
	Dust accumulation on heated vs. unheated surfaces (field)	Outdoor soiling microscopes pair
Hygroscopic material	Dust composition analysis	XRD, ion chromatography
	Water adsorption isotherms of natural vs. treated dust	Vapor adsorption machine
	Surface droplet growth of natural vs. treated dust (lab)	Humidity chamber with microscopes
Surface wettability	Surface droplet growth on glass vs. PTFE surfaces (field)	Outdoor soiling microscopes pair

Table 7. Summary of experiments performed to investigate condensation of soiled surfaces

7.1. Experiments

7.1.1. Preparation of Natural Dust Samples

Dust was collected from PV modules (at 22° tilt) at the Solar Test Facility in Qatar in August 2016. The modules had been exposed for approximately one month without cleaning. A metal scraper was used which removed the full depth of the dust layer. Approximately 200 ml was collected. This is referred to as the Raw Sample.

Approximately 50 ml of the Raw Sample was placed in a tall plastic vessel, to which approximately 1.5 l of purified water was added and agitated (Figure 66). The mixture was allowed to settle for one day, resulting in a layer of sediment (slurry) and a semi-opaque yellow-brown solution (supernatant) above it. Without disturbing the sediment, the supernatant was siphoned off and dried in a glass vessel on a heating pad, resulting in a mass of orange flakes named the Soluble Part.

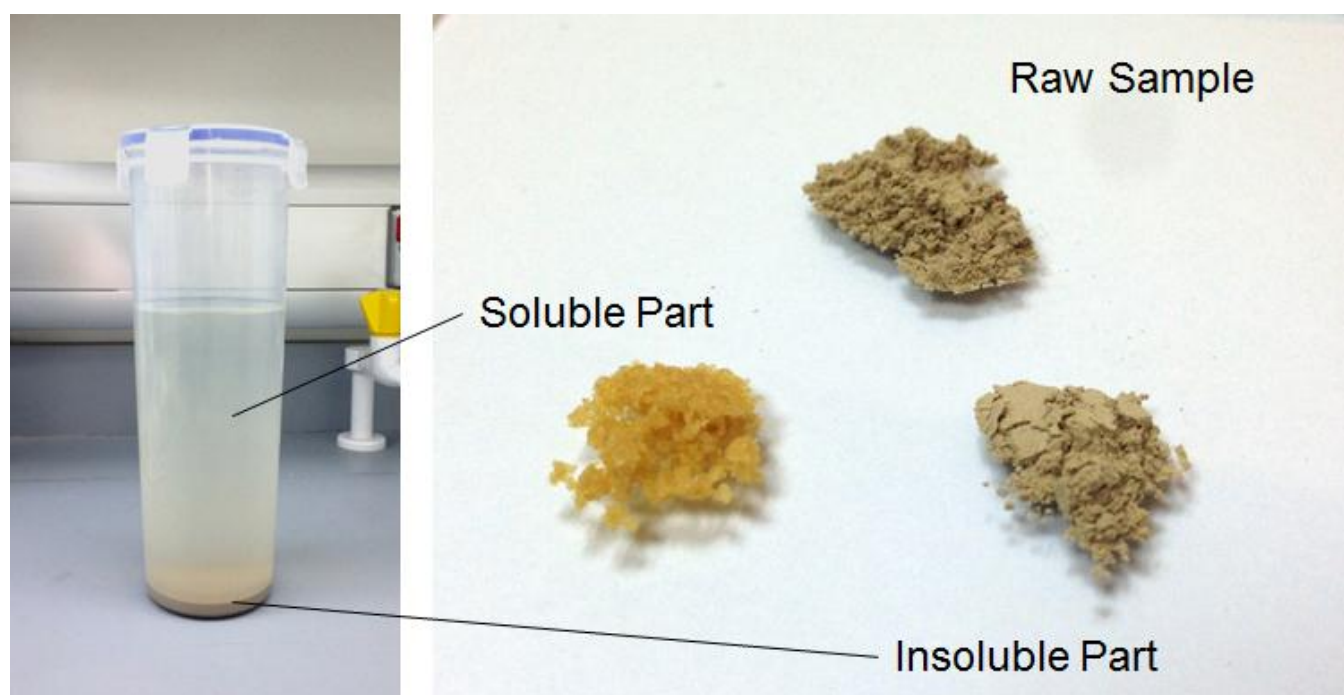


Figure 66. Soil collected from PV modules (Raw Sample) formed a slurry and supernatant in water (left). These were separated and dried to yield Insoluble and Soluble Parts (right).

The sediment was “washed” another five times (i.e. ~1.5 l of purified water added, allowed to settle, supernatant siphoned off, but these times the supernatant was discarded). On each washing the supernatant become progressively more opaque, until after five washings no distinct sediment layer formed, rather there was a gradual decrease in

opacity from bottom to top of the vessel. This entire mixture was dried in a glass vessel on a heating pad, yielding a grey-brown powder named the Insoluble Part.

7.1.2. Preparation of Synthetic Dust Samples

A synthetic approximation of natural Qatar dust was prepared using pure calcite, silica, gypsum, kaolinite and halite. Its purpose was to determine if these five species accounted for the hygroscopic behavior of natural dust, or if other trace materials were also important. The components and their proportions were based on an earlier analysis of dust at the same site by Javed et al. [30]. Calcite was chosen as the proxy for the carbonate content (calcite and dolomite), and kaolinite was the proxy for the clays (kaolinite, palygorskite and albite).

The following powders were obtained from Sigma Aldrich: silica fumed 99.8% (cat. 381276); calcium carbonate ReagentPlus® (cat. C6763); calcium sulfate (gypsum) 325 mesh 99% (cat. 237132); natural kaolinite (cat. 03584); sodium chloride (halite) ≥99.5% (cat. 31434). Quantities of each powder were weighed with a microbalance and combined to produce two samples of dry powder, one with all five compounds named the Synthetic Sample and one omitting halite named S.S. Minus Halite. Their compositions by weight are shown in Table 8.

Compound	Synthetic Sample (% weight)	S.S. Minus Halite (% weight)
Calcite	72.4	73.5
Silica	12.1	12.4
Gypsum	7.5	8.0
Kaolinite	5.9	6.1
Halite	2.0	-

Table 8. Composition of synthetic dusts as prepared

Dusts generated in wet conditions tend to be more hygroscopic than dry-generated equivalents [164]. Therefore to attempt to simulate the properties of natural dust, the two synthesized mixtures were each combined with purified water to form slurries, which were then dried in a glass vessel over low heat, and finally ground with a metal spatula into a fine powder. The two mixtures were white whereas as the Raw Sample was light brown, indicating there were additional species in the Raw Sample (beyond the four or five that were used in the synthetic mixtures). Aerosol particles generated from the synthetic mixtures were similar in size to those from the Raw Sample, as revealed by microscope images of deposited aerosol (Figure 75), which provided confidence for their use (i.e. their size resembled that of natural dust).

A summary of dust samples used in the experiments is provided in Table 9.

Sample	Description	Main Hygroscopic Species
Raw Sample	Natural soiling layer collected from PV modules in Doha, Qatar	Salts, nitrate, sulfate, nitrite
Soluble Part	Portion of the Raw Sample that dissolved or suspended in water	Salts, nitrate, sulfate, nitrite
Insoluble Part	Portion of the Raw Sample that did not dissolve or suspend in water	None
Synthetic Sample	Artificial dust mixture prepared with four mineral dusts plus NaCl	NaCl
S.S. Minus Halite	Same as the Synthetic Sample but without NaCl	None

Table 9. Summary of dust samples used in this study

7.1.3. Composition Analysis

Chemical compositions of the Raw Sample, Soluble Part and Insoluble Part were determined by XRD and ion chromatography by the Central Materials Facility at Texas A&M University at Qatar. A Rigaku Ultima IV Multipurpose X-ray Diffractometer (Rigaku Corp., Tokyo, Japan) equipped with cross beam optics, graphite monochromator and a scintillation counter was used to collect XRD patterns. The Cu-K α radiation source operated at 40 kV and 40 mA. The XRD data were collected in the 2 θ range of 3 to 90 degree with continuous scan mode and step width of 0.02 degree and 1 degree/minute scan speed. An integrated Rigaku PDXL2 software then used for data treatment and phase analysis.

Initially the Soluble Part was analyzed without pre-treatment and produced irregular XRD data. The flakes were thought to have absorbed a significant amount of water, given their known soluble nature. The sample was then dried in a Quincy lab oven at 70 °C for 12 hours, and this time produced reliable XRD data.

Ion chromatography was performed on a second Soluble Part sample to identify soluble species that did not crystallize upon drying and thus were not detectable by XRD. The chromatograph was a Dionex ICS-5000 device equipped with dual gradient pump, AS auto-sampler, AS19 separation column, ASRS 300-2mm suppressor and eluent generator. The mobile phase was 4.5 mM Na₂CO₃ / 0.8 mM NaHCO₃ aqueous solution at a constant flow rate of 0.25 ml min⁻¹. Because all supernatant solution of this second sample was preserved, and the mass of the raw dust used to prepare it was measured, it was possible to determine the percentage mass composition of the ions in the raw dust.

7.1.4. Vapor adsorption isotherms

Water vapor adsorption isotherms were measured the Laboratory of Engineering Sciences for the Environment (LaSIE) at the University of La Rochelle, France. The instrument used was a Belsorp Aqua3 device (Figure 67). The device can analyze isotherms from 0% RH to 98%. It uses a constant volumetric method to measure water vapor adsorption of samples.

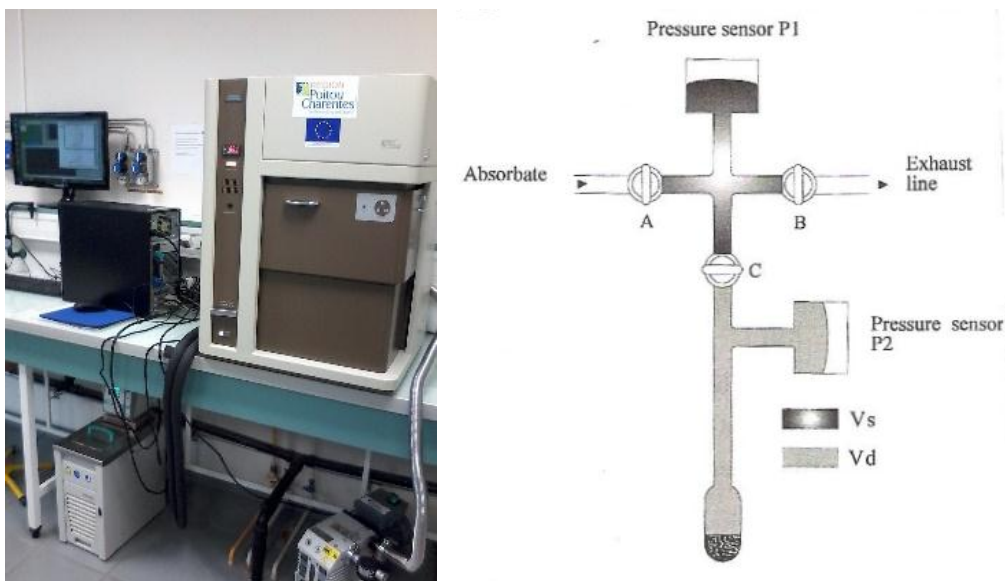


Figure 67. Left: Belsorp-Aqua3 device. Right: Schematic diagram of operation

The device's operation is described by Mme. Armelle Nouviaire of the laboratory as follows, with reference to the schematic diagram in Figure 67.

There are three measurement ports. The reference volume buffer V_s and each of three measurement ports V_d are equipped with a pressure sensor. V_s is specific to each instrument and V_d is assessed for each sample using diffusion of helium gas (helium adsorption is considered negligible). During the analyses, a calibrated quantity of vapor is introduced in V_s and then in V_d by opening valve C. The amount of water vapor adsorbed by the sample is calculated from the gas pressure change in the measurement system, using the gas state equation.

Isotherms were performed at 23 °C, maintained by a water bath with thermostat. Samples were pretreated by removing gas and moisture adsorbed on the surface without denaturalizing the material. Samples are first dried in a fanned convection oven at 30°C during 72 h. Then, about 1 g of each sample was placed in a test tube and dried under vacuum at 23 °C for 48 hours using a Vacprep device (Micromeritics, France). Finally, samples were weighed to measure their dry mass. This mass was used to calculate the water adsorbed content relative to the sample's dry mass (g water / g dry sample) at each point of the isotherm.

Isotherms were measured of the Raw Sample and Insoluble Part. It was assumed that the Soluble Part was mainly hygroscopic material and not suitable for isotherm measurement. For each sample a preliminary test was performed with only adsorption curve (RH increasing) to monitor their evolution and adjust the precision of the device. A second measurement, on another specimen on the sample with adsorption and desorption curves (RH decreasing), giving the complete isotherm and assessing the reproducibility.

7.1.5. Ambient Surface Droplet Growth

In this part of the study, instead of using outdoor soiling microscopes (OSMs) to record deposition and detachment of dust particles on the coupon, they were used to record nucleation and growth of condensation droplets. Note that droplets in this analysis were only a few microns to hundreds of microns wide, i.e. before dew was visible to the naked eye.

Two OSMs were installed side by side at the STF (Figure 2). One had a 5x5 cm borosilicate glass coupon as the work piece (“glass coupon”). The other had a similar coupon to which was attached a piece of transparent PTFE (Teflon®) one-sided adhesive tape (“PTFE coupon”). When cleaned the water contact angle on the glass coupon was measured to be $11 \pm 2^\circ$, and when freshly prepared the angle on the PTFE coupon was $87 \pm 3^\circ$.

OSM images were taken every 10 minutes. ImageJ software was again used to measure the projected areas of condensation droplets, as well as any dust particles present. Area measurements less than $10 \mu\text{m}^2$ (either droplets or dust particles) were discarded as this was the resolution limit of the apparatus, as described previously. Analyzed images were manually checked to ensure the software had correctly detected droplet edges, and corrected it when needed. Condensation was characterized by the projected area of droplets rather than their volume. This was because edges of droplets sometimes remained “pinned” in place on the surface as the droplet grew and shrank (condensed and evaporated), preventing estimation of the droplet’s contact angle and hence its volume. Also, from the perspective of light transmission through the surface (which is ultimately of interest in the case of PV), the proportion of surface area covered by droplets (which trap dust) is more relevant than their volume.

RH and ambient air temperature were measured as described in section 6.1. The temperature of the OSM coupons, T_S , could not be measured directly with existing equipment. To estimate T_S , a surrogate coupon identical to that used on the OSMs (5x5 cm borosilicate glass) was mounted ~25 m away from the OSM stand, also in horizontal orientation, with a PT1000 thermometer (accuracy 0.4%) adhered to its underside. Its temperature was recorded every minute. The surrogate coupon may have been at a slightly different temperature than the OSM coupons because of the thermal mass of the microscopes attached to the latter.

Dew point temperature T_{DP} was calculated using the Magnus formula:

$$\gamma = \ln(RH/100) + \frac{bT}{c + T} \quad (54)$$

$$T_{DP} = \frac{c\gamma}{b - \gamma} \quad (55)$$

where T is air temperature ($^\circ\text{C}$), $b = 17.67$ and $c = 243.5 \text{ }^\circ\text{C}$.

The surface/dew point temperature difference was calculated as $T_{S-DP} = T_S - T_{DP}$.

7.1.6. Laboratory Surface Droplet Growth

Measuring droplet growth in ambient conditions, as described above, is useful because it reveals real-world behaviors. However: dust composition on the coupons could not be controlled, wind could interfere with droplet size, only a limited (natural) RH range could be achieved, and the coupon and air temperatures could differ, all of which make it difficult to isolate the separate effect of any particular variable. Hence the ambient condensation observations were supplemented with laboratory experiments using controlled humidity chamber.

A purpose-built humidity chamber was constructed to study —in isolation — the effects on condensation of (i) dust composition and (ii) RH. It is shown in Figure 68. The chamber was designed to achieve identical test conditions for different dust samples, hence pairs of samples were tested simultaneously side-by-side. In order to approach thermal equilibrium (i.e. matching surface and air temperatures) the chamber was separated into vertical halves using a horizontal glass plate, which doubled as the soiling surface. The chamber comprised a rectangular glass box 20 cm high X 20 cm long X 10 cm wide, with all walls and the separation plate being 4mm float glass. Two microscopes like those used in the OSMs were attached to the underside of the separation plate, facing up, which captured images of dust and condensation on its upper surface every six minutes. LED backlights were positioned ~50 cm above the chamber, so they did not heat it. Dust samples were deposited by tapping a bulk quantity of the powder from a height of ~20cm above the separation plate, which allowed particles to drift down to the plate in a simulation of natural deposition. Air temperature and RH of the upper chamber were recorded every minute with an Extech Instruments RHT10 device, and air temperature of the lower chamber was recorded every minute with an Elitech RC-5 device. These two thermometers were calibrated against each other to provide accurate temperature-difference measurements. It was found that difference in air temperature between the chambers was almost always less than 0.5 °C. Thus the system was not in perfect thermodynamic equilibrium, but it was still useful for investigating the effects of dust composition and RH. After allowing the upper and lower chamber temperatures to equilibrate, water vapor was slowly introduced to the upper chamber by evaporation from a wick which drew purified water from an external container. The rate of increase of RH depended on test conditions, but as an example when the starting RH was 40%, RH in the chamber reached 70% after 50 minutes and 90% after 5 hours.

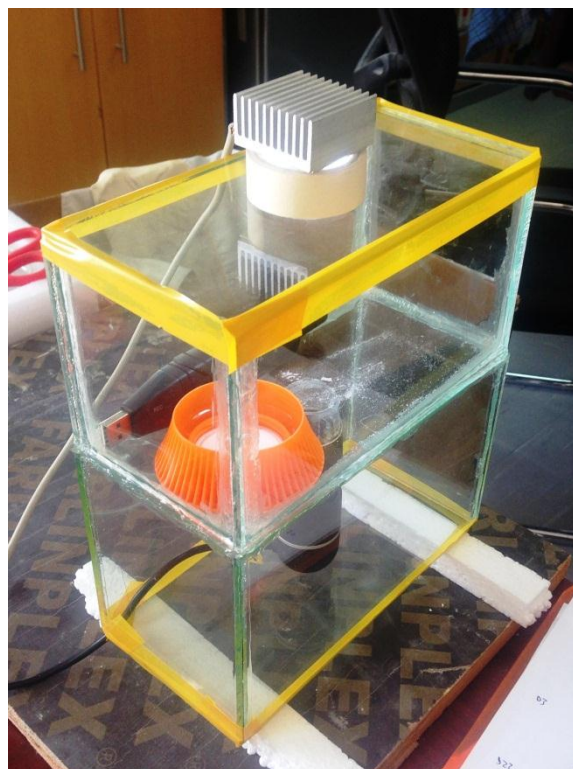
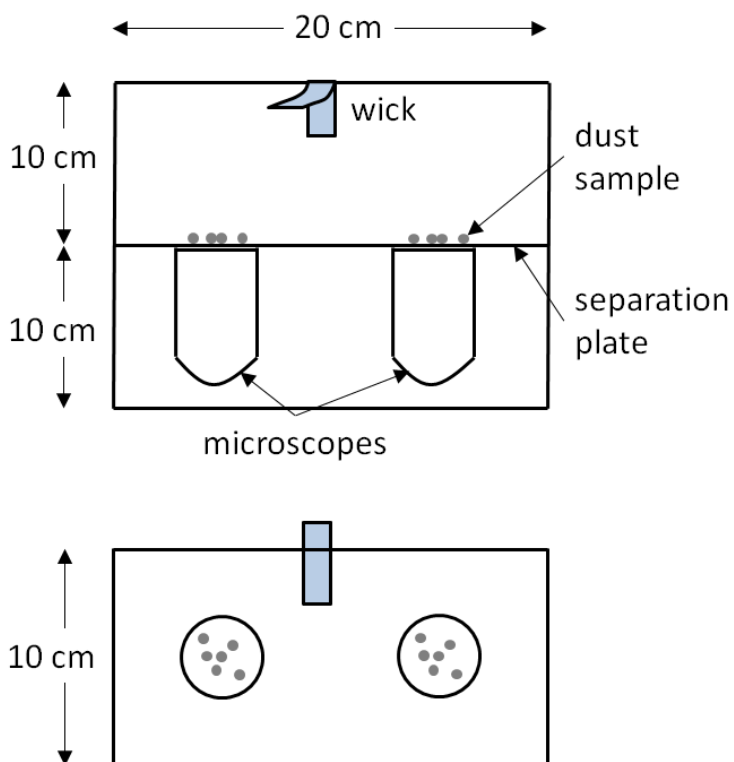


Figure 68. A humidity chamber with OSM microscopes was used to observe condensation on a pair of different dust samples under rising RH. It was designed to isolate the effects of dust composition and RH on condensation. Left: Schematic diagram of the chamber. Right: An earlier configuration using a single microscope, water dish instead of wick, and abutting backlight. The Extech Instruments RH and temperature recorder (USB device) is visible in the upper chamber

7.1.7. Surface Heating

As noted, a main reason for investigating condensation on soiled surfaces was that moisture greatly promotes dust adhesion and cementation. An obvious hypothesis is that heating an outdoor surface would reduce its dust accumulation, by eliminating those two mechanisms. To test this, an experiment was conducted at the STF as follows: A “heated OSM” was constructed by attaching a heating element to the back (under) side of the glass coupon. A reference OSM with unheated glass coupon was set up. The two OSMs (heated/unheated) were operated side-by-side, and dust deposition and detachment events and environmental parameters were obtained in a similar way as in section 6.4. (In this case because no greased coupon was used, hence slightly different flux-rate metrics were obtained as discussed in section 7.2.5).

The heated coupon was constructed by attaching a length of electrically-resistive nichrome wire (80% nickel, 20% chromium, 0.3 mm diameter) to the underside of a 5x5cm borosilicate glass coupon, using thermally-conductive silicone adhesive (Figure 69). A constant DC voltage (~ 2.5 V) was applied across the wire, which was found sufficient to heat the coupon to ~ 5 °C above that of the unheated OSM coupon as determined using a hand-held infrared thermometer. The temperature difference between the coupons was measured to vary from ~ 6 °C in no wind to ~ 4 °C in moderate wind.

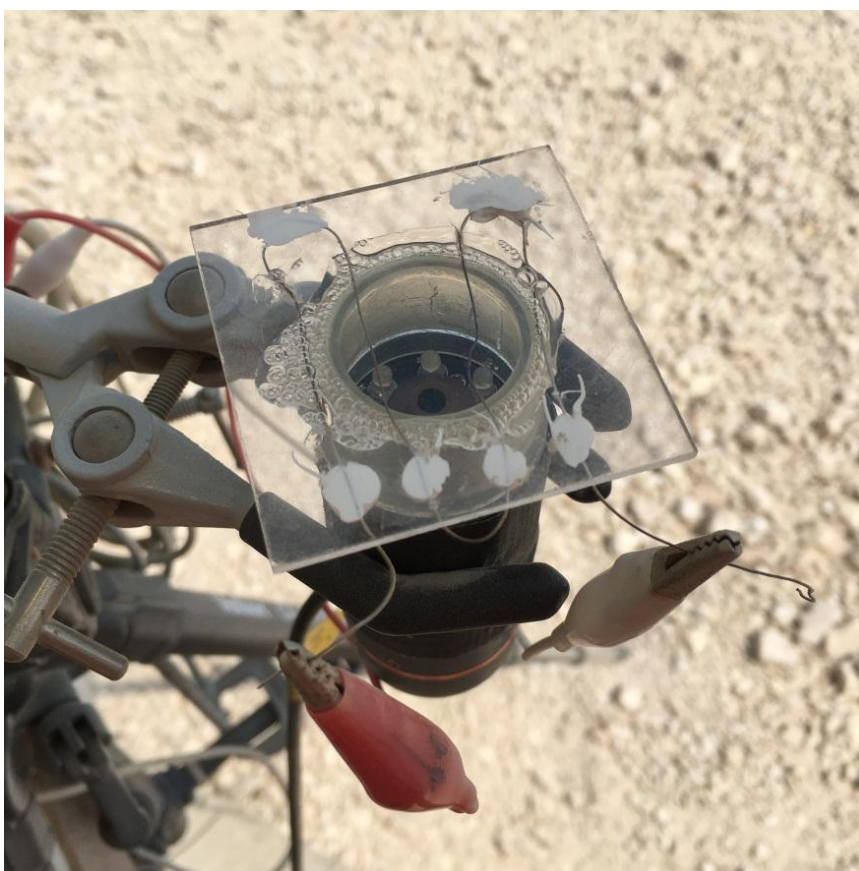


Figure 69. A heated OSM coupon was constructed using resistive nichrome wire. Its measurements were compared to those of an adjacent unheated coupon, to quantify the effect of condensation on dust flux rates in ambient conditions

Environmental parameters were measured in the same way as described in section 6.1, except that this time PM was measured using a beta attenuation monitoring (BAM) device (Thermo Scientific Continuous Ambient Particulate Monitor FH62C14), with a total suspended particles inlet head positioned ~ 4 m above ground, ~ 20 m from the OSM. It is noted that the instrument had a large intake air flow rate (stated as $16.67 \text{ l}\cdot\text{min}^{-1}$) and a heated, vertical inlet tube, which it was hoped would minimize loss of large particles reaching the detector and interference from suspended water droplets, thus improving quality of PM measurements. Temperature of the unheated coupon was estimated using the same method for T_s described in section 7.1.5. As mentioned, the heated coupon was roughly 5 ± 1 °C warmer than the unheated coupon. Dew-point temperature calculation method was the same as in section 7.1.5.

In this experiment no greased coupon was used. Therefore, per the technique described in section 5.4, it was possible to calculate *Net Deposition*, *Resuspension* and *Accumulation*, but not *Deposition* or *Rebound*. The heated/unheated OSM pair was operated at the Solar Test Facility in Qatar for 23 days over the period May – July 2017, and 2550 complete observations were obtained.

7.2. Results and Discussion

7.2.1. Composition

XRD scans of the three natural samples are shown in Figure 70, and the corresponding proportion by mass of each species is shown in Table 10. Anions concentrations in the Soluble Part are shown in Table 11.

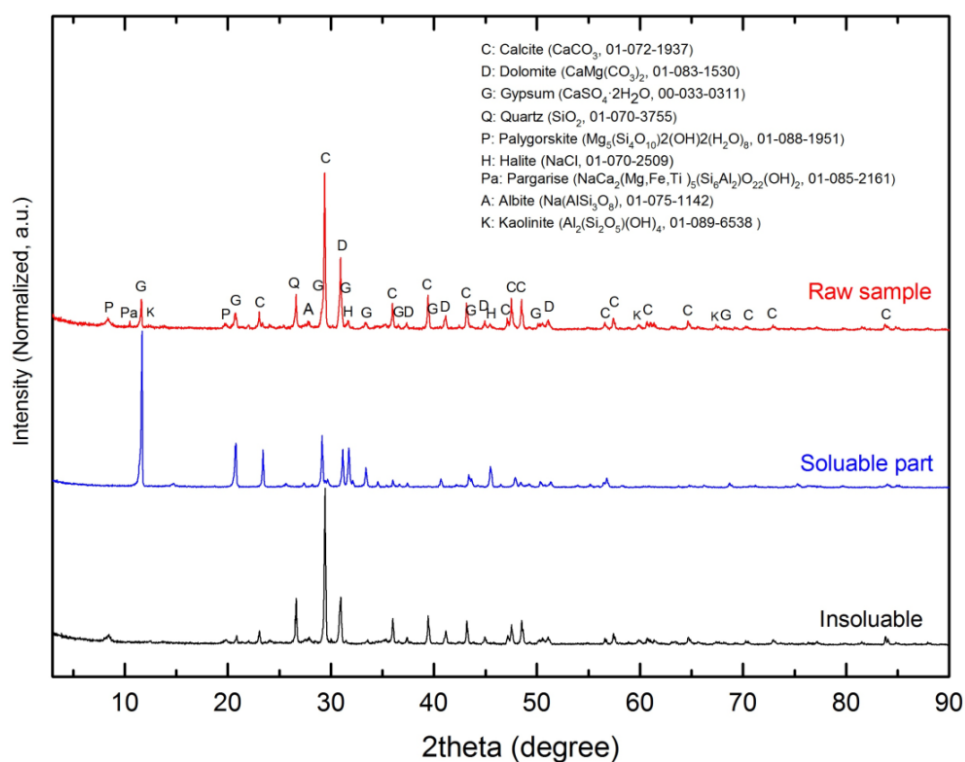


Figure 70. XRD results of the raw and separated natural dust samples

Type	Compound	Raw Sample [% wt.]	Soluble Part [% wt.]	Insoluble Part [% wt.]
Carbonates	Calcite	52.9	-	55.9
	Dolomite	11.0	-	22
Sulfates	Gypsum	14.4	83.2	-
	Bassanite	-	6.6	-
Oxides	Quartz	11.2	-	12.9
Alumino-silicates	Pargasite	3.7	-	-
	Palygorskite	2.6	-	4.6
	Kaolinite	1.0	-	0.9
	Albite	1.6	-	3.7
Salt	Halite	1.6	10.2	-

Table 10. Chemical composition of natural samples by XRD

Ion	Concentration [mg/l]	Raw Dust [% wt.]
Anions		
Sulfate, SO ₄ ²⁻	368	1.84
Nitrate, NO ₃ ⁻	129	0.64
Nitrite, NO ₂ ²⁻	28.6	0.14
Chloride, Cl ⁻	23.9	0.12
Cations		
Sodium, Na ⁺	156	0.78
Calcium, Ca ²⁺	110	0.55
Potassium, K ⁺	11.8	0.06
Magnesium, Mg ²⁺	11.2	0.06

Table 11. Major ions in Soluble Part solution by ion chromatography

It is seen that dust accumulating on PV modules in Doha (Raw Sample) is comprised mainly of carbonates, which reflects the region's geology. There are also significant amounts of gypsum, silica, and clays, as well as small but important amounts of halite and soluble sulfate and nitrate. When soaked in water the gypsum, salt and ions dissolved, and upon drying some of the gypsum crystallized as bassanite. The Insoluble Part comprised the remainder. Regarding the conversion of some minerals into other forms, the laboratory reported the following:

Soaking and drying caused disappearance of pargasite and also, due to removal of sulfates and halite, resulted in the increase of the relative weight percentages of remaining minerals such as palygorskite. Pargasite is a common mineral in the Earth upper mantle that stores water, however it is unstable in high water concentration, high temperature and pressure, especially when other minerals such as halite and quartz coexist in the mixture which affects solubility of pargasite. We believe that since the amount of pargasite was low and it was soaked in heated water with halite and other minerals, due to leaching of Na₂O the pargasite phase may have disappeared or reduced below the detection limit [184][185][186].

The formation of palygorskite is consistent with the description of dust cementation in Qatar by Ilse et al. [40] in which palygorskite needles were observed to form on a soiled glass coupon after cycles of condensation. All gypsum in the collected dust dissolved or suspended in water, yet no clay material remained suspended in water after 24 hours of settling.

As discussed in section 4.3, halite and nitrate (and less conclusively sulfate) are known to be hygroscopic. It is not obvious whether the gypsum and clay content of the Qatar dust would have also contributed to its water uptake. Several clays were shown by Wuddivira et al. [187] to adsorb some moisture at moderate RH, but dramatic water uptake did not occur until near 100% RH. Although the gypsum in Qatar dust was fully soluble, Ma et al. [163] found that gypsum particles were not hygroscopic: they attracted only 1-2 molecular layers of water on their surface near saturation humidity, and are poor cloud condensation nuclei.

From the local composition data and literature Dust reports, it appears the species most controlling water uptake by Qatar dust (i.e. its most hygroscopic species) were nitrate and halite, and possibly sulfate although reports of its hygroscopicity are inconsistent. Magnesium salts could potentially have been important because of their high

hygroscopicity, however their abundance was below the detection limit of XRD. Halite (NaCl) is very abundant but is less hygroscopic than the aforementioned species. Experiments to quantify the overall water uptake of Qatar dust, and distinguish the contribution of halite (NaCl) from the other species, are presented in the following sections.

7.2.2. Isotherms

Water vapor adsorption isotherms of the Raw Sample and Insoluble Part are shown in Figure 71. Two isotherm curves were obtained for each sample and show high reproducibility, providing confidence in the results. It is seen that the Raw Sample (dust collected “as is” from PV modules in Doha) started to adsorb moisture at around 60% RH, and adsorption increased dramatically at 80-90% RH. (Absorption may also have occurred, for legibility it is included here in references to adsorption). In contrast the Insoluble Part essentially did not adsorb water vapor.

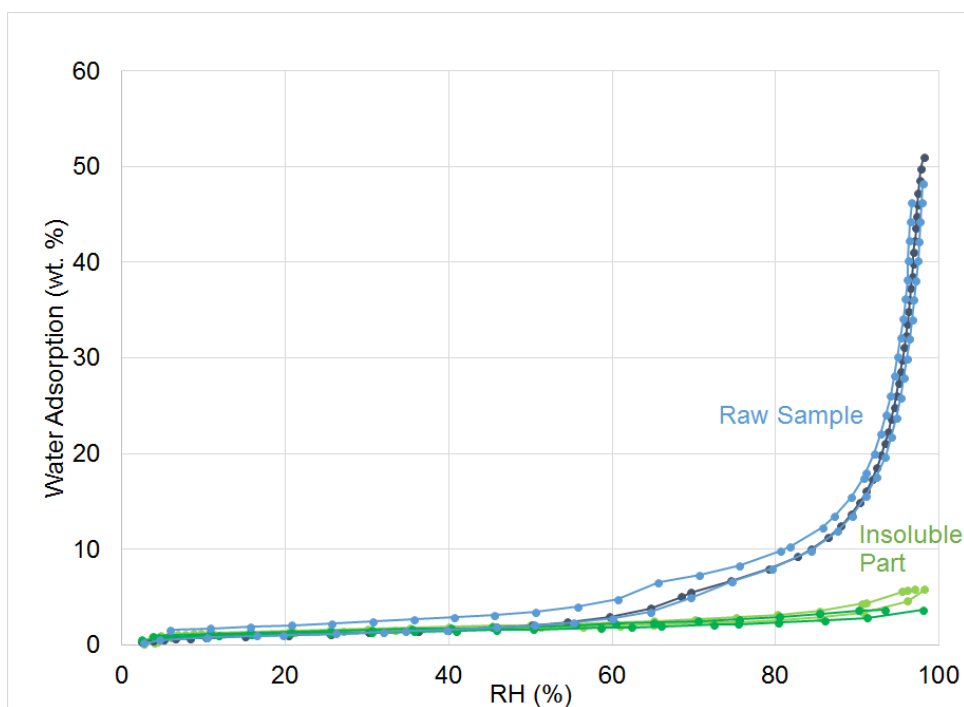


Figure 71. Vapor adsorption isotherm curves of Raw Sample (light and dark blue lines) and Insoluble Part (light and dark green lines). Adsorption expressed as water content on dry base (mass of adsorbed water divided by mass of dry sample, wt. %).

The isotherm results indicate that:

- Dust on PV modules in Qatar contains a significant amount of soluble, hygroscopic material
- That material adsorbs water vapor moderately from ~60% RH, and aggressively from ~80% RH
- The part of the dust which is insoluble is also hydrophobic.

These results are consistent with the literature discussed in section 4.3 and the composition analysis in section 7.2.1, i.e. pure mineral dusts are hydrophobic and insoluble, but in natural conditions they tend to be coated or combined with salts and ions that render the mixture hygroscopic. Isotherm shapes alone are not suited to identifying individual species — i.e. it is not possible to translate “bumps” in the isotherm curves with individual species. However the present isotherm results are consistent with the composition analysis, which indicated that dust collecting on PV modules in Qatar contains soluble species that render the dust hygroscopic.

7.2.3. Ambient Droplet Growth

As described in section 7.1.5, glass and PTFE-covered coupons were installed side-by-side at the STF test site, allowed to become naturally soiled, while being photographed every 10 minutes (day and night) from below with OSMs. The test was run for one week, and one particular night (8th February 2017) with much condensation was chosen for detailed analysis.

For each coupon, a surface region of 327 x 327 μm (350 x 350 pixels) was selected which contained at least six clearly-identifiable droplets. Images were then cropped to these fixed regions. Sample images from each coupon are provided in Figure 72, showing that condensation droplets as small as a few microns in diameter could be resolved. Because images were continually recorded, it was possible to measure their growth (in terms of projected area) over time.

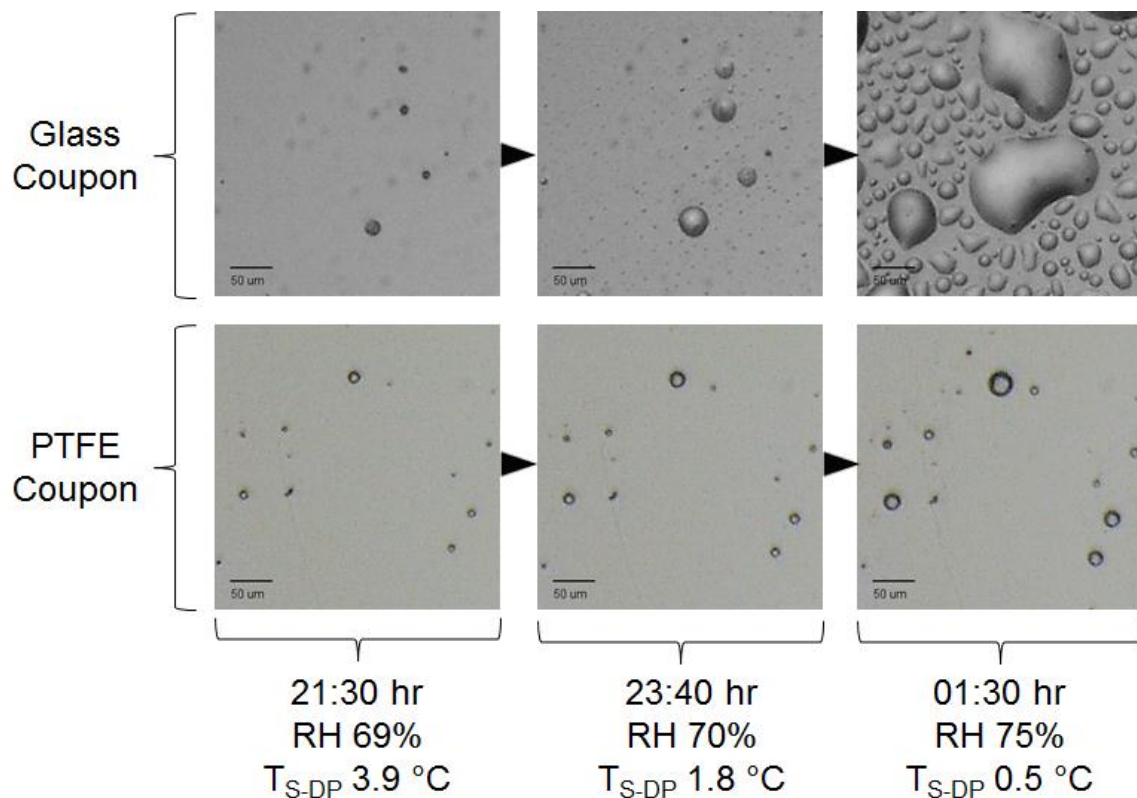


Figure 72. Sample OSM images of surface droplets on glass and PTFE surfaces, in ambient conditions at the STF, over a 4-hour period at night. Lower labels denote time of day, relative humidity, and surface–dew point temperature difference. Note that the droplets start off (at 21:30 hr) only a few microns in diameter

First, qualitative observations are made:

- On both glass and PTFE coupons, the first droplets were detected in OSM images around 15:30 hr, when RH was 47% and T_{S-DP} was 14 °C. Some droplets nucleated on visible dust particles, but most originated where no dust particles could be resolved
- Droplets grew more quickly on the glass coupon than on PTFE
- At 01:30 hr (RH 75%, T_{S-DP} 0.5 °C) the glass surface became saturated with condensation (i.e. droplets coalesced and flooded the surface) but the PTFE coupon did not
- At no point did the PTFE surface exhibit flooding, even when the most extreme condensation conditions were reached (80% RH, T_{S-DP} 0.5 °C, at 04:40 hr).

It is noteworthy that microscopic droplets first appeared in the late afternoon, i.e. while the coupon temperature was above well the dew point. They usually appeared at points where no dust particle was already present (which could be confirmed by viewing preceding OSM images). We speculate that such “warmer than dew point” droplets occurred because: (i) there was indeed hygroscopic dust already on that point of the surface, which nucleated condensation, but it was too small to be resolved by the microscope, and/or (ii) hygroscopic aerosol particles nucleated condensation *while still airborne* and then deposited onto the coupons. These propositions might be tested in future studies, for

example by taking OSM images at even higher frequency (every few seconds) and observing if “warmer than dew point” droplets appeared spontaneously (indicating aerosol deposition) or grew gradually (indicating condensation on very small surface particles).

Next, quantitative measurements were made of droplet growth rates. Projected areas of the six largest droplets on each coupon were measured image-by-image, as described in section 7.1.5. *Droplet Growth Rate* was defined as a droplet’s projected area divided by its area in the previous image (taken 10 minutes earlier), yielding units of [~/10min]. Figure 73 shows *Droplet Growth Rates* on the glass coupon (blue lines) and PTFE coupon (red lines), as well as prevailing T_{S-DP} (green line). The blue lines stop shortly after 01:00 hr as this is when droplets on glass coalesced and became impossible to distinguish. As the surface temperature neared the dew point, droplet sizes on both coupons fluctuated sharply with slight changes in ambient conditions. Droplets on both coupons grew or shrank synchronously, but the magnitude of size changes was much greater on the glass coupon. That is, the hydrophobic surface inhibited droplets’ growth and subdued their sensitivity to changes in atmospheric conditions.

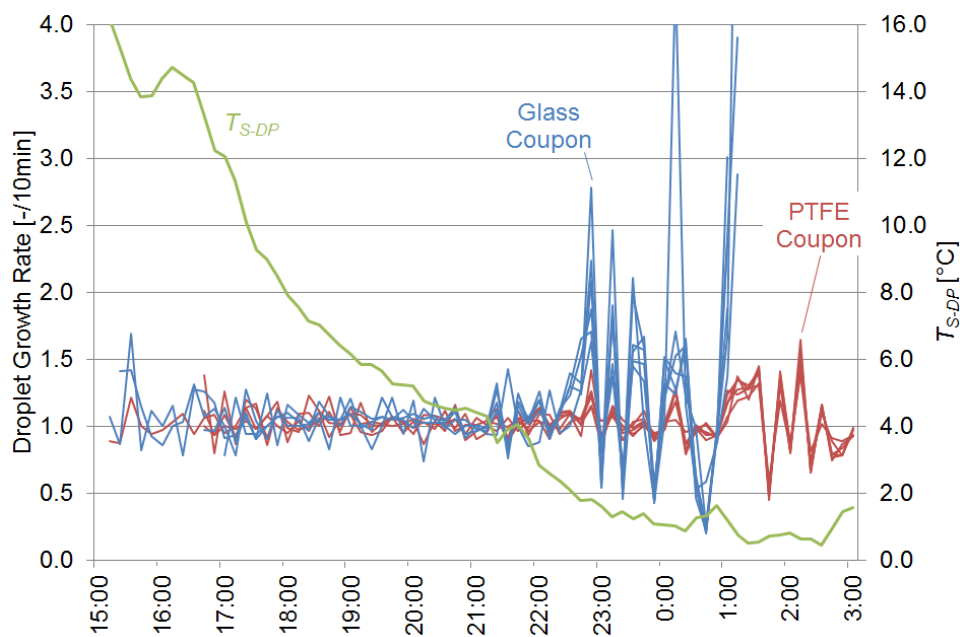


Figure 73. *Droplet Growth Rates* versus time-of-day on Glass Coupon (blue lines) and PTFE Coupon (red lines), expressed as change in droplet size over 10-minute intervals (left axis). Surface–dew point temperature difference (T_{S-DP} , °C) shown as green line (right axis). Six droplets on each coupon were tracked, resulting in six blue lines and six red lines.

It is also useful to plot droplet sizes as a function of T_{S-DP} (Figure 74). It is seen that for most droplets, their size was highly controlled by T_{S-DP} . This was true even when T_{S-DP} fluctuated over time (rose and fell repeatedly), which might have been expected to cause hysteresis in droplet size. Most droplets on both coupons started to grow when T_{S-DP} fell below ~8 °C (although there were two particles on the glass coupon that did not grow until T_{S-DP} reached <2 °C). In the T_{S-DP} range ~2–8 °C droplets grew more rapidly on the glass coupon than the PTFE coupon, i.e. the dots in Figure 74

slope more steeply for the glass coupon. As T_{S-DP} fell below 1–2 °C droplets on the glass coupon grew extensively and eventually flooded the surface, while those on PTFE roughly doubled in size but did not flood.

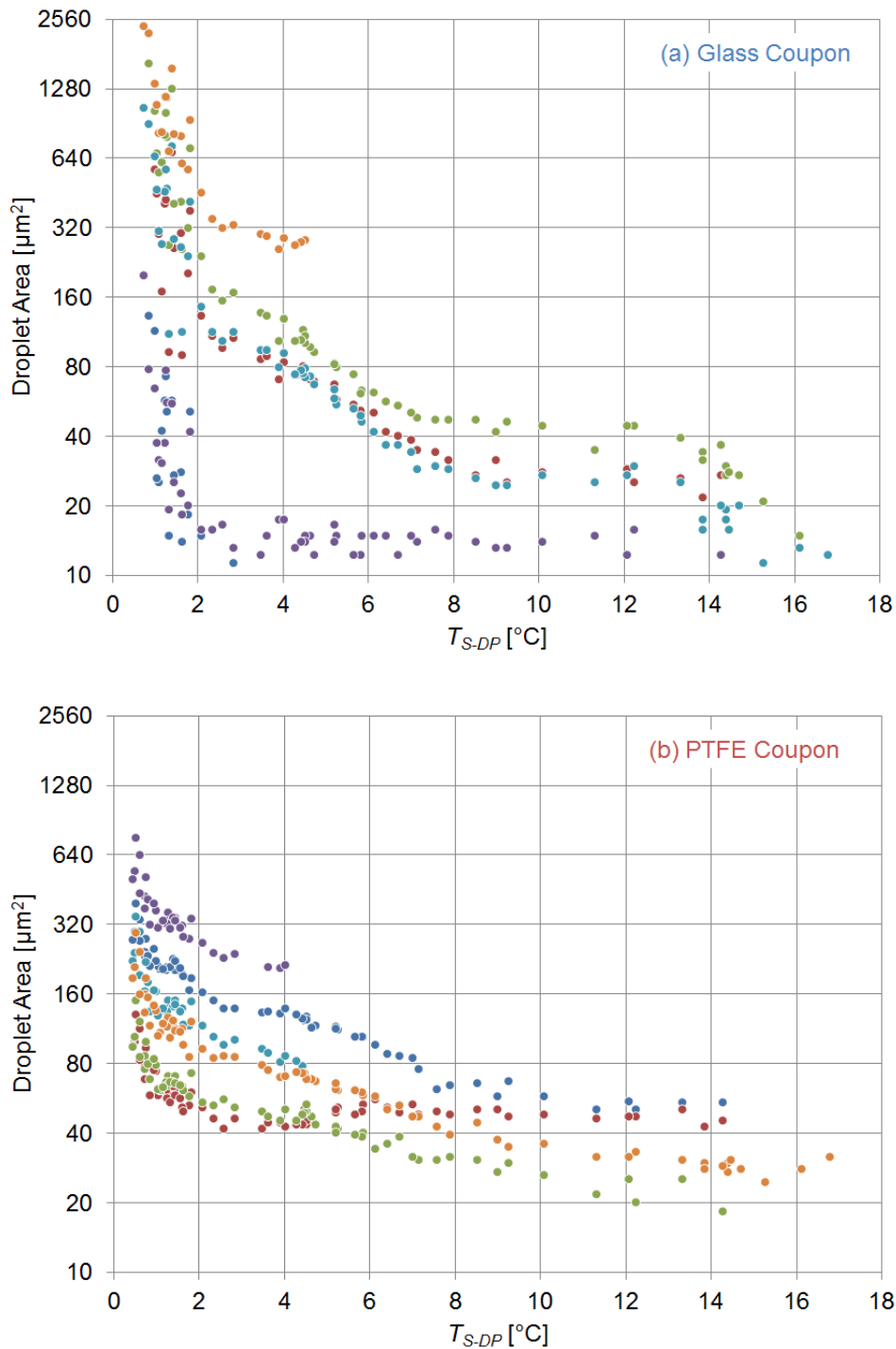


Figure 74. Droplet areas versus T_{S-DP} on (a) Glass Coupon and (b) PTFE Coupon. Each color on each coupon represents one droplet.

Overall, the ambient droplet growth measurements indicate that:

- Microscopic water droplets can exist on outdoor soiled surfaces even when the surfaces are much warmer than the dew point, regardless of surface wettability. This is possibly due to presence of hygroscopic matter on the surface or deposition of brine droplets from the atmosphere
- Most droplets on a surface grow at a similar rate to each other (i.e. logarithms of their projected areas plotted against T_{S-DP} form a consistent slope). However a few exhibited negligible growth until near saturation conditions. It is speculated that particles in the former group contain some critical amount of hygroscopic material, while those in the latter group contain negligible amounts and are essentially hydrophobic
- On both hydrophilic and hydrophobic surfaces that are soiled, droplets grow slightly when T_{S-DP} falls below ~ 8 °C and grow rapidly when it reaches 1-2 °C. However a hydrophobic surface greatly reduces the growth rate of droplets, and prevents them from coalescing and flooding the surface near saturation conditions.

7.2.4. Laboratory Droplet Growth

Composition analysis of the dust on PV modules in Qatar (section 7.2.1) identified several hygroscopic candidates. To distinguish which of these candidates most influenced condensation, a humidity chamber was used to observe droplet growth on pairs of dust samples. The samples, number of runs, and RH ranges are shown in Table 12. To aid interpretation of results, recall that the Raw Sample contained natural salts and soluble ions, the Synthetic Sample was prepared with NaCl but no other highly-soluble material, and neither the Insoluble Part nor S.S. Minus Halite contained any hygroscopic material.

Sample pair	Run #	Start RH [%]	Max. RH [%]
Raw Sample vs. Insoluble Part	1	24.5	83.9
	2	23.8	95.3
Raw Sample vs. Synthetic Sample	3	43.0	92.9
	4	54.8	93.1
	5	39.4	95.0
Synthetic Sample vs. S.S. Minus Halite	6	35.5	94.4
	7	43.2	86.7

Table 12. Details of humidity chamber experiments

Example images are provided in Figure 75, showing how some particles swelled due to deliquescence. Although not obvious in these sample images, it was also possible to detect when particles first started to reorient or reposition slightly on the surface, which was taken to indicate the formation of liquid bridges by capillary condensation. From the full set of images, the RH levels at which capillary condensation and deliquescence first occurred were manually noted. The results are plotted in Figure 76.

It is seen that the Raw Sample consistently exhibited swelling of many particles when RH reached 69.1-73.1%. The other samples essentially had no swelling. (One of the six runs with the Synthetic Sample showed swelling of one particle, however that specific specimen had been prepared approximately six months earlier whereas the five non-swelling specimens had been prepared just a few days before the experiment, suggesting that the aged specimen had adsorbed some hygroscopic material while stored). The results indicate that species other than NaCl (e.g. nitrate, sulfate, or other salts) were solely responsible for swelling of a dust mixture. Importantly, NaCl by itself did not cause particle swelling even at 95.0% RH (as demonstrated by Synthetic Sample in run #5), which was unexpected because it is reported to deliquesce at 76% RH.

Although particle swelling of the Raw Sample always occurred near the same RH (69.1-73.1%), capillary condensation commenced over a wide range of RH in different runs (even though the same bulk sample was used). Possibly this was due to the wide range of RH at which the experiments started (Table 12). As shown in Figure 76, capillary condensation generally started at lower RH on the Raw Sample than on the Synthetic Sample, except for one outlier in which the aged (and apparently contaminated) Synthetic Sample exhibited reorientation at just 33.6% RH.

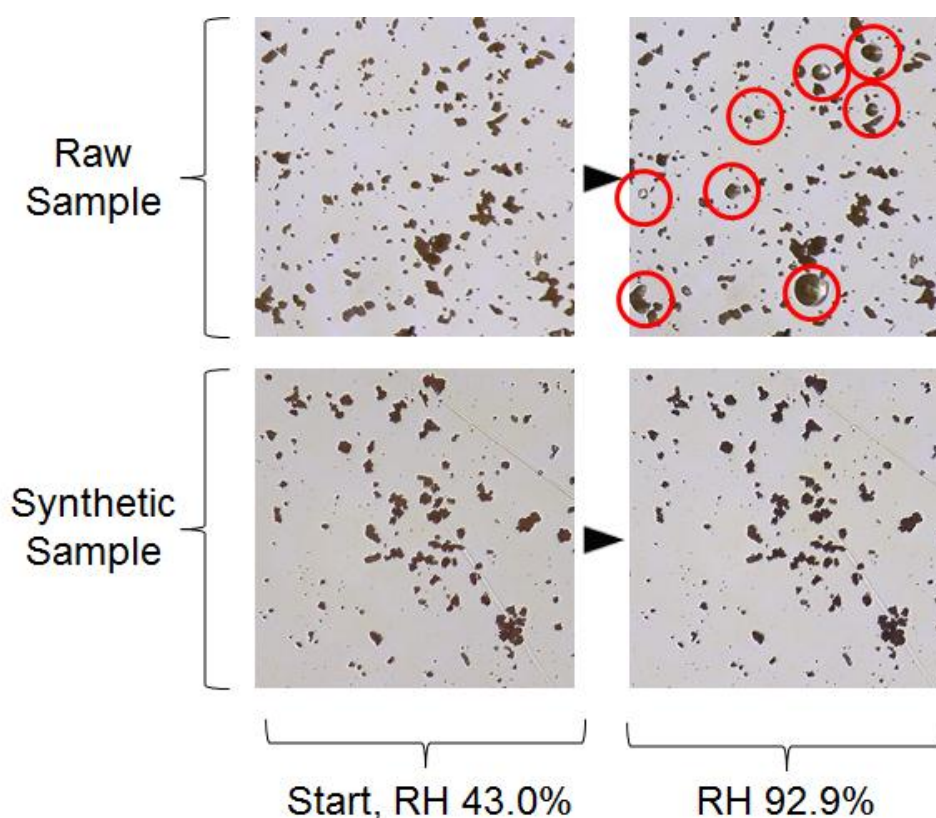


Figure 75. Sample images from the humidity chamber. Many particles of the Raw Sample swelled in high RH (top pair of images), while essentially none did of the Synthetic Sample (bottom pair) or other samples. The results show that NaCl alone did not lead to swelling, only other hygroscopic species did. Images are 402 x 402 μm .

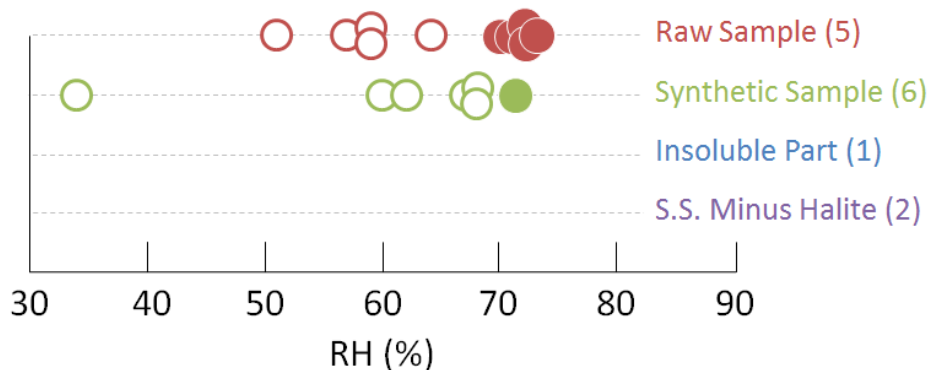


Figure 76. RH at which particles first exhibited capillary condensation (open circles) and swelling (filled circles) for different dust mixtures. Numbers in brackets indicate number of runs for each mixture.

In summary, the humidity chamber experiments indicated that deliquescence of dust was completely determined by naturally-occurring species *other* than NaCl (e.g. nitrate ions or other salts), and it occurred consistently at around 70% RH. Capillary condensation occurred only when NaCl or other hygroscopic species were present. It did not appear at a specific RH, even for the same sample, possibly due to differing starting RH of the tests.

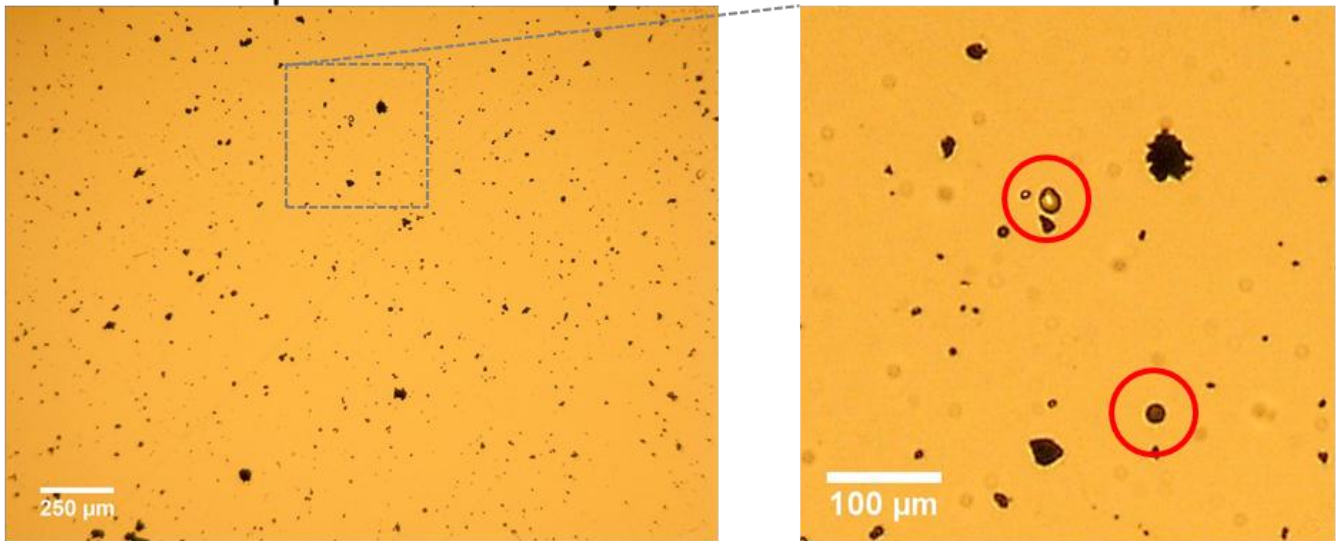
7.2.5. Surface Heating

— Qualitative observations

First, the degree to which the heating the coupon prevented condensation was qualitatively assessed. Pairs of OSM images (heated/unheated) throughout the test period were manually compared. Microscopic condensation droplets could be easily distinguished from dust particles because (i) they were circular, whereas dust particles tended to have irregular shapes, and (ii) they dried out during the following day. During this test microscopic droplets often condensed on the unheated coupon overnight, but it never became “flooded” with dew like it did in the ambient droplet growth experiment (section 7.2.3).

It was observed that the heated coupon exhibited far less condensation than the unheated one, but still occasionally exhibited a few microscopic droplets. Example images are shown in Figure 77, when conditions were as follows: time 2:00 am (25th July 2017), RH 60.0%, T_{amb} 34.0 °C, T_{DP} 25.1 °C, T_s unheated coupon ~31, T_s heated coupon ~36 °C. T_s values are reported here as estimates because they were not directly measured, but it is safe to assume that both coupons were well above the dew point temperature at this time, which is the key point. The example images illustrate that the unheated coupon had extensive microscopic condensation droplets at night, and the heated one occasionally had small droplets. This provides further evidence — in addition to the ambient droplet growth experiments — that “warmer than dew point” droplets can exist even on ambient surfaces, due to condensation on hygroscopic surface particles or brine droplets depositing from the atmosphere.

heated coupon



unheated coupon

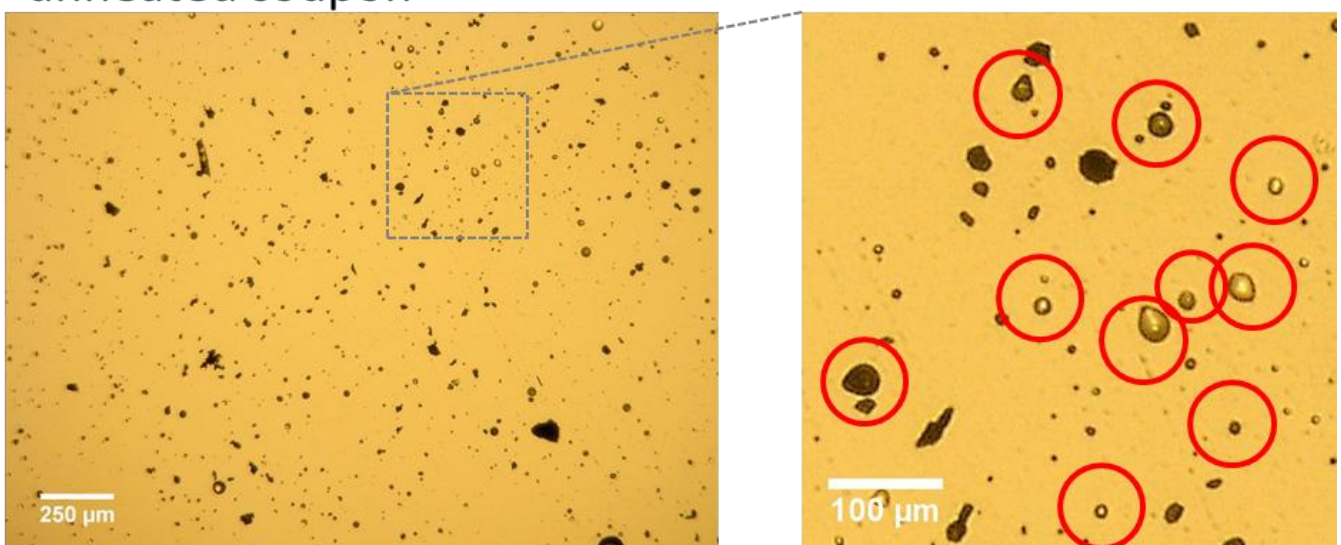


Figure 77. Sample images taken simultaneously from heated and unheated OSM coupons, at 2am at the STF. The unheated coupon exhibited widespread microscopic condensation droplets (circled in red), reaching diameters of tens of μm . The heated coupon occasionally also exhibited a few small droplets

— Suppression of *Accumulation*

Overnight dew formation has been reported to be “very important” to soiling of solar collectors [3], therefore it may be hypothesized that heating the surface would reduce dust accumulation. The present experiment investigated this by comparing the *Accumulation* flux rate [$\mu\text{g}\cdot\text{m}^{-2}\cdot\text{min}^{-1}$] on the heated coupon to that on the unheated coupon. Because *Accumulation* on each coupon was measured simultaneously (i.e. in identical environmental conditions), and the

population standard deviations (i.e. the “true” variance of *Accumulation* rate on each coupon) are not known, their means can be compared via a paired *t*-test.

For each 10-minute observation period, the difference between unheated and heated *Accumulation* rates was termed the *Accumulation Difference*. It was calculated for all 2550 periods. Positive values indicate the heated coupon had less dust accumulation than the unheated one, i.e. heating was effective at reducing soiling:

$$Accumulation\ Difference = Accumulation_{unheated\ coupon} - Accumulation_{heated\ coupon} \quad (56)$$

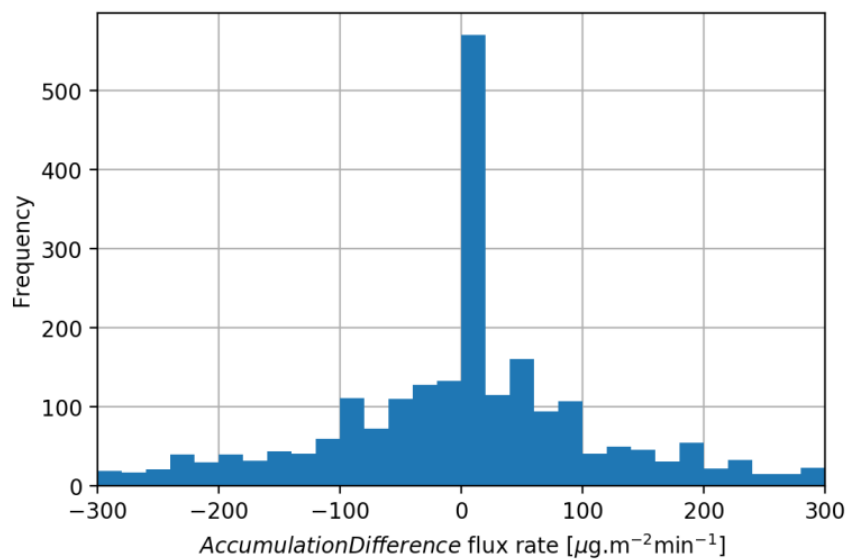


Figure 78. Distribution of *Accumulation Difference* observations. Positive values indicate the heated coupon had less soiling

The distribution of *Accumulation Difference* is shown in Figure 78. Although there is a prevalence of values near zero, the lack of skew and large sample size allows the paired *t*-test to be used. The hypotheses are stated as follows, where μ indicates population mean:

$$H_0: \mu_{Accumulation\ Difference} = 0$$

$$H_1: \mu_{Accumulation\ Difference} > 0$$

Parameter	Value
<i>Accumulation Difference</i>	7.94 $\mu\text{g}\cdot\text{m}^{-2}\cdot\text{min}^{-1}$
standard deviation	231.1 $\mu\text{g}\cdot\text{m}^{-2}\cdot\text{min}^{-1}$
<i>n</i>	2550
α	0.05
<i>T</i> critical	1.645
<i>T</i> statistic	1.736
outcome	Reject H_0
<i>p</i> value	0.0414

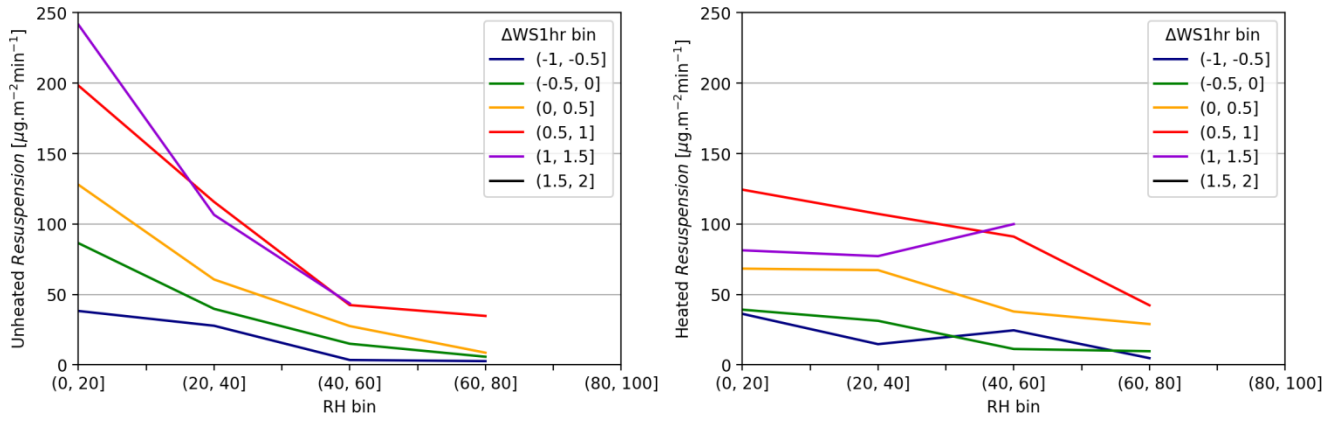
Table 13. Paired *t*-test on *Accumulation Difference* observations, indicating that it was greater than zero (i.e. heating the coupon reduced soiling) at 5% level of significance

The significance level was chosen as 5% and the test was one-sided. Statistical parameters were calculated as shown in Table 13. The test supports accepting H_1 , i.e. *Accumulation Difference* was greater than zero, hence heating the coupon reduced its dust accumulation rate. Although hypothesis H_1 was accepted, the *p*-value of 0.0414 was only marginally within the significance limit of 0.05, and the magnitude of the soiling reduction was small: just 7.94 $\mu\text{g}\cdot\text{m}^{-2}\cdot\text{min}^{-1}$. Compare this to the average *Accumulation* on the unheated coupon of 56.6 $\mu\text{g}\cdot\text{m}^{-2}\cdot\text{min}^{-1}$. A proportional difference as small as this could have been due to some unknown systematic experimental error, such as different air-flow patterns over the two OSMs. Overall, this part of the analysis weakly supports the conjecture that heating the coupon slightly reduces its soiling.

— Enhancement of *Resuspension*

So far it was shown that heating the coupon by $\sim 5^\circ\text{C}$ reduced (but did not eliminate) condensation, and slightly reduced its dust accumulation rate. It could be supposed that heating coupon would also increase its rate of particle detachment, because eliminating condensation would eliminate capillary adhesion. Further, one might expect that this effect (heating the coupon increasing its detachment rate) would be most pronounced in high RH, because in dry conditions there is no capillary adhesion on either coupon anyway.

To test this theory, *Resuspension* flux rates of the heated and unheated coupons were plotted as a function of RH (Figure 79). Because dust detachment is highly dependent on the wind speed relative to the preceding hour (see section 6.4.3), the data is presented at constant $\Delta\text{WS}_{1\text{hr}}$. It is seen that for the unheated coupon, *Resuspension* was strongly dependent on RH, and decreased consistently with RH at all levels. In comparison *Resuspension* from the heated coupon was much less dependent on RH, although showed signs of being suppressed only in RH >60%. These results provide strong evidence that, in ambient desert conditions, increasing RH leads to more condensation which greatly suppresses particle detachment.



(a) Unheated coupon

(b) Heated coupon

Figure 79. Resuspension flux rate vs. RH [%] and ΔWS_{1hr} [ms^{-1}], for (a) unheated coupon, (b) heated coupon. Observations binned by RH and ΔWS_{1hr} ($n \geq 10$)

In Figure 79 it is also seen that in very dry conditions (0-20% RH), Resuspension was actually greater from the unheated coupon than the heated one. At first this may seem to contradict the conclusion just made, that coupon heating increases its dust detachment. However it can be understood by dust *building up* on the unheated coupon during humid periods, and then blowing off during dry windy periods (i.e. high Resuspension). In contrast dust would never build-up on the heated coupon, and so dry windy periods would not cause high Resuspension. This explanation (cycles of humid build-up followed by dry detachment) is investigated by time-of-day weather patterns, in the following analysis.

— Time-of-day pattern of dust fluxes

Although only a small difference in Accumulation rate was observed between the heated and unheated coupons, it was noted they had very different Resuspension behaviors. This was apparently linked to daily weather cycles. To complete the picture of time-of-day dust patterns, it was desirable to also examine the dust Rebound rate. Because no greased coupon was used in this experiment, Deposition could not be measured; only Net Deposition, Resuspension and Accumulation could be determined. (Recall that $Net\ Deposition = Deposition - Rebound$). However, although the absolute values of Rebound could not be determined, their difference between the heated and unheated coupons could be. This was allowed by assuming (with high validity) that the same amount of dust impacted both coupons, i.e. they had the same Deposition rate. Then, the difference in Rebound between the two coupons could be calculated using eq. (40). The method is expounded in Table 14, which also shows the results.

Dust Flux	Heated Coupon [$\mu\text{g}\cdot\text{m}^{-2}\cdot\text{min}^{-1}$]	Unheated Coupon [$\mu\text{g}\cdot\text{m}^{-2}\cdot\text{min}^{-1}$]	Difference (Heated – Unheated) [$\mu\text{g}\cdot\text{m}^{-2}\cdot\text{min}^{-1}$]	Derivation
<i>Deposition</i>	x	x	zero	Unknown but equal <i>Deposition</i> rates (x) on each coupon
<i>Net Deposition</i>	92.4	106.4	-14.0	Directly measured by OSMs
<i>Rebound</i>	$x - 92.4$	$x - 106.4$	14.0	Eq. (40)
<i>Resuspension</i>	43.7	49.8	-6.1	Directly measured by OSMs
<i>Accumulation</i>	48.7	56.6	-7.9	Eq. (39)

Table 14. Differences in flux rates between heated and unheated coupons. Values in red show that there was greater *Rebound* on the heated coupon, but greater *Resuspension* on the unheated one

It is seen the heated coupon had greater *Rebound* than the unheated coupon, but the unheated coupon had greater *Resuspension*. The net result of these effects was that the heated coupon had less *Accumulation* (as discussed above). The differences are not large in proportional terms: the heated coupon had 14.0% less *Accumulation* and 12.2% less *Resuspension* than the unheated one (the proportional amount of *Rebound* difference could not be calculated).

The physical interpretation of these results is that heating the coupon increased the tendency for particles to immediately rebound from it. But that “benefit” was partly offset later on, when the unheated coupon shed more dust. This “delayed resuspension” happened mainly during the daytime, as shown by a plot of the difference in the coupons’ *Resuspension* rates versus time-of-day (Figure 80). The likely explanation is that dust built-up on the unheated coupon at night due to low RH and high RH, and then dispersed the following day as the coupon dried in the sun, RH decreased, and WS increased.

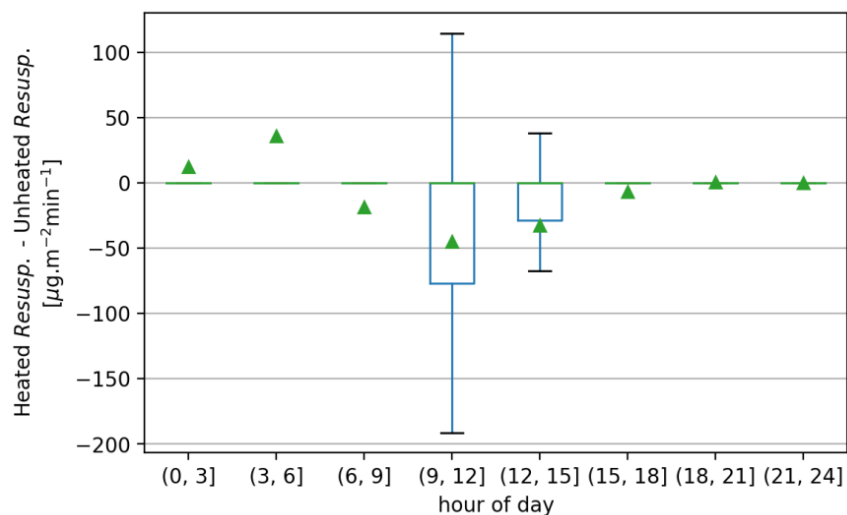


Figure 80. *Resuspension* from the unheated coupon exceeded that from the heated coupon during the daytime, suggesting that dust which adhered overnight on the unheated coupon (due to condensation) detached once the coupon dried out and wind speed increased (especially 9am-12pm). (Green markers = means, box edges = quartiles, non-visible boxes indicate Q1 = Q2 = Q3 = zero)

A simplified summary of these behaviors is shown in Table 15. The key observations are that:

- Dust tended to build-up on the (unheated) surface at night due to condensation, but largely be blown-off the following day
- Because of this day-time “self-cleaning”, artificially heating the surface had little overall benefit on the dust accumulation rate.

Time of Day	Dominant Weather Conditions	Heated Coupon Behavior	Unheated Coupon Behavior
Night	High RH Low WS	Low build-up of dust	High build-up of dust
Day	Low RH High WS	Low shedding of dust	High shedding of dust
Long-term flux rate averages (relative)		Low <i>Rebound</i> High <i>Resuspension</i> Moderate <i>Accumulation</i>	High <i>Rebound</i> Low <i>Resuspension</i> Moderate <i>Accumulation</i>

Table 15. Simplified summary of time-of-day effects on dust flux rates of heated and unheated coupons. The key observation is that overnight condensation causes dust to build-up overnight (on unheated surfaces) and largely resuspend the following day.

— Discussion

Overall, the heated/unheated OSM experiment showed that heating a surface had little effect on its overall dust accumulation in Qatar’s climate. Although there was a statistically-significant reduction in the average *Accumulation* rate on the heated coupon relative to the unheated one, the magnitude of that reduction was small. Detailed examination of the coupons’ dust flux rates revealed interesting phenomena: (i) When RH exceed 40-60%, dust resuspension from the unheated coupon was greatly inhibited, but this was not observed on the heated coupon. (ii) Particles had greater tendency to rebound from the heated coupon than the unheated one. (iii) The unheated coupon had greater dust accumulation at night, but also greater dust resuspension during the daytime.

The results reveal an important time-of-day pattern to soiling at the study site. Dust builds-up on the (unheated) surface overnight due to high humidity and low wind speed, but much of this build-up is shed the following day as the surface dries out and wind speed increases. Thus, the “benefit” of continually heating the surface (i.e. less trapping of dust by condensation) was offset by natural drying and wind-cleaning the following day. From the perspective of PV soiling mitigation, this suggests the possible strategy of minimizing overnight deposition (e.g. by tilting the modules to a steep angle, or covering them) and taking advantage of natural cleaning opportunities (e.g. maximizing airflow velocity over the modules during the day time).

8. Summary and Conclusions

The main motivation for this study was to improve understanding of how PV soiling occurs by shortening the time period of dust-flux measurements in the field. Because weather conditions vary continuously, it was hoped that a measurement period of minutes (instead of the conventional period of days) would better reveal the effects of environmental parameters on flux rates. To achieve this, an “outdoor soiling microscope” (OSM) was developed which comprised a low-power microscope, transparent dust collection surface, LED backlights, and customized digital image analysis. The OSM proved to be a practical tool for studying soiling in the field, and allowed novel measurements to be made. Its key features were:

- Operable in outdoor field conditions
- Operable day and night
- Measurement interval as short as several seconds, although 10-minute intervals were used in this study
- Measurement quantity as small as a single $\sim 4 \mu\text{m}$ dust particle
- Separate measurement of depositing and detaching particles, allowing dust accumulation to be separated into component flux rates: deposition, rebound, and resuspension
- Observation of condensation formation and growth
- Ability to apply surface “treatments”, e.g. grease, heating, and coatings
- Inexpensive and readily-available components.

The OSM had limitations in its present design, including:

- Inability to reliably measure sizes of particles smaller than $\sim 4 \mu\text{m}$, although this was not important for the present study because surface coverage was dominated by 10-40 μm particles
- Sensitivity of measured particle sizes to the image-analysis threshold setting. This was mitigated by programming the image-analysis script to adjust the threshold to account for variations in background light intensity
- Direct and moving sunlight sometimes caused irregular images, e.g. flares or particle shadows. This was avoided by placing the OSM in the shade of a building
- Tethering to a computer via USB cable, which limited its operating distance from a building to $\sim 10 \text{ m}$
- The undiluted petroleum jelly used to trap all impacting dust apparently allowed some particles to rebound in high wind speed. This might be improved in future by using a different grease formulation.

By using a pair of OSMs, one with a greased coupon and the other ungreased, it was possible to separate dust accumulation into three component flux rates: deposition, rebound (immediate detachment), and resuspension (delayed detachment). The technique yielded approximate rather than exact values of these flux rates, because the finite imaging interval (10 minutes) caused some particle resuspension to be misclassified as rebound, and (to a lesser degree) vice versa. Such misclassification could be reduced by shortening the imaging interval, at the expense of greater work of image filtering and analysis.

Strengths and weaknesses of the OSM as an experimental tool, and comparison with conventional laboratory and field techniques, are summarized in Table 16. The OSM is particularly suited to studying deposition and detachment of coarse dust particles ($> \sim 4 \mu\text{m}$) in outdoor settings. Further, it was straightforward to operate a pair of OSMs side-by-side, which was well-suited to study the relative effect of surface treatments in ambient conditions — for example dust flux rates and condensation droplets on a hydrophobic vs. hydrophilic coating. Laboratory wind tunnels are more suitable when test conditions need to be controlled and small particles ($< 4 \mu\text{m}$) are of primary interest. Long-term field trials with full-size operating PV modules are essential for verifying soiling rates and resulting energy losses on real PV systems. In summary, if one considers experimental goals of “realism” and “information” (on underlying physics), the OSM sits between laboratory wind-tunnel experiments and PV module field trials (Figure 81).

Experimental approach	Reveals particle mechanics	Control over parameters	Natural conditions	Realistic PV geometry	Short experiment duration	Greatest suitability
Laboratory wind tunnel	●●	●●		●	●●	Precise parametric soiling experiments, e.g. surface treatment, wind speed, tilt angle, dust size/composition
Outdoor soiling microscope (OSM)	●		●●	● ⁽¹⁾	●	Observation of coarse dust fluxes in natural conditions. Detailed surface-treatment trials in natural conditions
Outdoor PV modules			●●	●●		Verification of soiling and energy loss of actual operating PV modules

Table 16. Strengths and weaknesses of experimental approaches to PV soiling study. ●● = great strength, ● = moderate strength. (1) In principle the OSM could be set-up in the geometry of a PV array, although this was not done in the present study

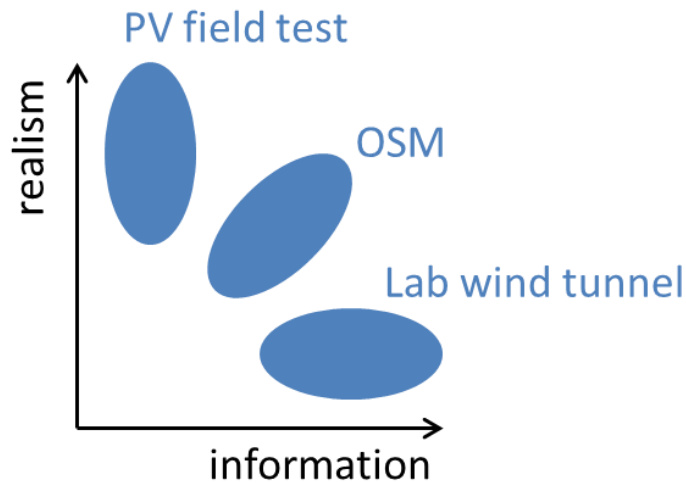


Figure 81. The OSM lies between laboratory wind-tunnel experiments and field tests of operating PV modules, in terms of soiling studies' realism and information on underlying mechanisms

A 51-day field test was carried out the Solar Test Facility in Doha, Qatar, in which component dust flux rates and environmental parameters were recorded. Key findings were:

- There was a pronounced “threshold response” of deposition to wind speed (WS), with constant deposition rate in $WS < 3.2 \text{ ms}^{-1}$ and approximately linear increase in $WS > 3.2 \text{ ms}^{-1}$. The threshold response was consistent with one particular model of inertial (wind-controlled) deposition in the literature, by Kim et al. [85]. That model had (like the present study) been derived from outdoor soiling measurements, whereas models derived from wind-tunnel experiments did not match the current results, either qualitatively or quantitatively. This suggests that it is difficult to predict outdoor soiling rates from wind-tunnel studies. When combined with a standard equation for the sedimentation (gravity-controlled) deposition rate, the model of Kim et al. closely predicted the present results. The physical cause of the threshold response is still not clear, although analysis of airflow and particle characteristics in this study suggest it was partly due to airborne particle size increasing with WS
- PM concentration had no effect on the dust deposition rate until it reached very high levels, $> 1 \text{ mg.m}^{-3}$. This was unexpected because all deposition models — and intuition — hold that the number of particles to impact a surface is proportional to the number of particles in a volume of air. The result was attributed to measurement inaccuracy: The particulate monitor may not have accurately measured large airborne particles, and at low concentrations a small change in the absolute amount of airborne dust would have a disproportionately large effect on the PM value, e.g. 0.2 mg.m^{-3} is much greater than 0.1 mg.m^{-3} in relative terms but not in absolute terms
- Dust particles had a great tendency to rebound from the surface. The rebound fraction reached $\sim 80\%$ at WS of 3 ms^{-1} (it may have reached an even higher percentage but for the apparent grease ineffectiveness previously mentioned). The result was consistent with theories of particle rebound, which hold that it occurs when a particle's kinetic energy exceeds the energy required to overcome adhesion to the surface. The study demonstrated that rebound has a powerful role in dust accumulation in outdoor surfaces, even in quite mild WS.

Reports in the literature indicated that rebound is suppressed by high RH, however this was not observed in the present study

- Resuspension of dust from the surface is of low magnitude and complicated by many factors. Although models of particle resuspension predict that it is powerfully influenced by wind speed (proportional to the square of wind speed or a high power), the present study showed weak correlation. This can be understood by considering that it is change of wind speed over time, rather than its absolute value, that dictates ambient resuspension. Resuspension rate was shown to be suppressed as RH increased, especially when it exceeded ~50%, and by longer exposure time on the surface. The results provide further evidence that particles become strongly adhered by capillary adhesion and cementation even in desert environments. An interesting result was strong time-of-day patterns in the component flux rates: dust tended to build-up on the surface at night, when RH was high and WS low, and then much of it was resuspended the following day as the surface dried out, RH fell and WS rose.

Linear regression models were constructed of the component dust flux rates (deposition, rebound and resuspension), using a stepwise process for selecting predictor variables. It was found that the OSM inherently produces stochastic flux-rate data, because the amount of dust to deposit/detach from a ~4 mm² surface area every 10 minutes is highly random. Because of this randomness, only a small proportion of the observed variation in the flux rates was accounted for by the regression models (R² values were 7-10%). However because of the large sample size that was also inherent in the OSM technique, the *relative influences* of the environmental parameters on the flux rates could be inferred with high statistical confidence. Using 5% significance level, it was found that:

- Dust deposition was most influenced by “supercritical wind speed” — the amount by which WS exceeded a critical threshold. In this experiment the threshold was 3.2 ms⁻¹. RH, PM, and interaction between RH and supercritical wind speed also had statistically-significant effects
- Rebound fraction was solely explained by WS. Statistical analysis confirmed the qualitative observation mentioned above, that RH did not significantly influence the particle rebound in this study
- Resuspension of dust was most powerfully predicted by the change in wind speed relative to the preceding hour, ΔWS_{1hr} . (This parameter explained more than ten times as much resuspension variation as did WS alone). Resuspension was suppressed by RH and exposure time, in statistically-significant amounts
- The overall dust accumulation rate was most strongly influenced by WS and ΔWS_{1hr} , in approximately equal extents. PM had a small but statistically-significant predictive contribution when added to the regression model, but RH did not
- The accumulation model predicted broad trends in the soiling rate but systematically underestimated the amount of soiling per day. A possible reason was the difference in dominant wind direction between the data-sets used to “train” and “test” the model, causing different amounts of deposition for the same conditions of WS, RH and PM.

A series of field and laboratory experiments were conducted to investigate condensation on soiled surfaces in outdoor conditions. Parameters tested were: RH, surface/dew point temperature difference, hygroscopic dust content, and surface wettability. Key findings were:

- Dust accumulating on PV modules in Qatar comprised mainly mineral particles, but also contained small but important amounts of known hygroscopic species: NaCl, nitrate and sulfate
- Capillary condensation occurred only when NaCl or other hygroscopic species were present in the dust — condensation was not observed on pure or washed mineral dusts even when RH exceeded 90%
- Dusts exhibited swelling (deliquescence) only when hygroscopic species other than NaCl were present, indicating that NaCl is not the main driver of water uptake by the soiling layer
- Natural Qatar dust adsorbed water vapor moderately from 60-70% RH, and greatly from 80-90% RH
- At the Qatar test site, during the night PV modules could become much cooler than the ambient air
- Glass coupons in the field bore microscopic droplets while still 14 °C above the dew point. The droplets grew when the surface/dew point temperature difference fell below 8 °C, and flooded the surface when it fell below 1-2 °C
- A hydrophobic PTFE coupon also showed microscopic droplets while still much warmer than the dew point, but compared to the glass coupon it inhibited growth of those droplets and prevented flooding as the coupon cooled.
- Heating the coupon reduced, but did not eliminate, the presence of microscopic condensation droplets, indicating that hygroscopic material in the dust plays an important role in promoting surface moisture
- An unheated coupon built-up more dust overnight than the heated coupon, but much of that extra build-up was dispersed during the daytime as the coupon dried out and wind speeds increased.

Original and important conclusions from this research are:

- The OSM is a useful tool for measuring soiling and condensation in field conditions, in particular allowing dust fluxes to be measured in small quantities and short time periods, and separating dust accumulation into its component flux rates. It is a novel experimental technique that complements laboratory wind-tunnels and field tests of operating PV modules
- The dust accumulation rate in desert environments is most strongly controlled by WS; RH and even PM have relatively little influence (except in dust-storm conditions). Although high wind speed increases both deposition and resuspension of dust, the net effect was that surfaces generally became cleaner average when WS exceeded

$\sim 3 \text{ ms}^{-1}$. The OSM revealed that this was largely due to higher rebound fraction of impacting particles, as WS increased

- Models of particle deposition derived from laboratory wind-tunnel experiments are less accurate than those derived from ambient observations, for predicting dust deposition in desert environments. In particular, the present results and one ambient model from Chicago show that the deposition rate has a threshold response to wind speed. In Qatar, in $WS < 3.2 \text{ ms}^{-1}$ deposition was fully accounted for by gravity, and in $WS > 3.2 \text{ ms}^{-1}$ inertial deposition became apparent
- Moisture is prevalent on glass surfaces even in desert environments, because (i) the surfaces can cool to well below the ambient temperature at night, and (ii) hygroscopic material in dust promotes water adsorption. It was even observed on hydrophobic coatings significantly warmer than the dew-point temperature. Its effects are to reduce the degree to which strong wind causes dust to resuspend (due to capillary adhesion), and reduce the resuspension rate over days of exposure (due to cementation)
- The effects of wind speed and surface moisture combine to create notable time-of-day patterns in dust flux rates on ambient surfaces. It was found that dust tends to build up on the surface overnight, when RH is high and WS low. Much of this build-up is then dispersed the following day as the surface dries out, RH decreases and WS increases. (These observations were enabled by the OSM's 10-minute measurement period and had not been previously revealed).

Based on these results, the following recommendations are made for PV soiling mitigation and future research:

- PV systems should be located at sites of high wind speed and low/moderate PM — Although windy conditions elevate both dust deposition and detachment, the net result was a powerful reduction of soiling with increasing WS. Especially, when WS reached $\sim 2.5 \text{ ms}^{-1}$, average dust accumulation was zero. PM concentration had little effect on soiling at low-to-moderate levels, but when it exceeded $\sim 0.2 \text{ mg.m}^{-3}$ dust accumulation increased rapidly. Further research is recommended to test the effectiveness of this strategy, by conducting field trials with full-size PV modules at multiple locations having a variety of WS and PM profiles
- PV mounting design can be optimized to reduce soiling — In addition to site selection, higher wind speed on PV modules can be achieved by their mounting. Elevating modules higher above the ground places them in faster air flow (and also lower PM concentration). Especially, mounting PV modules on a solar tracker creates the opportunity to adjust the tilt angle to take account of soiling conditions: the tracker might be programed to incline vertically at night to minimize deposition, and during dry windy periods incline at an angle that maximizes airflow friction velocity and achieves some dust resuspension. It would be a useful and practical exercise to construct several single-module trackers and program them with different tilt algorithms, to evaluate the effectiveness of such a technique

- Anti-soiling coatings should be studied with regard to condensation — It was found that microscopic droplets can exist even on hydrophobic surfaces much warmer than the dew point, due to hygroscopic matter on the surface or in depositing aerosol droplets. This suggests that, in coastal desert locations, it would be a difficult goal for an anti-soiling coating to eliminate condensation. It might be expected that a hydrophobic coating would reduce soiling because (i) this study demonstrated that they inhibit water uptake by the soiling layer, and (ii) the literature holds that particles experience weaker adhesion on hydrophobic surfaces at all RH levels. Yet it is not established that these effects translate to less soiling of hydrophobic-coated PV modules in real-world conditions. It might be that a hydrophilic coating could promote condensation, leading to beneficial water shedding and self-cleaning. Therefore it is recommended that tests of anti-soiling coatings be conducted in a range of RH conditions and tilt angles, while recording the degree of condensation and its run-off, to distinguish between coating performance in dry and humid conditions. Variation in these parameters may partly explain inconsistent results from anti-soiling coating field trials in the literature
- Specific wind-speed effects on particle motions should be studied further — Some striking and unexpected relations between WS and dust flux rates were observed. Particularly, there was a threshold WS above which deposition sharply increased, and a significant fraction of particle rebound even at near-zero wind speed. Conducting focused experiments to understand these phenomena might provide insights on aerosol mechanics in ambient conditions. For example, the WS threshold of deposition might be related to the geometry of the OSM and its coupon, which could be investigated by computational fluid dynamics. This study dealt with coupons at horizontal orientation (in order to eliminate wind direction as a source of variation), whereas PV modules are tilted. Hence further research might also be conducted of dust flux rates on tilted coupons in ambient conditions, as a function of wind direction.

9. References

1. Aluko, O., and Noll, K.E. (2006) Deposition and Suspension of Large, Airborne Particles. *Aerosol Sci. Technol.*, **40** (7), 503–513.
2. Figgis, B.W. (2016) Solar Test Facility in Doha, Qatar. DOI 10.13140/RG.2.2.21049.77925.
3. Goossens, D., Offer, Z.Y., and Zangvil, A. (1993) Wind tunnel experiments and field investigations of eolian dust deposition on photovoltaic solar collectors. *Sol. Energy*, **50** (1), 75–84.
4. Jamil, W.J., Abdul Rahman, H., Shaari, S., and Salam, Z. (2017) Performance degradation of photovoltaic power system: Review on mitigation methods. *Renew. Sustain. Energy Rev.*, **67**, 876–891.
5. Costa, S.C.S., Sonia, A., Diniz, A.C., and Kazmerski, L.L. (2016) Dust and soiling issues and impacts relating to solar energy systems : Literature review update for 2012 – 2015. *Renew. Sustain. Energy Rev.*, **63**, 33–61.
6. Mani, M., and Pillai, R. (2010) Impact of dust on solar photovoltaic (PV) performance: Research status, challenges and recommendations. *Renew. Sustain. Energy Rev.*, **14** (9), 3124–3131.
7. Said, S.A.M., and Walwil, H.M. (2014) Fundamental studies on dust fouling effects on PV module performance. *Sol. Energy*, **107**, 328–337.
8. Sayyah, A., Horenstein, M.N., and Mazumder, M.K. (2014) Energy yield loss caused by dust deposition on photovoltaic panels. *Sol. Energy*, **107**, 576–604.
9. Guo, B., Javed, W., Figgis, B.W., and Mirza, T. (2015) Effect of dust and weather conditions on photovoltaic performance in Doha, Qatar. *2015 1st Work. Smart Grid Renew. Energy, SGRE 2015*.
10. Boyle, L., Flinchpaugh, H., and Hannigan, M. (2016) Assessment of PM Dry Deposition on Solar Energy Harvesting Systems: Measurement - Model Comparison. *Aerosol Sci. Technol.*, **6826** (February 2016).
11. Musango, J. (2016) Measuring and modelling the influence of weather factors on CSP reflector soiling.
12. Micheli, L., Muller, M., and Kurtz, S. (2016) Determining the effects of environment and atmospheric parameters on PV field performance. *Photovolt. Spec. Conf. (PVSC), 2016 IEEE 43th*, 1724–1729.
13. Noll, K.E., Fang K. Y. P., and Watkins, L.A. (1988) Characterization of the Deposition of Particles from the Atmosphere to a Flat Plate. *Atmos. Environ.*, **22** (7), 1461–1468.
14. Bowling, R.A. (1985) An Analysis of Particle Adhesion on Semiconductor Surfaces. **157** (1980), 2208–2214.
15. Ziskind, G., Fichman, M., and Gutfinger, C. (1995) Resuspension of particulates from surfaces to turbulent flows- Review and analysis. *J. Aerosol Sci.*, **26** (4), 613–644.
16. Loosmore, G., and Hunt, J.R. (2000) Dust resuspension without saltation. *J Geophys Res.*, **105**, 20663–20672.
17. Goossens, D. (2005) Quantification of the dry aeolian deposition of dust on horizontal surfaces: An experimental comparison of theory and measurements. *Sedimentology*, **52** (4), 859–873.
18. Ibrahim, A.H., Dunn, P.F., and Brach, R.M. (2004) Microparticle detachment from surfaces exposed to turbulent air flow: Effects of flow and particle deposition characteristics. *J. Aerosol Sci.*, **35**, 805–821.
19. Sehmel, G.A. (1980) Particle and gas dry deposition: A review. *Atmos. Environ.*, **14** (9), 983–1011.
20. Ruijgrok, W., Davidson, C.I., and Nicholson, K.W. (1995) Dry deposition of particles - implications and recommendations for mapping of deposition over Europe. *Tellus Ser. B-Chemical Phys. Meteorol.*, **47** (5), 587–601.

21. Holsen, T.M., and Noll, K.E. (1992) Dry deposition of atmospheric particles: application of current models to ambient data. *Environ. Sci. Technol.*, **26** (9), 1807–1815.
22. Nicholson, K.W. (1988) A review of particle resuspension. *Atmos. Environ.*, **22** (12), 2639–2651.
23. Kim, Y., Gidwani, A., Wyslouzil, B.E., and Sohn, C.W. (2010) Source term models for fine particle resuspension from indoor surfaces. *Build. Environ.*, **45** (8), 1854–1865.
24. Habchi, C., Ghali, K., and Ghaddar, N. (2016) Coupling CFD and analytical modeling for investigation of monolayer particle resuspension by transient flows. *Build. Environ.*, **105**, 1–12.
25. Wood, N.B. (1981) A simple method for the calculation of turbulent deposition to smooth and rough surfaces. *J. Aerosol Sci.*, **12** (3), 275–290.
26. Qiang, M., Chen, F., Zhou, A., et al. (2007) Impacts of wind velocity on sand and dust deposition during dust storm as inferred from a series of observations in the northeastern Qinghai – Tibetan Plateau , China. *Powder Technol.*, **175**, 82–89.
27. Lombardo, T., Ionescu, A., Chabas, A., et al. (2010) Dose-response function for the soiling of silica-soda-lime glass due to dry deposition. *Sci. Total Environ.*, **408** (4), 976–984.
28. Goossens, D. (2018) Wind tunnel protocol to study the effects of anti-soiling and anti-reflective coatings on deposition, removal, and accumulation of dust on photovoltaic surfaces and consequences for optical transmittance. *Sol. Energy*, **163** (January), 131–139.
29. Lin, J.J., Noll, K.E., and Holsen, T.M. (1994) Dry Deposition Velocities as a Function of Particle Size in the Ambient Atmosphere. *Aerosol Sci. Technol.*, **20** (3), 239–252.
30. Javed, W., Wubulikasimu, Y., Figgis, B., and Guo, B. (2017) Characterization of dust accumulated on photovoltaic panels in Doha, Qatar. *Sol. Energy*, (142), 123–135.
31. Noll, K.E., and Fang, K.Y.P. (1989) Development of a dry deposition model for atmospheric coarse particles. *Atmos. Environ.*, **23** (3), 585–594.
32. Noll, K.E., and Aluko, O. (2006) Changes in large particle size distribution due to dry deposition processes. *J. Aerosol Sci.*, **37** (12), 1797–1808.
33. Figgis, B., Ennaoui, A., Ahzi, S., and Rémond, Y. (2016) Review of PV Soiling Measurement Methods. *Int. Renew. Sustain. Energy Conf. (IRSEC)*, 2016.
34. Biryukov, S. (1998) An experimental study of the dry deposition. *J. Aerosol Sci.*, **29** (1–2), 129–139.
35. Al-Hasan, A.Y., and Ghoneim, A.A. (2005) A new correlation between photovoltaic panel’s efficiency and amount of sand dust accumulated on their surface. *Int. J. Sustain. Energy*, **24** (4), 187–197.
36. El-Shobokshy, M.S., and Hussein, F.M. (1993) Degradation of photovoltaic cell performance due to dust deposition on to its surface. *Renew. Energy*, **3** (6–7), 585–590.
37. Elminir, H.K., Ghitas, A.E., Hamid, R.H., et al. (2006) Effect of dust on the transparent cover of solar collectors. *Energy Convers. Manag.*, **47** (18–19), 3192–3203.
38. Javed, W., Guo, B., Wubulikasimu, Y., and Figgis, B.W. (2016) Photovoltaic Performance Degradation Due to Soiling and Characterization of the Accumulated Dust. *IEEE 2016 Int. Conf. Power Renew. Energy*.
39. Klimm, E., Ost, L., Lorenz, T., et al. (2014) Impact of Sand Deposition and Adhesion on Solar Glass Under Dew Conditions. *Gleisd. Sol. 2014*.
40. Ilse, K., Werner, M., Naumann, V., et al. (2016) Microstructural analysis of the cementation process during soiling on glass surfaces in arid and semi-arid climates. *Phys. status solidi - Rapid Res. Lett.*, **10** (7), 525–529.

41. Wu, Y., Davidson, C.I., Lindberg, S.E., and Russell, A. (1992) Resuspension of Particulate Chemical Species at Forested Sites. *Environ. Sci. Technol.*, **26** (12), 2428–2435.
42. Aïssa, B., Isaifan, R.J., Madhavan, V.E., and Abdallah, A.A. (2016) Structural and physical properties of the dust particles in Qatar and their influence on the PV panel performance. *Sci. Rep.*, (6:31467), 1–12.
43. Appels, R., Muthirayan, B., Beerten, A., et al. (2012) The effect of dust deposition on photovoltaic modules. *Conf. Rec. IEEE Photovolt. Spec. Conf.*
44. Wohlgemuth, J., and Kurtz, S. (2014) International PV QA Task Force's Proposed Comparative Rating System for PV Modules. *SPIE Opt. Photonics 2014*.
45. John, J.J., Warade, S., Tamizhmani, G., and Kottantharayil, A. (2016) Study of soiling loss on photovoltaic modules with artificially deposited dust of different gravimetric densities and compositions collected from different locations in India. *IEEE J. Photovoltaics*, **6** (1), 236–243.
46. Sarver, T., Al-Qaraghuli, A., and Kazmerski, L.L. (2013) A comprehensive review of the impact of dust on the use of solar energy: History, investigations, results, literature, and mitigation approaches. *Renew. Sustain. Energy Rev.*, **22**, 698–733.
47. Figgis, B., Ennaoui, A., Guo, B., et al. (2016) Outdoor soiling microscope for measuring particle deposition and resuspension. *Sol. Energy*, **137**, 158–164.
48. Jiang, H., Lu, L., and Sun, K. (2011) Experimental investigation of the impact of airborne dust deposition on the performance of solar photovoltaic (PV) modules. *Atmos. Environ.*, **45** (25), 4299–4304.
49. Hegazy, A.A. (2001) Effect of dust accumulation on solar transmittance through glass covers of plate-type collectors. *Renew. Energy*, **22**, 525–540.
50. Yilbas, B.S., Ali, H., Al-Aqeeli, N., et al. (2016) Influence of mud residues on solvent induced crystalized polycarbonate surface used as PV protective cover. *Sol. Energy*, **125**, 282–293.
51. Bahattab, M.A., Alhomoudi, I.A., Alhussaini, M.I., et al. (2016) Solar Energy Materials & Solar Cells Anti-soiling surfaces for PV applications prepared by sol-gel processing : Comparison of laboratory testing and outdoor exposure. *Sol. Energy Mater. Sol. Cells*, **157**, 422–428.
52. Burton, P.D., Hendrickson, A., Ulibarri, S.S., et al. (2016) Pattern Effects of Soil on Photovoltaic Surfaces. *IEEE J. PHOTOVOLTAICS*, **6** (4), 976–980.
53. Brown, K., Narum, T., and Jing, N. (2012) Soiling test methods and their use in predicting performance of photovoltaic modules in soiling environments. *Conf. Rec. IEEE Photovolt. Spec. Conf.*, 1881–1885.
54. Brophy, B., Abrams, Z.R., Gonsalves, P., and Christy, K. (2015) Field performance and persistence of anti-soiling coatings on photovoltaic glass. *EU PVSEC 2015*.
55. Qasem, H., Betts, T.R., Müllejans, H., et al. (2014) Dust-induced shading on photovoltaic modules. *Prog. Photovoltaics Res. Appl.*, **22** (2), 218–226.
56. Gostein, M., Caron, J.R., and Littmann, B. (2014) Evaluation of a CdTe spectrally matched c-Si PV reference cell for outdoor applications. *2014 IEEE 40th Photovolt. Spec. Conf. PVSC 2014*, 771–775.
57. Gostein, M., Littmann, B., Caron, J.R., and Dunn, L. (2013) Comparing PV power plant soiling measurements extracted from PV module irradiance and power measurements. *Conf. Rec. IEEE Photovolt. Spec. Conf. 2013*, 3004–3009.
58. Dunn, L., Littmann, B., Caron, J.R., and Gostein, M. (2013) PV Module Soiling Measurement Uncertainty Analysis. *Proc. 39th IEEE Photovolt. Spec. Conf. 2013*, 658–663.
59. Roth, R. (2012) Effect of soiling on performances of crystalline silicon PV modules deployed in an arid climate in relation to front glass texture and treatment.

60. Hoffman, A.R., and Maag, C.R. (1980) Photovoltaic Module Soiling Studies. *May 1978–October 1980 DOE/JPL-1012-49*.
61. Goossens, D., and Kerschaefer, E.V.A.N. (1999) Aeolian Dust Deposition on Photovoltaic Solar Cells : the Effects of Wind Velocity and Airborne Dust Concentration on Cell Performance. *Sol. Energy*, **66** (4), 277–289.
62. Touati, F., Al-Hitmi, M.A., Chowdhury, N.A., et al. (2016) Investigation of solar PV performance under Doha weather using a customized measurement and monitoring system. *Renew. Energy*, **89**, 564–577.
63. Schill, C., Brachmann, S., and Koehl, M. (2015) Impact of soiling on IV-curves and efficiency of PV-modules. *Sol. Energy*, **112**, 259–262.
64. Gostein, M., Duster, T., and Thuman, C. (2015) Accurately measuring PV soiling losses with soiling station employing module power measurements. *IEEE 42nd Photovolt. Spec. Conf. (PVSC 2015)*.
65. Gostein, M., Stueve, B., Brophy, B., et al. (2016) Soiling Measurement Station to Evaluate Anti-Soiling Properties of PV Module Coatings. *IEEE 43rd Photovolt. Spec. Conf. (PVSC 2016)*.
66. Molki, A. (2010) Dust affects solar-cell efficiency. *Phys. Educ.*, **45** (5), 456–458.
67. Makrides, G., Zinsser, B., Schubert, M., and Georghiou, G.E. (2014) Performance loss rate of twelve photovoltaic technologies under field conditions using statistical techniques. *Sol. Energy*, **103**, 28–42.
68. Kaldellis, J.K., and Kapsali, M. (2011) Simulating the dust effect on the energy performance of photovoltaic generators based on experimental measurements. *Energy*, **36** (8), 5154–5161.
69. Abdulameer, A., and Al-Khazzar, A. (2015) A New Method to Reduce Soiling Effect on Performance of a Solar PV Module. *J. Adv. Res. Innov.*, **3** (4), 601–606.
70. Gostein, M., Caron, J.R., and Littmann, B. (2014) Measuring soiling losses at utility-scale PV power plants. *IEEE 40th Photovolt. Spec. Conf. (PVSC 2014)*, 885–890.
71. Dahneke, B. (1973) Measurements of the bouncing of small latex spheres. *J. Colloid Interface Sci.*, **45** (3), 584–590.
72. Wu, Y.-L., Davidson, C.I., and Russell, A.G. (1992) Controlled Wind Tunnel Experiments for Particle Bounceoff and Resuspension. *Aerosol Sci. Technol.*, **17** (4), 245–262.
73. Kassab, A.S., Ugaz, V.M., King, M.D., and Hassan, Y.A. (2013) High Resolution Study of Micrometer Particle Detachment on Different Surfaces. *Aerosol Sci. Technol.*, **47** (4), 351–360.
74. Farzi, B., Vallabh, C.K.P., Stephens, J.D., and Cetinkaya, C. (2016) Critical rolling angle of microparticles. *Appl. Phys. Lett.*, **108** (11), 111602-1-5.
75. Biryukov, S., Faiman, D., and Goldfeld, A. (1999) An Optical System for the Quantitative Study of Particulate Contamination on Solar Collector Surfaces. *Sol. Energy*, **66** (5), 371–378.
76. Barth, T., Preuß, J., Müller, G., and Hampel, U. (2014) Single particle resuspension experiments in turbulent channel flows. *J. Aerosol Sci.*, **71**, 40–51.
77. Kim, Y., Wellum, G., Mello, K., et al. (2016) Effects of relative humidity and particle and surface properties on particle resuspension rates. *Aerosol Sci. Technol.*, **50** (4), 2016, 339–352.
78. Yap, W.K., Galet, R., and Yeo, K.C. (2015) Quantitative Analysis of Dust and Soiling on Solar PV Panels in the Tropics Utilizing Image-Processing Methods. *2015 Asia-Pacific Sol. Res. Conf.*
79. Biryukov, S.A. (1996) Degradation of optical properties of solar collectors due to the ambient dust deposition as a function of particle size. *J. Aerosol Sci.*, **27**, S37–S38.
80. Hinds, W.C. (1999) *Aerosol Technology: Properties, Behavior, and Measurement of Airborne Particles*, 2nd

Edition, Wiley.

81. Noll, K.E., Jackson, M.M., and Oskouie, A.K. (2001) Development of an Atmospheric Particle Dry Deposition Model. *Aerosol Sci. Technol.*, **35** (2), 627–636.
82. Henry, C., and Minier, J.P. (2014) Progress in particle resuspension from rough surfaces by turbulent flows. *Prog. Energy Combust. Sci.*, **45**, 1–53.
83. Lu, H., Lu, L., and Wang, Y. (2016) Numerical investigation of dust pollution on a solar photovoltaic (PV) system mounted on an isolated building. *Appl. Energy*, **180**, 27–36.
84. Friedlander, S.K. (1977) *Smoke, Dust, and Haze*, John Wiley & Sons, Inc.
85. Kim, E., Kalman, D., and Larson, T. (2000) Dry deposition of large, airborne particles onto a surrogate surface. *Atmos. Environ.*, **34** (15), 2387–2397.
86. Weber, B., Quiñones, A., Almanza, R., and Duran, M.D. (2014) Performance reduction of PV systems by dust deposition. *Energy Procedia*, **57**, 99–108.
87. Barrie, L.A. (1985) Atmospheric particles: Their physical and chemical characteristics, and deposition processes relevant to chemical composition of glaciers. *Ann. Glaciol.*, **7**, 100–108.
88. Jahangiri, M., Ghaderi, R., Haghani, A., and Nematollahi, O. (2016) Finding the best locations for establishment of solar-wind power stations in Middle-East using GIS: A review. *Renew. Sustain. Energy Rev.*, **66**, 38–52.
89. Picotti, G., Borghesani, P., Cholette, M.E., and Manzolini, G. (2017) Soiling of solar collectors - Modelling approaches for airborne dust and its interactions with surfaces. *Renew. Sustain. Energy Rev.*, **81** (2), 2343–2357.
90. Kaaden, N., Massling, A., Schladitz, A., et al. (2009) State of mixing, shape factor, number size distribution, and hygroscopic growth of the Saharan anthropogenic and mineral dust aerosol at Tinfou, Morocco. *Tellus, Ser. B Chem. Phys. Meteorol.*, **61** (1), 51–63.
91. Lau, R., and Chuah, H.K.L. (2013) Dynamic shape factor for particles of various shapes in the intermediate settling regime. *Adv. Powder Technol.*, **24** (1), 306–310.
92. Sehmel, G.A. (1980) Particle resuspension: A review. *Environ. Int.*, **4** (2), 107–127.
93. Weber, R.O. (1999) Remarks on the definition and estimation of friction velocity. *Boundary-Layer Meteorol.*, **93**, 197–209.
94. Sehmel, G.A. (1973) Particle eddy diffusivities and deposition velocities for isothermal flow and smooth surfaces. *J. Aerosol Sci.*, **4** (2), 125–138.
95. Slinn, S.A., and Slinn, W.G.N. (1980) Predictions for particle deposition on natural waters. *Atmos. Environ.*, **14** (9), 1013–1016.
96. Nho-kim, E., Michou, M., and Peuch, V. (2004) Parameterization of size-dependent particle dry deposition velocities for global modeling. *Atmos. Environ.*, **38**, 1933–1942.
97. Zhao, B., and Wu, J. (2006) Modeling particle deposition onto rough walls in ventilation duct. *Atmos. Environ.*, **40** (36), 6918–6927.
98. Muyschondt, A., Anand, N.K., and Mcfarland, A.R. (1996) Turbulent Deposition of Aerosol Particles in Large Transport Tubes. *Aerosol Sci. Technol.*, **24** (2), 107–116.
99. Liu, B.Y.H., and Agarwal, J.K. (1974) Experimental observation of aerosol deposition in turbulent flow. *J. Aerosol Sci.*, **5** (2), 145–155.
100. Owen, P.R. (1969) Pneumatic transport. *J. Fluid Mech.*, **39** (2), 407.

101. Fromentin, A. (1989) Time dependent particle resuspension from a multi-layer deposit by turbulent flow. *J. Aerosol Sci.*, **20** (8), 911–914.
102. Noll, K.E., and Fang, K.Y.P. (1986) A Rotary Impactor for size selective sampling of atmospheric coarse particles. *79th Annu. Meet. Air Pollut. Control Assoc.*
103. Dahneke, B. (1971) The capture of aerosol particles by surfaces. *J. Colloid Interface Sci.*, **37** (2), 342–353.
104. Paw U, K.T., and Braaten, D.A. (1995) New Perspectives on Rebound and Reentrainment Processes. *Aerosol Sci. Technol.*, **23** (1), 72–79.
105. Bateman, A.P., Belassein, H., and Martin, S.T. (2014) Impactor Apparatus for the Study of Particle Rebound: Relative Humidity and Capillary Forces. *Aerosol Sci. Technol.*, **48**, 42–52.
106. Dahneke, B. (1975) Further measurements of the bouncing of small latex spheres. *J. Colloid Interface Sci.*, **51** (1), 58–65.
107. Kok, J.F., Parteli, E.J.R., Michaels, T.I., and Karam, D.B. (2012) The physics of wind-blown sand and dust. *Reports Prog. Phys.*, **75** (10).
108. Biryukov, S. (1998) Supplement - An experimental study of the dry deposition mechanism for airborne dust for airborne dust. *J. Aerosol Sci.*, **27** (Suppl 1), S77–S78.
109. Winkler, P. (1974) Relative Humidity and the Adhesion of Atmospheric Particles to the Plate of Impactors. *J. Aerosol Sci.*, **5**, 235–240.
110. Hall, D. (1988) Measurements of the mean force on a particle near a boundary in turbulent flow. *J. Fluid Mech.*, **187**, 451–466.
111. Gradon, L. (2009) Resuspension of particles from surfaces: Technological, environmental and pharmaceutical aspects. *Adv. Powder Technol.*, **20** (1), 17–28.
112. Ahmadi, G., Guo, S., and Zhang, X. (2007) Particle Adhesion and Detachment in Turbulent Flows Including Capillary Forces. *Part. Sci. Technol.*, **25** (1), 59–76.
113. Ibrahim, A.H., Dunn, P.F., and Brach, R.M. (2003) Microparticle detachment from surfaces exposed to turbulent air flow: controlled experiments and modeling. *J. Aerosol Sci.*, **34**, 765–782.
114. Cleaver, J.W., and Yates, B. (1973) Mechanism of detachment of colloidal particles from a flat substrate in a turbulent flow. *J. Colloid Interface Sci.*, **44** (3), 464–474.
115. Benito, J.G., Uñac, R.O., Vidales, A.M., and Ippolito, I. (2016) Validation of the Monte Carlo model for resuspension phenomena. *J. Aerosol Sci.*, **100**, 26–37.
116. Keedy, R., Dengler, E., Ariessohn, P., et al. (2012) Removal Rates of Explosive Particles From a Surface by Impingement of a Gas Jet. *Aerosol Sci. Technol.*, **46** (2), 148–155.
117. Reeks, M.W., Reed, J., and Hall, D. (1988) On the resuspension of small particles by a turbulent flow. *J. Phys. D. Appl. Phys.*, **21** (4), 574–589.
118. Gillette, D.A., Lawson, R.E., and Thompson, R.S. (2004) A “test of concept” comparison of aerodynamic and mechanical resuspension mechanisms for particles deposited on field rye grass (*Secale cereale*). Part 1. Relative particle flux rates. *Atmos. Environ.*, **38** (28), 4789–4797.
119. O’Neill, M.E. (1968) A sphere in contact with a plane wall in a slow linear shear flow. *Chem. Eng. Sci.*, **23** (11), 1293–1298.
120. Busnaina, A.A., and Elsayy, T. (2000) The effect of relative humidity on particle adhesion and removal. *J. Adhes.*, **74** (1–4), 391–409.

121. Vatistas, N. (1989) The Effect of Adhesion Time on Particle Deposition. *Chem. Eng. Sci.*, **44** (8), 1603–1608.
122. Zimon, A.D. (1969) *Adhesion of Dust and Powder*, Spring Science and Business Media.
123. Grzybowski, K., and Gradoń, L. (2004) Re-entrainment of particles from powder structures. *Adv. Powder Technol.*, **16** (2), 105–121.
124. Barth, T., Reiche, M., Banowski, M., et al. (2013) Experimental investigation of multilayer particle deposition and resuspension between periodic steps in turbulent flows. *J. Aerosol Sci.*, **64**, 111–124.
125. Reeks, M.W., and Hall, D. (2001) Kinetic models for particle resuspension in turbulent flows: theory and measurement. *J. Aerosol Sci.*, **32**, 1–31.
126. Henry, C., Minier, J.P., and Lefevre, G. (2012) Numerical study on the adhesion and reentrainment of nondeformable particles on surfaces: The role of surface roughness and electrostatic forces. *Langmuir*, **28** (1), 438–452.
127. Ionescu, A., Lefèvre, R.A., Chabas, A., et al. (2006) Modeling of soiling based on silica-soda-lime glass exposure at six European sites. *Sci. Total Environ.*, **369** (1–3), 246–255.
128. Autumn, K., Sitti, M., Liang, Y. a, et al. (2002) Evidence for van der Waals adhesion in gecko setae. *Proc. Natl. Acad. Sci. U. S. A.*, **99** (19), 12252–12256.
129. Israelachvili, J.N. (1992) *Intermolecular and Surface Forces, 2nd Edition*, Academic Press.
130. Leite, F.L., Bueno, C.C., Da Róz, A.L., et al. (2012) Theoretical models for surface forces and adhesion and their measurement using atomic force microscopy. *Int. J. Mol. Sci.*, **13** (10), 12773–12856.
131. Qi, Q., and Brereton, G.J. (1995) Mechanisms of removal of micron-sized particles by high-frequency ultrasonic waves. *IEEE Trans. Ultrason. Ferroelectr. Freq. Control*, **42** (4), 619–629.
132. Tomas, J. (2004) Mechanics of particle adhesion. *CHISA 2004, 16th Int. Congr. Chem. Process Eng. Prague*.
133. Berbner, S., and Loeffler, F. (1994) Influence of high temperatures on particle adhesion. *Powder Technol.*, **78**, 273–280.
134. Lomboy, G., Sundararajan, S., Wang, K., and Subramaniam, S. (2011) A test method for determining adhesion forces and Hamaker constants of cementitious materials using atomic force microscopy. *Cem. Concr. Res.*, **41** (11), 1157–1166.
135. Corn, M. (1961) The Adhesion of Solid Particles to Solid Surfaces, I. A Review. *J. Air Pollut. Control Assoc.*, **11** (11), 523–528.
136. Jones, R., Pollock, H.M., Cleaver, J.A.S., and Hodges, C.S. (2002) Adhesion forces between glass and silicon surfaces in air studied by AFM: Effects of relative humidity, particle size, roughness, and surface treatment. *Langmuir*, **18** (21), 8045–8055.
137. Ranade, M.B. (1987) Adhesion and Removal of Fine Particles on Surfaces. *Aerosol Sci. Technol.*, **7** (2), 161–176.
138. Bethea, R.M., Barriger, M.T., Williams, P.F., and Chin, S. (1981) Environmental effects on solar concentrator mirrors. *Sol. Energy*, **27** (6), 497–511.
139. Sayyah, A., Crowell, D.R., Raychowdhury, A., et al. (2017) An experimental study on the characterization of electric charge in electrostatic dust removal. *J. Electrostat.*, **87**, 173–179.
140. Castle, G.S.P. (1997) Contact charging between insulators. *J. Electrostat.*, **40–41**, 13–20.
141. Castle, G.S.P., and Schein, L.B. (1995) General model of sphere-sphere insulator contact electrification. *J. Electrostat.*, **36** (2), 165–173.

142. Cuddihy, E.F. (1980) Theoretical considerations of soil retention. *Sol. Energy Mater.*, **3** (1–2), 21–33.
143. Detry, J.G., Sindic, M., Servais, M.J., et al. (2011) Physico-chemical mechanisms governing the adherence of starch granules on materials with different hydrophobicities. *J. Colloid Interface Sci.*, **355** (1), 210–221.
144. Curry, J.E., and Kim, S. (2004) Adhesion between surfaces coated with self-assembled monolayers: effect of humidity, in *Dekker Encyclopedia of Nanoscience and Nanotechnology*, Marcel Dekker, Inc.
145. Fuji, M., Machida, K., Takei, T., and Watanabe, T. (1999) Effect of Wettability on Adhesion Force between Silica Particles Evaluated by Atomic Force Microscopy Measurement as a Function of Relative Humidity. *Langmuir*, **15** (13), 4584–4589.
146. Kim, D.I., Grobelny, J., Pradeep, N., and Cook, R.F. (2008) Origin of adhesion in humid air. *Langmuir*, **24** (5), 1873–1877.
147. Grant, D. (1974) The surface resistivity of a cooled glass surface at the onset of water vapour condensation.
148. Brambilla, S., Speckart, S., and Brown, M.J. (2017) Adhesion and aerodynamic forces for the resuspension of non-spherical particles in outdoor environments. *J. Aerosol Sci.*, **112**, 52–67.
149. Rabinovich, Y.I., Adler, J.J., Esayanur, M.S., et al. (2002) Capillary forces between surfaces with nanoscale roughness. *Adv. Colloid Interface Sci.*, **96** (1–3), 213–230.
150. Savoy, E.S., and Escobedo, F.A. (2016) Molecular simulation of the effects of humidity and of interfacial Si- and B-hydroxyls on the adhesion energy between glass plates. *J. Colloid Interface Sci.*, **465**, 233–241.
151. Quon, R.A., Ulman, A., and Vanderlick, T.K. (2000) Impact of humidity on adhesion between rough surfaces. *Langmuir*, **16** (23), 8912–8916.
152. McCormick, J.L., and Westwater, J.W. (1965) Nucleation sites for dropwise condensation. *Chem. Eng. Sci.*, **20** (12), 1021–1036.
153. Xiao, X., and Qian, L. (2000) Investigation of humidity-dependent capillary force. *Langmuir*, **16** (21), 8153–8158.
154. Eriksson, T.S., and Granqvist, C.G. (1982) Radiative cooling computed for model atmospheres. *Appl. Opt.*, **21** (23), 4381–4388.
155. Tang, R., Etzion, Y., and Meir, I.A. (2004) Estimates of clear night sky emissivity in the Negev Highlands, Israel. *Energy Convers.*, **45**, 1831–1843.
156. Yin, Y.L., Wang, R.Z., Zhai, X.Q., and Ishugah, T.F. (2014) Experimental investigation on the heat transfer performance and water condensation phenomenon of radiant cooling panels. *Build. Environ.*, **71**, 15–23.
157. Arsalan, N. (2011) Surface Energy Characterization of Reservoir Rocks.
158. Staffan Sjogren, N.O. (1976) Hygroscopic Properties of Organic and Inorganic Aerosols.
159. Shi, Z., Zhang, D., Hayashi, M., et al. (2008) Influences of sulfate and nitrate on the hygroscopic behaviour of coarse dust particles. *Atmos. Environ.*, **42** (4), 822–827.
160. Vlasenko, A., Sjögren, S., Weingartner, E., et al. (2005) Generation of Submicron Arizona Test Dust Aerosol: Chemical and Hygroscopic Properties. *Aerosol Sci. Technol.*, **39** (5), 452–460.
161. Curcio, J.A. (1976) Adsorption and Condensation of Water on Mirror and Lens Surfaces. *NRL Memo. Rep. 3359*.
162. Zelenyuk, A., Imre, D., Cuadra-Rodriguez, L.A., and Ellison, B. (2007) Measurements and interpretation of the effect of a soluble organic surfactant on the density, shape and water uptake of hygroscopic particles. *J. Aerosol Sci.*, **38** (9), 903–923.
163. Ma, Q., He, H., Liu, Y., et al. (2013) Heterogeneous and multiphase formation pathways of gypsum in the

- atmosphere. *Phys. Chem. Chem. Phys.*, **15** (44), 19196–19204.
164. Herich, H., Tritscher, T., Wiacek, A., et al. (2009) Water uptake of clay and desert dust aerosol particles at sub- and supersaturated water vapor conditions. *Phys. Chem. Chem. Phys.*, **11** (36), 7804–9.
 165. Balarew, C. (1987) Evaporite Minerals Succession. *Cryst. Res. Technol.*, **22** (10), 1241–1248.
 166. Jentzsch, P.V., Kampe, B., Ciobotă, V., et al. (2013) Inorganic salts in atmospheric particulate matter: Raman spectroscopy as an analytical tool. *Spectrochim. Acta - Part A Mol. Biomol. Spectrosc.*, **115**, 697–708.
 167. Gustafsson, R.J., Orlov, A., Badger, C.L., et al. (2005) A comprehensive evaluation of water uptake on atmospherically relevant mineral surfaces. *Atmos. Chem. Phys. Discuss.*, **5** (4), 7191–7210.
 168. Walker, J. (1980) *The Physics of Everyday Phenomena*, W.H.Freeman & Co Ltd.
 169. Wang, Y., Chen, L., Chen, R., et al. (2017) Effect of relative humidity on the deposition and coagulation of aerosolized SiO₂ nanoparticles. *Atmos. Res.*, **194**, 100–108.
 170. Zhuravlev, L.T. (2000) The surface chemistry of amorphous silica. Zhuravlev model. *Colloids Surfaces A Physicochem. Eng. Asp.*, **173** (1–3), 1–38.
 171. Simpson, J.T., Hunter, S.R., and Aytug, T. (2015) Superhydrophobic materials and coatings: a review. *Reports Prog. Phys.*, **78** (8), 86501.
 172. Nayshevsky, I., Xu, Q., Barahman, G., and Lyons, A. (2017) Anti-reflective and anti-soiling properties of KleanBoost™, a superhydrophobic nano-textured coating for solar glass. *2017 IEEE PVSC-44*.
 173. Pan, X., Zhang, S., Xu, J., et al. (2017) Performance of Different Anti-Reflective Coated Glass for PV Modules. *EU PVSEC 2017*.
 174. Ilse, K., Rabanal, J., Schönleber, L., et al. (2017) Comparison of Indoor and Outdoor Soiling Experiments for different Glass Coatings and Microstructural Analysis. *EU PVSEC 2017*.
 175. Quan, Y.-Y., and Zhang, L.-Z. (2017) Experimental investigation of the anti-dust effect of transparent hydrophobic coatings applied for solar cell covering glass. *Sol. Energy Mater. Sol. Cells*, **160** (August 2016), 382–389.
 176. Isbilir, K., Maniscalco, B., Gottschalg, R., and Walls, J.M. (2017) Test Methods for Hydrophobic Coatings on Solar Cover Glass. *EU PVSEC 2017*.
 177. Glaubitt, W., and Loebmann, P. (2011) Anti-soiling effect of porous SiO₂ coatings prepared by sol–gel processing. *J Sol-Gel Sci Technol*, (59), 239–244.
 178. Figgis, B., Ennaoui, A., Ahzi, S., and Rémond, Y. (2017) Review of PV soiling particle mechanics in desert environments. *Renew. Sustain. Energy Rev.*, **76**, 872–881.
 179. Walpole, R.E., Myers, R.H., Myers, S.L., and Ye, K. (2012) *Probability statistics for engineers scientists, 9th edition*, Prentice Hall.
 180. Thornton, J. (1992) The effect of sandstorms on PV arrays and components. *1992 Sol. World Congr.*
 181. Etyemezian, V. (2017) Mean flow through utility scale solar facilities and preliminary insights on dust impacts. *J. Wind Eng. Ind. Aerodyn.*, **162** (February 2016), 45–56.
 182. Dammak, R., Bahloul, M., Chabbi, I., and Azri, C. (2016) Spatial and temporal variations of dust particle deposition at three “urban/suburban” areas in Sfax city (Tunisia). *Environ. Monit. Assess.*, **188** (6), 336.
 183. Tamhane, A.C., and Dunlop, D.D. (2000) *Statistics and Data Analysis: From Elementary to Intermediate*, Prentice-Hall, Inc.

184. Green, D.H., Hibberson, W.O., Rosenthal, A., et al. (2014) Experimental study of the influence of water on melting and phase assemblages in the upper mantle. *J. Petrol.*, **55** (10), 2067–2096.
185. Khodirevskaya, L.I., and Aranovich, L.Y. (2016) Experimental Study of Amphibole Interaction with H₂O–NaCl Fluid at 900°C, 500 MPa: toward Granulite Facies Melting and Mass Transfer. *Petrologiya*, **24** (3), 235–254.
186. Frantz, J.D., Popp, R.K., and Boctor, N.Z. (1981) Mineral-solution equilibria—V. Solubilities of rock-forming minerals in supercritical fluids. *Geochim. Cosmochim. Acta*, **45** (1), 69–77.
187. Wuddivira, M.N., Robinson, D.A., Lebron, I., et al. (2012) Estimation of Soil Clay Content from Hygroscopic Water Content Measurements. *Soil Sci. Soc. Am. J.*, **76** (5), 1529–1535.